Solid oxide fuel cells for ships

System integration concepts with reforming and thermal cycles

van Biert, Lindert

DOI
10.4233/uuid:dd1f7899-38ee-4c78-a5b0-a6fa92c90f56

Publication date
2020

Document Version
Final published version

Citation (APA)
van Biert, L. (2020). *Solid oxide fuel cells for ships: System integration concepts with reforming and thermal cycles*. [Dissertation (TU Delft), Delft University of Technology]. https://doi.org/10.4233/uuid:dd1f7899-38ee-4c78-a5b0-a6fa92c90f56

SOLID OXIDE FUEL CELLS FOR SHIPS

SYSTEM INTEGRATION CONCEPTS WITH REFORMING AND THERMAL CYCLES

LINDERT VAN BIERT

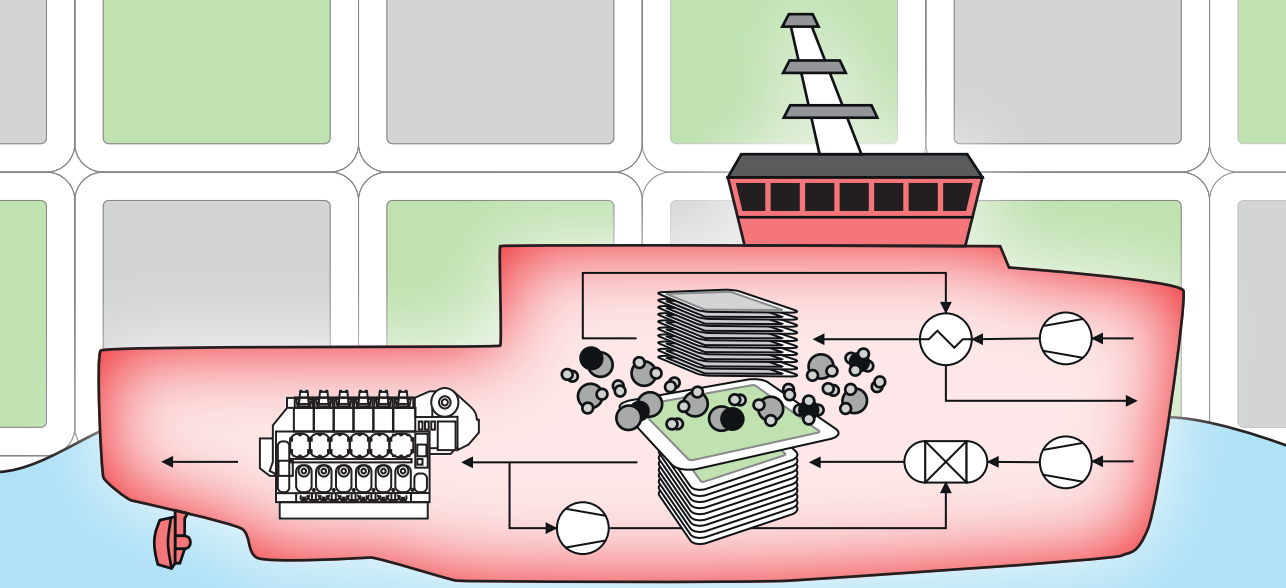

SOLID OXIDE FUEL CELLS FOR SHIPS

SYSTEM INTEGRATION CONCEPTS WITH REFORMING AND THERMAL CYCLES

SOLID OXIDE FUEL CELLS FOR SHIPS

SYSTEM INTEGRATION CONCEPTS WITH REFORMING AND THERMAL CYCLES

Proefschrift

ter verkrijging van de graad van doctor
aan de Technische Universiteit Delft,
op gezag van de Rector Magnificus prof. dr. ir. T. H. J. J. van der Hagen,
voorzitter van het College voor Promoties,
in het openbaar te verdedigen op
vrijdag 14 februari 2020 om 12:30 uur

door

Lindert VAN BIERT

Werktuigbouwkundig Ingenieur, Technische Universiteit Delft, Nederland,
geboren te Rotterdam, Nederland.

Dit proefschrift is goedgekeurd door de promotoren.

Samenstelling promotiecommissie:

Rector Magnificus	voorzitter
Prof. dr. P. V. Aravind	Technische Universiteit Delft, promotor
Ir. K. Visser	Technische Universiteit Delft, copromotor
Onafhankelijke leden:	
Prof. ir. J. J. Hopman	Technische Universiteit Delft
Prof. dr. ir. B. J. Boersma	Technische Universiteit Delft
Prof. dr. ir. R. G. van de Ketterij	Nederlandse Defensie Academie
Prof. dr. ir. D. M. J. Smeulders	Technische Universiteit Eindhoven
Dr. D. S. Ghosh	Simon Fraser University (Canada)

The research in this dissertation is part of the research programme '*GasDrive: Minimizing emissions and energy losses at sea with LNG combined prime movers, underwater exhausts and nano hull materials*' (project 14504) of the Netherlands Organisation for Scientific Research, domain Applied and Engineering Sciences (TTW).

Keywords: Solid oxide fuel cells, alternative fuels, maritime application, combined cycles, dynamic modelling, direct internal reforming, kinetics

Printed by: Ipskamp printing

Front & Back: *Sofcheckership* by L. van Biert

ISBN 978-94-6366-248-2

An electronic version of this dissertation is available at
http://repository.tudelft.nl/.

The value of an idea lies in the using of it.

Thomas Alva Edison

CONTENTS

SUMMARY

Shipping plays an important role in the global supply of goods and energy, as round 90% of international cargo is carried by ships. The maritime industry enables exploration, harvesting and transport of offshore resources as well, such as energy, food and minerals. In addition, ships are indispensable for coastal maintenance work and the transport of energy and information through a submarine network of pipelines and cables.

Although the cargo specific emissions are low, shipping contributes significantly to the global greenhouse gas and hazardous air pollutant emissions. Therefore, the International Maritime Organization has announced stringent emission limits on sulphurous and nitrous oxides emissions, particularly in environmental control areas, and agreed to reduce the greenhouse gas emissions from ships by at least 50% in 2050.

The fuel bound emissions, such as carbon dioxide and sulphurous oxides, can be reduced by adopting alternatives to the heavy fuel oils used today. In addition, fuel cells can convert clean fuels into electricity with high efficiencies, producing practically no hazardous compounds. The relatively high operating temperature makes solid oxide fuel cells especially interesting for three reasons: they are less prone to contamination, direct internal reforming (DIR) of hydrocarbons on the anode is possible and any remaining heat may be used in a thermal cycle.

In this dissertation, maritime fuel cell application is reviewed with regard to efficiency, gravimetric and volumetric density, dynamics, environmental impact, safety and economics. Subsequently, various aspects of SOFC system integration with thermal cycles and reforming are studied. Combining SOFCs with either gas turbines, a steam turbine or reciprocating engine is compared in a thermodynamic analysis. One-dimensional dynamic models are developed to simulate both single cells and stacks in detail, and experiments are conducted to derive intrinsic methane steam reforming (MSR) kinetics on nickel-ceria anodes. These kinetics are implemented in the stack model to analyse different reforming concepts in SOFC systems. Finally, challenges and oppotunities of maritime SOFC application are discussed.

The review of maritime fuel cell application shows that low temperature polymer electrolyte membrane fuel cells and liquefied hydrogen provide a compact solution if refuelling once in several hours is possible. However, SOFCs and more energy dense fuels, such as alkanes, alcohols, ethers or ammonia may be preferred for ships with longer mission requirements, particularly if the high temperature heat produced by the electrochemical reaction is used for reforming or to generate additional power in a thermal bottoming cycle.

System efficiencies of SOFCs combined with gas turbines, a steam turbine or reciprocating engine are compared in a thermodynamic analysis for various fuel utilisations, cell voltages and average temperatures in the stack, as well as different gas turbine compression ratios. The highest combined cycle efficiencies are attained by the SOFC-steam turbine combined cycle, at high fuel utilisations and cell voltages. Integration with gas

turbines is more attractive for moderate fuel utilisations and cell voltages. In contrast to the steam turbine-combined cycle, an optimum fuel utilisation exists for the gas turbine combined systems. The SOFC-reciprocating engine combined cycle yields the lowest system efficiencies, but may offer advantages regarding operational flexibility, load transients and reduced capital cost.

One-dimensional dynamic models are developed of a single cell and stack to study the effects of internal reforming. The stack model is validated with power curves reported by the manufacturer for three different fuel compositions. The single cell model is used to validate two kinetic models for the direct internal methane steam reforming (MSR) reaction, derived from experimental data in previous work. The kinetic models are then used to simulate DIR in the stack. Both predict more realistic temperature profiles in the stack than when the reaction is assumed to be infinitely fast, but the significant difference between the two models indicates the need to determine the intrinsic rate determining kinetics.

The individual effects of the methane, steam and hydrogen partial pressures as well as temperature on the MSR reaction rate are experimentally studied on single cells. Various kinetic models for the MSR reaction are regressed with an ideal plug flow reactor model. A Langmuir-Hinshelwood mechanism, consistent with associative adsorption of methane and dissociative adsorption of steam, is selected because it shows good agreement with the experimental data, provides a physically sound explanation and is thermodynamically consistent.

The Langmuir-Hinshelwood model is implemented in the dynamic stack model to simulate internal temperature profiles and cell voltages for various system concepts, in which a part of the fuel is pre-reformed prior to the stack. This is done either adadiabatic, which implies that the reacting gases are cooled by the endothermic reaction, or allothermal, where a contant temperature is maintained by an external heat source. Steam is either supplied by evaporating water, which is condensed from the exhaust gases, or by recirculating a part of the anode off-gas. The cell voltages obtained from stack simulations are then used to calculate the corresponding system efficiencies.

Adiabatic pre-reforming and anode off-gas recirculation are found to reduce the cell voltage compared to allothermal pre-reforming and water recycling for a constant stack power. In addition, adiabatic pre-reforming induces high temperature gradients in the stack. Anode off-gas recirculation increases the power density compared to water recirculation for low fuel utilisations, but this effect reverses for high fuel utilisations. The highest efficiencies are obtained with allothermal pre-reforming and water recirculation, but high stack efficiencies do not necessarily result in high system efficiencies. For example, high degrees of DIR lower the stack temperature, cell voltage and stack efficiency, but reduce the parasitic power consumption by the cathode air blower as well.

The main finding of the dissertation is that SOFC systems integrated with reforming and thermal cycles may provide electricity, heating and cooling on ships from a variety of fuels with high efficiency, reliability and availability, while they produce virtually no pollutants, noise and vibrations. The most important challenges are the reduction of the capital cost and time required for a cold start, as well as increasing the power density and load following capabilities.

SAMENVATTING

De scheepvaart speelt een belangrijke rol in het wereldwijde transport van goederen en grondstoffen, omdat ongeveer 90% van het internationale vrachtvervoer plaats vindt met schepen. De maritieme industrie maakt het mogelijk om energie, voedsel en mineralen te vinden, winnen en transporteren. Daarnaast is de scheepvaart onmisbaar voor onder andere kustonderhoud en het transport van energie en informatie via een netwerk van pijplijnen en kabels op de zeebodem.

Ondanks dat de emissies per ton mijl vervoerde vracht relatief laag zijn, is de scheepvaart verantwoordelijk voor een significant deel van de wereldwijde uitstoot van broeikasgassen en andere schadelijke stoffen. Daarom heeft the International Maritime Organization strikte emissienormen aangekondigd om de uitstoot van zwaveloxiden en stikstofoxiden te beperken, en zich bovendien ten doel gesteld om de totale broeikasgasuitstoot van de scheepvaart in 2050 ten minste te hebben gehalveerd.

De emissies die met de gebruikte brandstof samenhangen, zoals koolstofdioxide en zwaveloxiden, kunnen gereduceerd worden door alternatieven te gebruiken voor de fossiele olie die vandaag de dag gangbaar is, zoals *groene* waterstof of methanol. Brandstofcellen kunnen deze schone brandstoffen met hoge rendementen omzetten in elektriciteit, zonder dat daarbij schadelijke stoffen uitgestoten worden. De relatief hoge bedrijfstemperatuur maakt vaste-oxide brandstofcellen (solid oxide fuel cells, SOFCs) om drie redenen bijzonder interessant: ze zijn minder gevoelig voor vervuiling, direct intern reformen (direct internal reforming, DIR) van koolwaterstoffen aan de anode is mogelijk en eventuele restwarmte kan in een thermische cyclus benut worden.

In dit proefschrift wordt eerst een literatuuroverzicht gegeven van de toepassing van brandstofcellen in de scheepvaart, waarbij rendement, specifiek vermogen, compactheid, dynamica, impact op het milieu, veiligheid en kosten in beschouwing zijn genomen. Vervolgens worden verscheidene aspecten met betrekking tot de systeemintegratie van SOFCs met thermische cycli en reforming onderzocht. Systemen waarin SOFCs gecombineerd worden met gas turbines, een stoom turbine of zuigermotor worden vergeleken in een thermodynamische analyse. Eendimensionale dynamische modellen worden ontwikkeld om een SOFC-stack (stapel) in detail te simuleren, en de intrinsieke kinetica van de methaan-stoom reforming (methane steam reforming, MSR) wordt experimenteel bepaald op nikkel-cerium anodes. De kinetica wordt vervolgens gebruikt in het model van de stack om verschillende reformingconcepten in SOFC-systemen te onderzoeken. Uiteindelijk worden kansen en uitdagingen voor de maritieme toepassing van SOFCs besproken.

Het literatuuroverzicht laat onder andere zien dat brandstofcellen met een lage werkingstemperatuur in combinatie met waterstof een compacte oplossing bieden wanneer na een tiental uren nieuwe brandstof gebunkerd kan worden. SOFCs bieden in combinatie met brandstoffen met een hogere energiedichtheid, zoals alkanen, alcoholen, ethers of ammonia, mogelijk een beter alternatief wanneer minder frequent brandstof

gebunkerd kan worden. De toepassing van SOFCs is met name interessant wanneer de restwarmte die vrijkomt bij de elektrochemische reactie gebruikt wordt voor het reformen van brandstof of om extra vermogen op te wekken in een thermodynamische cyclus.

De systeemrendementen van SOFCs gecombineerd met gasturbines, een stoomcycles of zuigermotor, worden in een thermodynamische analyse vergeleken voor verschillende brandstofutilisatiefracties, celvoltages en temperaturen in de stack, en een reeks compressieratio's in de gasturbines. De hoogste rendementen worden gehaald door integratie met een stoomcycles, indien de brandstofutilisatiefractie en het voltage zo hoog mogelijk zijn. Integratie met gasturbines wordt echter aantrekkelijker naarmate de brandstofutilisatiefractie en het celvoltage afnemen. In tegenstelling tot de combinatie met een stoomcyclus blijkt er bovendien een optimale brandstofutilisatiefactor voor de met gasturbines gecombineerde systemen te zijn. Integratie van een SOFC met en zuigermotor leidt tot de laagste rendementen, maar ondanks dat kunnen de operationele flexibiliteit, dynamische belastbaarheid en lagere investeringskosten dit systeem interessant maken.

Om het effect van intern reformen nader te onderzoeken zijn eendimensionale dynamische modellen van een enkele SOFC en een stack ontwikkeld. Het model is gevalideerd met vermogenskrommen voor drie verschillende brandstofsamenstellingen, gespecificeerd door de fabrikant. Het model van de enkele cel is gebruikt om twee kinetische modellen voor de directe interne MSR reactie te valideren, verkregen middels regressie van experimentele data uit een eerdere studie. De twee kinetische modellen zijn vervolgens gebruik om DIR in de SOFC-stack te simuleren. Beiden voorspellen realistischere temperatuurprofielen in de stack dan wanneer aangenomen wordt dat de reactie oneindig snel is, maar het significante verschil tussen de twee modellen duidt erop dat de intrinsieke kinetica van de MSR reactie bepaald moet worden.

De individuele effecten van de partiële methaan-, stoom- en waterstofdruk en de temperatuur op de snelheid van de MSR reactie is experimenteel bepaald voor een enkele cel met een nikkel-ceriumanode. Een ideaal propstroomreactormodel is vervolgens gebruikt voor de regressie van verschillende kinetische modellen. Een Langmuir-Hinshelwood mechanisme, met associatieve adsorptie van methaan en dissociatieve adsorptie van stoom, is geselecteerd omdat het goed in overeenstemming blijkt met de experimentele data, fysisch plausibel is en thermodynamisch consistent is.

De Langmuir-Hinshelwood kinetica is geïmplementeerd in het dynamische model van de SOFC-stack om de interne temperatuurprofielen en voltages te simuleren voor verschillende systeemconcepten met reforming. Een deel van de brandstof wordt in de onderzochte concepten al voor de stack gereformd (pre-reformen). Dit gebeurt dan wel adiabatisch, waarbij het reagerende gas afkoelt door de endotherme reactie, dan wel allothermisch, waarbij de temperatuur constant gehouden wordt door een externe warmtebron. Stoom wordt bijgemengd door water te verdampen, dat op zijn beurt uit de uitlaatgassen is gecondenseerd, of door een deel van het uitlaatgas van de anode te recirculeren. De met deze simulaties verkregen voltages zijn vervolgens gebruikt om de overeenkomstige systeemrendementen te berekenen.

Adiabatisch pre-reformen en het recirculeren van het uitlaatgas van de anode blijken het celvoltage te verlagen ten opzichte van allothermische pre-reformen en het verdampen van water, indien het door de SOFC geleverde vermogen constant is. Adiabatisch pre-reformen leidt bovendien tot hogere temperatuurgradiënten in de stack. Het recir-

culeren van het anode-uitlaatgas blijkt de vermogensdichtheid in de stack te verhogen vergeleken met het verdampen van water als de brandstofutilisatiefractie in de SOFC laag is, maar het tegenovergestelde gebeurt wanneer de brandstofutilisatiefractie hoog is. De hoogste stack- en systeemrendementen worden verkregen door allothermisch pre-reformen van de brandstof in combinatie met stoom verkregen uit gecondenseerd water. Hoge stackrendementen leiden echter niet per definitie tot hoge systeemrendementen. Veel intern reformen verlaagt bijvoorbeeld de gemiddelde temperatuur in de stack, en daarmee het operationele voltage en het stackrendement, maar verlaagt ook het elektrisch vermogen dat de luchtpomp gebruikt.

De belangrijkste bevinding van deze dissertatie is dat systemen waarin SOFCs geïntegreerd zijn met reforming en thermodynamische cycli verschillende brandstoffen met hoge rendementen en betrouwbaarheid omzetten in elektriciteit, warmte en koude, waarbij bovendien nauwelijks schadelijke stoffen, geluid en trillingen worden geproduceerd. De grootste uitdagingen zijn het reduceren van de investeringskosten en de lange opstarttijden, alsmede het verhogen van de vermogensdichtheid en de snelheid waarmee de belasting veranderd kan worden.

1

INTRODUCTION

1

1.1. THE ENERGY TRANSITION IN THE MARITIME SECTOR

The shipping industry is of vital importance to the growing world population, as it provides a crucial link in the globalising production and use of raw materials, goods and energy. Over 90% of the worlds global trade is carried over seas by ships, as this is the most cost-effective way to transport intercontinental cargo [1]. It is expected that global trade will increase with more than 35% by 2050 [2].

Even though shipping provides the most efficient and cost effective global transport solution, it remains a significant contributor to the global emissions of greenhouse gases (GHGs), volatile organic compounds (VOCs), particulate matter (PM), sulphurous oxides (SO_X) and nitrous oxides (NO_X). The shipping industry currently accounts for 3-5% of global carbon dioxide (CO_2) emissions and about 5% of global SO_X emissions [3]. The expected increment in global trade will consequently increase the environmental impact of the shipping industry if no counter measures are taken [4].

GHG and SO_X emissions originate from the almost exclusive use of fossil fuels in shipping, such as heavy fuel oil [5]. Other emissions are associated with the combustion process in diesel engines, which have become the conventional power technology for the vast majority of the shipping industry. Diesel engines provide an efficient and reliable solution, but the high combustion temperature favours NO_X formation, while incomplete combustion results in the emission of VOCs [6]. Until recently, there was little incentive for the maritime industry to reduce emissions from their operations, since it increases the cost of ownership and few regulations on the environmental impact existed at sea [7].

The global community agreed in 2015 to eliminate the net emission of GHGs in the coming decades and limit global warming to a maximum of 1.5-2°C [8]. In response, the International Maritime Organization (IMO) agreed to cut the overall carbon dioxide emissions from the shipping sector by 50% in 2050 [9]. In addition, the IMO has announced stringent global emission limits on SO_X, and, in so-called environmental control areas, on NO_X [10]. A combination of new energy carriers and power conversion technology will be required to meet the ambitious targets and reduce both GHG and hazardous air pollutant (HAP) emissions from shipping.

1.2. REDUCING EMISSIONS FROM SHIPPING

The shipping sector relied on emission-free propulsion from sails until fuels were introduced around the start of the 19th century. Ships propelled with engines eventually outperformed their sailing competitors in terms of speed, reliability and economic profitability, despite the additional fuel costs. Although a revival of sail assisted propulsion can eliminate emissions from shipping entirely, these ships may not be able to comply with modern maritime transport requirements in terms of availability, reliability and redundancy. Therefore, alternative emission-free propulsion concepts are highly desired.

1.2.1. FUEL EMISSIONS

The adoption of conventional fuels from renewable feedstocks, so-called *drop-in* fuels like synthetic or biodiesel, may eliminate GHG emissions from shipping without substantial

changes to the fuel infrastructure and propulsion system [11]. However, it is unclear if such fuels can be produced at the scale and cost level required for the maritime industry. Therefore, the shipping sector is actively exploring alternatives to diesel fuel oils.

Liquefied natural gas (LNG) has been introduced in the shipping sector as a cost-competitive alternative for diesel, which reduces the emission of GHGs, PM, SO_X and NO_X [12]. The specific CO_2 emissions of engines fuelled with natural gas are usually lower than for diesel fuels. However, since LNG is still from fossil origin, it may only serve as a transition fuel towards alternatives produced from renewable feedstocks, such as *green* methane, alcohols, ammonia and hydrogen [13]. Battery-electric technology has become an interesting alternative for automotive applications, but the energy density of current battery technology is by far not sufficient to cover typical sailing distances [14].

Hydrogen is being adopted lately in other heavy duty transport sectors, such as buses, trucks and trains as an alternative to battery-electric propulsion [15]. In addition, hydrogen is gradually finding its way into passenger vehicles as well, despite the limited refuelling infrastructure [16]. Hydrogen has a high energy density compared to batteries, allows fast refuelling and offers a high availability, while it is emission-free if the hydrogen is produced from a renewable source, such as electrolysis of renewable electricity [17].

It remains unclear which renewable energy carrier is most suitable for the maritime sector, since the technical and economical requirements are distinctively different from land-based transportation. For example, hydrogen may not be sufficiently energy dense to cover longer sailing distances with acceptable storage volumes. Ultimately, the entire logistic chain, including production, transport, storage and use, determines the suitability of a renewable energy carrier [18]. Moreover, the most suitable renewable energy may differ for various types of vessels.

1.2.2. POWER PLANT EMISSIONS

Even if renewable fuels are introduced to eliminate fuel bound emissions, those originating from the combustion process in the engine still need to be addressed. Engine manufacturers attempt to do so by bringing down peak temperatures and pressures in the cylinder, while maintaining high efficiency, for example with exhaust gas recirculation, staged or sequential turbocharging, late Miller timing and advanced fuel injection systems [19, 20]. Alternatively, emissions can be eliminated from the exhaust gas with scrubbers or selective catalytic reduction [21]. A combination of engine improvements may be required to meet future emission regulations, and this will inevitably increase the complexity, size and cost of ship propulsion systems.

Diesel engines may eventually be replaced with cleaner alternatives, such as gas turbines or fuel cells. Gas turbines can attain lower NO_X emissions, have a high power density and good transient capabilities, but their fuel efficiency is relatively low and their maintenance cost is high [22]. The higher fuel consumption increases GHG emissions, especially when fossil fuels are used. This illustrates the intrinsic trade-off between CO_2 emissions and NO_X formation in conventional power plants based on thermal cycles, as both are favoured by high combustion temperatures. In contrast, fuel cells convert chemical energy directly into electricity without the need for high combustion temperatures. As a result, fuel cell systems can generate electricity with high efficiencies

and no emissions. Therefore, fuel cells can reduce both CO_2 and NO_X emissions, even if fossil fuels are used.

Low temperature polymer electrolyte membrane fuel cell (PEMFC) systems are currently the technology of choice for most transport applications, since they have a high power density and allow fast cold start-up and load transient [23]. Other fuel cell types, such as the phosphoric acid fuel cell (PAFC), molten carbonate fuel cell (MCFC) and solid oxide fuel cell (SOFC) are more often used in stationary applications, as they may offer higher efficiency, availability and durability, especially if other fuels than pure hydrogen are used [24]. MCFCs and SOFCs are, for example, deployed in distributed power, continuous uninterrupted power for datacentres and micro- combined heat and power for homes, fuelled with biogas or natural gas, for which an infrastructure is readily available [25].

It is unclear if fuel cells are suitable for maritime application and, if so, which type of system has the best prospects. Although PEMFCs are an obvious candidate if pure hydrogen is readily available, on-board hydrogen storage may take a lot of space on ships with longer mission profiles. In addition, the power requirements of ships may resemble more those of stationary than automotive applications, such as a high availability, efficiency and durability. SOFCs are typically used in stationary applications for these reasons and may, therefore, be suitable for vessels where a lower power density is acceptable and auxiliary energy storage systems can cover load transients.

Hybrid propulsion concepts may play an important role in the maritime energy transition. For example, vessels are already being equipped with dual-fuel propulsion plants to be able to use both diesel fuel or LNG, depending on local availability and regulations [26]. In addition, diesel-electric propulsion is being adopted as it enables advanced propulsion concepts, for example the use of batteries for redundancy, peak shaving, silent sailing and boost mode [14].

The Dutch national project *GasDrive* aims to investigate several aspects related to ships fuelled with natural gas. This includes the integration of SOFCs with combustion engines, using combustible elements in the fuel cell exhaust gases to enhance the combustion process in the engine. This reduces losses due to the limited fuel utilisation in the SOFC, while improving the efficiency of the engine and potentially reducing unburned hydrocarbon emissions. In addition, an underwater exhaust and gas lubrication system with nano hull-coatings is investigated to reduce the drag resistance of vessels. The combination of LNG, high power plant efficiencies, low emissions and reduced drag resistance may substantially reduce emissions of both GHGs and pollutants. This dissertation contributes to the investigation on the efficient use of LNG in SOFCs and the combined cycle operation with reciprocating engines in the GasDrive project.

1.3. POWER GENERATION WITH SOLID OXIDE FUEL CELLS

LNG is adopted by the maritime sector as an alternative for diesel fuel in the transition to renewable energy carriers, as it is available, affordable and enables to meet near-future emission limits without the need for exhaust gas after-treatment. SOFC systems can improve the well-to-propeller efficiency and reduce emissions from ships even further, since they can generate electricity with record efficiencies and virtually no emissions of NO_X, SO_X, PM and VOCs from natural gas [25]. Therefore, this section provides a

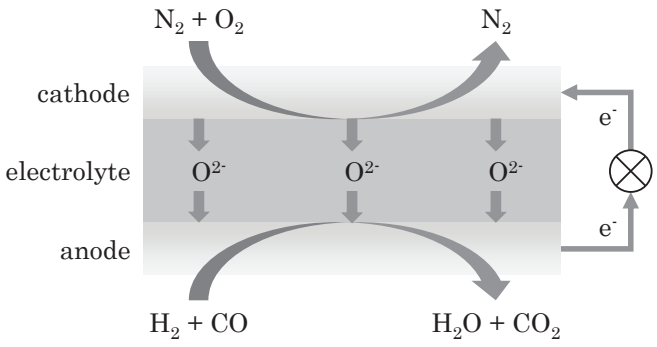

Figure 1.1: Schematic overview of the working principle of a SOFC.

background on the fundamental principles of SOFCs, their ability to reform natural gas internally, as well as systems and applications.

1.3.1. SOFC PRINCIPLES

SOFCs are usually constructed with two porous electrodes, separated by a dense oxygen ion conducting electrolyte [27]. The electrolyte material is a doped solid oxide, most commonly yttrium doped zirconium oxide (YSZ) or gadolinium doped cerium oxide (GDC). These materials conduct oxide ions at high temperatures. This principle is used to generate an electric current in an external circuit, shown in Figure 1.1. As a consequence, SOFCs have to be operated in a temperature range of 500-1000°C, which is high compared to other fuel cell types.

The fuel electrode, called the *anode*, is usually made from a mix of ceramic electrolyte material and a metal catalyst, most commonly nickel. This ceramic-metal hybrid design is referred to as a *cermet* electrode. Perovskites (ABO_3), such as lanthanum manganite, are often used for the air electrode, or *cathode*, usually with low-valance doping on the A-side to enhance electronic conduction and sometimes transition metal doping on the B-side to enhance oxide ion diffusion [28].

Various SOFC types have been developed in recent years, historically distinguished in tubular or planar design and either operating temperature or type of electrolyte, although these are typically closely related [29]. For example, electrolyte supported cells derive their structural integrity from a thick electrolyte, which dictates high operating temperatures to enhance oxygen diffusion. Other designs with a thin electrolyte supported on a thick anode can be operated at lower temperatures, but have a limited structural integrity. Alternatively, the active layers can be deposited on a perforated or porous sheet of steel. These designs have good mechanic properties, but the operating temperature is usually limited [30]. An overview of these options is presented in Table 1.1.

High operating temperatures enhance the electrochemical reactions, contaminant tolerance and heat integration opportunities. However, the material choices are restricted at these temperatures and the large thermal capacity limits the transient and cold start-up capabilities [31]. Low temperatures, on the other hand, enable the use of materials with

Table 1.1: Overview of common SOFC types distinguished by their structural support, and their type of electrolyte, design, operating temperature and most important advantages and disadvantages.

Structural support	Electrolyte	Cell design	Operating temperature	Advantages & disadvantages
electrolyte	thick YSZ ($\geq 100\,\mu$m)	tubular & planar	>800°C	stable, easy to seal, high ohmic resistance
electrode	thin YSZ ($10-20\,\mu$m)	planar	$600-800$°C	low ohmic resistance, less stable, difficult to seal
metal or substrate	thin YSZ or thick GDC	planar	<600°C	strong support, high polarization resistance

better robustness and manufacturability, but this may compromise the electrochemical performance and heat recovery possibilities [32]. Therefore, low temperature SOFCs are, for example, targeted for heavy duty transport applications, while their high temperature counterparts may be used in large-scale stationary power plants.

SOFCs are less susceptible to impure hydrogen than low temperature fuel cells, due to their higher operating temperature. For example, carbon monoxide can be readily oxidised in the SOFCs and is, therefore, a fuel instead of a contaminant [33]. Similarly, trace compounds like alkali metals and sulphur are less likely to be adsorbed on the catalyst surface at higher operating temperatures, resulting in a higher tolerance to these compounds [34]. This is particularly important when the fuel originates from impure feedstocks, such as fossil fuel or biomass. However, energy dense energy carriers usually still need to be converted to a hydrogen rich syngas mixture to before they can be electrochemically oxidised [35].

1.3.2. REFORMING IN SOFCS

There are several methods to convert hydrocarbons, alcohols and ethers into a mixture suitable for SOFCs, most importantly partial oxidation and reforming. Reforming is the most efficient of the two, and is an endothermic reaction which requires heat and a reforming agent, usually steam [36]. Moreover, the high temperature heat and steam produced by the electrochemical reaction in the SOFC can be used to reform the fuel. This integration option, together with the high tolerance to impurities and the ability to electrochemically oxidise carbon monoxide, makes SOFCs an appealing option if other fuels than hydrogen are used.

An example of a SOFC system fuelled with hydrocarbons is shown in Figure 1.2. The fuel is pre-reformed with steam and the air is pre-heated before they enter the anode and cathode compartment respectively. The outlet gases enter a catalytic burner to combust any un-used fuel. The hot flue gas is then used for pre-reforming, air pre-heating and steam generation. The water required to generate steam may be condensed from the exhaust gases.

An external reformer is often used in SOFC systems, but the reforming reaction may

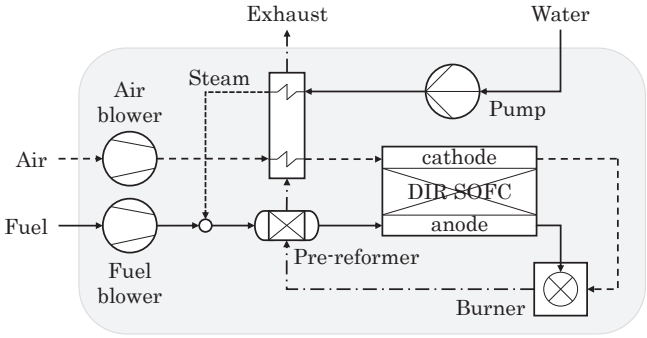

Figure 1.2: Example of an SOFC system layout in which the fuel is pre-reformed with steam.

also proceed directly on the nickel-based catalyst commonly used for the anode [37]. Direct internal reforming (DIR) enables the use of the heat and steam produced through electrochemical oxidation for the reforming reaction. Therefore, less heat and steam need to be supplied to an external reformer. Moreover, less cooling is required, which is usually done with excess cathode air. Since this reduces the power consumption from the cathode air blower, DIR is expected to enhance the efficiency of the SOFC system [38].

Although DIR seems beneficial from a system integration perspective, coupling the endothermic reforming and exothermic hydrogen oxidation reactions proves to be difficult in practice. Reforming tends to take place at the entrance region of the stack, where the methane concentration is high, while hydrogen oxidation is more pronounced at the hot outlet part of the stack [39]. The result is a high temperature gradient across the stack, which may impose deteriorating thermal stresses on the brittle ceramic cell materials [40]. For example, electrodes may delaminate from the electrolyte due to differences in their thermal expansion coefficients.

It is currently unclear to what extent methane can be reformed internally, and how this is affected by stack design and operating conditions. DIR is expected to affect various stack designs differently, and pre-reforming strategies in SOFC systems vary among different system integrators. Engineers may choose to condense water from the exhaust gases or recycle a part of the anode off-gas stream, and opt for different pre-reformer designs. Moreover, the kinetics of the reforming reaction on the anode of commercial SOFCs are usually unknown.

1.3.3. SOFC SYSTEMS AND APPLICATIONS

Most SOFC systems benefit from the possibility to efficiently convert hydrocarbon fuels and are designed to use natural gas or biogas. The high operating temperature of SOFCs offers additional advantages if the heat produced by the electrochemical reaction is further utilised, for example in combined heat and power (CHP) appliances. Various manufacturers offer micro-CHP products with an electric power rating up to 2 kW for residential applications. These units can attain electrical efficiencies over 60% and CHP efficiencies up to 90% based on the lower heating value (LHV), which is remarkable for

this power class [41].

SOFCs are employed in higher power classes as well, most notably in datacentres with powers up to 250 kW per unit [25]. Here SOFCs demonstrate their capability to provide continuous and reliable electricity with LHV efficiencies up to 65%, and a better availability and reliability than the local electricity grid [42]. SOFC developers are constantly extending the lifetime of their products, which is important for stationary applications [43]. It should be noted that this is important for many ships as well, where at least some of the engines are run over 6500 hours per annual [4].

Even higher electrical efficiencies are projected for the SOFC integrated with bottoming cycles, such as Brayton or Rankine cycles [44]. LHV efficiencies in excess of 70% are projected for gas turbines where the fuel combustor is partially replaced with a SOFC [45]. Alternatively, Rankine cycles may be used to recover heat from the hot SOFC exhaust gases [46]. More recently, integration with reciprocating engines was proposed, where unoxidised fuel from the SOFC is combusted in the engine, the heat rejected by the engine is used for reforming or both [47]. This is particularly interesting for ships, considering that reciprocating engines are the workhorse for the maritime industry.

1.4. RESEARCH OBJECTIVES AND SCOPE

This dissertation aims to contribute to the scientific challenges of the energy transition in the maritime industry, and was carried out in the framework of the *GasDrive* project, which aims to *minimise emissions and energy losses at sea with LNG combined prime movers, underwater exhausts and nano hull materials.* More specifically, it presents several studies related to the application of internal reforming solid oxide fuel cell-combined cycles on ships. The main research question of this dissertation is:

How can SOFCs be integrated with reforming and thermal cycles to reduce the emissions of ships?

There are clear opportunities of using internal reforming SOFC-combined cycles on ships. However, while fuel cell systems are slowly finding their way in a variety of products, maritime application is in its infancy. In addition, SOFC system integration concepts with reforming and thermal cycles have been proposed, and it is unclear which is most promising for ships. While DIR may enhance heat integration in SOFC systems, it is unclear how the electrochemical performance and thermal stresses in the stack are affected, especially if the SOFC is subjected typical vessel load transients. Therefore, the following sub questions are defined:

1. How does the application of fuel cell systems affect the design, operation, safety and economics of ships?

Fuel cells have been introduced in a wide variety of applications, such as space crafts, automotive, trains, waste-water treatment plants and datacentres. However, there is little experience with the use of fuel cells on-board ships. Moreover, it is foreseen that

the adoption of fuel cell technology in shipping will be accompanied by a change of the bunker fuel as well.

2. How is the efficiency and power density of different SOFC-combined cycles affected by the operating conditions?

SOFC systems are usually designed for stand-alone operation only, while integration with gas turbines, steam turbines or reciprocating engines may provide operational advantages, such as improvements in the efficiency and load transient capabilities. However, a direct comparison between different combined cycle systems is difficult due to different stack operating parameters assumed in various studies.

3. How can reforming data from single cell experiments be used to model DIR in SOFC stacks dynamically?

Since heat and fuel from the SOFC are used in a bottoming system in combined cycle operation, less heat is available for external reforming and the degree of internal reforming may increase. Therefore, accurate stack models are required to predict the consequences of combined cycle operating conjurations and stack operating parameters on the electrochemical performance and temperature gradients in the stack, for example in control-oriented models used to assess the transient capabilities of SOFCs.

4. What are the intrinsic rate determining kinetics of the methane steam reforming reaction on functional nickel-ceria SOFC anodes?

Accurate simulation of the temperature distribution and electrochemistry within the SOFC stack requires calculation of the spatial distribution of the internal reforming rate on the anode. Kinetic models have been reported in literature, but the majority has been derived on Ni-YSZ substrates rather than the functional Ni-GDC cell assemblies used in many SOFC stacks. Moreover, they are often either empirical or require the evaluation of a numerically stiff multi-step reaction mechanism.

5. How do different steam reforming concepts affect the electrochemistry and temperature gradients in SOFCs?

Various choices can be made regarding the way steam and heat are supplied for the reforming reactions. Steam might be condensed from the exhaust gases, evaporated and mixed with the fresh fuel. The heat in the exhaust gases can be used for evaporation and reforming. However, this may not be ideal if the exhaust gases are further used in a bottoming cycle. In that case, water recycling may be replaced by recirculation of a part of the anode outlet gas, referred to as anode off-gas recirculation (AOGR), and the heated reformer can be replaced with an adiabatic reformer. Although this may prove advantageous from a system efficiency perspective, it affects the electrochemistry and temperature gradients in the SOFC.

6. What are the challenges and opportunities of applying internal reforming SOFCs combined with thermal cycles on ships?

Even if SOFC-combined cycle systems are able to generate electricity from LNG with high efficiencies and low emissions, they should meet several additional requirements to be suitable for maritime power generation. Some of these requirements may impose challenges on the implementation of SOFC technology on vessels, while others can provide additional opportunities for maritime applications.

1.5. RESEARCH METHODOLOGY AND DISSERTATION OUTLINE

Each of the research questions posed in the previous section is addressed in a single chapter of this dissertation. Although they are all related to aspects of the maritime application of DIR SOFC-combined cycles, various methodologies are required to answer every sub question, including a literature survey, a thermodynamic analysis, dynamic modelling, an experimental study, data regression and combinations of those. The dissertation consists of eight chapters, structured as shown in Figure 1.3.

The influence of fuel cell application on the design, operation, safety and economics of ships is investigated in a literature survey in Chapter 2 . The review covers the adoption of alternative ship fuels as well, since the choice for a logistic fuel affects the efficiency of the evaluated fuel cell systems differently. An overview of notable maritime fuel cell demonstrators is presented as well.

A thermodynamic analysis is used to assess the efficiency and exergy losses in different DIR SOFC-combined cycle systems in Chapter 3. System models are built in the in-house developed thermodynamic flow-sheet program Cycle-Tempo. A plug flow reactor model of the SOFC is implemented in Matlab to calculate the power density in the stack with an electrochemical model described by Aguiar et al. [48], since the component model incorporated in Cycle-Tempo accounts for ohmic losses only. The thermodynamic analysis includes a sensitivity analysis to important operating parameters, such as the fuel utilisation in the SOFC, cell voltage, average stack temperature and gas turbine pressure ratio.

In Chapter 4 a detailed 1D SOFC model is developed in Matlab/Simulink to simulate the dynamic behaviour of both an experimental single cell test setup and an integrated stack module (ISM), by changing geometrical information and boundary conditions only. The ISM model is validated with data from the manufacturer, and reforming kinetics are validated with data from single cell experiments. The model calculates species concentration and temperatures profiles from inlet to outlet, and accounts for heat transfer effects in the inactive area of the stack and to the surroundings. Therefore, it can accurately predict the electrochemistry and temperature gradients in the SOFC stack.

Detailed calculation of the temperature gradients and electrochemistry in the ISM under DIR conditions requires an intrinsic description of the methane steam reforming (MSR) kinetics. Therefore, Chapter 5 presents MSR experiments carried out on the same electrolyte supported cells with Ni-GDC anodes used in the simulated commercial ISM. The experimental data is then used to parameterise and determine intrinsic internal MSR kinetics. Since the experiments are carried out on the same type of cells used in the commercial ISM used in Chapter 4, the kinetic model can be directly implemented in the dynamic stack model.

Different reforming strategies, based on combinations of either water recycling or

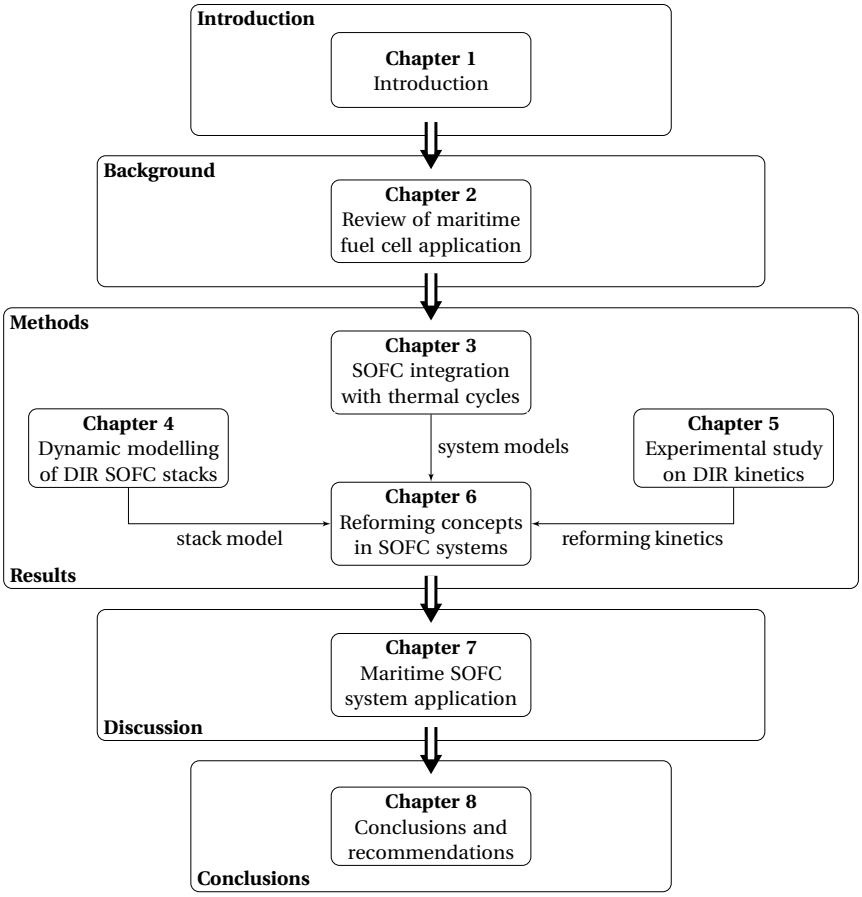

Figure 1.3: Overview of the structure of this dissertation. Chapter 2 discusses fuel cell application in the maritime industry in general. Thermodynamic system models, a dynamic stack model and reforming kinetics are then developed in Chapters 3 to 5 respectively. These are then used to analyse different internal reforming concepts for SOFC systems in Chapter 6. Finally, Chapter 7 discusses the implications of SOFC application on ships.

AOGR and isothermal or adiabatic pre-reforming, are evaluated in Chapter 6. The electrochemical performance and temperature gradients in the stack are simulated in detail with the dynamic model developed in Chapter 4 and the reforming kinetics obtained in Chapter 5. Moreover, a thermodynamic analysis as presented in Chapter 3 is used to calculate the system efficiencies for different reforming strategies based on the electrochemical performance simulated with the dynamic model.

Chapter 7 discusses the implications of the different reforming concepts presented in Chapter 6 for the thermal cycle integration options analysed in Chapter 3. Moreover, the power, size, fuel efficiency, life-cycle costs, dynamics, reliability, availability, maintainability, safety, emissions and comfort of SOFC systems is analysed to assess their suitability for maritime application, and challenges and opportunities are identified. Finally, the status of maritime SOFC application is presented and an outlook is provided.

Chapter 8 summarises the findings in different parts presented in this dissertation. In addition, the conclusions regarding the main and sub research questions are provided, and recommendations are given for future work.

2

FUEL CELL SYSTEMS FOR MARITIME APPLICATIONS

This chapter has been published in Journal of Power Sources **327**, (2016) [49].

2.1. INTRODUCTION

Clean and efficient alternatives for internal combustion engines are highly desired in shipping, and fuel cells are considered to be one of the most promising solutions [50]. Fuel cell systems have proven their ability to produce electricity with LHV efficiencies up to 60% using natural gas (NG) in residential applications [41]. Moreover, efficiencies over 70% are projected when they are combined with gas turbines or reciprocating internal combustion engines [45, 51, 52].

Fuel cell technology prospects have motivated several studies to assess the potential and applicability of such systems in the maritime environment. In addition, a number of demonstrator systems has been developed and tested on ships. These investigations vary from a feasibility study of various diesel-fuelled fuel cell systems [53], to a commercialised, hydrogen fuelled, air independent propulsion system for submarines [54]. Whether fuel cell systems will be applied more general in the maritime environment depends on their ability to meet the requirements of on-board power generation.

Fuel cell systems differ substantially from each other, and it is not clear which system has the best future prospects. Therefore, an overview of fuel cell systems is provided in Section 2.2. Various fuel cell systems are then evaluated in Section 2.3 against important performance criteria for maritime application: fuel consumption, power and energy density, load-following capabilities, environmental impact, safety and economics. An overview of experience with maritime fuel cell application is presented in Section 2.4, Section 2.5 summarises the findings, and concluding remarks are made in Section 2.6.

2.2. FUEL CELL SYSTEMS

Electrical power in ships is mainly used for auxiliaries, although there is a tendency towards the use of electricity for propulsion as well. For example in hybrid configurations, and in the *all-electric ship* concept, where advanced electrical propulsion techniques and electrical storage components can be used [55, 56].

A vast majority of ships currently uses diesel generators to produce electricity, where chemical energy is converted into electricity via thermal and mechanical energy. In contrast, fuel cells convert chemical energy directly into electrical energy, thus omitting the indirect route via thermal energy in combustion engines. The absence of expansive, high temperature combustion reduces NO_X formation, noise and vibrations, while high efficiencies can still be achieved [57].

Just like batteries, fuel cells are modular in nature and the intrinsic performance of a single cell is not different from a large stack [58]. As a result, power production can be distributed over the ship without a penalty of increased fuel consumption, while electricity transport losses are reduced and redundancy is improved. For this reason, fuel cell systems are successfully applied in back-up power systems and data centres [59]. Furthermore, fuel cell systems have good part load characteristics, since increased mechanical losses affect only the parasitic load of the auxiliary components, such as compressors, while electrochemical losses are reduced [41, 60].

The selected fuel cell system and logistic fuel will have a large impact on the suitability for maritime application. Therefore, the implications of fuel cell system choices on overall

efficiency, complexity and power density are analysed in this section. Commonly applied fuel cell types, fuelling options and fuel processing equipment, used to convert various logistic fuels into hydrogen rich gas, are discussed.

2.2.1. FUEL CELL TYPES

A variety of fuel cell types with distinct characteristics has been developed. The low and high temperature (LT/HT) PEMFC, PAFC, MCFC and SOFC will be considered in this review and are briefly introduced. Some relevant characteristics are summarised in Table 2.1.

The LT-PEMFC has known rapid development in the last decades, and achieved high power densities and good transient performance. Its membrane consist of a proton-conducting wetted solid polymer [61]. The necessity of a wet membrane, while the gas-diffusion pores have to remain dry, dictates an operational temperature of 65 to 85°C and complicates water management [62]. At low temperatures, the use of platina is required to catalyse the electrochemical reaction [63]. Another important disadvantage of the low operational temperature is the limited tolerance to fuel impurities. In particular carbon monoxide (CO) deactivates the catalyst, because of its strong surface adsorption at low temperatures [64, 65].

The membrane of the PAFC consists of a silicon carbide matrix saturated with liquid phosphoric acid. The higher operating temperature, 140 to 200°C, reduces the required platinum loading and increases CO tolerance. The low power density and durability issues have so far limited the commercial success of the PAFC. A new membrane operating in the same temperature region has been developed in the past decade in an attempt to overcome these issues. This membrane essentially combines a polymer electrolyte and phosphoric acid membrane, and is therefore known as the high temperature HT-PEMFC [66, 67].

Platinum can be replaced with cheaper catalysts, such as nickel, in the high temperature fuel cell classes. Furthermore, CO becomes a fuel rather than a contaminant to the fuel cell. Another advantage is the opportunity to use high temperature waste heat and steam, for example in a bottoming cycle or for fuel processing. The MCFC is a relatively mature high temperature fuel cell and operates in a range of 650 to 700°C. MCFCs are commercially available, but still struggle with high cost, limited life time and low power density [68, 69].

The SOFC has been heavily investigated during recent decades, and various classes of SOFCs have been developed over the years, with operating temperatures ranging from 500 to 1000°C. The low temperature classes are mainly applied in stand-alone fuel cell products, with electrical efficiencies up to 60% [41, 70], while the high temperature SOFCs are targeted for combined operation with gas turbines, where efficiencies over 70% are projected [45]. Although a promising type, their limited development state, mechanical vulnerability and high cost have so far limited wide-spread adoption of SOFC technology [71].

Table 2.1: Overview of commonly applied fuel cell systems, their temperature range, fuel requirements, and the opportunity to reform fuel directly in the fuel cell.

Fuel cell type	Temperature [°C]	Fuel	Poisonous substances	Internal reforming
LT-PEMFC	65-85	H_2	S, CO>10 ppm [65]	no
HT-PEMFC/ PAFC	140-200	H_2	S, CO>3% [67]	no
MCFC	650-700	H_2, CO	S	yes
SOFC	500-1000	H_2, CO	S	yes

2.2.2. BALANCE OF PLANT COMPONENTS

Auxiliary components are required to generate electrical power with a fuel cell stack. These components are usually referred to as the balance of plant (BoP), and make up a large part of the overall system. A distinction can be made between *hot* and *cold* BoP components in high temperature fuel cell systems and systems with fuel processing equipment. Hot BoP components include, for example, heat exchangers and fuel processors, while power conditioning and system controls are classified as cold parts. Many BoP components consume parasitic power or additional fuel.

One class of BoP components is used to supply fuel and oxidant to the stack, and includes pumps, blowers and compressors. Depending on the type of fuel cell, heat exchangers may be present to bring the gas flows to the right temperature, and evaporators are used if liquid fuels are supplied. Gas streams often need filtration and humidification, and the exhaust gasses may contain a significant amount of combustible components, which are usually burned in a catalytic combustor. All gas flows are regulated with control systems and actuators, such as blowers speeds, valves and pressure regulators.

High temperature fuel cells are often equipped with burners to heat the system during start-up. Although high temperature fuel cells are usually cooled with cathode air, the temperature gradients in low temperature fuel cells are too small to achieve sufficient cooling in this way. Therefore, these systems will usually have a separate cooling system.

Since fuel cells generate direct current (DC) power with variable voltage and current, power conditioning equipment, such as DC to alternating current (AC) inverters, are used to generate electricity at grid voltage and frequency. Fuel processing equipment is another important part of the BoP with a substantial influence on the overall efficiency, and will be discussed in detail in Section 2.2.4.

2.2.3. LOGISTIC FUELS

Diesel oil is currently the dominant energy carrier in the maritime industry. Conventional diesel engine-generator sets are entirely accustomed to these fuels, but they can't be used in fuel cells directly. Although direct electrochemical oxidation of various fuels is possible in some fuel cell types, the relatively fast hydrogen oxidation kinetics dominate at practical power densities. This implies that most fuel cells effectively run on hydrogen [72]. Especially low temperature fuel cells oxidise hydrogen exclusively, while some alternative

fuels, such as methane and CO, can be converted internally to hydrogen rich gas in high temperature fuel cells [35, 48].

Most maritime fuel cell studies consider on-board conversion of diesel to hydrogen, since a diesel infrastructure is readily available and hydrogen is significantly more expensive and considerably less energy dense [53, 73–81]. However, the diesel fuel processor increases complexity, cost and size of the fuel cell system. Furthermore, the need to reduce and eventually obviate GHG emissions make the consideration of alternative logistic fuels indispensable. Even though the use of fossil fuels is probably still necessary in the near future, renewable alternatives, for example biofuels or so-called *solarfuels*, will become more important on the long term [82–84].

A paradigm shift towards cleaner fossil fuels and renewable fuels is thus foreseen, but their adoption will depend, among others, on their availability, infrastructure, environmental impact, safety, price, regulations and technical suitability. Logistic fuel selection is part of a larger debate and the interested reader is directed to various dedicated reviews [85–87]. However, the technical suitability for maritime fuel cell systems is part of the scope of this review, hence some options are briefly discussed in this section. An overview of both gravimetric and volumetric energy densities of these fuels is provided in Figure 2.1, showing the energy density of the pure fuel as well as with the storage system included.

HYDROGEN

Hydrogen is the most abundant element in the universe, but is rarely found in its pure form [95]. Although hydrogen can be obtained from various sources, such as biomass or electrolysis, it is currently mostly produced from NG [96]. Hydrogen is suitable for fuel cells, as the electrochemical oxidation kinetics are fast, even at low temperatures. Therefore, it can be used without extensive pre-treatment. As a result, pure hydrogen systems can achieve notable overall power densities [97]. Conversion of hydrogen to electricity with fuel cells is usually more efficient than with internal combustion engines [98, 99].

The low storage density is the most important drawback of hydrogen as a logistic fuel. Hydrogen is often stored in pressurised vessels at either 350 or 700 bar for automotive applications. Alternatively, hydrogen can be stored cryogenic at a temperature of -253°C at ambient pressure, or somewhat higher temperatures and elevated pressures, referred to as *cryocompressed* hydrogen (LH_2) [92–94, 100]. The latter is currently most energy dense physical storage method and, therefore, considered throughout this review. Other options, such as storage in metal hydrides and chemical compounds, are still under investigation [95]. It should be noted that all logistic fuels discussed hereafter can effectively be regarded as hydrogen carriers.

DIESEL

Diesel fuels belong to the heavier crude oil distillation fractions. The carbon chains are relatively long, resulting in a viscous and dense fuel, which is usually difficult to process to a hydrogen-rich gas. The high sulphur content is an additional problem, as both the fuel processing equipment and fuel cell have limited sulphur tolerances (see Table 2.1) [74, 75]. Therefore, the sulphur content should be lowered dramatically for fuel cell application. Alternatively, low-sulphur diesel can be synthesised with the Fischer-Tropsch process [101]. These synthetic diesel fuels can originate from fossil feedstocks,

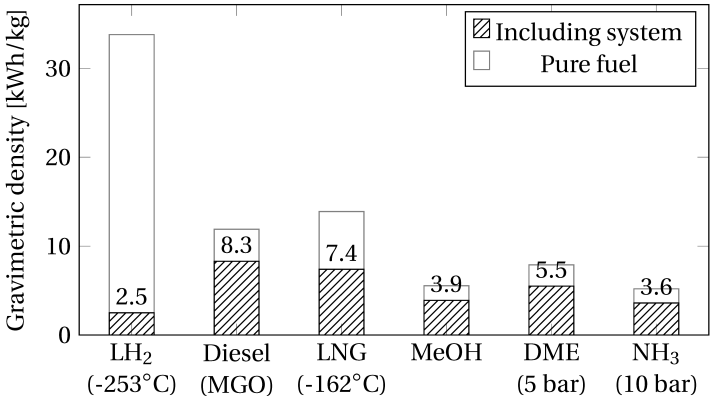

(a) Estimated gravimetric energy densities.

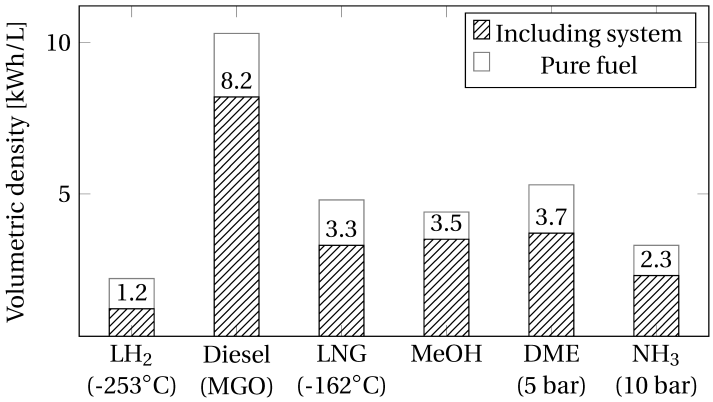

(b) Estimated volumetric energy densities.

Figure 2.1: Estimated gravimetric (Figure 2.1a) and volumetric (Figure 2.1b) energy densities of pure fuels and respective actual densities when the storage system is included. Based on the LHV and [88–94].

usually NG, but also from biogas or CO_2 and renewable electricity, using power to gas and gas to liquid conversion processes [102, 103].

Diesel is considered to be an inconvenient fuel for fuel cell systems due to fuel processing complications. Still, it is the most investigated fuel for maritime fuel cell systems, as it is cheap, energy dense, and the infrastructure is fully deployed. Depending on the fuel cell system and type of diesel fuel, various fuel processing steps are required to obtain a feed-gas with sufficient purity. These processing steps will lower both the overall efficiency and power density of the overall system [53]. In this review only low-sulphur marine gas oil (MGO) is considered.

NATURAL GAS

The use of NG for land-based power generation has increased during recent decades, mostly because of the increasing availability and few emission related problems [82]. The composition can vary considerably for various sources, but it usually contains mostly methane, some higher alkanes and small amounts of impurities [104]. Although it is currently produced from fossil feedstocks, it can be produced from biomass or synthesised from CO_2 and renewable hydrogen. Stored at cryogenic conditions, below -162°C at environmental pressure, it is referred to as liquefied natural gas (LNG). Although not yet available everywhere, the LNG infrastructure is expanding [105]. Alternatively NG can be compressed (CNG). The effective volumetric energy density of both LNG and CNG is low compared to diesel fuels.

It should be noted that NG is currently the most important source of both hydrogen and methanol [96, 106]. On-board hydrogen production from LNG is probably cheaper, more efficient and more dense than using hydrogen which is produced elsewhere [107, 108]. In addition, it can pave the way for the use of future renewable gaseous fuels on-board [109]. Fuel processing is relatively simple, and sulphur is easily removed with adsorbents [110]. In addition, many high temperature fuel cell systems are already designed to use NG, and have demonstrated high electrical efficiencies [41, 111].

METHANOL

Methanol (MeOH) is another important hydrogen carrier, with the main advantage that it is a liquid at ambient temperatures and can, therefore, be used in the conventional liquid fuel infrastructure with minimal adjustments [112]. However, the energy density of the pure fuel is significantly lower than diesel fuels, and it is corrosive towards some metals that are used in the current infrastructure. Although MeOH can be produced from various sources, such as synthetic gas, biomass and hydrogen with CO_2, most of it is still produced from NG [106, 113].

MeOH can be used in a direct methanol fuel cell, but the efficiency of this fuel cell is poor due to fuel crossover. Alternatively, it can be reformed at moderate temperatures, either in a separate system or integrated in the fuel cell system. Methanol reformers have been successfully integrated within HT-PEMFC systems [114–116]. Few studies have investigated the use MeOH in high temperature fuel cells, as these systems are typically configured to use NG, but direct and indirect utilisation of MeOH in these fuel cells is, at least in principle, possible [35, 117, 118].

DIMETHYL ETHER

Dimethyl ether (DME) is obtained by MeOH dehydration or directly from synthesis gas [119–121]. It can be stored in liquid form at the relatively low pressures of 5 bar, similar to liquefied petroleum gas (LPG). Furthermore, the energy density is somewhat higher than MeOH and it is non-toxic. Since it contains no carbon-carbon bonds, it can used in internal combustion engines without soot formation [91]. The absence of these bonds may lower the susceptibility to coking in fuel cell systems, which is a common problem for fuels with carbon-to-carbon bonds, such as ethanol [122, 123].

AMMONIA

The logistic fuels discussed so far can be synthesised from renewable electricity and CO_2. It should be noted that a carbon-neutral fuel is only obtained if the CO_2 required for this synthesis is captured from the atmosphere. However, CO_2 is difficult to extract from the atmosphere, since the concentration is very low. Nitrogen, on the other hand, is available in abundance and can be used as a hydrogen carrier in the form of ammonia [124].

Ammonia is a liquid at a temperature of -33°C and environmental pressure, or under a mild pressure of 10 bar. Its energy density is somewhat lower than that of MeOH [88, 124], and it can be decomposed to hydrogen at temperatures between 300 and 520°C. Since it contains no carbon, it can be used directly in fuel cells without CO poisoning or the risk of coking [125, 126]. However, even traces of ammonia poison LT-PEMFCs, and ammonia is severely toxic to humans and animals [127].

2.2.4. FUEL PROCESSING

Fuel purity requirements depend on the type of fuel cell, as indicated in Table 2.1. Low temperature fuel cells, for example, need hydrogen with a relative high purity. More importantly, gases that compete with hydrogen for surface adsorption on the platinum catalyst, most notably CO, inhibit reaction sites and, therefore, affect the cell performance significantly [64]. In contrast, high temperature fuel cells accept fuels of lower quality, can use CO as a fuel [67], and fuel processing can take place directly in the fuel cell [128].

The required fuel processing equipment thus depends on the implemented fuel cell type and logistic fuel, and this has a significant influence on overall system characteristics, such as efficiency, size, weight, cost and transient behaviour. Commonly applied processing equipment can be subdivided in the following steps:

- Reforming: used to convert carbon hydrates into a hydrogen rich mixture;
- CO clean-up: to lower CO content and maximise hydrogen yield;
- Purification: necessary if hydrogen with a high purity is required;
- Other: includes equipment such as evaporators, burners and desulphurisation (DeS).

This section gives an overview of these fuel processing steps.

REFORMING

Reforming is the most widely applied method to convert hydrocarbon fuels into a mixture of hydrogen and CO, commonly referred to as *syngas*. Many fuel cell systems using hydrocarbon fuels are equipped with an external reformer. Light hydrocarbons can be reformed internally if high temperature waste heat is available. In high temperature fuel cell systems waste heat from the electrochemical reaction can be used to reform fuel in indirect internal reforming (IRR) stacks. In direct internal reforming (DIR) fuel cells, hydrocarbons are reformed directly on the anode, using both heat and steam from the electrochemical oxidation of hydrogen.

Steam reforming Steam reforming (SR) is a common reforming method. The endothermic reaction between hydrocarbons and steam produces syngas with a high hydrogen content in the following equilibrium reaction:

$$C_nH_m + nH_2O \rightleftharpoons (n + \frac{m}{2})H_2 + nCO$$

Although the carbon is oxidised in SR, the hydrogen released from the steam maximises overall hydrogen yield. SR takes place at temperatures between 500 and 1000°C in the presence of a catalyst, usually nickel [129, 130]. Reforming at higher temperatures is technically feasible [131], but besides improved reaction kinetics there are few advantages. For some fuels near-complete reforming is possible at low temperatures. For example, MeOH can be reformed at temperatures as low as 200°C [114].

Both heat and steam need to be supplied to sustain the reaction, which reduces the overall system efficiency. Anodic recirculation, where a part of the anode tail gas is mixed with the fresh fuel, can be used in high temperature fuel cells to supply heat and steam for reforming and lower the fuel utilisation per anode pass [132–134]. The enhanced system integration improves the overall system efficiency.

DIR at the fuel cell anode results in optimised heat integration, as waste heat is directly used for reforming and less cooling air is required [135]. DIR can be deployed in high temperature fuel cells exclusively, where the SR reaction is promoted by the high temperatures and the formation of steam in the anode. Unfortunately, degradation issues related to carbon deposition, thermal stress and inhomogeneous current distributions, limit the extent of DIR in fuel cells. Therefore, a pre-reformer is still present in the most systems [134, 136].

Catalytic partial oxidation The exothermic catalytic partial oxidation (CPOX) process is another reforming method, that is sometimes used because of its simplicity. It relies on the oxidation of carbon, usually with air:

$$C_nH_m + \frac{n}{2}O_2 \rightarrow \frac{m}{2}H_2 + nCO$$

The hydrogen yield is limited compared to SR, since no additional hydrogen is produced from steam, and a part of the hydrogen is inevitably oxidised. Air is usually used as an oxidant, which dilutes the product gas further, since nitrogen is added. This reaction typically takes place between 700 and 900°C, where the hydrogen yield is highest [137].

Although the efficiency is low compared to SR, this reactor is sometimes preferred for its simplicity and compactness, since the use of steam generators, burners and heat exchangers is avoided. This simplification also results in reduced start-up times, which could be advantageous for transport applications [135, 138].

Autothermal reforming Autothermal reforming (ATR) essentially combines SR and CPOX. A part of the carbon is oxidised with air, and the heat that is released from this reaction is used for additional SR:

$$2C_nH_m + \frac{n}{2}O_2 + nH_2O \rightarrow (n+m)H_2 + 2nCO$$

Advantages of ATR are a higher hydrogen yield and a wide temperature window, between 600 and 1000°C, compared to the CPOX reactor [139–141]. Like CPOX, ATR does not require an additional burner to supply heat, although a steam generator is still needed. Perceived advantages over SR are a compact design, lower susceptibility for carbon formation and fast transient behaviour.

CO CLEAN-UP

In particular low temperature fuel cells have limited CO tolerance. The CO content has to be lowered to allowable levels for these fuel cells (Table 2.1). The hydrogen is preferably maximised in the CO clean-up process to enhance fuel cell performance.

Water gas shift The water gas shift (WGS) reaction follows usually after the reforming reaction. The CO produced during reforming reacts further with steam, and forms hydrogen and CO_2:

$$CO + H_2O \rightleftharpoons H_2 + CO_2,\ \Delta H_{298} = -41\ kJ/mol$$

The slightly exothermic WGS reaction is characterised by relatively fast kinetics, and occurs in the SR reactor as well. This equilibrium reaction shifts to the right at low temperatures, where highest hydrogen yields and lowest CO concentrations are obtained [142]. A significant amount of steam is often added to minimise the CO concentration in the product stream.

Syngas is directly used as a fuel in high temperature fuel cells, and the WGS reaction proceeds directly on the anode [143, 144]. CO content in the fuel has to be lowered as much as possible for low temperature fuel cells. Therefore, it is common to use two WGS reactors. One operates at a higher temperature (HT-WGS), usually >350°C, where the kinetics are faster [145], while a second reactor operates a lower temperature (LT-WGS), typically between 150 and 250°C, where the equilibrium concentration of CO is lower [146, 147].

Preferential oxidation The allowable CO concentration in low temperature fuel cells is usually lower than obtained in shift reactors. To achieve this, preferential oxidation (PrOX), also known as selective oxidation, can be used as a final clean-up method, where air is supplied to oxidise CO to CO_2:

$$CO + \frac{1}{2}O_2 \rightarrow CO_2,\ \Delta H_{298} = -283\ kJ/mol$$

Important advantages of this process are the simplicity and low pressure of the reaction and, hence, relatively low cost and small size [148, 149]. An operational temperature in the range of 80 to 200°C is common, since this reactor is usually placed between a LT-WGS reactor and a PEMFC stack [150]. Waste heat recovery options are limited due to the moderate temperatures. In addition, some hydrogen is inevitably oxidised, lowering the hydrogen concentration in the product gas.

Selective methanation Selective methanation (SMET) can be used as an alternative way to reduce the CO concentration in the fuel, although it is in fact reverse SR of methane:

$$CO + 3H_2 \rightleftharpoons CH_4 + H_2O,\ \Delta H_{298} = -206\ kJ/mol$$

A SMET reactor is typically operated at low pressures, and temperatures ranging from 250 to 350°C, where the equilibrium of the SR reaction of methane reverses [151–153]. Although it reduces the hydrogen content in the product, there are advantages to the SMET process, as it reduces the CO content in the fuel without oxidising a part of it. The catalyst is preferably selective towards the reaction of CO, to minimise the undesired methanation of CO_2.

A high calorific product gas is obtained compared to the PrOX reactor, which is particularly beneficial if the tail gas of the fuel cell is further utilised, for example in burners or heat engines [154]. In addition, reactor design and operation is relatively simple, as no air has to be supplied. Waste heat recovery is possible, since the heat produced has a relatively high temperature. Furthermore, it has been reported that a SMET reactor is inherently easier to control [152, 155].

PURIFICATION

Hydrogen purification is a necessary step for many LT-PEMFC systems using hydrocarbon fuels, due to the sensitivity of this type of fuel cell to contaminants, most noticeable CO.

Membrane separation Membrane separation is a powerful process used to obtain a product gas of relatively high purity. A variety of types exist for hydrogen production. Of these, dense metal and ceramic membranes have the highest selectivity towards hydrogen. Alternatively, porous ceramics and carbon as well as dense polymers can be used, but their selectivity is more limited [156]. Depending on the type of membrane and process conditions, a significant amount of hydrogen remains in the retentate gas and is lost in the process, unless the residual gasses can be burned to supply heat to the reforming reactor [157].

State of the art hydrogen separation membranes are made from palladium-silver alloys and are therefore relatively expensive. They have a high selectivity for hydrogen at temperatures above 250°C. However, the maximum operation temperature is limited to 600°C by the chemical stability of the membrane material. Operation at temperatures up to 900°C is possible with silica-based membranes. However, being ceramics, silica-based membranes are brittle and susceptible to degradation. Moreover, their selectivity towards hydrogen is usually lower [158].

Membranes can be used as a separate fuel processing step, but also in so-called *membrane reactors*, where hydrogen is separated in the reforming or water gas shift reactor. The removal of hydrogen from the reactor shifts the reaction equilibrium, thus maximising hydrogen yield [159]. The complicated design, close coupling of heat and mass transfer and stability issues of the membrane material are challenging aspects of this reactor type.

Pressure swing adsorption Pressure swing adsorption (PSA) is another commonly used hydrogen purification process. In PSA, the syngas is fed to a pressure vessel, containing a

solid adsorbent. The stronger adsorption of heavier molecules on the adsorbent results in a high purity hydrogen flow at the reactor outlet. The adsorbent is easily regenerated by lowering the pressure. As with membrane separation, the tail gas still contains some of the hydrogen, and 15 to 30% of the hydrogen is lost in the process if the tail gas cannot be used for other purposes [160, 161].

A continuous flow of hydrogen is produced by placing two PSA vessels in parallel, one adsorbing while the other regenerates. A series of PSA units is usually installed to obtain hydrogen with the required purity [162]. The PSA process is simple, reliable and cost effective. Drawbacks are the relatively large size, elevated pressure and parasitic power consumption of the compressors.

OTHER

Fuel processing equipment includes some other equipment as well, such as burners and heat exchangers. These are covered in detail, but desulphurisation (DeS) is discussed in this section.

Desulphurisation Fossil fuels contain sulphur compounds to a certain extent. Since sulphur deactivates the catalysts used in reformers, shift reactors and fuel cells, Desulphurisation is usually required in fuel cell systems using fossil fuels. There are several techniques to do so, ranging from wet scrubbing to hydrodesulphurisation, and at process conditions varying from ambient up to 1200°C and 50 bar [163, 164].

Which desulphurisation process is most suitable depends on the type of fuel and sulphur tolerance levels. When considering the typical scale of fuel cell systems and ship-board applications, conventional industrial processes, like hydrodesulphurisation, are probably too bulky, costly and un-safe [164]. Surface adsorbents are of most interest for fuel cell systems, as they resemble a simple method which is able to reduce the sulphur content to low levels. A drawback of surface adsorbent is the need for either replacement or regeneration.

Hydrogen sulphide can be removed effectively from a gas stream at moderate temperatures between 300 and 550°C [165]. However, this method was found to reduce the sulphur content of diesel fuels insufficiently [74, 75]. Alternative adsorbents operating in the range of 20-200°C have been tested for these fuels. Although this method is in principle capable of achieving low sulphur levels, relatively long residence times are required and the sorbent capacity is limited, restricting the suitability of the process to low sulphur fuels [164].

2.2.5. FUEL CELL SYSTEMS OVERVIEW

Since the required fuel processing steps are determined by both the selected logistic fuel and fuel purity requirements of the fuel cell type, a choice for a specific combination has important implications on the overall system characteristics. Many of the discussed chemical reactors require specific operation temperatures, pressures levels and heat management. In addition, the chemical composition of the fuel needs to be suitable for the fuel processing equipment. The sulphur content, for example, has to be within

tolerable levels, while the oxygen-to-carbon ratio should be sufficiently high to prevent any carbon from depositing.

Figure 2.2 gives an overview of the discussed fuel processing steps and fuel cell systems, and indicates their operational temperature as well. The black lines represent the fuel flow direction, starting from either liquid or gaseous fuel, going through various fuel processing steps until the destined fuel cell system is reached. Other solid lines indicate heat flows, steam or oxygen (air). Dashed lines represent additional system integration options, and dotted lines indicate off-gas streams.

The fuel processing overview presented in Figure 2.2 not only visualises various fuel processing routes, but indicates their operational temperatures as well. Therefore, integration opportunities for fuel processing and fuel cell systems can be quickly identified from this graph. For example, it is clear that high temperature waste heat of MCFC and SOFC systems can be used for reforming, and exhaust gasses from fuel cells and purification processes can be used to generate heat and steam. Both increase the overall system efficiency.

Another observation the reader should take away from this graph, is the complexity of using low temperature fuel cells with non-hydrogen fuels. The overall efficiency is limited by the need to generate high temperature heat and steam for reforming, and losses in CO clean-up and purification equipment. In addition, the large number of processing steps affects the power density and transient response times of the total system. Furthermore, it should be noted that water vapour is generated at the cathode in proton conducting fuel cells and, therefore, more difficult to use for fuel processing. This could imply that purified water has to be produced on-board, reducing the power density and increasing parasitic losses.

2.3. MARITIME POWER PLANTS

It is assumed that the purpose of an electrical power plant in a transport application is to *supply an amount of electric power for an amount of time*, for either propulsion, auxiliaries or both. The suitability for a particular application depends on specific characteristics of the power plant. Important aspects that determine the suitability of a power plant for maritime application are:

- Electrical efficiency;
- Power and energy density;
- Load transients and system start-up;
- Environmental impact;
- Safety and reliability;
- Economics.

Therefore, this section reviews fuel cell systems and compares them to conventional maritime solutions according to the criteria listed above. However, it should be noted that fuel cell systems have other potential benefits, such as:

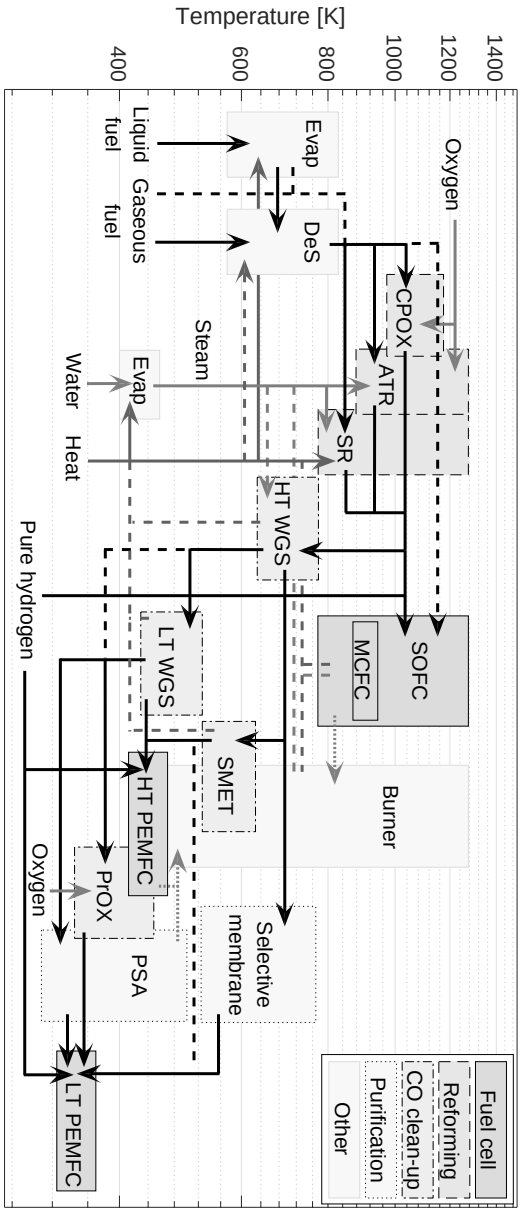

Figure 2.2: Overview of on-board fuel processing steps in fuel cell systems, with indication of their operational temperature. The solid black lines indicate the common process flow direction, while the dashed lines are optional. Other solid lines represent flows of heat, steam and oxygen. Off-gas streams are shown as dotted lines.

- Noise and vibration reductions;
- Reduced infra-red signatures;
- Reduced maintenance;
- Modular and flexible design;
- Improved part load efficiency;
- Water generation.

Although these aspects can be attractive for various vessels, they may be application specific. In addition, the potential benefits are currently uncertain and need further study. Therefore, they are not covered in detail in this review.

2.3.1. ELECTRICAL EFFICIENCY

The higher electrical efficiency compared to conventional generators is an important incentive to apply fuel cell technology in ships. The high efficiency is partly a result of the direct conversion of chemical energy into electricity, whereas internal combustion engines convert chemical energy into electricity via thermal and mechanical energy. As fossil fuels may remain an important energy source in the near future, efficiency improvements may result in net GHG emission savings.

CONVENTIONAL MARITIME POWER PLANTS

On-board ships, electricity is most commonly produced with diesel generators. Heavy duty generator sets provide power in an efficient and cost effective way. Data provided by manufacturers reveals a peak efficiency of approximately 45% for MW-scale medium-speed diesel generator sets. Lean burn, spark ignited gas generator sets in the same power class are reported to achieve efficiencies up to 47% [166, 167].

Generator sets are generally not operating in their most efficient operational point. Most ships have a significant overcapacity installed, both for peak loads and redundancy requirements. The mechanical losses are relatively large in part-load, since the rotational speed has to be maintained to match grid frequency. Therefore, depending on the generator type and operational point, the practical efficiencies of state-of-the-art heavy duty diesel generators are commonly reported to be in the range of 25 to 40% [168, 169].

Gas turbine generators are sometimes applied in the maritime field. They are widely applied by the aviation industry, since they have a high specific power and require little maintenance compared to reciprocating internal combustion engines [170]. With peak efficiencies in the range of 30 to 40% for heavy duty maritime gas turbine generators, and subsequently lower practical efficiencies, they are somewhat less attractive from a fuel consumption perspective [171].

FUEL CELL SYSTEMS

Fuel cells have been considered an alternative for heat engines for decades. Already in the 1970s, the German Navy started developing a PEMFC system for air-independent propulsion (AIP) of their submarines [54]. Due to the confidentiality of these military

programs, studies only appeared in literature from the early nineties. Both the study of Adams [172] and Sattler [54] discuss the possibility to apply fuel cells in naval submarines, for increased AIP, as well as naval surface ships, where noise, vibrations and infra-red signatures can be reduced.

In his early publication, Adams claims that electricity production with fuel cells is up to two times more efficient than generating electricity with diesel generators. Sattler reports efficiencies varying from about 40%, for PEMFCs on reformed hydrocarbons, up to 60% for NG-fuelled SOFC systems. According to a report on civilian maritime fuel cell application, published by Rolls-Royce' Strategic Systems Engineering group [173], fuel cells have to demonstrate significant efficiency improvements to justify the increased cost and lower specific power compared to diesel generators. They see SOFCs as the most promising technology, as a distinct efficiency improvement over existing equipment can be achieved.

Although PEMFCs have demonstrated electrical efficiencies up to 70% on pure hydrogen and oxygen [173], the overall efficiency does not exceed 40% when they are equipped with diesel reformers [74, 75, 77]. This eliminates an important advantage associated with fuel cell systems, since benefits are restrained to reductions in emitted noise, vibrations and infra-red signatures.

When fuelled with diesel, MCFC systems are expected to achieve higher efficiencies than PEMFCs. Only partial reforming of the fuel is sufficient for MCFC systems, and this can be achieved at lower temperatures. Moreover, high temperature waste heat from the stack can be used for this purpose. A diesel-fuelled MCFC plant is designed in a study by Spcchia et al. [78]. It has an electrical efficiency of only 29%, but an improved system design in a follow-up study achieves an efficiency of 50.6% [79]. A more detailed design of such an MCFC system is discussed by Allen et al. [76] for a U.S. Coast Guard vessel, for which an efficiency of 54% is expected by the author.

SOFC technology is recently getting more attention, as even higher efficiencies are projected. Leites et al. [53] study various diesel-fuelled systems, concluding that an SOFC is preferred over alternative fuel cells, because the BoP can be simplified and it offers inherently higher efficiencies. A diesel-fuelled SOFC system with an efficiency of 55% is designed in a study by Ezgi et al. [80].

As mentioned earlier, part load characteristics are different in fuel cell systems and peak efficiency is usually achieved at relatively low loads. Still, the efficiency typically reduces for even lower loads, since the parasitic consumption of the BoP becomes relatively large. However, this may be of limited concern if a part of the fuel cell modules can be switched off during low load conditions.

COMBINED CYCLES

Electrical efficiencies can be increased when power cycles are combined. The gas turbine with heat recovery steam generators, where the Brayton cycle is equipped with a Rankine bottoming cycle, is a well-known example of a combined cycle power plant. Outstanding efficiencies up to 60% and good part load characteristics are achieved by a combination of these cycles [176]. Waste heat can be recovered from reciprocating internal combustion engines as well, but the electrical efficiency gain is usually less substantial. Although combined electrical efficiencies up to 55% are projected for these systems, the gain is less

Table 2.2: Reported electrical efficiencies based on the LHV with air as oxidant. Part load efficiencies can be significantly lower, which is expected to be less detrimental in fuel cell systems due to the possibility of modular switch-off.

Generator type	**Diesel [%]**		**NG [%]**		**H_2 [%]**	
Piston engine	35-45	[168, 169]	35-47	[174]		
Gas turbine	25-40	[171]	25-40	[171]		
PEMFC	30-40	[74, 75, 77]	35-45	[173, 174]	40-60	[173]
MCFC	29-54	[76, 78, 79]	40-55	[54, 174]		
SOFC	45-55	[53, 80]	45-65	[42, 54]		
SOFC combined			55-70	[45, 175]		

than five percent point in most cases, while the system is expensive and complicated [177, 178].

High temperature fuel cells can be equipped with bottoming cycles, since the hot exhaust gasses from the fuel cell stack still contain thermochemical energy. Un-used fuel is usually burned in a catalytic converter, raising the temperature of the exhaust gasses even further. Integration with gas turbines is particularly advantageous, since it provides good integration with the cathode air flow. Efficiencies up to 70% are projected for fuel cell-gas turbine combined systems [45], although some studies predict even higher efficiencies [51]. SOFC gas turbine hybrids have been studied for maritime application in a system designed by Tse et al. [179], where electricity, heat and cooling is generated for a luxury yacht. Alternative options to use the waste heat of high temperature fuel cells for additional electricity generation are Rankine cycles, Stirling engines and indirect gas turbine coupling [46, 180].

Rather than burning the fuel in a catalytic converter, some authors have proposed to burn the remaining fuel in a reciprocating internal combustion engine. Although the cathode air is not used as effectively in this case, the remaining fuel is used efficiently and high combined efficiencies up to 70% may be achieved [47, 52, 181]. Such a system has a limited degree of coupling compared to a SOFC/gas turbine combined cycle, since close matching of mass and heat flows is not necessary. In a similar fashion, hydrogen rich anode off-gas from high temperature fuel cells can be purified and used in low temperature fuel cells. This enables the use of high temperature electrochemical waste heat for reforming, while a part of the power is provided with low temperature fuel cells [182].

AUXILIARY ENERGY STORAGE SYSTEMS

Alternatives for energy storage in logistic fuels are, for example, batteries, where energy is stored in a chemical compound within the device, supercapacitors, storing electric charge directly, and flywheels, which store momentum in a rotating disc. Round trip efficiencies range from just over 65% for Ni-Cd batteries, to more than 90% for Li-ion batteries, supercapacitors and flywheels [183, 184]. Although especially batteries could be a viable options for specific vessels with relative long berth and short sailing times, these systems are expected to be mainly used for auxiliary energy storage, for example

during start-up and load transients.

2.3.2. POWER AND ENERGY DENSITY

The volume and weight of power plants are critical design aspects for any transport applications, since volume and weight are commonly restricted for practical reasons, while a certain amount of power and endurance is required. Depending on the type of application and power plant, designs are typically either volume critical, weight critical, or both. For example, if lead-acid batteries are applied in cars, the allowable weight is likely to restrict the size of the battery [185], and hence the driving range, whereas if hydrogen fuel cells are selected, the volume of the hydrogen tanks is more likely to limit the endurance of the car [95].

FUEL CELL SYSTEMS

The high volumetric energy density compared to batteries is an important motivation to use fuel cells for AIP purposes. As pointed out by Adams [172], this allows submarines to be submerged for longer periods. Although the volumetric power density is low compared to batteries and internal combustion engines, the energy storage density is significantly increased, which allows extended submerged operation. For larger submarines with even longer mission requirements, on-board hydrogen production from MeOH has been demonstrated [186].

Modern ships are commonly volume critical, although specific designs (e.g. high speed vessels) benefit from low weight as well. Like the overall system efficiency, power and energy density of fuel cell systems are determined by the combination of fuel cell type and logistic fuel. Adams [172] compares the weight and volume of typical diesel generator sets to several fuel cell systems equipped with NG reformers, and concludes that fuel cell systems take up more space than diesel generator sets for the same amount of power. However, the opportunity to reduce the volume of the storage tanks due to the reduced fuel consumption is not taken into account.

Projected power densities of fuel cell systems in a Rolls-Royce publication generally exceed those of diesel engines [173]. However, such high power densities have so far not been achieved in practice. Allen et al. [76] give a more realistic density estimation of NG-fuelled fuel cell systems. Still, their densities estimations are high compared to those achieved in practice. For example, the estimated densities of a NG-fuelled MCFC system, 37-110 W/kg and 17-36 W/L, are one order of magnitude above the achieved 15 W/kg and 3 W/L in a 330 kW demonstration system [174].

SOFC systems are expected to attain higher power densities than MCFC systems [76, 173], while having similar characteristics. Conceptual designs of maritime SOFC systems are discussed in a number of studies, reporting power densities varying from 20 W/kg and 8 W/L to 230 W/kg and 60 W/L [73, 80, 187]. The highest power densities are obtained with PEMFCs. However, the fuel processing components of PEMFC systems reduce the effective density considerably if they are not operating on pure hydrogen [75].

It should be noted that the discussed gravimetric and volumetric power densities have a rather theoretical value. It is just as important to study how fuel cells can be applied in actual ship designs. A detailed design for a U.S. Coast Guard vessel revealed that, although

the MCFC system was heavier than the original diesel generator, removal of exhaust stacks, sound isolation bedplates and a smaller cooling systems resulted in a net weight reduction [76].

As mentioned before, the modularity of fuel cells gives an additional degree of freedom in the layout of the energy system, allowing ship designers to use the available space more effectively. In addition, power density has not yet been an important design objective for all fuel cell systems, as in particular high temperature fuel cell systems have been mainly developed for stationary electricity generation where power density is of limited importance.

RAGONE CHARTS

It has become customary in the field of energy storage to compare the differences in power and energy density in so-called *Ragone charts*, where power density is plotted versus energy density [184, 188]. This approach is relatively straightforward for appliances that combine storage and conversion in a single device, such as batteries. The solution with the highest density can be identified from the chart if the characteristic timescale of the application is known.

Ragone chart comparison may seem less obvious for systems with separate storage and conversion devices, but there is essentially no difference. However, the power and storage capacity can be scaled individually to a relatively large extend. This implies that the effective power and energy density of the complete solution depends on the power density of the conversion device, the energy density of the storage device, the conversion efficiency, and the timescale of the application.

In this review, both gravimetric and volumetric density of a number of fuel cell systems and logistic fuels are compared. The densities of conventional diesel and gas generator sets, as well as gas turbine generators, are included for reference. For practical reasons, the fuel cell systems considered are a PEMFC, MCFC and an SOFC, and the fuelling options are limited to those discussed in Section 2.2.3. However, this analysis can be extended to other fuels and conversion devices, or adapted for new data.

Energy density The energy density is defined as the amount of electrical energy available per unit of either mass or volume. It thus deviates from the energy density of a pure fuel, due to the volume and weight of storage system components, and losses in the conversion process. Therefore, the energy density depends on the fuel properties, storage system and the overall efficiency of the conversion process.

Power density The power density of a conversion process is obtained from specifications of commercial maritime electricity generators [166, 167]. A similar approach is used for fuel cell systems, including BoP equipment, although a 50% upper margin is added to account for:

- Their relatively limited development state;
- Their modularity, which may allow more flexible integration into ship designs;
- The possible removal of exhaust stacks, sound isolation bedplates and a smaller cooling system.

An overview of the parameters assumed in this study is given in Appendix A.1.

Effective density The effective density can be calculated if the timescale of the application is known. This timescale t is defined by the ratio of the effective energy storage density $\bar{W}_{eff}$ and power density $\bar{P}_{eff}$ of the complete power plant:

$$\frac{\bar{W}_{eff}}{\bar{P}_{eff}} \equiv t \tag{2.1}$$

The power density of the conversion device $\bar{P}$ is corrected for the energy density of the fuel storage $\bar{W}$ and the conversion efficiency η to obtain the effective power density $\bar{P}_{eff}$ of the power plant:

$$\bar{P}_{eff} = \frac{\bar{P}}{(1 + t\frac{\bar{P}}{\eta \cdot \bar{W}})} \tag{2.2}$$

The effective energy storage density $\bar{W}_{eff}$ then follows from Equations (2.1) and (2.2):

$$\bar{W}_{eff} = t \cdot \bar{P}_{eff} = \frac{t \cdot \bar{P}}{(1 + t\frac{\bar{P}}{\eta \cdot \bar{W}})} \tag{2.3}$$

It can be verified that the these equations approach the limits $\bar{P}_{eff} \approx \bar{P}$ and $\bar{W}_{eff} \approx \eta * \bar{W}$ for $t = 0$ and $t = \infty$ respectively. In some cases fuel processing equipment is included as well, in which case the overall power density and conversion efficiency can be calculated from:

$$\bar{P} = (\frac{1}{\bar{P}_{fuel\ cell}} + \frac{1}{\bar{P}_{fuel\ processing}})^{-1} \tag{2.4}$$

$$\eta = \eta_{fuel\ cell} \cdot \eta_{fuel\ processing} \tag{2.5}$$

The obtained values for $\bar{P}_{eff}$ and $\bar{W}_{eff}$ can be plotted against each other in a Ragone chart to compare the densities of various power plants. Due to the uncertainty and spread in the data, two lines are plotted for each system in this study. The solid lines indicate the projected maximum density that can be achieved, while the dotted lines correspond to the minimal density expected by the author.

GRAVIMETRIC DENSITY

In Figure 2.3a various maritime power plants are compared in a gravimetric Ragone chart. It is clear that the Brayton turbine generator offers the highest density potential for most timescales. A higher fuel efficiency only starts to pay off when hundreds of hours independent operation is required. From a gravimetric perspective, diesel-fuelled SOFCs and LNG-fuelled MCFCs seem to perform comparable, and the same holds for Diesel generators and LNG-fired Otto generators. Cryogenic hydrogen and PEMFCs could provide an interesting alternative up to several dozens of hours.

Fuel cell systems with various logistic fuels are compared in Figure 2.3b. PEMFCs offer a dense solution up to about 12 hours, after which the higher energy density of ammonia and MeOH starts to pay off. Although the storage tank decreases the effective storage

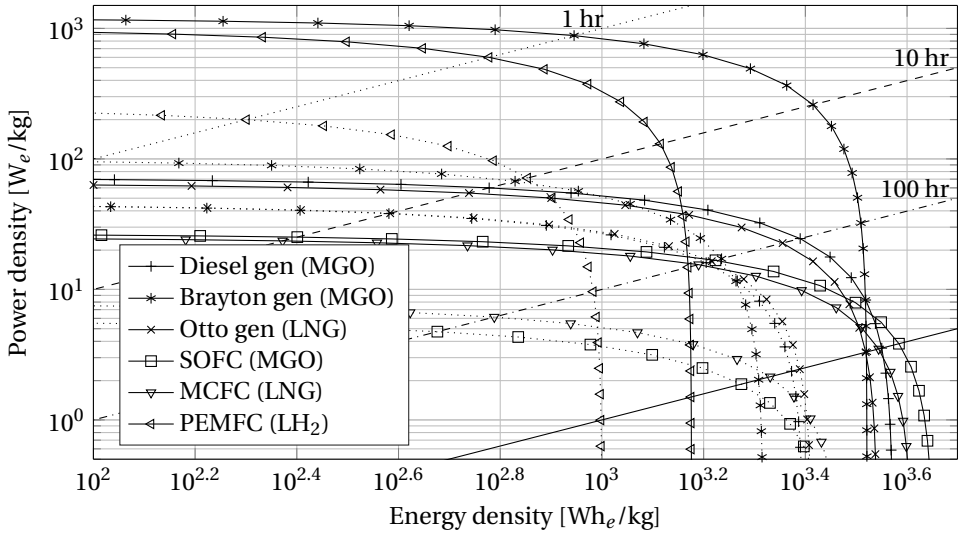

(a) Gravimetric density of various maritime power plants.

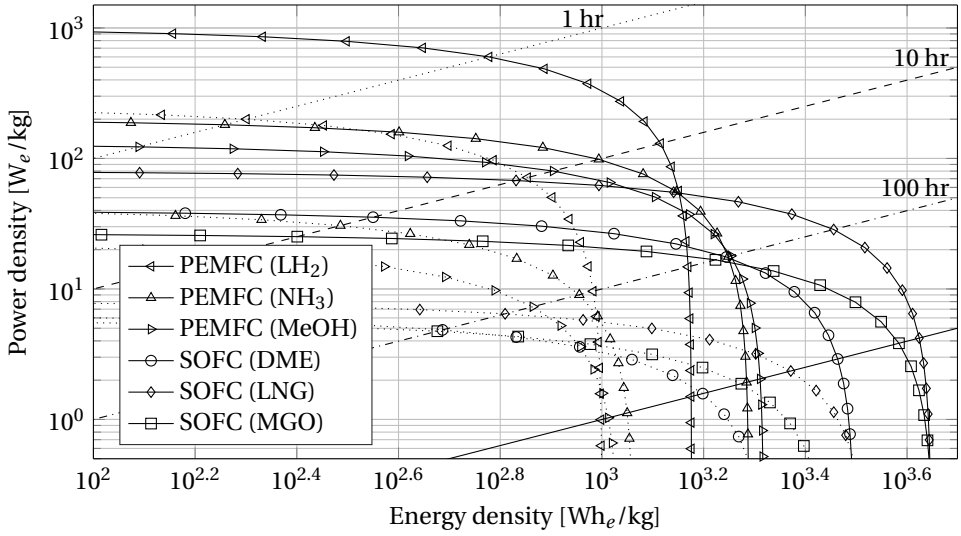

(b) Gravimetric density of fuel cell systems with various logistic fuels.

Figure 2.3: Gravimetric Ragone charts for various maritime power plants (Figure 2.3a) and fuel cell systems with several logistic fuels (Figure 2.3b). The solid and dashed lines represent the expected maximum and minimum densities respectively. The density of conventional generators is based on manufacturer data. For the fuel cell systems there is more uncertainty due to the limited development state. An overview of the data used can be found in Appendix A.1.

density of LNG considerably, NG-fuelled fuel cell systems are still expected to offer the highest gravimetric density for sailing times over several dozens of hours, partly due to the high efficiency of NG-fuelled SOFC systems. DME is inherently easier to store, hence less weight is allocated to the storage system. However, this is insufficient to compensate for the lower energy density of the pure fuel.

From the Ragone chart it is concluded that MGO- and LNG-fuelled systems have comparable effective gravimetric energy densities. However, the gravimetric power density of systems using LNG is expected to be higher than those on MGO and DME. The gravimetric density of LNG-fuelled systems is expected to increase even further when SOFC combined cycles become available. Hydrogen could be an good alternative if the refuelling interval is limited to tens of hours, while MeOH seems most interesting for the region between 12 and 100 hours.

VOLUMETRIC DENSITY

The volumetric Ragone chart for various maritime power plants, shown in Figure 2.4a, reveals that the fuel densities are differ significantly more from a volumetric perspective. MGO can be stored more dense than the considered alternatives, thus diesel-fuelled systems are superior from a volumetric perspective. However, PEMFCs with hydrogen stored under cryogenic conditions can still prove an interesting alternative for diesel generators up to 15 hours of independent operation.

Differences in volumetric energy density dominate Figure 2.4b as well, where various fuelling options for fuel cell systems are plotted. The diesel-fuelled SOFC system is expected to achieve a reasonable power density, and probably offers the most dense solution for timescales over 100 hours. From a volumetric density perspective, this seems to be the best choice for vessels with long mission requirements, such as cargo carriers and offshore ships. Fuel cell systems fuelled with LNG, MeOH or DME are very comparable from a volumetric energy density perspective, but they are significantly less energy dense then diesel-fuelled systems.

Liquefied hydrogen and ammonia are expected to offer the most compact overall system for sailing times up to dozens of hours. However, for longer mission requirements the limited volumetric storage density of liquefied hydrogen results in relatively large system volumes. For a 100 hour refuelling interval the hydrogen-fuelled PEMFC system is expected to be 1.5 to 2 times larger than the alternatives. For 1000 hours independent operation, not uncommon for some types of vessels, the high volume of liquefied hydrogen storage tanks results in total system volumes about 1.75 times larger compared to ammonia, to roughly 2.5 times larger than LNG, MeOH or DME and up to 5 times larger compared to MGO-fuelled SOFC systems.

In contrast to the gravimetric density, it appears to be difficult to achieve the volumetric densities of diesel engine-generator sets with fuel cell systems and unconventional fuels. However, the volumetric density of diesel engine-generators is expected to decrease in the future due to emission requirements, which forces ship owners to install auxiliary equipment that will inevitably lower the efficiency and power density of the overall system. In addition, the difference seems acceptable for applications with sailing times up to several hundreds of hours, corresponding to a sailing time of a couple of days. The introduction of SOFC combined cycles can decrease the gap between conventional engine-generator sets and SOFC systems.

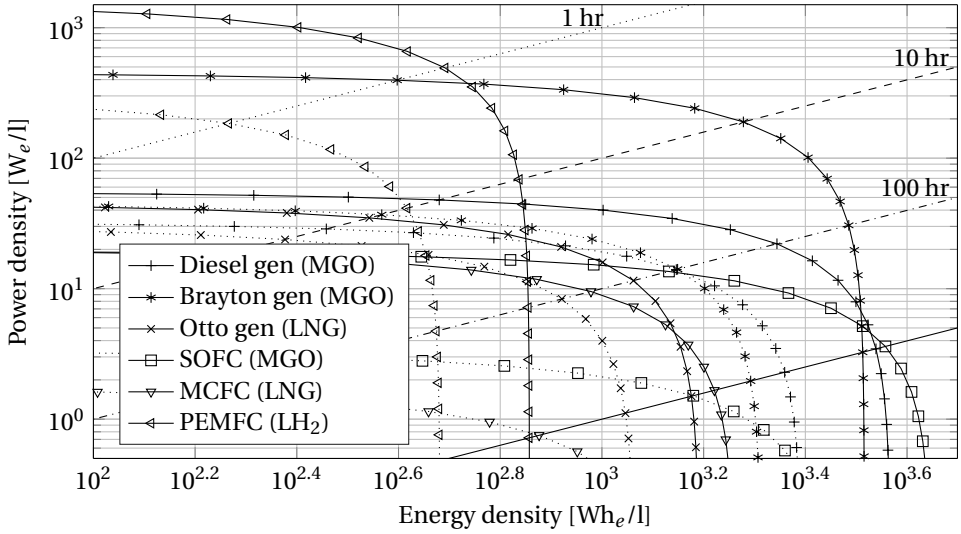

(a) Volumetric density of various maritime power plants.

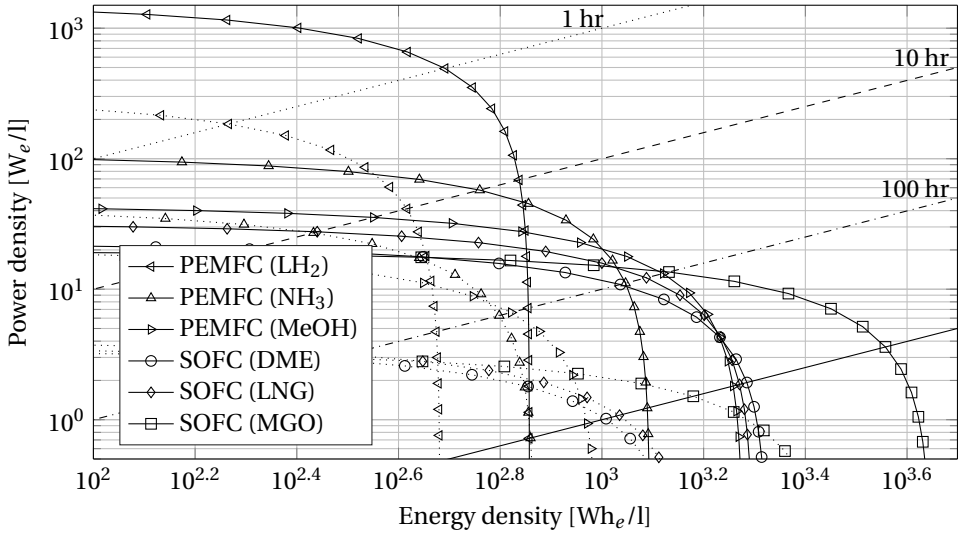

(b) Volumetric density of fuel cell systems with various logistic fuels.

Figure 2.4: A volumetric equivalent of Figure 2.3 for various maritime power plants (Figure 2.4a) and fuel cell systems with several logistic fuels (Figure 2.4b). The solid and dashed lines represent the expected maximum and minimum densities respectively.

2.3.3. LOAD TRANSIENTS AND SYSTEM START-UP

Depending on the type of vessel and operational profile, electrical power demand on ships is usually subjected to significant changes over various timescales. Furthermore, system start-up times should be reasonable and at least comparable to the conventional electricity generators. Since electrification of on-board power distribution is anyway required if fuel cell technology is adopted, hybridisation with auxiliary electricity storage components can be used to meet these requirements if fuel cell systems alone are unable to do so.

FUEL CELL SYSTEMS

The type of fuel cell and logistic fuel determine many system characteristics, and this is not different for dynamic behaviour. For example, PEMFC systems fuelled with hydrogen accept significant load steps in seconds, but the transient performance is probably dominated by the fuel processing equipment if they are running on NG [173]. The inclusion of a hydrogen buffer could, at least partially, overcome this issue.

Even if a fuel cell system is capable of meeting the demanded load transient or delivering peak power for a short amount of time, this could result in an increased rate of degradation [189]. Therefore, even LT-PEMFCs, which have good transient response capabilities, are often combined with supercapacitors. An additional advantage is the opportunity to decrease the required size of the fuel cell stack, which results in weight and cost savings [190].

High temperature fuel cells are known to have long start-up times and to allow only slow load changes, since the high temperature requires heating of a large thermal mass. The allowable temperature gradients in SOFCs are limited by the brittle ceramics they are made of. Metal-supported SOFCs are reported to be more robust and to enable fast thermal cycling [30]. Still, high temperature fuel cell systems have a notable BoP, and the increased thermal mass and interdependency of individual components limits their transient capabilities.

Hybridisation with gas turbines, characterised by relatively rapid start-up and load-following, seems promising to address the limitations of high temperature fuel cell systems. However, since the fuel cell and gas turbine are closely coupled in such systems, the transient behaviour of the slowest component may restrict the overall system dynamics. For example, fast transients in turbomachinery may induce unacceptable operational conditions on the SOFC stack [191].

In general, the number of system components and the total thermal mass seem to be good indicators for system start-up and load response times. Simplification of the BoP and fuel processing equipment could be an effective method to enhance the transient performance. Unfortunately, this may result in an increased fuel consumption as well. CPOX reactors, for example, can achieve short start-up and load response times, but the overall system efficiency compared to SR is low [36].

AUXILIARY ELECTRICITY STORAGE

Storage components with good transient capabilities can be used to compensate for the limited dynamics of fuel cell systems. Batteries, supercapacitors and flywheels could be

suitable for this purpose, as the power-to-energy ratio of these components is relatively high, which allows them to discharge in seconds to minutes [192].

Batteries are best applied to supply power for minutes and up to hours from a power density perspective [183]. However, their specific power and number of charge and discharge cycles is limited. Therefore, they appear to be most suitable to cover loads during cold start-ups of the fuel cell system and large transients [193].

The specific energy storage capacity of supercapacitors is limited compared to batteries, but their power density is high, allowing them to charge and discharge in seconds [183]. In addition, they can take many charge and discharge cycles without a significant loss in capacity and power [194]. These characteristics make supercapacitors more suitable for peak-shaving.

Flywheels are placed between batteries and supercapacitors in terms of power and energy density. Conventional flywheels are made from steel and have limited density, but are relatively mature. Advanced composite flywheels outperform these, but their development state is more limited. Although round-trip efficiencies of flywheels are usually somewhat lower than of batteries and supercapacitors, they are expected to offer cost savings [195].

A part of the energy is lost in any auxiliary electricity storage equipment, and this should not exceed the power gained by the slow prime power conversion device. Preferably, the losses in the auxiliary storage equipment are small compared to the efficiency gain in the fuel cell system. In addition, the inclusion of auxiliary electricity storage equipment lowers the overall power density of the power plant. Careful scaling of the storage device will be necessary to maximise the reduction in fuel consumption and capital cost, and maximise the power density of the system.

2.3.4. ENVIRONMENTAL IMPACT

The potential reduction of local emissions during operation is an important incentive to apply fuel cell systems in ships, since these are typically subject of environmental regulations. For example, Ludvigsen et al. [174] discuss the possibility to eliminate local HAP emissions completely and reduce local GHG emissions significantly. No SO_X, low NO_X and 40% reduced CO_2 emissions were demonstrated with a 20 kW MeOH-fuelled maritime SOFC system in the METHAPU project [187].

Figure 2.5 shows typical local emission levels for engine-generator sets and high temperature fuel cell systems, fuelled with either MGO or LNG. Engine data is obtained from Bengtsson et al. [5], and fuel cell system data from Altmann et al. [196]. Gas engines have significantly lower emissions of NO_X and PM compared to diesel engines, but fuel slip results in much higher emissions of VOCs, mostly methane, and CO. Fuel cell systems have virtually zero emissions of NO_X, PM, VOCs and CO, and the higher electrical efficiency results in reduced CO_2 emissions.

Although Figure 2.5 illustrates the potential of fuel cells to reduce local emissions during their operational life, it represents only a part of the environmental impact over a complete life cycle. Next to the impact during the operational life, the complete environmental burden from maritime electricity generators is determined by contributions from:

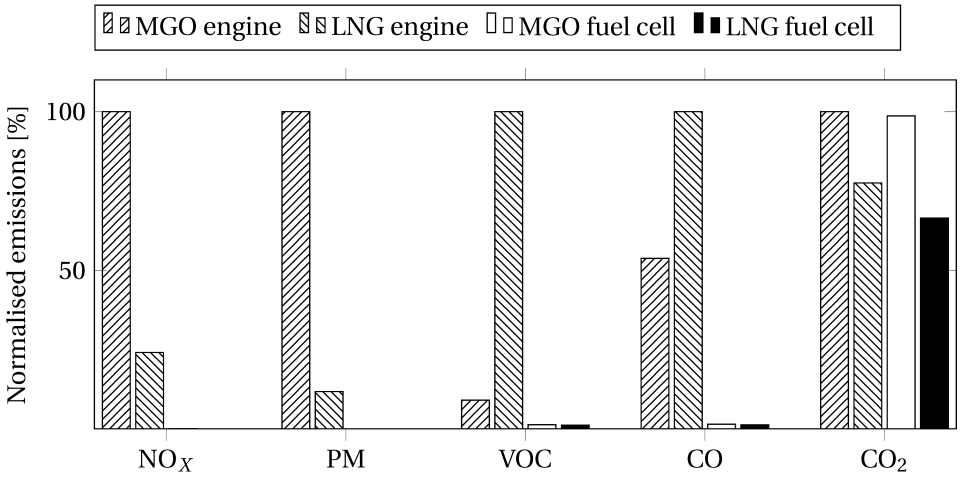

Figure 2.5: Normalised local tank-to-electricity emissions of NO_X, PM, VOC, CO and CO_2 for various maritime power plants. Original data (g/kWh$_e$) extracted from [5, 196].

- Manufacturing;
- Maintenance;
- Decommissioning;
- Fuel supply.

Manufacturing, maintenance and decommissioning stages may be important, since the energy intensive production processes and limited lifetimes of fuel cell systems can result in a net increase in environmental impact [197]. Fuel supply considerations account for the production, processing and transportation of fuels. For example, although Figure 2.5 shows reduced tank-to-electricity CO_2 emissions for LNG compared to MGO, it has been argued that methane emissions associated with its production and distribution may in some cases result in a net increase in GHG impact [198, 199].

In contrast to the manufacturing, maintenance and decommissioning stages, fuel supply considerations are only partly fuel cell specific. Stringent fuel quality requirements may impose additional fuel processing, and the supplied fuel may influence the performance of the fuel cell system. Other aspects of fuel supply, such as origin and transport, are similar for fuel cell systems and combustion engines and are, therefore, out of the scope of this review. However, it should be noted that these aspects have an important contribution to the environmental impact of maritime electricity generation.

Three life cycle assessments have been carried out for maritime fuel cell systems. Two of them assume continued use of diesel fuels for the traditional engine-generator sets, while renewables are considered only for the fuel cell system [118, 196]. However, a complete life cycle assessment should evaluate the use of renewable fuels in conventional generators as well. Pehnt [200] shows, for example, that using renewable hydrogen in an

internal combustion engine may still result in lower GHG emissions compared to a fuel cell based drivetrain over a complete life cycle, although others argue differently [201].

Altmann et al. [196] analyse the life cycle performance of diesel engines, fuelled with heavy fuel oils, as well as high temperature fuel cells using low sulphur diesel fuels or LNG and low temperature PEMFCs on hydrogen from various sources. Emissions of HAPs are found to be much lower for fuel cell systems. Although different fuelling options are considered for the investigated systems, various hydrogen origins are analysed for the PEMFC system, showing that reduced GHG emissions are only achieved if the hydrogen is produced from a renewable source.

In a study by Strazza et al. [118] a traditional diesel-generator set is compared to a maritime SOFC system. Rather than frequent stack replacement, maintenance after every 6000 operating hours is assumed to be sufficient. Similar to the study of Altmann et al. [196], several fuelling options are analysed for the SOFC system, while only diesel fuel is considered for the internal combustion engine. The results show that the environmental impact of SOFC operation and manufacturing is low compared to the fuel extraction and refining phase.

Alkaner et al. [81] compare a conventional diesel-generator to a diesel-fuelled MCFC system. They conclude that the net environmental impact of the MCFC system is lower, mainly due to reduced emissions during its operational life. However, the manufacturing phase of the MCFC is responsible for a significantly higher environmental impact than that of the diesel-generator. This is partly due to necessary stack replacement every 5 years. Maintenance requirements for the diesel generator are neglected in this study.

Similar assessments have been carried out for non-maritime applications. An SOFC auxiliary power unit fuelled with diesel is compared to electricity generation with an idling truck diesel engine in a study by Baratto et al. [202]. Clear advantages in environmental impact for the fuel cell unit are reported, partly because idling diesel engines operate far from their optimal operational conditions. Although this comparison is not representative for heavy duty diesel-generator sets, it demonstrates the potential to reduce the environmental impact of ships in low load conditions. Fuel cell generators can offer an alternative for so-called *cold ironing*, where ships are connected to the land-based electricity grid during berth. Pratt et al. [203] analysed a conceptual barge-mounted hydrogen fuelled PEMFC system for cold ironing purposes, concluding that such a system could be both technically and commercially feasible.

Life cycle assessments aspects for fuel cell systems are discussed by Pehnt [200]. A detailed analysis of both low and high temperature fuel cells is presented, for mobile applications as well as stationary power generation, and several important uncertainties are pointed out. For example, fuel cell production methods vary and are still likely to change, and the possibility of recycling is often unknown. The study concludes that high temperature fuel cell systems have clear environmental benefits over conventional generators during a complete life cycle, due to fuel savings and emission reductions during their operational life. Low temperature fuel cells have this potential if renewable hydrogen is available.

2.3.5. SAFETY AND AVAILABILITY

Like every power plant for maritime applications, fuel cell systems will have to comply with classification standards. These regulations usually differ from land-based systems, and make sure that a vessel can be operated safely and reliably. For example, single point failures should be avoided, since complete loss of power due to an emergency shut down is not desirable [204]. It is expected that a redundant fuel cell system design, equipped with adequate ventilation, fire suppression, monitoring and control systems, will meet all classification requirements [73].

Fuel cell systems have few mechanical parts and tend to degrade rather than fail, which results in a high availability [173]. This is further enhanced by the modularity of fuel cell systems, which allows clean, silent and reliable distributed electricity production next to large consumers. This increases the redundancy of the electricity grid, and is one of the reasons some companies have, although yet modest, commercial success applying fuel cell systems in data centers and backup power generation for telecom systems [59, 205].

Next to the fuel cell system itself, classification rules on logistic fuels are of particular importance. Fuels that are either harmful, hazardous or have a flash points below 60°C, will need special precautions before their use on-board will be allowed. Some fuels, such as ammonia and MeOH, are toxic to humans and animals, while other alternatives, such as hydrogen and DME have the advantage that they are non-toxic, non-mutagenic and non-carcinogenic [91, 127, 173]. It should be noted that conventional diesel oils are toxic as well [206],

Volatile, low flashpoint fuels, such as hydrogen and NG, impose the risk of explosions in closed spaces. These fuels will have to comply with the two-barrier-principle for gas supply, which is either achieved by double-walled piping, ventilation ducts or gas tight enclosures [204]. This may be necessary as well for outlet piping, as these can still contain traces of hydrogen and CO. These issues are addressed by the recently approved International Code of Safety for Ships using Gases or other Low-flashpoint Fuels (IGF Code), although this code initially focusses on LNG and its applicability is restricted to vessels under the International Convention for the Safety of Life at Sea (SOLAS) [207].

There is some awareness of these issues among fuel cell developers and classification societies, which is reflected in two recent publications. In particular the publication by Vogler et al. [204] addresses several issues regarding gas safety, such as venting, explosion protection and high pressure storage. Ludvigsen et al. [174] shortly discusses two different class notations for maritime fuel cell systems, *FC-SAFETY* and *FC-POWER*, both developed by DNV. However, current standards by classification bodies are based on limited experience with a small number of systems. Communication between system designers and classification societies should result in safe, yet not overly stringent rules for future fuel cell applications [73]. In addition, the possibility to improve the redundancy an reliability of the electricity grid should be studied further.

2.3.6. ECONOMICS

The development of naval fuel cell systems commenced by the 1970s, and the first demonstration projects of the technology followed in the next two decades. Still, fuel cell systems

have no substantial market share, and high costs are often mentioned as the main reason [208]. PAFCs and MCFCs currently have the most advanced development state, and so far several MWs have been installed for stationary power. Despite this, capital investment cost is reported to be over 5000 $/kW for both system types [209]. The HT-PEMFC, is anticipated to be more efficient and less expensive than the PAFC, although both fuel cell types still struggle with a limited lifetime [66, 210].

Fuel cell systems in their current development state are significantly more expensive than conventional generators, but many companies see potential to reduce the cost of fuel cell technology. Especially the LT-PEMFCs for the automotive sector have seen major price cuts in recent years. Although stack prices at the current production volume, 500 to 1000 midsized fuel cell vehicles per year, are typically still >1000$/kW, projected production costs for automotive LT-PEMFC stacks vary from 280 $/kW at an annual production volume of 20,000 units to 50 $/kW for 500,000 units [211, 212]. A price level of 50 $/kW would put them in direct competition with diesel engines, although lifetime issues and the high cost of the BoP, in particular if hydrocarbon fuels are used, still remain important issues [213].

Although the expected price level of high temperature fuel cell systems is higher, the reduced consumption of hydrocarbon fuels might provide a decent return on investment for these systems. The need for expensive platinum is omitted in high temperature fuel cells, but their active layers rely on rare earth oxides. Although these are far cheaper than platinum, a substantially larger amount is needed. In addition, the high operational temperature limits the material choices for other stack components, the specific power is usually lower and manufacturing costs are relatively high [214, 215].

Lee et al. [216] conclude from a study of stand-alone NG-fuelled SOFC systems that there is a need to bring down the capital costs of the stack and the inverter to make these systems economically viable, even if this would result in a lower system efficiency. The limited lifetime of the stack has an important effect on the results. Most studies assume a system life cycle of 20 to 30 years, whereas stack lifetime is currently 2 to 3 years [217]. Although some manufacturers aspire lifetimes in the range of 5 to 7 years, this is still an ambitious target for most suppliers [218].

Although fuel cell systems already provide an economically attractive choice in specific business cases, such as material handling and back-up power, it is often stated that they will be economically attractive for a wider range of applications if a substantial market volume is attained. However, a recent study of domestic fuel cell systems by Staffel et al. [213] shows that full market penetration may be required to achieve target prices at the current learning rates. This would imply that the fuel cell market will depend on government support programs for several decades, which leads to the conclusion that incremental learning should not be the only route to cost reduction.

While several car manufacturers are scaling up their LT-PEMFC production volume, researchers have taken SOFCs back to the laboratory to develop more cost effective fuel cell concepts before scaling up. Although it is difficult to estimate just how effective these efforts will be, some promising results have been published. Researchers in the SECA program claim that stack production costs of 175 $/kW can be achieved with current technology [58]. In general, estimates of mass produced SOFC stack production cost vary from 150 to 1500 $/kW [219]. This would be a competitive price level, provided that the

cost of the BoP is lowered accordingly.

2.4. EXPERIENCE IN MARITIME FUEL CELL APPLICATION

2.4.1. MARITIME FUEL CELL RESEARCH PROJECTS

Several research projects have been carried out during the last two decades, varying from naval programs to industrial projects. The most noticeable projects are briefly discussed in this section.

Class 212 submarines The first preliminary studies of PEMFC based AIP systems for submarines started in the 1970s. This resulted in the development of such a system in the early 1980s, and finally the production of the *Class 212 submarines* by Howaldtswerke-Deutsche Werft (HDW) in 1998 [54]. The Siemens fuel cell system consists of two 120 kW PEMFC modules, hydrogen is stored in metal hydrides, and liquid oxygen is carried in a vacuum-insulated tank. Over thirty submarines with a fuel cell AIP system have been commissioned so far.

SSFC The *ship service fuel cell* (SSFC) project started in 1997 and aimed to develop diesel-fuelled fuel cell systems for naval ships and other vessels. The goals were to reduce fuel consumption, noise, thermal signatures, maintenance cost and emissions. In addition, the distribution of generators throughout the ship should enhance survivability. Conceptual designs for a 2.5 MW MCFC and PEMFC system were developed, and demonstrators 0.5 MW were tested. High complexity, long start-up times and prices were pointed out as the most important issues [76, 77, 173].

DESIRE The *diesel reforming with fuel cell* (DESIRE) project commenced in 2001 and developed a 25 kW technology demonstrator of a diesel fuel processor for PEMFCs, to be used for naval application. A small fuel cell system was successfully connected to the fuel processor. Promising results were presented, but problems with sulphur removal, load transients and robustness were identified [75].

FCSHIP In the *fuel cell technology for ships* (FCSHIP) project a large consortium of European partners cooperated in providing a roadmap for future research and development on waterborne fuel cell application. Operational and safety requirements were investigated, and conceptual designs were developed. Finally, the life cycle impact of a marinised MCFC system was assessed and compared to a conventional diesel engine-generator set [81].

FellowSHIP A 330 kW LNG-fuelled MCFC was installed on-board of the offshore supply vessel 'Viking Lady' in the *fuel cells for low emissions ships* (FellowSHIP) project. The fuel cell system was operated successfully for 18500 hours, and demonstrated a net electrical efficiency of ~44.4% with no detectable NO_X, SO_X and PM emissions [174, 221].

Table 2.3: An overview of the most noticeable maritime fuel cell application research projects.

Program	Period	Fuel cell type	Logistic fuel	Application	Project lead	References
Class 212	1980-1998	PEMFC	Hydrogen	Submarine AIP	Howaldtswerke-Deutsche Werft	[54, 220]
SSFC	1997-2003	MCFC/PEMFC	Diesel	Naval ship	Office of Naval Research	[76, 77, 173]
DESIRE	2001-2004	PEMFC	Diesel	Naval ship	Energy Research Centre Nld	[75]
FCSHIP	2002-2004	MCFC	Diesel		Norwegian Shipowners' Ass.	[81]
FellowSHIP	2003-2013	MCFC	LNG	Offshore supply	DNV Research and Innovation	[174, 221]
FELICITAS	2005-2008	SOFC/GT	Diesel, LPG, CNG	Mega yacht	Frauenhofer Institute	[179]
MC-WAP	2005-2011	MCFC	Diesel	RoPax, RoRo	CETENA	[78, 79]
ZEMSHIP	2006-2010	PEMFC	Hydrogen	Passenger	ATG Alster Touristik GmbH	[204, 222]
METHAPU	2006-2009	SOFC	MeOH	Car carrier	Wärtsilä Corporation	[118, 223]
Nemo H_2	2008-2011	PEMFC	Hydrogen	Passenger	Fuel Cell Boat BV	[204, 220]
SchIBZ	2009-2016	SOFC	Diesel	Multipurpose	ThyssenKrupp Marine Systems	[53, 224, 225]
PaXell	2009-2016	HT-PEMFC	MeOH	Cruise ship	Meyer Werft	[224, 225]

FELICITAS The *fuel cell power trains and clustering in heavy-duty transport* (FELICITAS) project studied multiple heavy duty power trains, among which a SOFC auxiliary power unit for a mega yacht. Various marinisation aspects of SOFC technology where investigated, as well as hybridisation with flywheels. Furthermore, coupling of the SOFC systems with a gas turbine and the heating ventilation and air-conditioning system was examined [179].

MC-WAP The objective of the 2005 *molten-carbonate fuel cells for waterborne application* (MC-WAP) project was to develop and test a 0.5 MW MCFC auxiliary power generators for on-board testing on RoPax, RoRo and cruise vessels. Eventually tests were performed on an existing MCFC research plant and various conceptual designs were developed [78, 79].

ZEMSHIP The passenger vessel *FCS Alsterwasser* was equipped with a hydrogen-fuelled PMEFC system in the *zero emission ship* (ZEMSHIP) project, and was operated successfully for two seasons. The vessel was heavily damaged in a fire during a test run, caused by overheating of the lead-acid batteries. Since the fuel cell system and the hydrogen storage were not damaged, the incident proved the suitability of the applied hydrogen safety concept [204].

METHAPU In the *methanol auxiliary power unit* (METHAPU) project a 20 kW SOFC demonstrator was marinised and tested on-board of the car carrier 'Undine'. Additional objectives of the project were to facilitate the introduction of international regulations on MeOH as a marine fuel, and to assess the environmental impact of such applications [118, 223].

Nemo H_2 Fuel Cell Boat BV has developed the passenger vessel *Nemo H_2* for canal cruises in Amsterdam. It is propelled with a 60-70 kW PEMFC system, hybridised with a 55 kW lead acid battery pack [220]. The vessel was delivered in 2011, but has not entered active service as of now due to the absence of a permanent hydrogen fuelling station.

SchIBZ The *ship-integrated fuel cell project* (SchIBZ) started in 2009 and is still ongoing. The target of the project is to install and evaluate a 0.5 MW diesel-reformer integrated SOFC system on the vessel 'MS Forester'. Design calculations showed that LHV efficiency up to 55% can be obtained. So far, a 27 kW system demonstrated an electrical efficiency over 50% on low sulphur diesel for more than 1000 hours. Tests with a 50 kW system at sea are planned for 2016 [53, 224, 225].

Pa-X-ell The Pa-X-ell project is part of the same program as the SchIBZ project. The Pa-X-ll project focusses on the integration and safety aspects of MeOH-fuelled HT-PEMFC systems in cruise ships. Investigations include the placement of fuel cells in different fire zones, safe supply of low-flashpoint fuels, and thermal and electrical integration of fuel cells. A 120 kW fuel cell container has been developed for long term trials [224, 225].

2.4.2. LESSONS LEARNED

The first noticeable projects focussed on using fuel cell systems with conventional diesel as a logistic fuel. This proved to be problematic due to the sulphur susceptibility of catalysts in both reformers and fuel cells. The use of diesel fuels in LT-PEMFCs was shown to be inefficient compared to diesel engine-generator sets. Although diesel-fuelled MCFC systems were expected to achieve significantly higher efficiencies, this was never successfully demonstrated on-board.

More recently, the focus shifted towards the use of LNG and MeOH as logistic fuels. The METHAPU and especially the FellowSHIP project managed to test systems on-board for significant periods, demonstrating high electrical efficiencies and low emissions. The Pa-X-ell project seems to take MeOH-fuelled systems to the next level, aiming to demonstrate a significant amount of distributed power generation on a cruise vessel. The SchIBZ project seems on track to show robust and highly efficient electricity generation from low-sulphur or synthetic diesel fuels with an SOFC system.

There has been significant progress during recent decades in the development of fuel cell systems. However, some specific maritime requirements have hardly been addressed. For example, LNG-fuelled SOFC systems have never been demonstrated on vessels, although this seems to be an obvious choice given recent developments in NG-fuelled stationary SOFC systems. More specifically, SOFCs combined with reciprocating engines, as proposed by several authors [47, 52, 181], may offer a near-future solution to reduce fuel consumption and specific emissions considerably compared to conventional generators. In addition, hybridisation with auxiliary energy storage components to improve transient capabilities, which is well developed in automotive applications, has hardly been addressed.

2.5. SUMMARY

This review provided a resume of fuel cell types, logistic fuels and fuel processing equipment, to provide insight into the implications of choices for fuel cell types and logistic fuels on the overall fuel cell system characterises. This supported an analysis of the suitability of the these systems for electrical power generating on-board ships, for which electrical efficiency, gravimetric and volumetric density, system dynamics, environmental impact, safety and economics were discussed. Finally an overview of research projects on maritime fuel cell application was presented.

Low temperature fuel cells can achieve high electrical efficiencies if hydrogen is available as a logistic fuel. However, the efficiency is significantly reduced if hydrocarbon fuels are used, mostly due to the need to reform and clean these fuels, and subsequent parasitic losses. As a result, heavy duty internal combustion engine-generators are probably more efficient. High temperature fuel cells provide better integration with fuel processing equipment, and have higher tolerances for impurities in the fuel. Especially when combined with gas turbines or reciprocating engines, these fuel cell systems can attain higher electrical efficiencies than conventional generators.

Competitive power densities have already been demonstrated by some fuel cell car developers with hydrogen-fuelled LT-PEMFCs, as this is an important development objec-

tive for automotive application. The power density achieved by high temperature fuel cell systems is lower, which is partly due to the increased BoP and heat insulation. However, a Ragone chart comparison showed that fuel savings by high temperature fuel cell systems and the higher energy density of hydrocarbon fuels result in a more compact system when operation over several dozens of hours is required. The total volume of a LT-PEMFC plant with cryogenic hydrogen storage is shown to be 1.5 to 5 times larger than alternative options for vessels with refuelling intervals over 100 hours.

Load transient capabilities of fuel cell systems have a similar dependence on the fuel cell type and fuel processing requirements. In general, systems with a large BoP and thermal mass have longer start-up times and limited load-following capabilities. Therefore, hybridisation with auxiliary electricity storage components, such as batteries, supercapacitors or flywheels will be required in many cases to meet maritime power requirements.

Various assessments have shown that fuel cell systems can achieve a lower environmental life cycle impact than diesel engine-generators sets, mainly due to reduced local emissions during their operational life time. However, the manufacturing stage has a relatively large impact, and the environmental gains depend on the life time of the stacks and recyclability of stack materials. High temperature fuel cells have a clear potential to reduce greenhouse gas emissions over their life cycle due to the high efficiencies that can be achieved, even if fossil fuels are used. Their low temperature counterparts have this potential if renewable hydrogen is available.

Some classification standards have been developed for maritime fuel cell systems, but currently provide no general approach for safety assessment of all fuel cell systems, and can be overly stringent. In particular storage and handling of volatile, low flash point fuels needs careful consideration. On the other hand, the high availability and the opportunity to distribute power generation over the vessel can improve the redundancy of electricity generation. This should be further studied for future classification standards.

It is expected that fuel cell systems will remain relatively expensive in the near future. However, significant cost reductions have been demonstrated lately, and novel concepts have shown the potential to reduce investment costs even further. It is expected that price levels can be achieved where reductions in fuel consumption, emissions, noise and vibrations would justify the higher a higher capital cost.

2.6. CONCLUDING REMARKS

Fuel cell systems provide an efficient way to generate electricity on-board from a variety of logistic fuels, with few HAP emissions. Liquefied hydrogen-fuelled LT-PEMFC systems provide a power dense solution for ships with mission requirements up to a dozen hours. However, for sailing times over 100 hours the limited hydrogen storage density is expected to result in 1.5 to 5 times larger total system volumes compared to alternative systems with more energy dense logistic fuels.

High temperature fuel cell systems can achieve high overall system efficiencies using various hydrocarbon fuels, especially when equipped with bottoming cycles. Such systems can attain relatively low emission levels and reasonable density for ships with mission requirements of several days. For vessels that require longer independent opera-

tion, ship owners may face a trade-off between smaller fuel tanks using a dense logistic fuel, such as diesel, and fuel savings using a less energy dense gaseous fuel, for example NG.

Several challenges will have to be addressed before fuel cell systems are able to meet all maritime power requirements and can compete with state-of-the-art maritime solutions. The following topics are identified as most interesting for immediate further study:

- The increasing availability of LNG and the rapid development of NG-fuelled fuel cell systems justifies maritime demonstration of such systems;
- Fuel cell combined cycles have the potential to attain an even lower fuel consumption. Combining SOFCs with reciprocating engine generator sets seems particularly interesting for near-future maritime application;
- Hybridisation with auxiliary electricity storage components, capable of following the demanded load transients, requires further development;
- Classification standards on opportunities to increase the redundancy of power supply with distributed electricity generation should be investigated.

Currently available fuel cell systems are significantly more expensive than conventional generators, but it is expected that system prices can be reduced to levels where the higher investment cost is justified by the advantages. These benefits stand out for vessels which operate in ECA zones, since exhaust gas cleaning is avoided entirely. LNG fuelling is already being adopted for these ships to meet stringent emission requirements.

Although environmental benefits from LNG as a logistic fuel are debatable from a total life cycle perspective, NG-fuelled fuel cell systems have a relatively advanced development state, and the application of SOFC-combined cycles can further improve the well-to-wave efficiency. In addition, most alternatives, such as hydrogen, MeOH and DME, are currently produced from a fossil feedstock, and NG can be produced from renewable sources as well. Therefore, a detailed analysis of various SOFC-combined cycles fuelled with NG is presented in the next chapter.

3

A COMPARISON OF SOFC-COMBINED CYCLES

This chapter has been published in Journal of Power Sources **397**, (2018) [226].

3.1. INTRODUCTION

In the previous chapter, it was concluded that SOFCs combined with thermal cycles may offer a promising solution for ships with mission requirements of several days or longer. Integration with reciprocating engines, the conventional power technology in shipping, was identified as particularly interesting. Although a variety of integration options for SOFCs with thermal cycles has been proposed, the combination with reciprocating engines has not been investigated in detail. Moreover, comparing a SOFC-reciprocating engine system to other integration schemes is challenging due to inconsistency in the operating parameters assumed in different SOFC-combined cycles studies.

A thermodynamic comparison of different SOFC-combined cycles and a stand-alone system is presented in the chapter. Section 3.2 discusses notable literature from the past 20 years on SOFC-combined cycles. The systems selected for this study, including integration with a reciprocating engine, are then described in Section 3.3. Section 3.4 gives the methodology used for the thermodynamic analysis, as well as a plug flow reactor SOFC model for stack power density calculations. The results are presented in Section 3.5 and discussed in Section 3.6, after which the conclusions follow in Section 3.7.

3.2. SOFC-COMBINED CYCLES

High electrical efficiencies are expected if waste heat or fuel from the high temperature SOFC is further utilised in thermal cycles. Efficiencies in excess of 70% are, for example, projected for the SOFC-gas turbine combined cycle concepts [45, 227]. A variety of SOFC-combined cycle configurations has been studied, mostly with either gas turbines or Rankine cycles [46, 47, 180, 228]. Alternatively, integration with Stirling engines, reciprocating engines and polymer electrolyte fuel cells has been proposed [180, 181, 229]. An overview of notable SOFC-combined cycle studies is shown in Table 3.1.

Although the SOFC-gas turbine cycle was first proposed over 30 years ago, the technology has not yet left the demonstration phase [227, 239, 240]. Moreover, no system has demonstrated the record level efficiencies predicted from system calculations, which has been attributed to mismatching between the SOFC and gas turbine subsystem [111]. Meanwhile, stand-alone SOFC systems demonstrate higher efficiencies than originally anticipated, while their operating temperature is lowered and fuel utilisation maximised [42]. This raises the question what added value is offered by integration with thermal cycles, and how changing the stack operation affects different SOFC-combined cycle configurations.

The potential of combining cycles is usually investigated through a thermodynamic analysis, sometimes in comparison to stand-alone SOFC operation. For example, Campanari et. al. [44] showed that the integration of an SOFC with a gas turbine yields slightly higher electrical efficiencies than a steam turbine combined cycle configuration. However, they report ultimate efficiencies in excess of 75% for both systems, while Whiston et al. [238] recently reported an electrical efficiency of only 52.9% for a similar gas turbine combined cycle. Although the discrepancy may be explained by different modelling assumptions among these studies, such contradictory results illustrate that a comprehensive comparison is difficult.

Table 3.1: Notable SOFC-combined cycle studies in the past 20 years in chronological order, the assumed fuel utilisation and operation temperature of the SOFC and the maximum electrical efficiency reported.

Reference	Thermal cycle	Fuel utilisation factor [-]	Stack temperature [°C]	Electrical efficiency [% LHV]
Massardo et al. [45]	Pr. GT	-	877-1027	76
Campanari [230]	Pr. GT+RC	0.85 (sp)	1000	74.3
Campanari [231]	Pr. GT	0.8 (sp)	1000	64.9
Costamagna et al. [232]	Pr. GT	0.85	850-950	61
Chan et al. [233]	Pr. GT	0.85	925	61.9
Park et al. [234]	Amb./Pr. GT	0.7 (sp)	800-1000	66.5/72.5
Calise et al. [235]	Pr. GT	0.7-0.9	800-1100	60
Roberts et al. [236]	Amb. GT	0.85	750	66
Rokni et al. [46]	RC	0.72-0.83	780	67
Gandiglio et al. [237]	RC/Pr. GT+RC	0.85	800	64.6/71.9
Park et al. [47]	Amb. GT/RE	0.75	850	58.6/59.5
Campanari et al. [44]	RC/Pr. GT	0.85	750	75.2/78.7
Whiston et al. [238]	Pr. GT	0.77-0.9	650-850	52.9

Pr. GT = pressurised SOFC-gas turbine
Amb. GT = ambient pressure SOFC-gas turbine
(sp) = for a single pass, anode off-gas recirculation
RC = SOFC-Rankine cycle
RE = SOFC-reciprocating engine

A thermodynamic comparison of a stand-alone SOFC reference system and four SOFC-combined cycles is presented in this chapter. The investigated combined cycles include a steam turbine combined cycle and two gas turbine combined cycles with the stack at ambient and elevated pressure respectively. In addition, a relatively unexplored reciprocating engine combined cycle is included. Reciprocating engines provide a cost effective solution in a variety of applications and are, therefore, expected to facilitate system integration with limited complexity and consequently cost reductions.

The wide range of efficiencies reported in Table 3.1 for similar systems indicates that no meaningful comparison can be made between SOFC-combined cycles if the assumptions regarding the stack operation are different. Fuel utilisation, cell voltage, stack temperature and pressure affect the chemical and thermo-mechanical exergy in the outlet flows of the SOFC, while the ability to use this exergy differs among the investigated combined cycles. Therefore, fuel utilisation, cell voltage, stack temperature and gas turbine compression ratio are not selected based on pre-defined system operation, but varied in the analysis.

Inspired on conventional power plant analysis, for which the performance is usually mapped within the operating window, the results are presented in contour plots of constant system efficiency, stack power density and the fraction of total power delivered by the thermal cycle for the investigated SOFC parameter range. This new approach enables a true comprehensive comparison of SOFC-combined cycles, since their performance is analysed across the entire SOFC operating envelope rather than for one arbitrarily

defined point. Moreover, an exergy analysis is included to investigate how the studied SOFC-combined cycles utilise the exergy flows leaving the SOFC, and provide guidance for potential further improvement.

3.3. DESCRIPTION OF THE INVESTIGATED SYSTEMS

Five representative configurations are selected for this study. First of all a stand-alone SOFC system is defined as a reference system for comparison with SOFC-combined cycles. An SOFC-steam turbine combined cycle is selected, which provides a relatively simple way to convert waste heat available in the SOFC exhaust into additional electricity using established power plant technology. In addition, an SOFC-reciprocating engine combined cycle is included, where anode off-gas is combusted in a lean burn spark ignited engine, thus using chemical rather than thermo-mechanical exergy from the SOFC. Finally, two SOFC-gas turbine combined cycle layouts are studied, since these enable a synergetic coupling through the use of cathode air, the cooling medium and oxygen source in the SOFC, as the gas turbine working fluid. The SOFC stack is operated at ambient and elevated pressure respectively in the two different systems. The flow sheets of the investigated combined cycle configurations are shown in Figure 7.1.

3.3.1. STAND-ALONE SOFC SYSTEM

The stand-alone reference SOFC system, shown in Figure 3.1a, is based on configurations reported in literature [134, 241]. An air blower provides pre-heated air to the cathode of the SOFC. Fresh fuel is mixed with recirculated anode exhaust gas, pre-heated and passed through the adiabatic pre-reformer before entering the anode compartment. The remaining fuel is burned in a combustor with air from the cathode, and the hot flue gas is used to provide heat to fuel and air pre-heater.

3.3.2. SOFC-STEAM TURBINE COMBINED CYCLE

Figure 3.1b shows the flow sheet of the SOFC-steam turbine combined cycle in this study, based on a conventional medium-scale power plant design [44, 46]. An economiser, evaporator and superheater recover waste heat from the SOFC exhaust gas to generate high-pressure steam. The steam is then expanded in a turbine, condensed and passed through a deaerator before re-entering the feed water pump. Air is bypassed to the combustor if its outlet temperature exceeds 1150°C, the maximum temperature allowed for metallic recuperators [242]. In addition, this air bypass ensures that sufficient air is available for complete combustion of anode off-gas.

A maximum steam superheat temperature of 500°C is assumed, as well as a condenser pressure of 3 mbar. This corresponds to a condenser temperature of 24°C, and results in a 9°C temperature difference for a cooling water temperature of 15°C. The turbine inlet pressure is fixed at 34.4 bar, allowing a maximum moisture content of 9% in the turbine outlet. The pinch point temperature difference in the evaporator is 15°C.

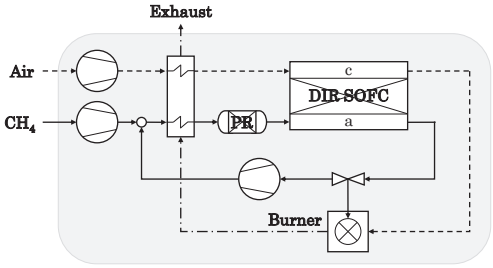

(a) Stand-alone reference SOFC system.

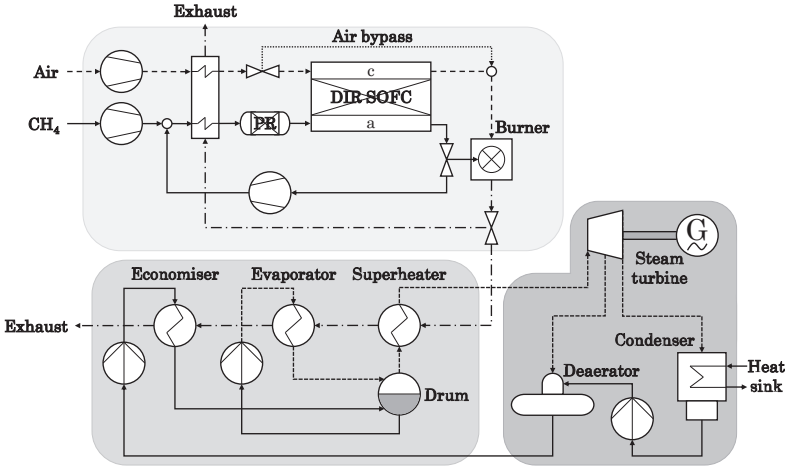

(b) SOFC-steam turbine combined cycle.

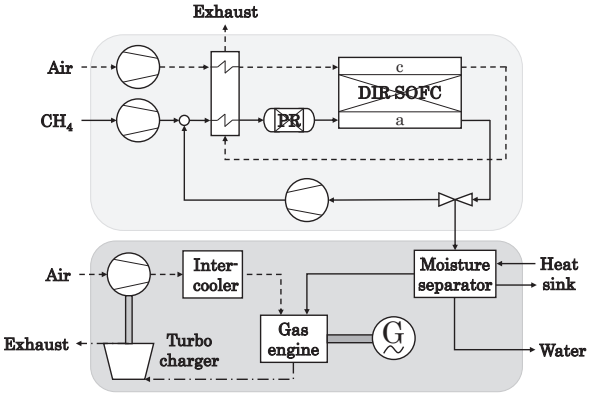

(c) SOFC-reciprocating engine combined cycle.

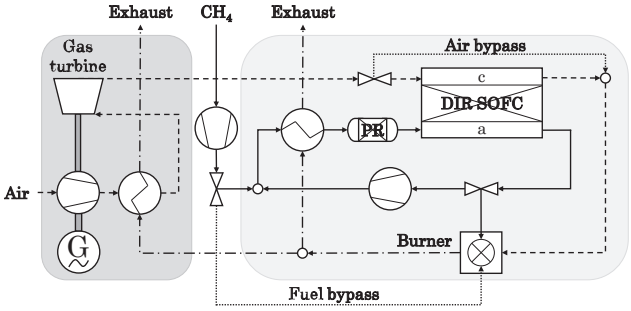

(d) Ambient SOFC-gas turbine combined cycle.

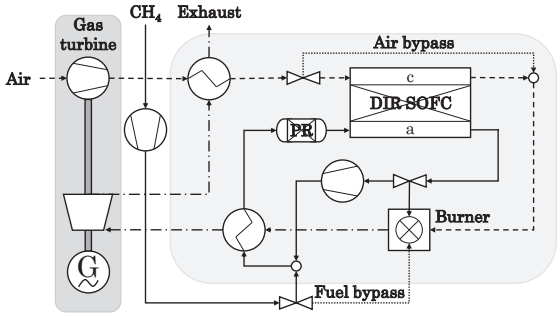

(e) Pressurised SOFC-gas turbine combined cycle.

Figure 3.1: Flow sheets of the investigated stand-alone and combined cycle configurations.

3.3.3. SOFC-RECIPROCATING ENGINE COMBINED CYCLE

The second integration option studied is relatively unconventional and fundamentally different in nature. Rather than using the high temperature waste heat to produce additional power, combustibles in the anode off-gas are burned in a reciprocating engine. There is no air coupling on the cathode side and, hence, no need to control the adiabatic temperature in the combustor. A part of the steam is condensed from the anode off-gas by cooling it to 50°C, since excessive amounts of steam are reported to cause ignition problems in the engine [243]. The system layout is shown in Figure 3.1c.

The reciprocating engine is model is based on a state-of-the-art lean burn spark ignited gas engine-generator set fuelled with natural gas [244]. A Seiliger cycle is assumed, comprising isentropic compression of air and fuel with a specified compression ratio, a combination of isochoric and isobaric combustion with resulting mean effective pressure rise, and isentropic expansion of the reaction products. Furthermore, a turbocharger, an intercooler and an electricity generator are included in the model. Charge pressure, compression ratio, mean effective pressure and air excess ratio are known for the modelled engine, while values for mechanical losses, heat losses and fuel slip due to scavenging and incomplete combustion are adjusted to match its generator curve. The verification of

Table 3.2: Specific fuel consumption calculated with the reciprocating engine model and values reported for a natural gas-fuelled lean burn spark ignited gas engine [244].

Engine load	Specific fuel consumption [kJ/kWh]	
[% rated power]	Model	Reference
100	7.50	7.52
50	8.16	8.15
25	10.06	10.00

the model is shown in Table 3.2.

3.3.4. AMBIENT SOFC-GAS TURBINE COMBINED CYCLE

Two fundamentally different SOFC-gas turbine system layouts can be found in literature, referred to as the *indirect* and *direct* heated configuration [234]. In the indirect heated system, waste heat from an SOFC operating at ambient pressure is transferred to the high pressure working medium in the gas turbine. Therefore, this is referred to as the *ambient SOFC-gas turbine combined cycle* in this study, while the configuration with the SOFC in the high pressure loop is referred to as the *pressurised SOFC-gas turbine combined cycle*.

The layout of the ambient SOFC-gas turbine cycle, adopted from previous studies [45, 236], is shown in Figure 3.1d. Since the airflow in the gas turbine and cathode are coupled to enhance system efficiency, the turbine outlet temperature should match the SOFC inlet temperature. Therefore, the turbine inlet temperature (TIT) is determined by the stack inlet temperature and gas turbine pressure ratio. Additional fuel or air can be supplied to the combustor if the TIT becomes either too low or too high, for example at high fuel utilisation or low cathode over-stoichiometry.

3.3.5. PRESSURISED SOFC-GAS TURBINE COMBINED CYCLE

The layout of the pressurised SOFC-gas turbine combined cycle, shown in Figure 3.1e, reflects the most commonly reported scheme [231–233, 235]. It resembles a recuperated gas turbine where a part of the combustion takes place in the SOFC stack. The higher operating pressure increases the reversible voltage and reduces polarisation resistance [245]. In contrast to the indirect heated gas turbine, the exhaust gas from the combustor is directly expanded in the turbine, thus reducing exergy losses due to high temperature heat exchange.

The SOFC and gas turbine are coupled even more in the pressurised SOFC-gas turbine combined cycle than in the ambient pressure combined cycle. Similar to the ambient pressure equivalent, the temperature of the flue gas leaving the turbine should be sufficient to transfer heat to the recuperator, and additional fuel or air can be supplied to the combustor to attain the TIT required to achieve this.

3.4. METHODOLOGY

3.4.1. CYCLE-TEMPO CALCULATIONS

The thermodynamic analysis is performed with Cycle-Tempo, a flow-sheet program developed in-house to evaluate the performance of combined cycle power plants. The program incorporates a model database of common components, such as heat exchangers, rotating equipment, evaporators, condensers, combustors, chemical reactors, electricity generators and fuel cells. Each component model adds equations for mass and energy to the system matrix, which is iterated to obtain pressures, mass flows, compositions of flows and temperatures in the system and calculate the power generated. The results can be used to analyse the efficiency of the power plant designs and exergy losses in different components [246, 247].

The majority of previous SOFC-combined cycle system studies assumes natural gas fuelling. In this study, pure methane is selected to facilitate interpretation and comparison of the results. Although any fuel can be electrochemically oxidised in theory, it is commonly assumed that the fast kinetics of the hydrogen oxidation reaction dominate the electrochemistry at the SOFC anode [248]:

$$H_2 + \frac{1}{2}O_2 \Rightarrow H_2O \tag{3.1}$$

To attain satisfactory power densities in the stack, fresh fuel is preferably first converted to a hydrogen rich mixture. Methane steam reforming is an efficient way to accomplish this

$$CH_4 + H_2O \rightleftharpoons 3H_2 + CO, \tag{3.2}$$

followed by the water gas shift reaction [135]:

$$CO + H_2O \rightleftharpoons H_2 + CO_2 \tag{3.3}$$

Both the reforming and shift reaction are assumed to be in chemical equilibrium at the outlet temperature of the adiabatic pre-reformer, and its composition is obtained through Gibbs free energy minimisation. As a result, more methane is pre-reformed for higher operating temperatures.

The reactions then proceed further internally on the SOFC anode. It is assumed that the reactions proceed fast and are, therefore, in chemical equilibrium along the anode. Especially for lower operating temperatures methane conversion might be overestimated by this assumption, since the reforming reaction is most likely kinetically limited. The SOFC outlet compositions follow from chemical equilibrium and the fuel utilisation for a single pass

$$u_{f,sp} = \frac{I}{\dot{n}^{in} \cdot 2F \cdot (y^{in}_{H_2} + y^{in}_{CO} + 4y^{in}_{CH_4})}, \tag{3.4}$$

where I is the total current, $\dot{n}^{in}$ is the inlet fuel flow, F is Faradays constant and y^{in}_i is the concentration of species i at the anode inlet. The outlet composition of the combustor is calculated assuming complete conversion of combustibles:

$$mCH_4 + nCO + oH_2 + (2m + \frac{n}{2} + \frac{o}{2})O_2 \Rightarrow (m+n)CO_2 + (2m+o)H_2O \tag{3.5}$$

Mechanical losses and isentropic efficiencies are defined for pumps, blowers and turbomachinery equipment. The power generated or consumed in these components are calculated from:

$$P_{compressor} = \dot{n} \cdot \frac{(h_{is}^{out} - h^{in})}{\eta_m \cdot \eta_{is,comp}}, \tag{3.6}$$

$$P_{turbine} = \dot{n} \cdot \eta_{mech} \cdot \eta_{is,turbine} \cdot (h^{in} - h_{is}^{out}) \tag{3.7}$$

where h is the specific fluid enthalpy, and the subscript is refers to the outlet state for an isentropic process.

The prime focus of the analysis is the net electrical efficiency, defined as

$$\eta_{AC} = \frac{P_{SOFC,AC} + P_{gen,AC} - P_{aux}}{\dot{n}_f^{in} \cdot LHV_f}, \tag{3.8}$$

since improving this is the main objective of combining cycles. The fraction of power delivered by the generator of the thermal cycle, defined as

$$f_{P,gen} = \frac{P_{gen,AC}}{P_{SOFC,AC} + P_{gen,AC}}, \tag{3.9}$$

is reported as an additional metric. Exergy available in the exhaust gas of the system is considered lost when calculating exergy efficiencies in the system. The exergy loss is determined for every component using an exergy flow balance

$$\dot{Ex}_{loss} = P_{AC}^{out} - P_{AC}^{in} + \sum \dot{Ex}^{in} - \sum \dot{Ex}^{out}, \tag{3.10}$$

where the total exergy is the sum of the thermo-mechanical and chemical exergy of a flow, calculated from

$$\dot{Ex}_{tm} = \dot{n} \cdot \{(h - h_0) - T_0 \cdot (s - s_0)\}, \tag{3.11}$$

$$\dot{Ex}_{ch} = \dot{n} \cdot \left\{ \sum_i y_i \cdot ex_{0,i} + \bar{R} T_0 \sum_i y_i \cdot ln(y_i) \right\}, \tag{3.12}$$

in which s is specific fluid entropy, ex_i is the specific exergy of component i, $\bar{R}$ is the universal gas constant and the subscript 0 indicates at reference environment conditions.

The exergy loss for a component n is then normalised by the total exergy of the fuel to obtain the relative exergy loss:

$$\delta_n = \frac{\dot{Ex}_{loss,n}}{\dot{Ex}_f^{in}} \cdot 100\% \tag{3.13}$$

Ideal gas law is assumed for all gas flows, and the IAPWS-IF97 steam tables are used for the steam turbine bottoming cycle calculations. The environment like Bahr is assumed for the exergy calculations. Table 3.3 specifies the SOFC system and combined cycle-specific parameters for the studied configurations.

Table 3.3: Parameters for the SOFC and combined cycle systems.

General	**Units**	**Value**
Reformer inlet temperature, T^{in}_{ref}	[°C]	T_{stack}-25
Cathode inlet temperature, T^{in}_{ca}	[°C]	T_{stack}-75
Stack outlet temperature, T^{out}_{stack}	[°C]	T_{stack}+25
Minimal HEX temp. difference, $min(\Delta T_{hex})$	[°C]	50
Anode pressure drop, Δp_{an}	[bar]	0.03
Cathode pressure drop, Δp_{ca}	[bar]	0.05
Heat exchanger pressure drop, Δp_{hex}	[bar]	0.02
Isentropic efficiency blower, $\eta_{is,blower}$	[-]	0.7
Mechanical efficiency blower, $\eta_{m,blower}$	[-]	0.8
Inverter efficiency, $\eta_{inverter}$	[-]	0.95
Electricity generator efficiency, η_{gen}	[-]	0.95
Steam turbine		
Steam turbine inlet temperature, $T^{in}_{turbine}$	[°C]	500
Steam turbine inlet pressure, $p^{in}_{turbine}$	[bar]	34.4
Condenser pressure, $p_{condenser}$	[bar]	0.03
Pinch point temperature difference, ΔT_{pinch}	[°C]	≥15
Maximum flue gas temperature, $max(T^{out}_{comb})$	[°C]	1150
Isentropic efficiency steam turbine, $\eta_{is,turbine}$	[-]	0.85
Isentropic efficiency feed water pump, $\eta_{is,pump}$	[-]	0.85
Mechanical efficiency feed water pump, $\eta_{m,pump}$	[-]	0.9
Reciprocating engine (rated power)		
Charge pressure, p_{charge}	[bar]	4
Compression ratio, Π_{comp}	[-]	12
Mean effective pressure, $p_{mean,eff}$	[bar]	18.1
Intercooler outlet temperature, $T^{out}_{intercooler}$	[°C]	50
Condenser outlet temperature, $T^{out}_{condenser}$	[°C]	50
Air excess ratio	[-]	2.2
Mechanical efficiency, η_{mech}	[-]	0.965
Heat loss in cylinder, Δh_{loss}	[kJ kg^{-1}]	16
Fuel slip (fraction of unburned fuel), f_{slip}	[-]	0.01
Gas turbines		
Isentropic efficiency compressor, $\eta_{is,comp}$	[-]	0.78
Isentropic efficiency turbine, $\eta_{is,turbine}$	[-]	0.82
Mechanical efficiency shaft, $\eta_{mech,shaft}$	[-]	0.98

3.4.2. STACK POWER DENSITY CALCULATIONS

The operational conditions imposed on the stack do not affect its electrical efficiency, since the SOFC is operated at a constant cell voltage [249]. Nonetheless, the current density is expected to differ substantially with temperature, pressure, fuel inlet composition, fuel utilisation and operational voltage in the stack. This in turn affects the average stack power density and consequently the capital cost of the system.

The power density in the stack is estimated using an isothermal plug flow reactor model of the SOFC, by multiplication of the average current density with the cell voltage. The average current density follows from integration of the local current density for the reaction coordinate ϑ, which is the fraction of fuel that has been electrochemically converted:

$$\bar{P}_{stack} = j \cdot U_{cell} = \frac{u_{f,sp} \cdot U_{cell}}{\int_0^{u_{f,sp}} d\vartheta / j(\vartheta)} \tag{3.14}$$

It is thus necessary to determine the local current density j as a function of reaction coordinate ϑ. Local concentrations can be calculated as a function of ϑ if chemical equilibrium is assumed. The local current density then follows from an electrochemical model adopted from Aguiar et al. [48]. The ohmic ($\hat{\eta}_{ohm}$), activation ($\hat{\eta}_{act}$) and concentration ($\hat{\eta}_{conc}$) overpotential losses follow from the subtraction of the operating voltage from the Nernst voltage:

$$\begin{aligned} \hat{\eta}_{loss}(\vartheta) &= U_{Nernst}(\vartheta) - U_{cell} \\ &= \hat{\eta}_{ohm}(\vartheta) + \hat{\eta}_{conc}(\vartheta) + \hat{\eta}_{act,an}(\vartheta) + \hat{\eta}_{act,ca}(\vartheta) \end{aligned} \tag{3.15}$$

Since the hydrogen oxidation reaction is assumed to dominate the electrochemistry, the local Nernst voltage is given by

$$U_{Nernst}(\vartheta) = U^0_{rev} + \frac{\bar{R}T_{stack}}{2F} ln\Big\{ \frac{\sqrt{y_{O_2}(\vartheta)} \cdot y_{H_2}(\vartheta)}{y_{H_2O}(\vartheta)} \sqrt{\frac{p}{p_0}} \Big\}, \tag{3.16}$$

where U^0_{rev} is the reversible potential for hydrogen oxidation at standard pressure (p_0) and average stack temperature and y_i is the local concentration of species i. The ohmic resistance is constant along the cell, since the SOFC is modelled as an isothermal plug flow reactor. The resulting voltage loss follows from

$$\hat{\eta}_{ohm}(\vartheta) = j(\vartheta) \cdot \Big(\frac{\tau_{an}}{\sigma_{an}} + \frac{\tau_{el}}{\sigma_{el}} + \frac{\tau_{ca}}{\sigma_{ca}} \Big), \tag{3.17}$$

where τ and σ are the thickness and conductivity of the anode, electrolyte and cathode respectively. The concentration losses account for the deviation of the gas concentrations at the triple phase boundary from the bulk flow, mathematically expressed as:

$$\begin{aligned} \hat{\eta}_{conc}(\vartheta) = &\frac{\bar{R}T_{stack}}{2F} ln\Big(\frac{p_{H_2O,tpb}(\vartheta) \cdot p_{H_2}(\vartheta)}{p_{H_2O}(\vartheta) \cdot p_{H_2,tpb}(\vartheta)} \Big) \\ &+ \frac{\bar{R}T_{stack}}{4F} ln\Big(\frac{p_{O_2}(\vartheta)}{p_{O_2,tpb}(\vartheta)} \Big), \end{aligned} \tag{3.18}$$

in which the reactant partial pressures at the triple phase boundary $p_{i,tpb}$ depend on partial pressures in the bulk flow, stack temperature, effective diffusion coefficient and local current density:

$$p_{H_2,tpb}(\vartheta) = p_{H_2}(\vartheta) - \frac{\bar{R}T_{stack}\tau_{an}}{2FD_{eff,an}} j(\vartheta), \tag{3.19}$$

$$p_{H_2O,tpb}(\vartheta) = p_{H_2O}(\vartheta) + \frac{\bar{R}T_{stack}\tau_{an}}{2FD_{eff,an}} j(\vartheta), \tag{3.20}$$

$$p_{O_2,tpb}(\vartheta) = p_{stack} - (p_{stack} - p_{O_2}(\vartheta)) exp\Big(\frac{\bar{R}T_{stack}\tau_{ca}}{4FD_{eff,ca}p_{stack}} j(\vartheta)\Big) \tag{3.21}$$

The activation overpotential losses in the anode are calculated from a corrected Butler-Volmer equation, which gives a better description of the activation losses if charge and mass transfer are co-limiting the electrochemical reaction

$$\begin{aligned} j(\vartheta) = j_{0,an} \cdot \Big[& \frac{p_{H_2,tpb}(\vartheta)}{p_{H_2}(\vartheta)} \cdot exp\Big(\frac{\omega 2F}{\bar{R}T_{stack}} \hat{\eta}_{act,an}(\vartheta)\Big) \\ & - \frac{p_{H_2O,tpb}(\vartheta)}{p_{H_2O}(\vartheta)} \cdot exp\Big(-\frac{(1-\omega)2F}{\bar{R}T_{stack}} \hat{\eta}_{act,an}(\vartheta)\Big)\Big], \end{aligned} \tag{3.22}$$

while it is assumed that activation losses in the cathode are dominated by charge transfer losses only:

$$\begin{aligned} j(\vartheta) = j_{0,ca} \cdot \Big[& exp\Big(\frac{\omega 2F}{\bar{R}T_{stack}} \hat{\eta}_{act,ca}(\vartheta)\Big) \\ & - exp\Big(-\frac{(1-\omega)2F}{\bar{R}T_{stack}} \hat{\eta}_{act,ca}(\vartheta)\Big)\Big] \end{aligned} \tag{3.23}$$

The symmetry factor ω is assumed to be 0.5 and the exchange current density j_0 is calculated from:

$$j_0 = \hat{k}_0 \cdot \frac{\bar{R}T_{stack}}{zF} \cdot exp\Big(-\frac{E_a}{\bar{R}T_{stack}}\Big) \tag{3.24}$$

Subsequently, Equations (3.15) to (3.24) can be solved to determine the current density j for the reaction coordinate ϑ. The average power density in the stack then follows from Equation (3.14). Properties used for the electrochemical model are obtained from [48], and provided in Table 3.4.

The goal of this electrochemical model is to give an indication of the effect of changing the operating conditions on the power density of an anode supported intermediate temperature SOFC. However, it should be mentioned that a more accurate calculation of the power density requires consideration of the internal temperature distributions in the SOFC, as well as kinetics of internal reforming and water gas shift reactions. Moreover, detailed information on the geometry, materials used and electrochemical properties is required, which varies among products.

Table 3.4: Parameters used to in the electrochemical model, adopted from [48].

Parameter	Units	Value
Anode		
Thickness, τ_{an}	[m]	500e-6
Electric conductivity, σ_{an}	[Ω^{-1}m^{-1}]	8e4
Diffusion coefficient, $D_{eff,an}$	[m^{2}s^{-1}]	3.66e-5
Exchange current density factor, $\hat{k}_{0,an}$	[Ω^{-1}m^{-2}]	6.54e11
Activation energy, $E_{a,an}$	[J mol^{-1}]	137e3
Cathode		
Thickness, τ_{ca}	[m]	50e-6
Electric conductivity, σ_{ca}	[Ω^{-1}m^{-1}]	8.4e4
Diffusion coefficient, $D_{eff,ca}$	[m^{2}s^{-1}]	1.37e-5
Exchange current density factor, $\hat{k}_{0,ca}$	[Ω^{-1}m^{-2}]	2.35e11
Activation energy, $E_{a,ca}$	[J mol^{-1}]	140e3
Electrolyte		
Thickness, τ_{el}	[m]	20e-6
Ionic conductivity, σ_{el}	[Ω^{-1}m^{-1}]	33.4e3 $exp(-10.3e3/T_{stack})$

3.4.3. SYSTEM ANALYSIS

ANODIC RECIRCULATION & CARBON DEPOSITING

Operating SOFCs on pure hydrocarbon fuels can compromise the electrochemical performance, induce high temperature gradients, and cause carbon deposits on the anode [37, 250, 251]. Solid carbon can be formed through the methane dissociation, Boudouard and reverse gas shift reactions

$$CH_4 \rightleftharpoons C(s) + 2H_2, \tag{3.25}$$

$$2CO \rightleftharpoons C(s) + CO_2, \tag{3.26}$$

$$CO + H_2 \rightleftharpoons C(s) + H_2O, \tag{3.27}$$

and can be supressed by sufficiently raising the oxygen partial pressure in the fuel inlet flow. Anodic recirculation is adopted in this study for this purpose, since it simplifies the system by omitting the use of water recovery and steam generation equipment. In addition, it might increase the overall fuel utilisation in the SOFC [252]. The amount of anodic recirculation, defined by the recirculation ratio

$$RR = \frac{\dot{n}_{recycle}}{\dot{n}_{an}^{out}}, \tag{3.28}$$

should be sufficient to ensure that carbon formation is not thermodynamically favourable, but not reduce the cell voltage too much due to excessive steam partial pressures [253].

Since it is expected that the amount of recirculation required can be reduced for higher fuel utilisations, as the amount of steam and carbon dioxide in the recirculated stream

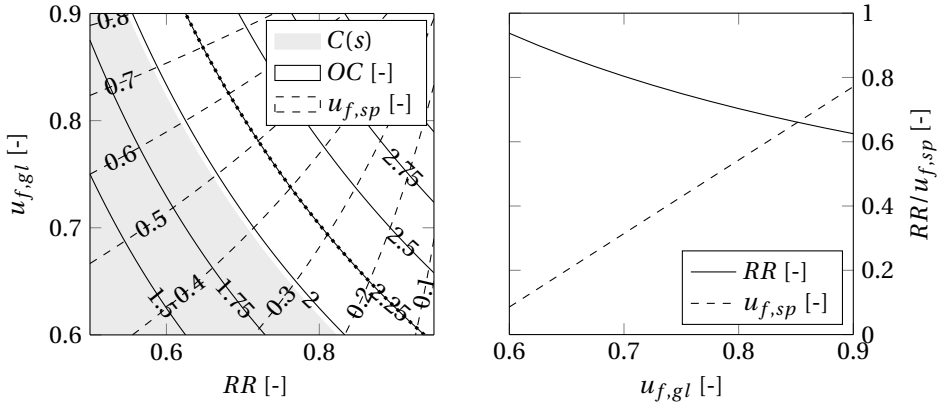

(a) Carbon deposition analysis.

(b) OC ratio = 2.25.

Figure 3.2: Carbon prone region for temperatures ≤575°C and contours of the OC and single pass fuel utilisation for various global fuel utilisations and anode off-gas recirculation ratios (Figure 5.3), and recirculation ratio and single pass fuel utilisation as a function of global fuel utilisation at OC ratio = 2.25 (Figure 3.2b)

increases, a parametric investigation is carried out in this study to determine an appropriate recirculation ratio for different fuel utilisation ratios. The fuel inlet composition is determined for the adiabatic pre-reformer for recirculation ratios from 0.5 to 0.95 and global fuel utilisations between 0.6 and 0.9. The thermodynamic limit of graphite formation is then calculated using Gibbs free energy minimisation, for ambient pressure and a temperature of 575°C. This limit is considered safe, since Halinen [254] reported no carbon depositing in a pre-reformer for temperatures below 600°C, contrary to predictions from thermodynamic equilibrium calculations. This indicates that carbon formation kinetics are sufficiently slow at these temperatures.

Combinations of the global fuel utilisation and recirculation ratio that are prone to graphite formation are indicated in Figure 5.3, together with contours of constant oxygen-to-carbon (OC) ratios and fuel utilisations for a single pass. The single pass fuel utilisation is calculated from the global fuel utilisation and the recirculation ratio according to [133]:

$$u_{f,sp} = \frac{u_{f,gl} \cdot (1 - RR)}{1 - RR \cdot u_{f,gl}} \tag{3.29}$$

The amount of anodic recirculation is often chosen to satisfy a specific design criterion, usually the steam-to-carbon ratio [44, 238]. However, Figure 5.3 shows that the OC is a more appropriate indicator for SOFCs using anodic recirculation, as the anode off-gas contains large amounts of carbon dioxide as well. It is decided to operate the system at an OC of 2.25, since no carbon depositing is expected for OC ≥2. The recirculation ratio and respective single pass fuel utilisation as a function of the global fuel utilisation are shown in Figure 3.2b.

Table 3.5: Overview of the investigated SOFC operating parameters in the combined cycle analysis.

Parameter	Nominal	Range	Interval	Remarks
$u_{f,gl}$ [-]	-	0.6-0.9	0.025	For all conditions
U_{cell} [V]	0.7	0.6-0.8	0.05	
T_{stack} [°C]	700	600-800	50	
Π_{comp} [-]	4	2-6	0.5	SOFC-GT combined cycles

PARAMETRIC ANALYSIS

Although complete system models are built in Cycle-Tempo, the procedure may be divided in two parts: the analysis of the SOFC and the combined cycle respectively. A flowchart of the SOFC analysis is visualised in Figure 3.3a. The partial pressures along the anode and cathode compartments for the reaction coordinate ϑ can be calculated from the isothermal stack temperature, isobaric stack pressure and global fuel utilisation by Gibbs free energy minimisation. The cathode outlet temperature is then calculated from the from the reforming, shift and electrochemical reaction rates, cell voltage and an estimate of the cathode oxygen utilisation. The oxygen utilisation is iterated until the desired cathode outlet temperature is reached, and the specific in- and outflows of the SOFC are obtained. Finally, the average power density in the stack is obtained using the procedure described in Section 3.4.2.

The results from the SOFC analysis can be directly used to study the combined cycle performance, for which a global scheme is presented in Figure 3.3b. The molar flows and stack temperature are used to calculate the combustor outlet temperature. Additional fuel or air is bypassed if the combustor outlet temperature is not sufficient for heat recuperation in the SOFC-gas turbine combined cycles, or exceeds the heat exchanger temperature limit for the SOFC-steam turbine combined cycle. Subsequently, the power generated by the combined cycle and consumed by auxiliaries is calculated from the parameters provided in Table 3.3. With all pressures, temperatures and flows in the system known, the overall electrical efficiency, generator power fraction and relative exergy losses are calculated.

All systems are subjected to a parametric analysis of SOFC operating variables. The fuel utilisation is varied between 0.65 and 0.9 by adjusting the ratio between current and fuel flow in Equation (3.4). Furthermore, the cell voltage is varied from 0.6 to 0.8V in Equation (3.15), and the average stack temperature between 600°C and 800°C. In addition, the sensitivity towards compression ratios from 2 to 6 is analysed for the gas turbine-combined cycles. The analysis is carried out with finite parameter intervals, and cubic spline interpolation is used to obtain continuous contours. An overview of the investigated parameter range is presented in Table 3.5.

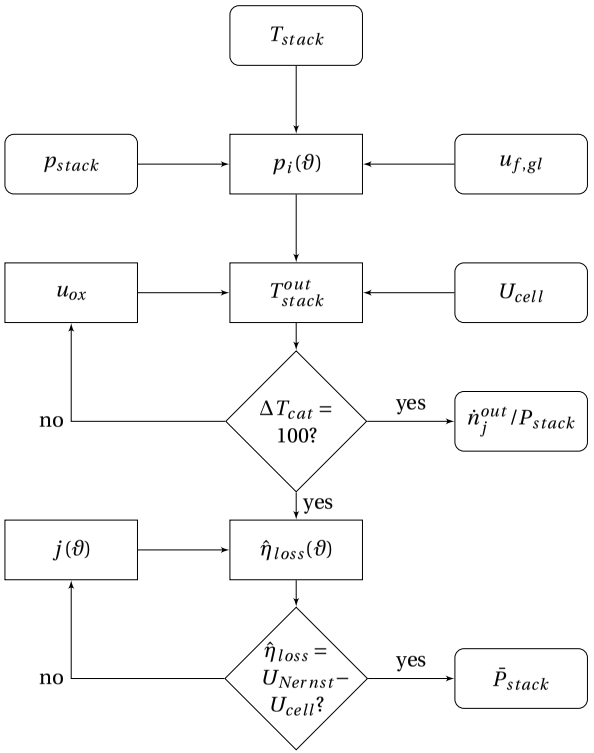

(a) Flowchart of the SOFC stack analysis.

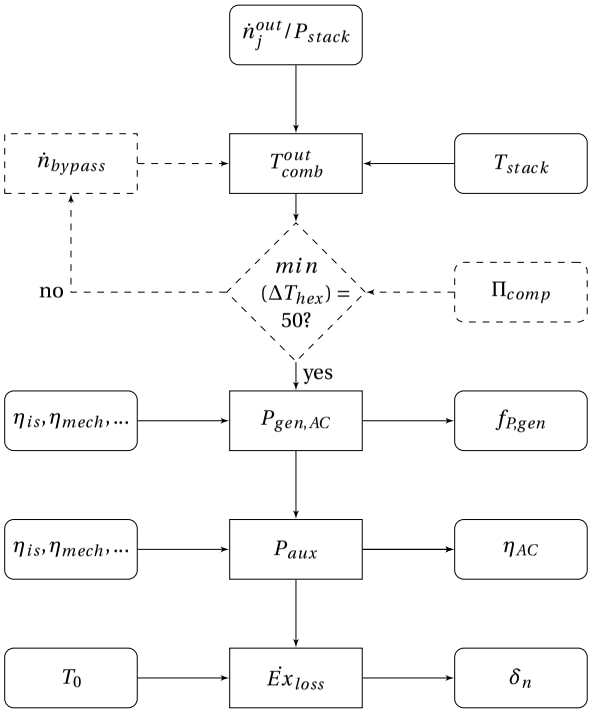

(b) Flowchart of the combined cycle analysis.

Figure 3.3: Overview of the procedures used to analyse the SOFC stack (Figure 3.3a) and combined cycle system (Figure 3.3b).

3.5. RESULTS

3.5.1. CELL VOLTAGE

Figure 3.4a shows contours of net electrical efficiency and average stack power density of the stand-alone reference SOFC system for various global fuel utilisations and cell voltages. Since less waste heat is produced at lower fuel utilisations and higher cell voltages, less cathode air is required to cool the stack and the oxygen utilisation increases. Oxygen utilisations ≤0.5 are considered unfeasible, as these result in high cathode concentration losses [252]. Therefore, these operating conditions are not considered.

The system efficiency increases for higher cell voltages and global fuel utilisations, since the electrochemical losses decrease and less fuel leaves the system unused. The stand-alone system has an electrical efficiency of 62.7% for a global fuel utilisation of 0.9 and a cell voltage of 0.8V. Although high fuel utilisations and cell voltages thus improve the system efficiency, both reduce the average stack power density. Decreasing the fuel utilisation from 0.9 to 0.65 improves the power density by 12.5%, and reducing the cell voltage from 0.8 to 0.6 with ~92%.

Figures 3.4b to 3.4e show contours of constant net electrical efficiency for the investigated SOFC-combined cycle systems. Contours of the fraction of total power produced by the thermal cycle electricity generator are plotted as well. While the response of the net electrical efficiency to an increase in cell voltage is similar to the stand-alone reference system, a more complex dependency on the global fuel utilisation is found.

The steam turbine combined cycle, shown in Figure 3.4b, improves the efficiency of the reference system from ~8% points at high cell voltages and fuel utilisations to more than 20% points for low cell voltages and fuel utilisations. The efficiency decreases faster close to the oxygen utilisation limit of 0.5, as air is bypassed to the combustor to limit the flue gas temperature to 1150°C. The fraction of power generated by the steam turbine decreases for higher fuel utilisation and cell voltage, from over 35% to less than 10%.

The characteristics of the reciprocating engine combined cycle are similar to the steam turbine combined cycle, as is shown in Figure 3.4c. The engine generator power fraction is in the same range, but the electrical efficiencies are ~2% points lower. The electrical efficiency is primarily affected by the cell voltage, and improves only slightly for higher fuel utilisations. The fraction of power generated by the reciprocating engine is almost inversely proportional to the global fuel utilisation and independent of the cell voltage. This illustrates that the reciprocating engine primarily uses the chemical energy left in the anode off-gas. In contrast to the steam turbine combined cycle, waste heat produced in the SOFC is removed in the condenser and not used to generate additional electricity.

Both gas turbine combined cycles, shown in Figures 3.4d and 3.4e, exhibit a high fuel utilisation dependency compared to the other combined cycles. While higher cell voltages always improve the electrical efficiency, an optimum fuel utilisation exists for gas turbine combined cycles. This optimum coincides with the operational point where no fuel or air is bypassed to the combustor and increases for higher cell voltages, since the adiabatic temperature in the combustor increases due to the reduced cathode air flow. The power fraction produced by the gas turbine generator shows a similar, but inversely proportional dependency. Thus, the generator power fraction increases for lower cell

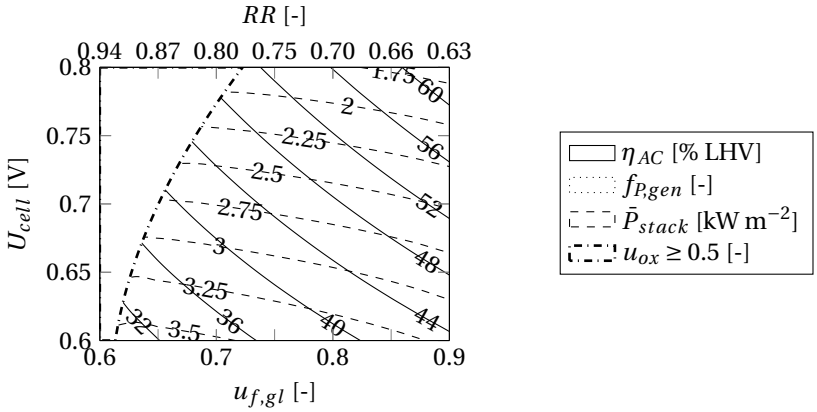

(a) Stand-alone reference SOFC system.

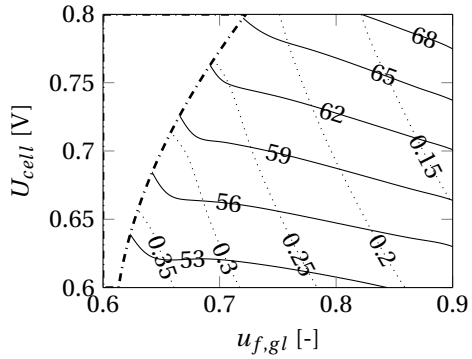

(b) SOFC-ST combined cycle.

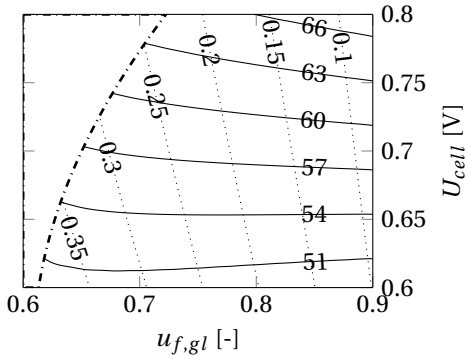

(c) SOFC-RE combined cycle.

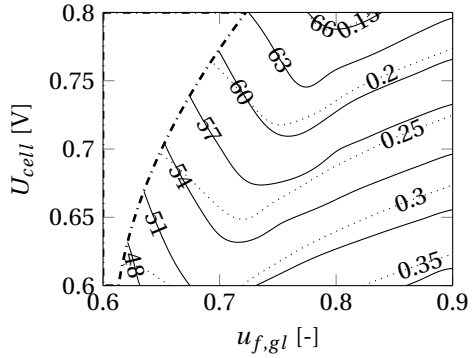

(d) Ambient SOFC-GT combined cycle.

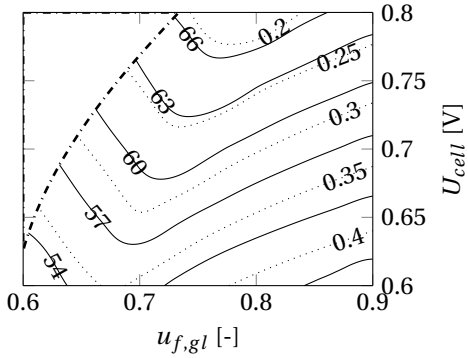

(e) Pressurised SOFC-GT combined cycle.

Figure 3.4: Contour plots of the net electric efficiency and stack power density for the stand-alone reference system (Figure 3.4a) or fraction of total power delivered by the auxiliary generator for the SOFC-combined cycle systems (Figures 3.4b to 3.4e), for various global fuel utilisations and cell voltages at an average stack temperature of 700°C.

voltages and an increased bypass of air or fuel to the combustor.

The pressurised SOFC-gas turbine combined cycle achieves higher electrical efficiencies than its ambient counterpart. The improvement is more pronounced at lower cell voltages, indicating that the pressurised system uses the exergy leaving the SOFC more effectively. This finding is in line with the higher gas turbine power fractions found for the pressurised SOFC-gas turbine combined system. The increased pressures affect the net heat production in the SOFC, through changes in the Nernst voltage and chemical equilibrium in the anode compartment. As a result, the cathode overstoichiometries and oxygen utilisations change, which is visible in the different 0.5 oxygen utilisation limit between Figures 3.4d and 3.4e.

3.5.2. STACK TEMPERATURE

A second series of contour plots is generated to quantify the influence of the stack temperature on the efficiency of the combined cycle, in which the stack temperature is varied between 600°C and 800°C at a constant cell voltage of 0.7V. Figure 3.5 shows the resulting contours of constant efficiency and fraction of electricity produced by the combined cycle electricity generator. Only fuel utilisations from 0.65 to 0.9 are considered, as the oxygen utilisation exceeds 0.5 for lower fuel utilisations at the specified cell voltage of 0.7V.

Figure 3.5a shows that the average stack temperature has almost no effect on the efficiency of the stand-alone reference SOFC system, since the cell voltage remains constant and waste heat recovery is not considered. Therefore, only the power consumption by the recirculation blower is affected by the temperature of the anode off-gas. The results confirm that the power density is substantially increased at higher stack temperatures, mainly due to exponential nature of the ohmic conductivity of the electrolyte. The power density improves with a factor of ~10 if the stack temperature is increased from 600°C to 800°C. However, the stack operating temperature and internal resistance are defined by material and design choices in practice.

The SOFC-steam turbine combined cycle efficiencies, shown Figure 3.5b, generally improve for higher average stack temperatures, since more exergy is available in the exhaust gases. However, the trend reverses for the higher stack temperatures and low fuel utilisations, since air is bypassed to the combustor to restrict its outlet temperature to 1150°C. The fraction of total power produced by the steam turbine is directly proportional to the waste heat available in the SOFC exhaust gases, and increases for lower global fuel utilisations and higher average stack temperatures.

Figure 3.5c shows a small increase in the efficiency of the reciprocating engine combined cycle for higher average stack temperatures. This is most likely a result of the increased chemical exergy of the anode off-gas, due to the shifting methane steam reforming equilibrium, since the increase in thermo-mechanical exergy is lost in the condenser where the gas is cooled to 50°C. This effect causes a small increase in the generator power fraction as well.

The efficiency improvements at higher average stack temperatures are most pronounced in the SOFC-gas turbine combined cycles, shown in Figures 3.5d and 3.5e. This is in line with the increasing theoretical gas turbine efficiencies for higher TITs. The efficiency and fraction of power generated by the gas turbine are higher for the pressurised

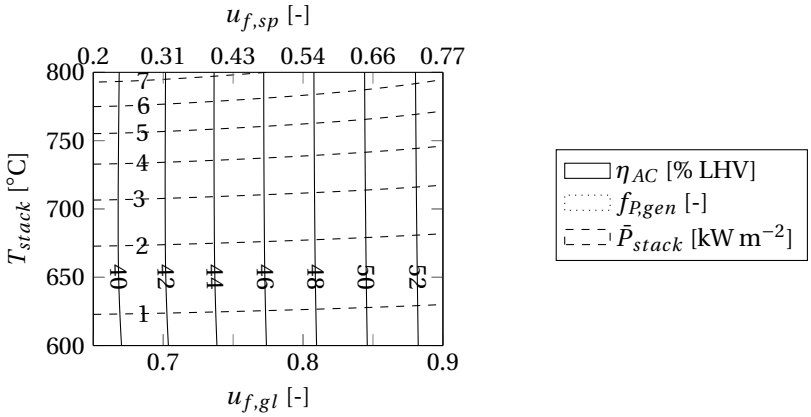

(a) Stand-alone reference SOFC system.

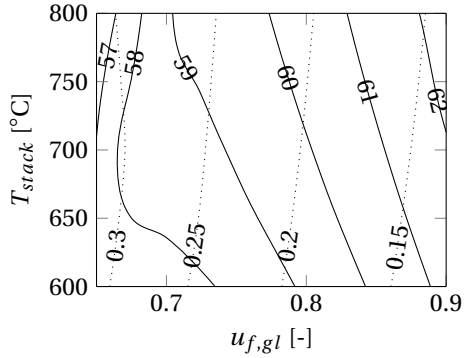

(b) SOFC-ST combined cycle.

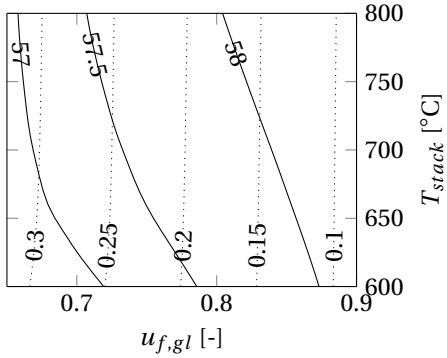

(c) SOFC-RE combined cycle.

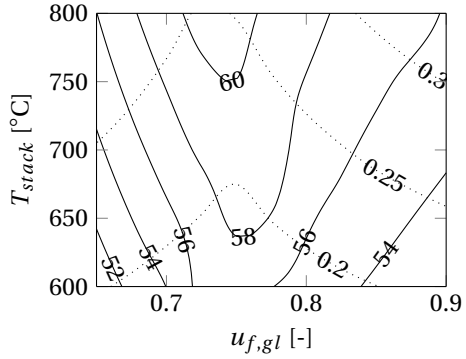

(d) Ambient SOFC-GT combined cycle.

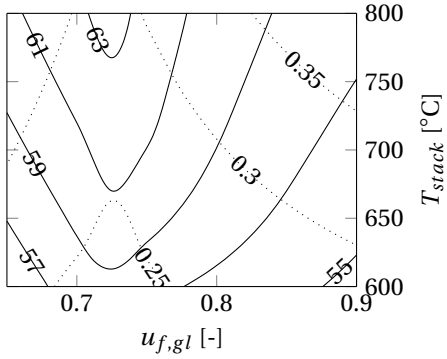

(e) Pressurised SOFC-GT combined cycle.

Figure 3.5: Contour plots of the net electric efficiency and stack power density for the stand-alone reference system (Figure 3.4a) or fraction of total power delivered by the auxiliary generator for the SOFC-combined cycle systems (Figures 3.4b to 3.4e), for various global fuel utilisations and average stack temperatures at a cell voltage of 0.7V.

system. The results confirm that highest electrical efficiencies are achieved for global fuel utilisation where no air or fuel is bypassed to the combustor, and the gas turbine power fraction reaches a minimum. This optimal fuel utilisation is virtually independent of the stack temperature, but slightly lower for the pressurised than for the ambient SOFC-gas turbine combined cycle.

3.5.3. GAS TURBINE PRESSURE RATIO

A compression ratio of 4 was assumed for the nominal operation point of both gas turbine combined cycles, which is a common value for the micro turbines often considered for this type of system [232]. However, the pressure ratio significantly affects the optimal design conditions and electrical efficiency of gas turbine combined cycles, since it determines the temperature changes due to adiabatic compression and expansion in the turbomachinery equipment. Therefore, pressure ratios between 2 and 6 are analysed for the gas turbine combined cycles, assuming an average stack temperature of 700°C and cell voltage of 0.7V.

Pressurised SOFC operation increases the average power density in the stack, due to the higher Nernst voltage and reduced polarisation losses [245]. Contours of the average pressurised stack power density for various compression ratios and global fuel utilisations are shown in Figure 3.6a. The increase in the average SOFC power density is more pronounced for low compression ratios and high fuel utilisations. The increment in power density varies from ~9.3% for $\Pi_{comp} = 2$ at the highest fuel utilisations to ~18.6% for $\Pi_{comp} = 6$, at minimal fuel utilisation.

Contours of net electrical efficiency and generator power fraction of the gas turbine combined cycles are shown in Figures 3.6b and 3.6c for various compressor pressure ratios and global fuel utilisations. The optimal fuel utilisation factor shifts to the left at higher compression ratios for both gas turbine combined cycles. Increasing expansion ratios in the turbine require higher TITs to maintain an outlet temperature suitable for recuperation, which requires a higher adiabatic temperature in the combustor and, consequently, adjustments to the air or fuel bypass.

The electrical efficiency of both gas turbine combined cycles is found to decrease for higher compression ratios. The ideal theoretical efficiency of a recuperated Brayton cycle follows from

$$\eta_{th} = 1 - \frac{T^{in}_{comp}}{T^{in}_{turb}} \cdot \left(\frac{p^{in}_{turb}}{p^{in}_{comp}} \right)^{\frac{\kappa-1}{\kappa}}, \tag{3.30}$$

where κ is the ratio of specific heats of the working fluid. If the expansion is assumed to be isentropic, Equation (3.30) is mathematically equivalent to

$$\eta_{th} = 1 - \frac{T^{in}_{comp}}{T^{out}_{turb}} \cdot \left(\frac{p^{out}_{turb}}{p^{in}_{comp}} \right)^{\frac{\kappa-1}{\kappa}} \tag{3.31}$$

The effect of the pressure ratio on the efficiency of the recuperated gas turbine should thus be limited, since both the temperature and pressure ratio in Equation (3.31) are assumed constant in this study and the isentropic efficiency is high. Therefore, the lower electrical efficiencies for higher pressure ratios are most likely a result of the reduced load share of the more efficient SOFC.

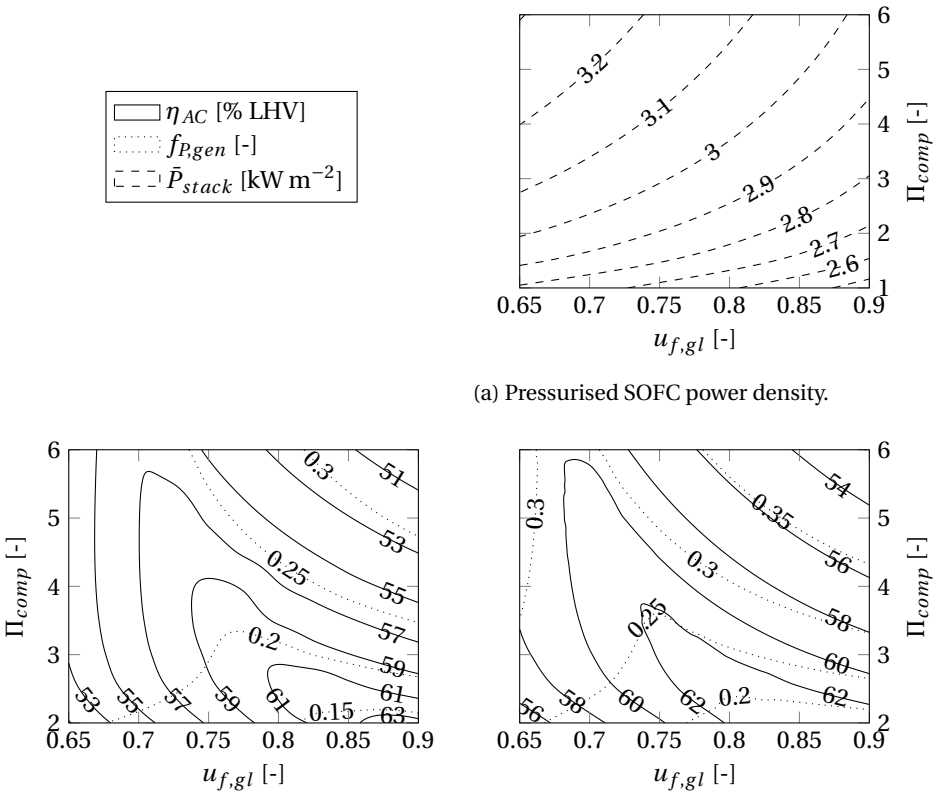

(a) Pressurised SOFC power density.

(b) Ambient SOFC-GT combined cycle.

(c) Pressurised SOFC-GT combined cycle.

Figure 3.6: Contours of the net electric efficiency and generator power fraction of the combined cycle systems for various global fuel utilisations and pressure ratios, at an average stack temperature of 700°C and cell voltage of 0.7V.

3.5.4. EXERGY LOSSES

The relative exergy losses are calculated for global fuel utilisations between 0.65 and 0.9 at an average stack temperature of 700°C and cell voltage of 0.7V. For clarity, only the most significant exergy losses are reported individually, while the remaining losses are added up and referred to as *other*. Figure 3.7a shows that the stand-alone reference system loses most of the exergy in the SOFC stack, air pre-heater, combustor and exhaust gases. The relative exergy losses are highest for lower fuel utilisations, since the exhaust gases still contain a lot of exergy. The air pre-heater destroys more exergy at high fuel utilisation, due to the relatively high cathode air overstoichiometry. The exergy losses in both the exhaust gas and air pre-heater can be reduced through combined cycle integration.

The relative exergy losses in both the SOFC stack and combustor of the steam turbine combined cycle are, indeed, equal to those of the stand-alone reference system, shown in Figure 3.7b, but the use of waste heat reduces the exergy losses in the air pre-heater and exhaust. The relative exergy losses increase for lower fuel utilisations, particularly in the steam cycle. This increase is due to the higher load share of the steam turbine and the rising temperature of the flue gas, which increases the exergy losses in the heat recovery steam generator. Losses in the steam generator may be reduced through optimisation of the steam pressure and steam superheat temperature [46].

Similar to the steam turbine combined cycle, the relative exergy losses in the SOFC stack in the reciprocating engine combined cycle equal those in the stand alone system. The sum of the exergy losses in the SOFC stack and the engine are almost constant with fuel utilisation. The losses in the combustor are low compared to other combined cycles, since the fuel is combusted at relatively high pressures and temperatures, and low air overstoichiometries. In addition, the exergy losses in the recuperator are relatively low, as the fresh air is pre-heated with exhaust air only. Since the exergy left in the exhaust gas is high compared to the steam turbine combined cycle, there is potential for improvement.

The exergy losses in the pressurised and ambient gas turbine combined cycles are shown in Figures 3.7d and 3.7e respectively. The exergy losses in the turbine are low compared to those in the steam cycle and reciprocating engine, although this is counteracted by the increased losses in the air compressor. The higher compressor outlet temperatures reduce the exergy losses in the recuperator. Overall, the sum of the exergy losses in the stack, turbine, compressor and recuperator are always below 20%. However, the exergy losses in the combustor and exhaust are relatively high, even at optimal fuel utilisations. This indicates that further improvements can be made to reduce these losses, for example by inclusion of an organic Rankine bottoming cycle.

3.5.5. COMBINED CYCLE COMPARISON

The contour plots presented in the previous sections reveal detailed dependencies of combined cycle efficiencies, generator power fraction and stack power density on fuel utilisation, cell voltage, stack temperature and gas turbine compression ratio. Figure 3.8 presents a direct comparison of the investigated combined cycles based on the results of the individual cycles.

Figure 3.8a shows the net electrical efficiencies and combined cycle generator power fractions for global fuel utilisations from 0.65 to 0.9 at nominal conditions. The efficiency

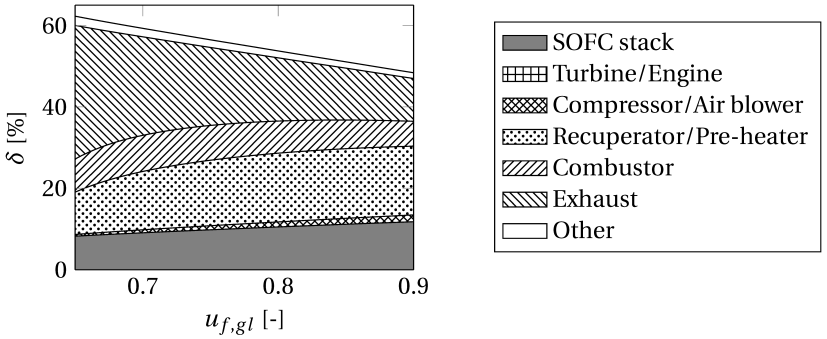

(a) Stand-alone reference SOFC system.

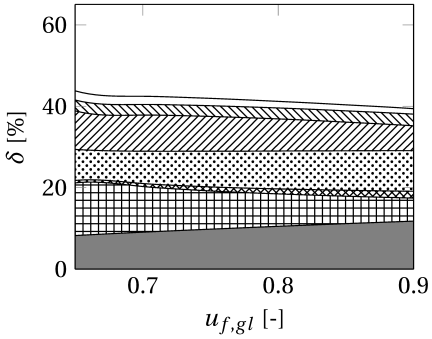

(b) SOFC-ST combined cycle.

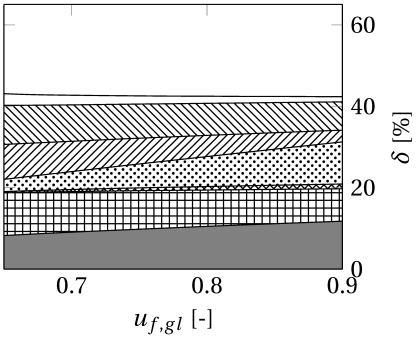

(c) SOFC-RE combined cycle.

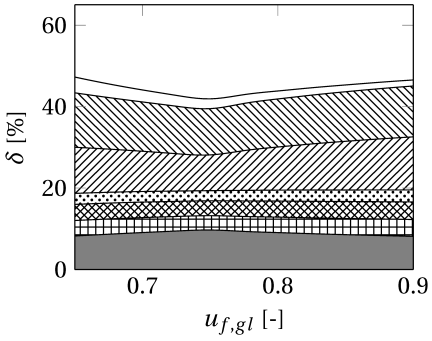

(d) Ambient SOFC-GT combined cycle.

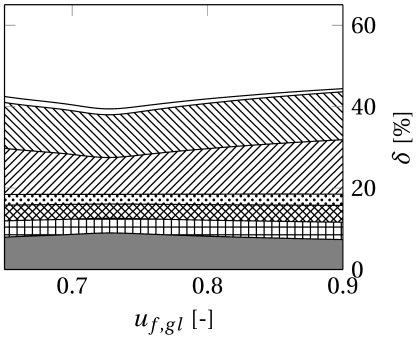

(e) Pressurised SOFC-GT combined cycle.

Figure 3.7: Relative exergy losses in the main components of the studied systems as a function of global fuel utilisation for a stack temperature of 700°C and cell voltage of 0.7V.

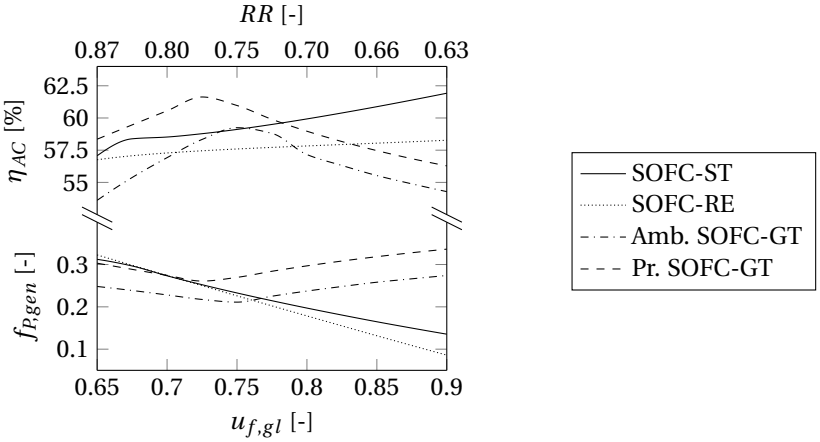

(a) U_{cell} =0.7V, T_{stack} = 700°C and Π_{comp} = 4.

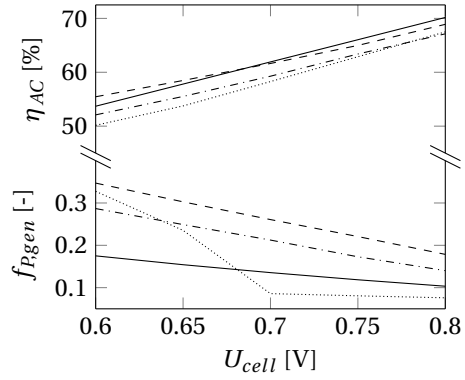

(b) $max(\eta_{AC})$, T_{stack} = 700°C and Π_{comp} = 4.

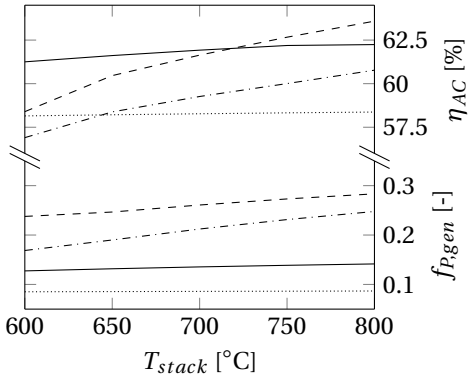

(c) $max(\eta_{AC})$, U_{cell} = 0.7V and Π_{comp} = 4.

Figure 3.8: Net electric efficiency and generator power fraction as a function of global fuel utilisation for the investigated combined cycles at nominal operating conditions (Figure 3.8a), and as a function of cell voltage (Figure 3.8b) or average stack temperature (Figure 3.8c) at the global fuel utilisation where the highest electrical efficiency is obtained.

of the steam turbine and reciprocating engine combined cycle increase monotonically with the fuel utilisation, while optimal fuel utilisations are identified for the SOFC-gas turbine combined cycles. The SOFC and gas turbine are well matched in this optimum, since no additional fuel or air needs to be bypassed to the combustor to maintain the required turbine inlet temperature. The steam turbine combined cycle attains the highest electrical efficiency at nominal conditions, at a fuel utilisation of 0.9. However, only 13.5% of the total system power is produced by the steam turbine at these conditions, while the pressurised SOFC-gas turbine combined cycle achieves similar efficiencies at a fuel utilisation of 0.72, producing 26% of the total electric power.

Figure 3.8b shows the maximum electrical efficiency obtained by the SOFC-combined cycles for different cell voltages at an average stack temperature of 700°C and gas turbine compression ratio of 4, as well as the generator power fraction at those conditions. The efficiency increases and the generator power fraction decreases for higher cell voltages for all combined cycles. The steam turbine and reciprocating engine combined cycle are more sensitive towards the cell voltage, because the load share of the SOFC is higher in these systems. An optimum fuel utilisations is found for the reciprocating engine combined cycle at low cell voltages, due to the increasing balance of plant losses at higher fuel utilisations.

A comparison of the combined cycle sensitivity towards the average stack temperature is shown in Figure 3.8c. Gas turbine integrated schemes clearly benefit from a higher stack temperature, while the steam turbine combined cycle efficiency increases only slightly due to the limited steam superheat temperature. The reciprocating engine combined cycle efficiency is virtually independent of the stack temperature, and could thus be an interesting option for low temperature SOFC products. Given low thermal mass and limited coupling between SOFC and reciprocating engine of such a system, it is anticipated that it is interesting for applications with highly fluctuating load factors.

3.6. DISCUSSION

The presented comparison shows how the ability to use the exergy in the outlet flows of the SOFC differs among combined cycles, and that differences in SOFC stack operation should be considered when comparing different system integration options. The fuel utilisation is shown to be particularly important for SOFC-gas turbine combined cycles, since it determines the adiabatic combustion temperature. The steam turbine and reciprocating engine combined cycles are shown te be interesting for SOFC products operating at low stack temperatures and high cell voltages, while especially the pressurised SOFC-gas turbine combined cycle achieves high efficiencies at higher stack temperatures and lower cell voltages.

The reported efficiencies of SOFC-gas turbine combined cycles vary widely in literature. This is illustrated by two recent publications on pressurised gas turbine cycles, reporting entirely different net electrical efficiencies of 52.9 and 78.7% [44, 238]. An overall fuel utilisation factor of 0.85 and stack temperature of ~750°C is assumed in both studies. However, a cell voltage of 0.7V is assumed for the less efficient system, while the high efficiency combined cycle operates at a cell voltage of 0.86V and incorporates an intercooled gas turbine, high temperature air pre-heater, as well as more efficient turbomachinery.

An efficiency of 58.1% is found in our analysis for the pressurised SOFC-gas turbine combined cycle at a fuel utilisation of 0.85, cell voltage of 0.7V and average stack temperature of 750°C. The difference with the efficiency reported by Whiston et al [238] is attributed to the different fuel pre-heating configuration in our configuration, which enables a reduced turbine outlet temperature. Moreover, our analysis shows that the efficiency can be improved to 62.7% if the fuel utilisation is lowered to 0.725, thus clearly demonstrating the limitations of treating the fuel utilisation as a pre-defined operating metric. Extrapolation of our results suggests that operation of the SOFC at 0.86V can increase the net electrical efficiency to ~75.5%, which is in line with the finding of Campanari et al [44].

Park et al. [234] compare ambient and pressurised SOFC-gas turbine combined cycle designs. The current density is constant in their study, which results in a strong dependency of the cell voltage and efficiency on the stack temperature and pressure. The authors conclude that lower Nernst voltages and TITs encountered in the ambient design yield significantly lower efficiencies. The constant voltage analysis presented in our study provides a more direct comparison of the different gas turbine integration schemes. Efficiencies of 59.2% and 61.6% are found for the ambient and pressurised SOFC-gas turbine combined cycle respectively at a stack temperature of 700°C and cell voltage of 0.7V, a difference of only 2.4% point. However, the ambient system is operated at a higher fuel utilisation, and the gas turbine power fraction and the stack power density are lower than for the pressurised design.

A comprehensive study of an SOFC-steam turbine combined system is reported by Rokni [46]. The author shows how the live steam pressure can be optimized for the heat recovery steam generator gas side inlet temperature, which has not been considered in our study. In addition, the efficiency decreases for higher fuel utilisations in contrast to our findings. However, this is most likely a result of the constant SOFC area and fuel flow assumed by Rokni [46], causing the cell voltage to decrease for higher fuel utilisations. Nonetheless, the maximum reported efficiency of 68% is in good agreement with our findings.

A stand-alone SOFC system is compared to an ambient gas turbine and reciprocating engine combined cycle by Park et al. [47], reporting efficiencies of 51.7%, 58.6% and 59.5% for the stand-alone, reciprocating engine and gas turbine combined cycles respectively, for a stack temperature of 850°C, a cell voltage of 0.79V and fuel utilisation factor of 0.75. The corresponding efficiencies of 52.0%, 64.0% and 64.5% in our analysis for a cell voltage of 0.79V confirm that the reciprocating engine combined cycle is most efficient at these conditions. However, its electrical efficiency is ~5% point higher in our analysis, which is attributed to assumptions on the combined cycle operation, since the efficiency of the stand-alone system is only 0.3% point higher.

The objective of this work is to determine the thermodynamic potential of coupling SOFCs with different thermal cycles. However, market uptake may ultimately be determined by other factors like the reliability, flexibility, emission regulations and levelised cost of electricity. Although high efficiencies reduce cost by lowering the fuel consumption, the livelized cost of electricity is affected by the capital cost of the system, maintenance costs, fuel price, carbon tax and life time as well. Nowadays, SOFCs are confronted by relatively high capital cost and hardly available on power scale of conventional technology.

However, competitive price levels are projected for large scale SOFC production [219].

The results of the power density study can be used in future cost optimisation studies, since an increase in power density implies that the number of stacks and consequently the capital cost is reduced. The isothermal SOFC model shows that increasing the average stack temperature from 600°C to 800°C results in a 10 fold higher power density. Reducing the fuel utilisation or increasing the compression ratio improves the stack power density with 10-20%, and it almost doubles when the cell voltage is changed from 0.8V to 0.6V. Although the stack operating temperature and internal resistance are determined by material and design choices in practice, this demonstrates that operating at low fuel utilisations, low cell voltages and high stack temperatures is favourable from a power density perspective.

The stand-alone system attains a net electrical efficiency of ~61.5% when operating at an average stack temperature of 700°C, cell voltage 0.79V and a fuel utilisation of 0.9, while the steam turbine and pressurised gas turbine combined cycle operating at the same temperature attain similar efficiencies for a cell voltage of 0.7V and fuel utilisations of 0.9 and 0.725 respectively, resulting in stack power density improvements of ~25% and ~75%. Therefore, combining SOFCs with thermal cycles may be help to reduce the number of stacks required, and thus reduce the capital cost without compromising the electric efficiency.

3.7. CONCLUSIONS

A thermodynamic analysis of different SOFC-combined cycles, including a novel reciprocating engine integrated scheme, was presented. Since the fuel utilisation, cell voltage, stack temperature and gas turbine compression ratio affect the exergy in the outlet flows of the SOFC, while the ability to use this exergy differs among in the investigated cycles, these parameters were varied in the analysis. The results were mapped in contour plots of constant efficiency, stack power density and fraction of total power delivered by the combined cycles to study differences between the combined cycles within the SOFC operating envelope.

It was found that the efficiencies of the stand-alone SOFC system as well as the steam turbine and reciprocating engine combined cycles increase for higher fuel utilisations, while an optimum exists for gas turbine combined cycles. This optimum is virtually independent of the stack temperature, but increases for higher cell voltages and lower compression ratios. In addition, an optimum levelised cost of electricity may exist for all combined cycles, since the electrical efficiency and the thermal cycle power fraction were mostly inversely correlated.

The exergy analysis revealed that exergy losses in the steam turbine combined cycle can be further reduced if the live steam pressure is adjusted according to the combustor outlet temperature. The reciprocating engine combined cycle system destroys a substantial part of the exergy in the moisture separator and exhaust, which may be improved using waste heat recovery systems. The exergy losses in the combustor and exhaust are most pronounced in both gas turbine combined cycles, but may be reduced by adjustment of the compression ratio and optimisation of the fuel utilisation.

A direct comparison suggested that gas turbine integration is most attractive if the

SOFC is operated at relatively low fuel utilisations, moderate cell voltages and high stack temperatures, while integration with steam turbine bottoming cycles may be more beneficial for low temperature SOFC stacks operated at high voltage. Notably, the average stack power density in the pressurised SOFC-gas turbine and steam turbine combined cycle are respectively ~75% and ~25% higher than for a stand-alone system with a similar electrical efficiency. Reciprocating engine integration seems to yield lower efficiencies than the steam turbine combined cycle, but may offer operational advantages, such as operational flexibility, improved load response and reduced capital cost.

The presented analysis illustrates the importance of comparing combined cycles within the operating envelope of the SOFC, because the stack is ideally operated differently from stand-alone systems. However, the off-design performance of SOFC stacks should be studied in more detail, especially for high degrees of internal reforming. Therefore, a detailed 1D dynamic DIR SOFC stack model is developed in the next chapter.

4

DYNAMIC MODELLING OF DIRECT INTERNAL REFORMING SOFCS

This chapter has been published in Applied Energy **250**, (2019) [255].

4.1. INTRODUCTION

The extent in which the electrical efficiency of internal reforming SOFC systems can be increased by integration with different thermal cycles was analysed in the previous chapter. The results showed that the optimal SOFC operating conditions differ among the investigated combined cycles. Therefore, it is important to analyse the off-design performance of internal reforming SOFC stacks. The isothermal plug flow reactor SOFC model used in the previous chapter gives an indication of the effects of varying operating conditions on the electrochemistry in the stack, but does not capture the effects of off-design operating conditions and DIR on the temperature profiles in the stack. Therefore, a more detailed model of a DIR SOFC is required to evaluate the effects of different operating conditions on the stack.

This chapter discusses the development and validation of a 1D dynamic modelling platform for both single SOFCs and stacks. DIR reforming kinetics from single cell experiments can be validated with the single cell model, and subsequently applied in stack models. This methodology is further explained in Section 4.2. The equations, implementation, geometry and boundary conditions of the models are given in Section 4.3. Validation and simulation results are presented in Section 4.4 and discussed in Section 4.5, after which conclusions are drawn in Section 4.6.

4.2. MODELLING METHODOLOGY

DIR SOFCs have been modelled in a number of studies, usually to evaluate their electrochemical performance or develop appropriate control strategies. The MSR reaction is most commonly assumed to be in chemical equilibrium, and thus considered to proceed infinitely fast. Alternatively, authors have implemented kinetics which assume a first order dependency on the methane partial pressure only [48, 256, 257]. The multi-step reaction mechanism derived by Hecht et al. [258] for Ni-YSZ cermet anodes has been implemented in more comprehensive computational fluid dynamics (CFD) models [38, 259].

Te level of detail is typically limited In control-oriented dynamic SOFC models to reduce the computational demand. Multi-step reaction mechanisms are, therefore, less suitable for such models, while simple first order kinetics may yield inaccurate results [260]. Alternatively, Langmuir-Hinshelwood (LH), Hougen-Watson (HW) or Eley-Rideal (ER) kinetics can be used if the reaction can be described by a single rate determining step on the catalyst surface. Power law (PL) kinetics may allow the inclusion of the effects of other reactants and products on the reaction rate without knowledge on the reaction mechanism [135, 261, 262]. However, it is unknown if any of those kinetic mechanisms can be used to accurately predict the spatial distribution of the reforming reaction within the stack.

Acknowledging the need for reforming kinetics derived at conditions relevant for stack operation, MSR experiments were carried out on a functional single cells with a Ni-GDC cermet anode in a previous study [263]. The data was then used in a follow-up study to derive PL and HW kinetics [264]. In addition, a CFD model of the test setup was developed and both kinetic models where implemented. Although both models accurately predicted the overall methane conversion, different spatial distributions of the MSR rates were

obtained. Whether this is also the case for stack operation, where the conditions differ substantially from the controlled environment in single cell experiments, is not clear.

Since the DIR experiments were carried out on the same commercially available single cells applied in stacks, direct transfer of the kinetics to stack models is in principle possible. Two 1D dynamic SOFC models are developed in this study, one for the single cell test station and the other representing a commercial stack using the same type of cells. The structure and equations are the same for the two models, but the boundary conditions are adjusted to account for the physical differences between single cell setup and ISM operation.

The stack model developed in this study not only includes the active area of the stack, but accounts for heat transfer in the inactive in- and outflow sections and heat losses to the surrounding as well. In this way, a commercially available integrated stack module (ISM) is modelled, which contains two 30 cell stack towers connected in series with internal fuel manifolding, placed in a thermally insulated box and external air manifolding [265]. The ISM is equipped with connections for the fuel and air in- and outlets, electric power cables and temperature monitoring [266]. However, the ISM does not include balance of plant components such as a (pre-)reformer, afterburner and heat exchanger, as is the case in other ISMs [267, 268].

The ISM model is validated with operating parameter and power curves published by the manufacturer for hydrogen-nitrogen, CPOX and SR fuels. The single cell model is validated using experimental data and the CFD model developed in previous work [263, 264]. Finally, the two DIR models obtained in the single cell experiments are implemented in the stack model to compare the predicted spatial distributions of species concentrations, temperatures and reaction rates. A schematic overview of this approach is shown in Figure 5.5.

4.3. MODEL DESCRIPTION

This section describes the 1D modelling framework developed to simulate single cells, stacks and integrated stack modules based on a single set of equations. Separate control volumes are defined for air, fuel, interconnect and the positive electrode-electrolyte-negative electrode (PEN) assembly, which are then discretised in the flow direction. The model formulation is dynamic to enable application in future transient simulation and development of control strategies.

It is commonly assumed that the solid temperatures dominate the transient behaviour of SOFCs and should thus be solved dynamically, while the remaining equations are can be formulated quasi-static [256, 257]. In that case, however, the accuracy of the time dependent solid temperature depends on the time interval at which the quasi-static properties are updated. Moreover, quasi-static mass balances require iterative solving, while stiff solvers can deal with the different time scales encountered, yielding acceptable runtimes. Therefore, all mass and energy balances are formulated dynamically in the model.

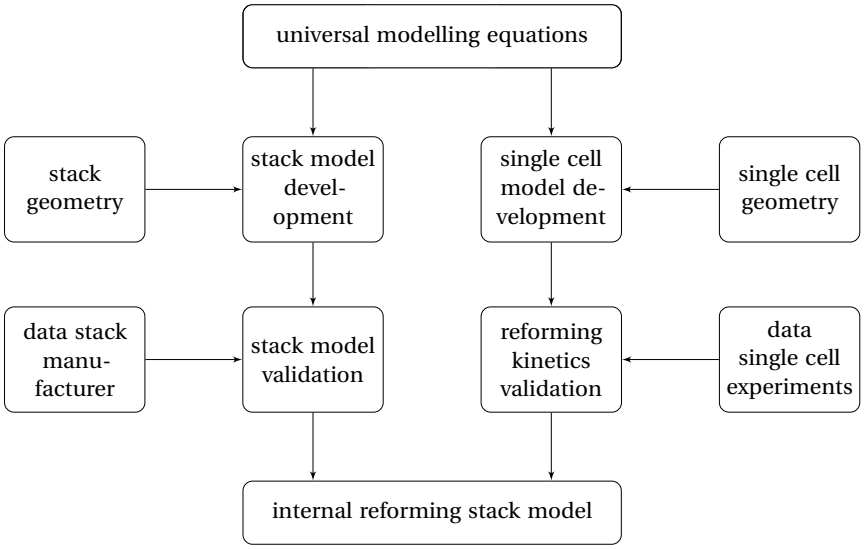

Figure 4.1: Flowchart of the dynamic DIR stack model development using manufacturer data and single cell reforming experiments.

4.3.1. MASS AND ENERGY BALANCES

Dynamic mass and energy balances are implemented in the model. The gas channels of the SOFC are modelled as a series of continuously stirred-tank reactor control volumes, in analogy to Hosseini et al. [269]. The local time derivative of the molar concentration a species follows from a molar balance, divided by molar capacity of the control volume, determined by its size and ideal gas law:

$$\frac{\partial y_i}{\partial t} = \frac{\bar{R}T}{pV_{cv}}\left\{\dot{n}_i^{in} - \dot{n}_i^{out} + \sum_m \nu_{i,m} r_m A_{cv}\right\} \tag{4.1}$$

The outlet flow of species i is calculated from its concentration multiplied by the total molar outflow, which follows from the total molar inflow and the sum of moles produced and consumed by reactions. It is assumed that the changes in the total molar flow settle infinitely fast and can thus be assumed quasi-static.

It is assumed that all chemical reactions take place on the solid anode and cathode catalyst interface of the SOFC, and the heat from chemical reactions is, therefore, assigned to the PEN control volume and not to the gases. The dynamic energy balance of a gaseous control volume thus only depends on the change in enthalpy of the inlet gas flow due to the temperature difference with the previous control volume and the convective heat transfer to or from the solid parts, divided by the heat capacity of the control volume

$$\frac{\partial T_g}{\partial t} = \frac{\bar{R}T}{pV_{cv}\sum_i y_i c_{p,i}}\left\{\sum_i \dot{n}_i^{in}(h_i^{in} - h_i^{out}) + \sum \bar{h} A_{cv}(T_s - T_g)\right\}, \tag{4.2}$$

while the enthalpy change from inlet to outlet due to chemical reactions is thus accounted

for in the energy balance of the PEN. The thermodynamic properties of the gases, such as heat capacities, enthalpies and entropies are calculated using the Shomate equation with coefficients provided by the National Institute of Standards and Technology Chemistry WebBook [270, 271]. The dynamic energy balance of the solid control volumes has the following form:

$$\frac{\partial T_s}{\partial t} = \frac{1}{\rho_s c_{p,s} \tau_s} \left\{ \sum \bar{h}(T_g - T_s) + \lambda_s \tau_s \frac{\partial^2 T_s}{\partial x^2} + \sum_m \Delta H_m r_m - j U_{cell} - \dot{Q}_{loss} \right\} \tag{4.3}$$

Here, the first two terms on the right hand side represent the convective heat transfer to or from the gases and heat conduction, and apply to both the interconnect and PEN, including its inactive area. The sum of the heat of reactions and electric power drawn from a control volume only apply to the active parts of the PEN. The heat loss to the surroundings $\dot{Q}_{loss}$ is applied to the boundaries and is zero everywhere else, as is discussed in Section 4.3.6.

4.3.2. CHEMICAL REACTIONS

The chemical reactions considered to take place on the anode of the SOFC are the WGS and MSR reaction. Since the WGS is assumed to proceed infinitely fast, its reaction quotient Q_{WGS} is assumed to be equal to the chemical equilibrium constant K_{WGS} along the active area of the SOFC

$$Q_{WGS} \equiv \frac{a_{H_2}\, a_{CO_2}}{a_{H_2O}\, a_{CO}} = K_{WGS}, \tag{4.4}$$

which is achieved by selecting an arbitrary high value for the frequency factor of the WGS reaction. Assuming ideal gas behaviour for the reactants and products, the fugacity constant $\phi \approx 1$ and the activities are calculated from:

$$a_i = \phi_i\, y_i \frac{p}{p_0} \approx y_i \frac{p}{p_0}, \tag{4.5}$$

where p_0 is the standard pressure. A similar approximation may be used for the MSR reaction if the kinetics are not known, yielding:

$$Q_{MSR} \equiv \frac{a_{CO}\, a_{H_2}^3}{a_{CH_4}\, a_{H_2O}} = K_{MSR} \tag{4.6}$$

The equilibrium constants in Equations (4.4) and (4.6) are obtained from the Gibbs free energy change of the reaction at standard state:

$$K_m = exp\Big(- \frac{\Delta G_m^0}{\bar{R} T} \Big) \tag{4.7}$$

However, a kinetic model is required if the reaction does not proceed infinitely fast, which is commonly reported to be the case for methane. Therefore, two kinetic MSR models were derived in a previous study using data obtained from experiments on an

electrolyte supported cell with a Ni-GDC anode [263, 264]. One is a global kinetic model of the PL type and depends on reaction orders α and β for the reactants methane and steam respectively and the activation energy E_a:

$$r_{MSR} = k_0\, p_{CH_4}^{\alpha}\, p_{H_2O}^{\beta}\, exp\Big(-\frac{E_a}{\bar{R}T}\Big)\Big(1-\frac{Q_{MSR}}{K_{MSR}}\Big), \tag{4.8}$$

The second kinetic model is of the HW type, assuming that the dehydrogenation of the CHO radical on the catalyst surface is rate determining. This mechanism was proposed by Xu et al. [129] for steam reforming reactors with nickel catalysts, and yields the following expression for the MSR rate:

$$r_{MSR} = k_0\, \frac{p_{CH_4}\, p_{H_2O}}{p_{H_2}^{2.5}\,(den)^2}\, exp\Big(-\frac{E_a}{\bar{R}T}\Big)\Big(1-\frac{Q_{MSR}}{K_{MSR}}\Big) \tag{4.9}$$

where the denominator is a Langmuir adsorption isotherm accounting for the surface coverage by adsorbed oxygen from a steady state of steam adsorption and hydrogen desorption, leading to:

$$den = 1 + \bar{A}_O\, exp\Big(-\frac{\Delta\bar{H}_O}{\bar{R}T}\Big)\frac{p_{H_2O}}{p_{H_2}} \tag{4.10}$$

In this isotherm, $\bar{A}_0$ is pre-exponential factor of the temperature dependent adsorption equilibrium constant with associated enthalpy $\Delta\bar{H}_O$. Four parameters should be obtained from experimental data in both kinetic models. While these are fully independent in the PL expression, two temperature dependent constants are required for the HW kinetics, as the dependence on the reactant and product partial pressures is determined by the rate limiting reaction step.

4.3.3. ELECTROCHEMICAL REACTIONS

The electrochemical model is similar to the one described in Section 3.4.2. The spatial distribution of the electrochemical reaction rate, more commonly referred to as the current density, is calculated using the equipotential assumption, i.e. the voltage is uniform on the cell plane. The bisection algorithm is used to determine the resulting cell voltage for the total current drawn. This means that the current density distribution is calculated for which the sum of the overpotentials equals the difference between cell voltage and the Nernst voltage through Equations (3.15) and (3.16).

The ohmic resistance in Equation (3.15) of the PEN structure depends on the individual resistances of the anode, cathode and electrolyte, and is proportional to their thickness and disproportional to their electronic or ionic conductivity, described by Equation (3.17). However, a contact resistance $R_{contact}$ is now included to account for non-ideal electrical contacts in the single cell test station and stack assembly:

$$\hat{\eta}_{ohm} = j\left(\frac{\tau_{an}}{\sigma_{an}} + \frac{\tau_{el}}{\sigma_{el}} + \frac{\tau_{ca}}{\sigma_{ca}} + R_{contact}\right) \tag{4.11}$$

It is assumed that the electrical conductivities of the anode and cathode can be estimated with constant values for the operating condition of the stack, since their temperature dependence is limited and their conductivity is high for SOFC operating temperatures.

The ionic conductivity of the electrolyte, on the other hand, has a strong temperature dependency and is thus calculated for the local PEN temperature. A reasonable value for the contact resistance of a well-designed stack is obtained from Liu et al. [272], while the contact resistance for the single cell test setup was estimated based on an experimental IV-curve.

Concentration losses typically start to dominate the electrochemical losses only for higher current densities. The local current density can be high even if the overall current density is limited, especially toward the outlet of a stack, where the temperature is usually highest. The departure of the cell voltage from Nernst as a result of the concentration gradient in the electrode is calculated through Equations (3.18) to (3.21).

In the previous chapter, the activation losses were calculated with the asymmetric Butler-Volmer equation (Equations (3.22) and (3.23)). However, Noren et al. [273] showed that assuming symmetry between the anodic and cathodic reaction is sufficient in mosts cases:

$$\hat{\eta}_{act} = \frac{\bar{R}T}{F} sinh^{-1}\Big(\frac{j}{2j_0}\Big), \tag{4.12}$$

Although mathematically convenient, it should be noted that the anode exchange current density j_0 in the Butler-Volmer equation depends on the concentrations of the reactants and products of the electrochemical reaction. This is partly due to the *equilibrium potential effect* discussed by Bessler et al. [274], since the forward and backward reactions on the electrodes are affected by the electrical potential difference, which depends on the reactant and product concentrations. The global influence of the reactants and products concentrations on j_0 can be shown to depend on these concentrations themselves and the rate limiting charge transfer mechanism [274].

It should be noted that Equation (4.12) is only valid if a single charge transfer reaction is rate limiting and the reactant and product concentrations are constant, which is generally not the case for cermet electrodes. In order to deal with the limited understanding of the fundamental electrochemical oxidation kinetics, it has become customary to introduce global reaction orders for the reactant and product activities in the exchange current densities [248]:

$$j_{0,ca} = \hat{k}_{0,ca}\, a_{O_2}^{\hat{\epsilon}} exp\Big(-\frac{E_{a,ca}}{\bar{R}T}\Big) \tag{4.13}$$

$$j_{0,an} = \hat{k}_{0,an}\, a_{H_2}^{\hat{\gamma}}\, a_{H_2O}^{\hat{\beta}} exp\Big(-\frac{E_{a,an}}{\bar{R}T}\Big) \tag{4.14}$$

The values of the reaction orders $\hat{\epsilon}$, $\hat{\gamma}$ and $\hat{\beta}$ depend on the rate limiting kinetics of the electrochemical reactions, temperature, reactant and product concentrations and absolute electric potential difference. A value of 1/4 is often used for $\hat{\epsilon}$, but for $\hat{\gamma}$ and $\hat{\beta}$ values from 0 to 1 and -1/2 to 1 respectively can be found in literature [274, 275]. Since the partial pressures of hydrogen and steam vary substantially along the anode, especially under internal reforming conditions, the values of $\hat{\gamma}$ and $\hat{\beta}$ are determined with power curves provided by the manufacturer.

4.3.4. EFFECTIVE DIFFUSION COEFFICIENTS

Effective diffusion coefficients are required to calculate the mass transfer losses in the anode and cathode. Diffusion in the porous SOFC electrodes has been extensively studied and various models have been presented, usually accounting for multicomponent diffusion and wall-surface interaction in the channels of the electrode material. In this model, effective diffusion coefficients for hydrogen and steam in a multicomponent gas mixture and oxygen in air are calculated within the porous electrodes, since they are only used to calculate concentration overpotentials for limiting current densities.

The approach in this study is similar to the one proposed by Chan et al.[276]. Effective diffusion coefficients for hydrogen and steam in a mixture are calculated from:

$$D_{eff} = \sum_i y_i D_{eff,i} \tag{4.15}$$

Since the pore diameters in the porous electrodes of SOFCs are typically comparable to the mean free path of the gas molecules, Kundsen diffusion should be accounted for. The Bosanquet formula is used to calculate an effective diffusion coefficient for species i, which is then corrected for the tortuous path of the molecule and the porosity of the electrode:

$$D_{eff,i} = \frac{\varepsilon}{\iota}\left(\frac{1}{D_{g,i}} + \frac{1}{D_{k,i}}\right), \tag{4.16}$$

The Knudsen diffusion coefficient for species i is calculated from kinetic theory, in analogy with Yakabet et al. [277]

$$D_{k,i} = \frac{2}{3}\sqrt{\frac{8RT}{\pi M_i}}\bar{r}, \tag{4.17}$$

where $\bar{r}$ is the mean pore radius of the electrode and M_i the molecular mass of species i. The molecular diffusion coefficient of species i in a multicomponent mixture is calculated from using Blanc's law,

$$D_{g,i} = \frac{1 - y_i}{\sum_{j \neq i} y_j / D_{ij}} \tag{4.18}$$

in which the binary diffusion coefficients D_{ij} are calculated using Fuller's method [278, 279]:

$$D_{ij} = \frac{0.00143\, T^{1.75}}{p\sqrt{2(1/M_i + 1/M_j)^{-1}}(\sqrt[3]{V_i} + \sqrt[3]{V_j})^2} \tag{4.19}$$

4.3.5. HEAT TRANSFER COEFFICIENTS

Heat transfer in SOFCs proceeds via conduction in the solid parts, convection between the gases and the solids and radiation. It has been shown that radiative heat transfer can be ignored in most cases for planar stack designs, since the temperature gradients perpendicular to the cells are usually small [280]. The convective heat transfer coefficient between the solid parts and the gases in the SOFC can be calculated from the Nusselt number

$$\bar{h} = Nu\frac{\lambda_g}{d_h}, \tag{4.20}$$

which is assumed to be independent of the Reynolds number due to the laminar flow conditions, and has a constant value of 3.09 [48]. The hydraulic diameter of the square gas channels follows from their width w_{ch} and height τ_{ch}

$$d_h = \frac{2 w_{ch} \tau_{ch}}{w_{ch} + \tau_{ch}}, \tag{4.21}$$

where the width of the channels is calculated from the width of the cell, number of channels and interconnect thickness:

$$w_{ch} = \frac{w_{cell}}{N_{ch}} - 2 \cdot \tau_{IC} \tag{4.22}$$

The heat conductivity of the gas mixture is calculated using the Wassiljewa equation [281]

$$\lambda_g = \sum_i \frac{y_i \lambda_i}{\sum_j y_j \Phi_{ij}}, \tag{4.23}$$

where λ_i is the thermal conductivity of the individual gas species, calculated from an estimation method recommended by Todd et al. [279]

$$\lambda_i = 0.01 \sum_n C_n \left(\frac{T}{1000} \right)^n, \tag{4.24}$$

and Φ_{ij} a function depending on the thermal conductivity and molecular mass of the species involved, proposed by Mason et al. [282]:

$$\Phi_{ij} = \frac{[1 + \sqrt{\lambda_i / \lambda_j} \sqrt[4]{M_i / M_j}]^2}{\sqrt{8 (1 + M_i / M_j)}} \tag{4.25}$$

4.3.6. PARAMETERS AND BOUNDARY CONDITIONS

In principle, all equations discussed so far apply to both the model of the single cell test setup and the stack. The difference between the two models is in the geometrical parameters and boundary conditions assumed. The cell parameters are based on ESC2 cells obtained from Kerafol/H.C. Starck, for which MSR kinetics were derived in previous work [263, 264]. These cells have a Ni-GDC anode and an 8YSZ/LSM-LSM double layer cathode supported on a dense 3YSZ electrolyte [283]. The stack model is based on Mk200 stacks and the ISM V3.3 produced by Sunfire/Staxera, which relies on the same cells [284]. The parameters assumed in the model are summarised in Table 4.1.

Figure 4.2 illustrates the differences between the ISM and single cell configuration. The Sunfire/Staxera ISM V3.3 contains a single tower of two Mk200 stacks consisting of 30 cells each with internal fuel manifolding. The stack is placed in a thermally insulated box, which provides external air manifolding and has connections for the fuel and air in- and outlets, electric power cables and instrumentation. The ISM offers a flexible solution for system integrators, since other balance of plant components, such as heat exchangers, blowers or (pre-)reformers, are not included.

Table 4.1: Parameters assumed in the stack and single cell test setup SOFC models, based on ESC2 cells obtained from Kerafol/H.C. Starck and the ISM V3.3 from Sunfire/Staxera.

Geometric properties	**Units**	**ISM**	**Single Cell**
No. of cells, N_{cells}	[-]	60	1
Cell length, L_{cell}	[m]	0.164	0.1
Active area length, L_{aa}	[m]	0.09	0.09
Cell width, w_{cell}	[m]	0.142	0.09
No. of channels, N_{ch}	[-]	24	22
Channel height, τ_{ch}	[m]	1e-3	2.5e-3
Electrolyte thickness, τ_{el}	[m]	90e-6	90e-6
Anode thickness, τ_{an}	[m]	35e-6	35e-6
Cathode thickness, τ_{ca}	[m]	35e-6	35e-6
Interconnect thickness, τ_{IC}	[m]	500e-6	-
No. of control volumes, N_{cv}	[-]	50+(2×21)	250
Thermal properties			
PEN density, ρ_{PEN}	[kg m^{-3}]	5900	
PEN heat capacity, $c_{p,PEN}$	[J kg^{-1} K^{-1}]	500	
PEN thermal cond., λ_{PEN}	[W m^{-1} K^{-1}]	2	
IC density, ρ_{IC}	[kg m^{-3}]	8000	
IC heat capacity, $c_{p,IC}$	[J kg^{-1} K^{-1}]	500	
IC thermal cond., λ_{IC}	[W m^{-1} K^{-1}]	24	
Ins. thermal cond., λ_{ins}	[W K^{-1}]	2.91e-3	
Electrolyte and electrode properties			
Electrolyte conductivity, σ_{el}	[Ω^{-1} m^{-1}]	20.5e3 exp(-9.03e3/T)	
Anode conductivity, σ_{an}	[Ω^{-1} m^{-1}]	30.3e3	
Cathode conductivity, σ_{ca}	[Ω^{-1} m^{-1}]	12.9e3	
Contact resistance, $R_{contact}$	[Ω m^2]	5e-6	5.5e-5
Electrode porosity, ε	[-]	0.3	
Electrode tortuosity factor, ι	[-]	6	
Electrode pore radius, $\bar{r}$	[m]	5e-7	

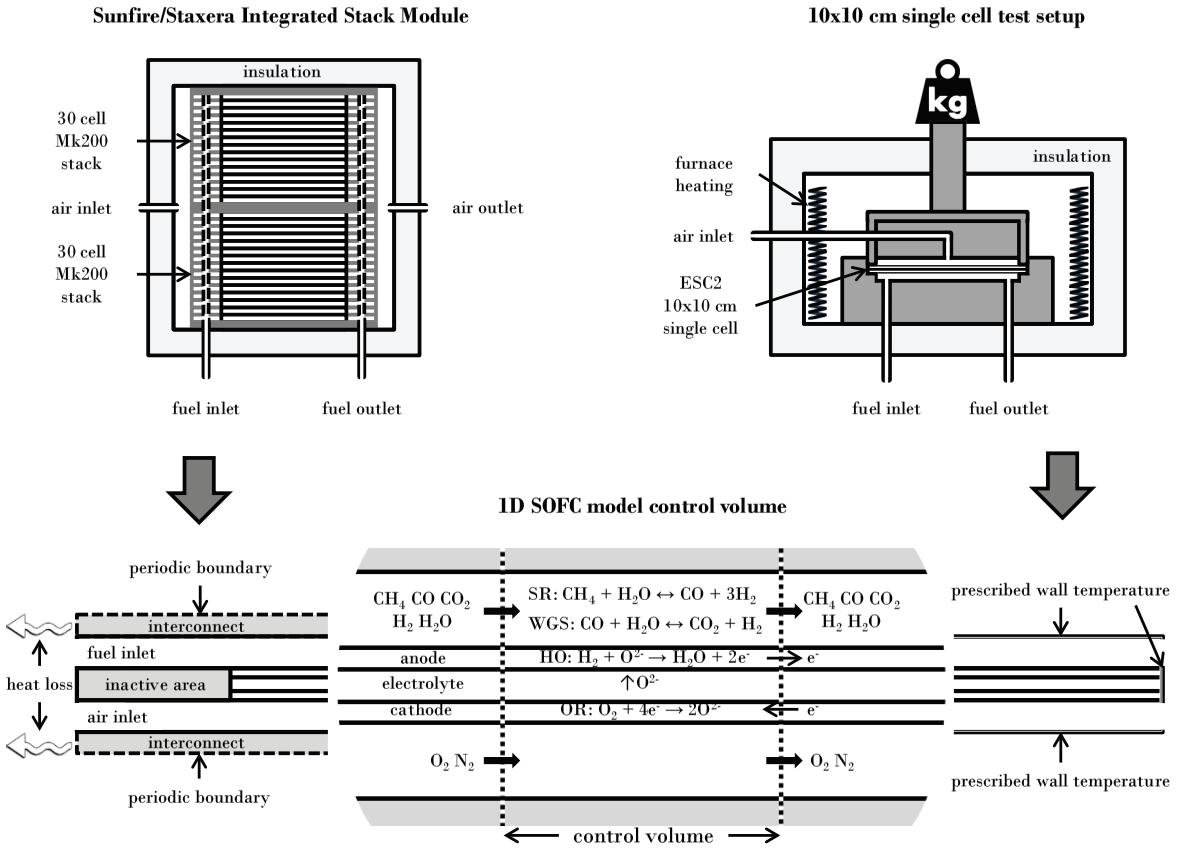

Figure 4.2: Graphical representation of the modelling platform. A schematic overview of the ISM is shown on the top left and the single cell test station on the top right. A control volume including the relevant reactions is shown in the bottom centre, with the boundary conditions for the two modelled geometries on the sides.

The cells are contained in metal cassettes in the stack. Therefore, it has an inactive in- and outflow manifold where only heat transfer is expected to occur. The temperature of the ISM is sustained with heat produced by the electrochemical reaction. Overheating of the stack is prevented by control of the cathode air flow, although heat will be lost through the insulation as well. The active area of the stack is discretised into 50 control volumes, and the inactive in- and outlet areas are divided into 21 control volumes each.

In the single cell test setup, 10x10 cm cells are placed in a ceramic holder with fuel and air manifolding. Compression seals are used to seal the anode and cathode compartments, and nickel meshes are used as current collector. The ceramic holder is placed in an isolated furnace, equipped with electric heaters and temperature control. This is used to maintain a constant cell temperature in the ceramic block during the MSR experiments. The active area of the single cell is discretised into 250 control volumes to accurately capture the sharp temperature gradients encountered at the inlet, a result of the prescribed wall temperature boundary condition.

Spatial variations perpendicular to the flow direction are ignored, since the model is formulated in 1D. Therefore, only boundary conditions on the inlets, outlets and perpendicular to the cell assembly need to be defined. A periodic boundary condition is assumed on the interconnect in the stack model, thus assuming an infinitely repeated stack assembly. It is assumed that the temperature gradient in the boundaries of the PEN structure is negligible due to ideal isolation, hence a Neumann boundary condition is applied:

$$\left.\frac{\partial T_{PEN}}{\partial l}\right|_{l=0 \vee l=L} \approx 0 \tag{4.26}$$

A convection, or Newton, boundary condition is applied to the boundary of the interconnect to account for the heat loss to the environment. The heat loss is proportional to the temperature difference with the environment multiplied by an effective heat transfer coefficient λ_{ins}. This implies that a source term is added to Equation (4.3) in the boundaries of the interconnect:

$$\dot{Q}_{loss} = \begin{cases} \lambda_{ins}(T_{IC} - T_{env}) & \text{if } l = 0 \vee l = L \\ 0 & \text{if } l \neq 0 \vee l \neq L \end{cases} \tag{4.27}$$

An environmental temperature of 25°C is assumed. The heat transfer coefficient of the ISM isolation is estimated based on a reference operating point specified by the manufacturer of the ISM, which results in a total heat loss of ~250 W for the 60 cell ISM. This is in good agreement with the value reported by a system integrator [284].

A prescribed temperature, or Dirichlet, boundary condition is applied to the cell boundaries and the walls representing the ceramic block in the single cell model, since the temperature of the ceramic block was controlled in the experiments with the furnace heating:

$$T_{PEN}|_{l=0 \vee l=L} = T_{wall} = T_{furnace} \tag{4.28}$$

Table 4.2: Reference operating temperatures, fuel utilisation and fuel compositions specified by Sunfire/Staxera for their ISM V3.3 [265, 266].

Reference operating conditions	**Units**	**Value**
Anode gas inlet temp, T_{an}^{in}	[°C]	800
Cathode gas inlet temp, T_{ca}^{in}	[°C]	650
Max PEN temperature, $max(T_{PEN})$	[°C]	850-860
Fuel utilisation, u_f	[-]	0.75

Air and fuel compositions (by volume)	
Air	O_2 (20%) N_2 (80%)
H_2/N_2	H_2 (40%) N_2 (60%)
CPOX	H_2 (31%) N_2 (47%) H_2O (5%) CO (15%) CO_2 (2%)
SR	H_2 (53%) H_2O (24%) CO (6%) CO_2 (9%) CH_4 (8%)

4.4. RESULTS

4.4.1. STACK MODEL VALIDATION AND EVALUATION

The ISM model is validated with power curves published by Sunfire/Staxera for their ISM V3.3 [265, 266]. These specify the stack power for different stack currents at reference conditions for three gas compositions: a hydrogen-nitrogen mixture, a CPOX reformate and a SR. An overview of these reference operating conditions and fuel compositions is given in Table 4.2. The manufacturer advices temperature control trough manipulation of the cathode airflow or inlet temperature. Therefore, a control loop is implemented in the model, which adjusts the airflow such that a maximum PEN temperature of 850°C is maintained.

The hydrogen content of the fuel mixture specified varies from 31% in the CPOX reformate to 53% in the SR. In addition, the SR contains 24% steam, while the hydrogen-nitrogen mixture is dry. The hydrogen and steam partial pressure affect the cell voltages and consequently the power curves due to changes in the Nernst potential and the anode exchange current density [274]. However, the dependency of the anode exchange current density is a subject of debate and thus unknown. Therefore, appropriate values are determined for the investigated stack using the power curves reported for three different gas compositions.

The activation polarization model proposed by Costamagna et al. [275] is implemented, which relates exchange current densities to global dependencies on the reactants and products and an Arrhenius temperature dependency. In addition, all parameters for the cathode are adopted, i.e. the cathode pre-exponential factor $\hat{k}_{0,ca}$, reaction order for oxygen $\hat{\epsilon}$, as well as the activation energies for the exchange current densities of both electrodes. However, reaction orders for hydrogen $\hat{\gamma}$ and steam $\hat{\beta}$, ranging from 0 to 1 and -1/2 to 1 respectively, are evaluated. The value of the pre-exponential factor is determined for hydrogen-nitrogen operation at a stack current of 27 A for every combination of $\hat{\gamma}$ and $\hat{\beta}$. Table 4.3 presents a selection of evaluated values for Equations (4.13) and (4.14).

Table 4.3: Parameters used in Equations (4.13) and (4.14) to calculate the exchange current densities for different global dependencies on the oxygen, hydrogen and steam partial pressures.

Cathode

$\hat{\epsilon}$ [-]	$\hat{k}_{0,ca}$ [A m^{-2}]	$E_{a,ca}$ [J mol^{-1}]
1/4	7e8	120e3

Anode

$\hat{\gamma}$ [-]	$\hat{\beta}$ [-]	$\hat{k}_{0,an}$ [A m^{-2}]	$E_{a,an}$ [J mol^{-1}]
1/2	0	1.81e9	120e3
1	-1/2	1.381e9	
0	0	9e8	
1	1	4.2e10	

Figure 4.3 shows the power curves simulated with the ISM model for four exchange current density models compared to the values published by the manufacturer for the three fuel compositions. The model predicts the power curve for hydrogen nitrogen operation with reasonable accuracy, regardless of the formulation of the anode exchange current density. Most formulations perform reasonable well for CPOX reformate as well, but clear differences are observed for SR. The model with proportional dependence on the steam and hydrogen partial pressure predicts higher cell voltages for SR operation than hydrogen nitrogen operation, while the opposite is reported by the ISM manufacturer. The best results are obtained for a square root dependence on only the hydrogen partial pressure (R^2 = 0.99). Therefore, this anode exchange current density formulation is selected.

Table 4.4 compares the simulation results to reference operating parameters specified by the manufacturer. The simulated cathode outlet temperature is only 3.2°C lower than the manufacturer reference, probably because a 0.7 Nl min^{-1} higher cathode airflow is required to limit the PEN temperature to 850°C in the model. The stack voltage and power are in good agreement as well, demonstrating the ability of the model to simulate the behaviour of a commercial stack with high accuracy. The results confirm that the assumed heat transfer coefficient results in the expected heat loss of ~250 W at reference conditions [284].

The advantage of 1D models over the more commonly used lumped parameter models is in the ability to resolve spatial distributions of temperatures, concentrations and reaction rates along the flow direction. Figure 4.4 shows the temperature profiles of air, fuel, interconnect and PEN structure along the inactive and active area of stack for the operating conditions shown in Table 4.4. The temperature difference between the four layers is relatively small along the flow direction, with the exception of a small inlet section. The temperatures are substantially higher at the beginning and end of the active area than in the inactive boundaries due to heat losses to the surroundings. The PEN temperature initially drops while heat is transferred from the hot fuel to the cold cathode air. It then increases along the active area, as waste heat is produced by the electrochemical reaction,

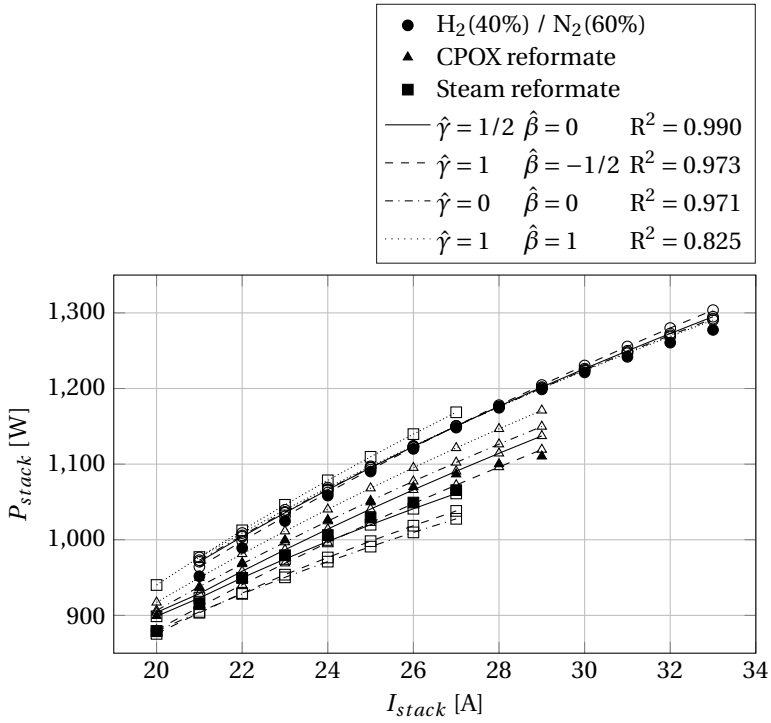

Figure 4.3: Simulated power curves for H_2/N_2 (○), CPOX (△) and SR (□) fuel versus data provided by Sunfire/Staxera for their ISM V3.3 (●▲■) for differen global reaction orders for hydrogen ($\hat{\gamma}$) and steam ($\hat{\beta}$) in the anode exchange current density.

Table 4.4: Simulated operating conditions for the ISM operating at reference conditions when a current of 26.2 A is drawn and 36 Nl min^{-1} H_2/N_2 fuel is supplied. The cathode airflow is controlled to limit the maximum PEN temperature to 850°C.

Operating parameter	**Units**	**Simulated**	**Specified**
Cathode outlet temp, T_{ca}^{out}	[°C]	821.8	~825
Cathode inlet flow, $\dot{V}_{ca}^{in}$	[Nl min^{-1}]	150.7	~150
Oxygen utilisation, u_{ox}	[-]	0.17	-
Stack voltage, U_{stack}	[V]	42.66	≥42
Stack power, P_{stack}	[W]	1118	≥1100
Heat loss, $\dot{Q}_{loss}$	[W]	250.3	-

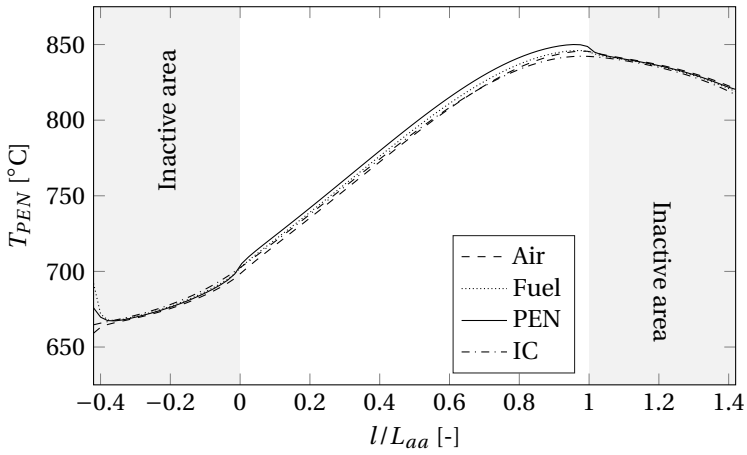

Figure 4.4: Temperature profiles of air, fuel, PEN structure and interconnect along the flow direction, both in the inactive and active area of the stack, for the conditions presented in Table 4.4.

and finally drops again due to heat loss to the surroundings.

Figure 4.5a compares the PEN temperature profile for hydrogen-nitrogen, CPOX and SR operation. The current density distributions and temperature gradients predicted for the active area are shown in Figures 4.5b and 4.5c respectively. The average PEN temperature is highest for hydrogen-nitrogen operation, closely followed by CPOX. Endothermic cooling from the reforming reaction, assumed to react to chemical equilibrium instantly, causes the PEN temperature to drop sharply at the beginning of the active area for SR.

The current density distribution is relatively homogeneous for the hydrogen-nitrogen fuel mixture, since the effect of a decreasing hydrogen and increasing steam concentration on the Nernst voltage along the flow direction is compensated by the increasing PEN temperature. The presence of steam in fuel and the higher air flow required to cool the stack result in a larger current density variation for CPOX. Similarly, the low inlet temperatures caused by the endothermic DIR reaction induce large current density variations for SR. Therefore, the temperature gradients are substantially higher for SR compared to hydrogen-nitrogen and CPOX fuel mixtures.

4.4.2. TRANSIENT STACK SIMULATIONS

Since the stack model developed is dynamic, it can be used to simulate transient operation of the ISM. The validation of the stack model is limited to steady-state performance in this study due to the lack of reliable data. For completeness, the transient capabilities of the model are demonstrated by simulating the start-up behaviour of the ISM. According to the manufacturer, the stack should be pre-heated to a temperature ≥650°C by a start-up burner, after which current is drawn to support further heating to the operating temperature. The current should not be increased faster than 2 A min^{-1}, and a stack voltage below 36 V has to be avoided.

Figure 4.6 shows the simulated ISM start-up behaviour assuming hydrogen-nitrogen

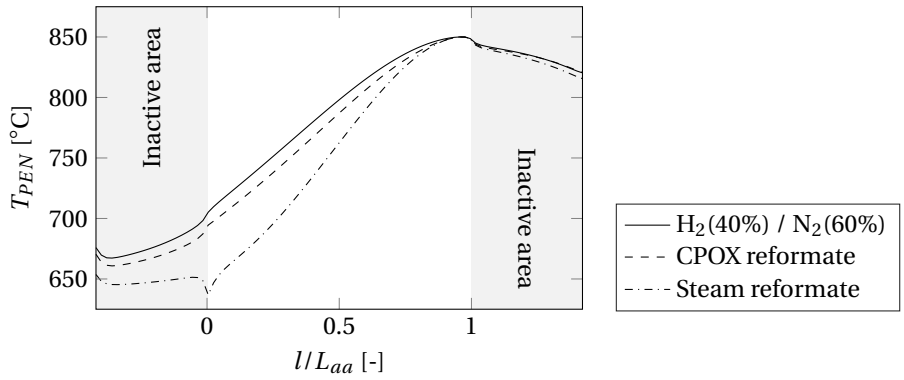

(a) PEN temperature profiles.

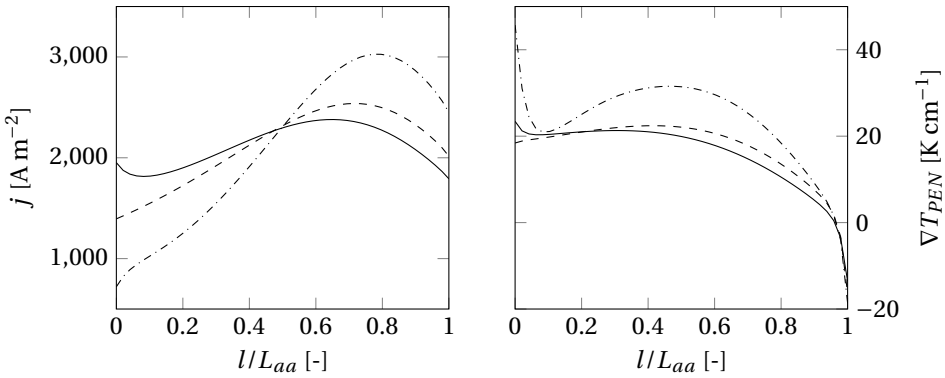

(b) Current density distributions.

(c) PEN temperature gradients.

Figure 4.5: PEN temperature profiles along the flow direction in the stack (Figure 4.4), as well as the current density distribution (Figure 4.5b) and PEN temperature gradient in the active area (Figure 4.5c) for a reference operating conditions and fuel compositions specified in Table 4.2 and a stack current of 27 A.

operation at reference conditions. Two scenarios are simulated: in the first one, the current is ramped to the nominal value of 27 A with the maximum rate specified by the manufacturer, while the current is stepped to the final value in the second scenario. Figure 4.6b shows that application of the specified current ramp results in a gradual change of the stack voltage, while a step change of the current causes an instant drop below the minimum specified for safe operation. The relatively high voltage drop for a step change is a result from the high electrolyte resistance at a lower average PEN temperature.

Safe heating of the stack to the desired temperature with the specified current ramp can take up to half an hour, as can be seen in Figure 4.6c. A higher current ramp may bring this down to 15 minutes, but will cause the stack voltage to drop below acceptable values. This may cause large cell-to-cell variations in the stack, resulting in potentially deteriorating local hot spots. In addition, rapid ramping may induce relatively large local

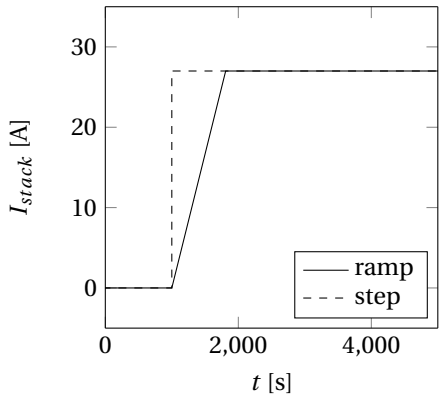

(a) Stack current.

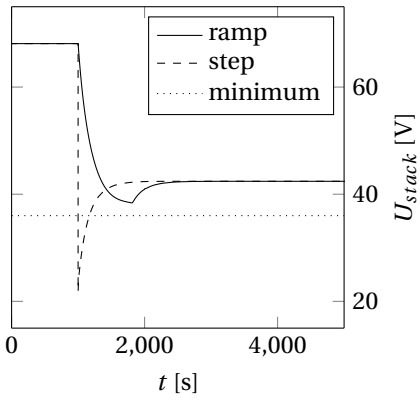

(b) Stack voltage.

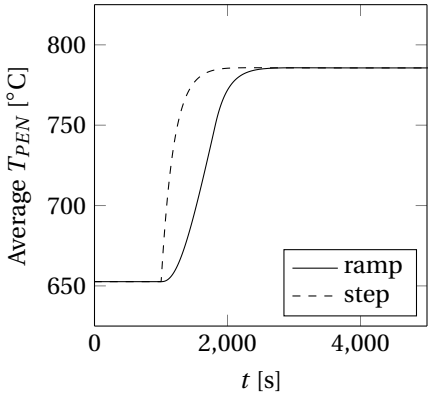

(c) Average PEN temperature.

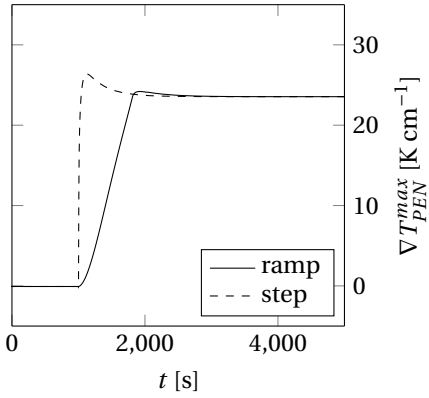

(d) Maximum PEN temperature gradient.

Figure 4.6: Stack voltage, average PEN temperature and maximum PEN temperature gradient (Figures 4.6b to 4.6d) for a simulated system start-up, either by a step change to the stack current or with the maximum allowable current ramp specified by the ISM manufacturer (Figure 4.6a).

temperature gradients, as is evident from the maximum PEN temperature gradient in Figure 4.6d. The resulting thermal strain may damage the stack.

4.4.3. DIRECT INTERNAL REFORMING ON SINGLE CELLS

Direct internal MSR was experimentally studied by Fan et al. [263] on 10x10 cm single ESC2 cells obtained from Kerafol (former H.C. Starck). The reforming data was used to parameterise two different kinetic models, one of the PL and the other of the HW type [264]. The rate equations were then implemented in a CFD model. Both kinetic models predicted comparable overall MSR rates, but higher temperature gradients were predicted by the HW kinetics due to their non-monotonic dependency on the steam-to-hydrogen ratio.

Table 4.5: Overview of the conditions simulated for the experiments on ESC2 cells obtained from Kerafol/H.C. Starck [263]. The volume flows are specified for atmospheric pressure and a temperature of 120°C, such that all steam is evaporated.

Gas compositions					**Temperatures**	**Current density**
[Nml min^{-1}]	CH_4	H_2O	H_2	N_2	[°C]	[A m^{-2}]
GC 1	220	450	80	270		
GC 2	300	450	80	190	700, 725, 750	0, 600, 1000
GC 3	220	540	80	180		

Table 4.6: Parameters used in the MSR Equations (4.8) to (4.10), obtained from previous work [264]. The frequency factors k_0 are fitted to the experimental conversioins for GC 1 at 725°C and open circuit conditions in Table 4.5.

Power law

α [-]	β [-]	k_0 [mol Pa$^{-0.561}$ s^{-1} m^{-2}]	E_a [J mol^{-1}]
0.6505	-0.0895	1.67e-2	62.99e3

Hougen-Watson

$\bar{A}_0$ [-]	$\Delta\bar{H}_O$ [J mol^{-1}]	k_0 [mol Pa$^{0.5}$ s^{-1} m^{-2}]	E_a [J mol^{-1}]
268.0	38.4e3	5.92e10	165.1e3

The objective of this study is to transfer the kinetic models derived in previous work to the 1D ISM model. A general problem when transferring kinetic mechanisms derived on substrate materials to stack models is the selection of an appropriate value for the frequency factor k_0 in Equations (4.8) and (4.9). Data fitting typically yields an arbitrary rate constant in mol s^{-1}, which can be normalised by, for example, the anode volume, active area or the weight or surface area of the catalyst. However, it is difficult to account for geometrical, structural and material variations between different anodes.

It would be more appropriate to obtain an appropriate value for k_0 from stack operation data, but this is difficult as all methane is typically converted within the stack, and hence no reforming rates can be deduced. However, in this case the reforming parameters are derived using data obtained from same cells used in the Sunfire ISM V3.3. In theory, this enables direct transfer of the MSR kinetics to the stack model. To demonstrate the validity of this approach, the original experimental conditions are simulated using a single cell version of the 1D model.

Table 4.5 presents an overview of the simulated experimental conditions. The values of k_0 are chosen such that the simulated methane conversion matches the experimentally observed value for gas composition (GC) 1 at 725°C and open circuit conditions. However, the values are found to be within 10% of those obtained in the fitting procedure, in which a simplified isothermal ideal plug flow reactor model was assumed. An overview of the parameters used in the PL and HW rate equation is given in Table 4.6.

Figure 4.7a shows temperature profiles along the flow direction calculated with 1D

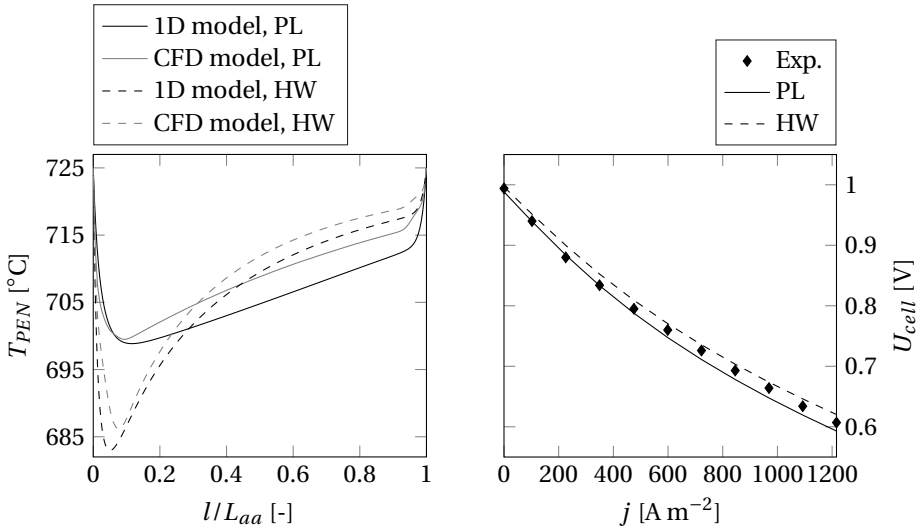

(a) Comparison to CFD model.

(b) Comparison to IV curve.

Figure 4.7: Comparison of the temperature profiles predicted with the PL and HW kinetics to those obtained with CFD modelling in previous work [264], and predicted IV curves compared to the experimental data.

single cell model and those obtained with the 3D CFD model published earlier for GC 1 at 725°C and open circuit conditions [264]. The temperature profiles predicted with the 1D model are qualitatively in good agreement with the CFD model, especially considering that it lacks most geometrical information, such as the shifted position of the fuel in- and outlet tubes. Both models predict higher temperature gradients for the HW kinetics.

Figure 4.7b shows a comparison of the current-voltage characteristics predicted with the PL and HW rate equations to experimental data. These are obtained with the electrochemical model derived for the ISM model, although the contact resistance is adjusted to account for non-ideal contacting in the experimental setup. This uncertainty is difficult to eliminate, since the contact resistance depends on the contact between the anode and the current collector. This varies from experiment to experiment, for example due to changes in the compression seals. Nonetheless, it can be seen that the predicted open circuit voltages agree well with the experimental value. Higher voltages are predicted using HW kinetics, probably since the reforming reaction proceeds faster at the entrance according to this reaction model.

Figure 4.8 shows a comparison between the experimental MSR rates and simulation results for some of the conditions specified in Table 4.5. Both the PL and HW model show good agreement with the experimental data, although the PL rate equation performs slightly better, in contrast to finding using the CFD model [264]. In general, the validation results give confidence for implementation of the MSR kinetics in the ISM model.

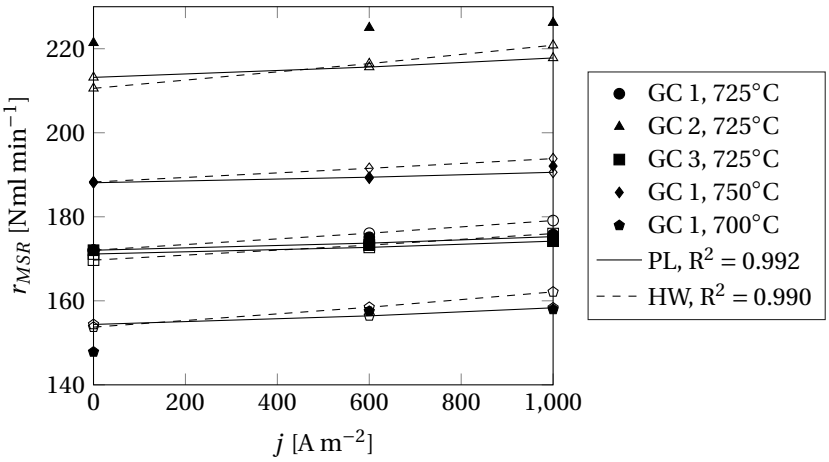

Figure 4.8: Overall methane steam reforming rates predicted with the 1D single cell model with PL and HW kinetics (○△□◇⬠) versus the experimental values (●▲■◆⬟) for various gas compositions, temperatures and electrochemical current densities.

4.4.4. DIRECT INTERNAL REFORMING IN STACKS

Figure 4.9b compares the MSR rates predicted along the active area of the stack with the PL and HW rate expression to the original results assuming chemical equilibrium, for ISM operation, at the reference conditions specified in Table 4.2 for SR fuelling. As expected, the MSR rates are considerably lower for the kinetic models, revealing that the MSR reaction is kinetically limited for typical stack operating conditions.

The PL kinetics predict higher reaction rates at the entrance of the active area than the HW rate equation, in contrast to the findings for the experimental conditions. This is attributed to the relatively low steam-to-hydrogen ratio in the partly pre-reformed fuel compared to the experiment, where the fresh fuel consisted primarily of methane and steam only. Still, even with the slower HW kinetics all methane is reformed within the stack length.

Figure 4.9a compares the PEN temperature profiles in the active and inactive area of the stack predicted by the PL and HW rate expression to assuming chemical equilibrium. The wider distribution of the endothermic MSR reaction results in a more gradual increase of the PEN temperature. In addition, the somewhat unlikely cold spot predicted assuming chemical equilibrium disappears. As a result, the PEN temperature gradients are smoothened as well, as is shown in Figure 4.9c. The maximum PEN temperature gradients are 45.7, 31.9 and 30.2°C cm^{-1} for chemical equilibrium, PL and HW kinetics respectively.

Figure 4.10 shows there is little influence of the internal MSR kinetics on the overall power production by the stack. The predicted power curve is closest to the one reported by the manufacturer with the HW kinetics, followed by the PL kinetics. However, the overall maximum deviation between the predicted stack powers is only ~5 W. This emphasises that realistic predictions of the DIR rate is primarily important for accurate thermal stress predictions.

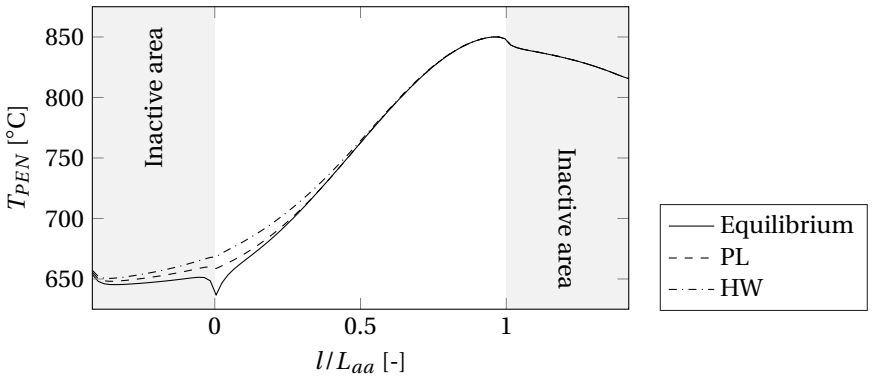

(a) PEN temperature profiles.

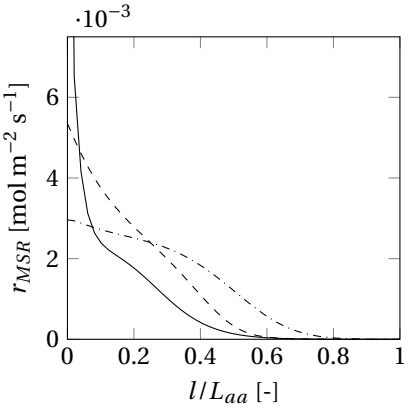

(b) Methane steam reforming rates.

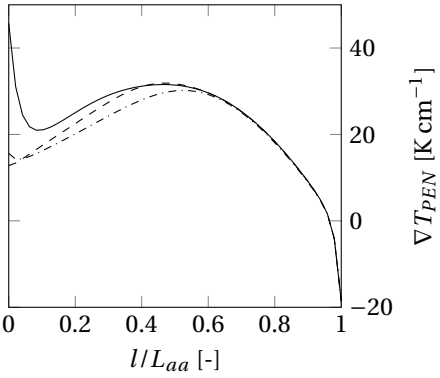

(c) PEN tempearture gradients.

Figure 4.9: PEN temperature profiles in the active and inactive area of the stack (Figure 4.9a), and methane steam reforming rates (Figure 4.9b) and PEN temperature gradients (Figure 4.9c) along the active area for SR operation with different reforming models.

4.5. DISCUSSION

The 1D dynamic modelling platform presented in this study enables the simulation of both a single cell experimental setup and a commercial ISM with a single set of equations, changing only geometrical parameters and boundary conditions. Therefore, it enables validation of kinetics derived from single cell experiments, and allows for direct transfer to models for stack simulation. Single cell experiments are expected to yield more reliable reforming kinetics than data collection from substrate reactors, while being substantially less complicated and easier to instrument and control than experiments on complete stack assemblies.

Dynamic models of the same stack design have been developed by Kupecki et al. [285, 286], Sorce et al. [257] and Greco et al. [287]. Kupecki et al. [286] validated the voltages predicted by their quisi-1D model dynamically with current ramps for two gas composi-

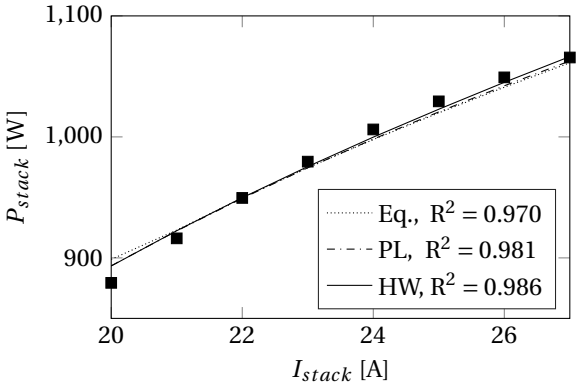

Figure 4.10: Simlated power curves with different MSR kinetics versus data published by the manufacturer (■).

tions containing methane. Greco et al. [287] used a full 1D dynamic model to study faulty states, for example due to reformer malfunctioning. However, it appears that heat transfer in the inactive area of the stack was not included in these models. Moreover, chemical equilibrium was assumed for the internal reforming reaction.

It was shown in this work that assuming chemical equilibrium for the reforming reaction results in unrealistic temperature profile predictions. Thermal stresses can be estimated more accurately using appropriate kinetic models for the MSR reaction on the anode. However, the PL and HW kinetics derived in previous work yielded different reaction rates temperature profiles in the 1D stack model, even though both were derived from the same experimental data and shown capable to reproduce the experimentally observed conversions in the 1D single cell model.

The total number of parameters is higher for the HW than the PL kinetics. However, both the PL and HW kinetics have four free-fitted parameters, since the reactant and product partial pressure dependency is not fitted but based on an intrinsic rate limiting mechanism. The parameters are entirely independent in the PL kinetics, while two pre-exponential factors and their respective energies are determined for the HW kinetics. Statistically, the PL kinetics showed slightly better agreement with the experimental data, but the HW kinetics ideally contain information on the intrinsic rate determining mechanism and are, therefore, expected to predict the internal reforming kinetics more accurately.

Although PL kinetics do not contain any mechanistic information, they may still yield more realistic temperature profiles than assuming the reforming reaction to be in equilibrium. Assuming proportional dependency on the methane partial pressure might be acceptable as well if some inaccuracy in the predicted thermal stresses is allowed. However, it is not clear if this holds for more substantially deviating operating conditions, such as changes in the extent of pre-reforming, oxygen-to-carbon ratio in the fuel, inlet temperatures of air and fuel, fuel utilisation and anodic off-gas recirculation. Further study is required to discriminate between different kinetic models and determine the rate limiting step(s) of the reforming reaction on different SOFC anode materials.

The electrochemical reactions in the anode were accounted for using a symmetric

Butler-Volmer equation, as it is numerically convenient and Noren et al. [273] showed that errors due to this assumption are small for typical SOFC operation. This result was confirmed in our simulations as well. Global reaction orders for hydrogen and steam were determined in the anode exchange current density to account for the rate limiting hydrogen oxidation kinetics, using power curves from the stack manufacturer for three different fuel compositions.

Bessler et al. [274] pointed out the limitations of using global dependencies, since the hydrogen oxidation reaction is a complicated multi-step process, and there is no agreement the on exact mechanism. Depending on the rate determining step, the global reaction orders may depend on the hydrogen and steam partial pressure themselves, temperature and anode material. However, implementing a multi-step heterogeneous reaction mechanism for the hydrogen oxidation reaction may be overly complicated for control-oriented computationally inexpensive dynamic models.

Good results were obtained for a square root dependency of the anode exchange current density on the hydrogen partial pressure, while no evidence of the influence of the steam partial pressure was found. Ignoring these global dependencies or using values reported in literature yielded inaccurate predictions of the ISM power when the fuel composition was changed. Although the global reaction order for hydrogen supports a hydrogen spill-over charge transfer mechanism, a positive steam partial pressure dependency is reported for most charge transfer rate limiting reactions. While hydrogen oxidation kinetics have been studied extensively on Ni-YSZ anodes, this result highlights the necessity to study them on other anodes such as Ni-GDC and wider steam-to-hydrogen ratios as well.

The approach presented was shown to enable simulation of the performance of both single cell experiments as well as a commercial ISM with high accuracies. The model formulation is dynamic, and load transient could be simulated with good numerical stability and reasonable computational time. In addition, thermal stresses induced by DIR in a commercial ISM could be predicted based on reforming data obtained in single cell experiments. Therefore, the modelling platform may be a powerful tool for future studies on design, operation and control of SOFC stacks and systems.

The model was only validated with the available data specified by a single manufacturer in this work. However, the approach may be extended to different stack designs and validated for more operating conditions, such as variations in the extent of pre-reforming, oxygen-to-carbon ratio in the fuel, inlet temperature of air and fuel, fuel utilisation and anode off-gas recirculation. In addition, further validation of the transient predictions is required, as well as further study on the intrinsic kinetics of both the reforming and electrochemical reactions.

The dynamic modelling approach developed in this study can be used to study off-design operation of commercial ISMs and integration with balance of plant components. The models developed can be used to predict the electrochemical performance of the stack, air flow required to maintain a constant temperature as well as thermal stresses induced. In addition, the model may be used to simulate transient operation and develop adequate control logic for integrated systems.

4.6. CONCLUSIONS

A 1D dynamic SOFC modelling platform was developed in this chapter to simulate a single cell experimental setup as well as a commercial ISM, changing only geometrical parameters and boundary conditions. The ISM model was validated with data from the manufacturer, and PL and HW MSR kinetics were validated with data from single cell reforming experiments. The kinetics were implemented in the ISM model to predict the spatial distribution of the MSR reaction.

Both the PL and HW kinetics predicted more realistic temperature profiles in the ISM model than assuming chemical equilibrium, indicating that DIR is kinetically limited for the investigated conditions. This demonstrates that an appropriate description of the DIR kinetics is required to simulate potentially deteriorating temperature gradients in the stack. However, further study on the rate limiting steps in the reforming reaction is required, since the predicted spatial distributions of the MSR reaction differed between the PL and HW kinetics. Therefore, an experimental study on the rate limiting reforming kinetics is presented in the next chapter.

5

REFORMING KINETICS ON NICKEL-CERIA SOFC ANODES

This chapter has been published in Journal of Power Sources **443**, (2019) [288].

5.1. INTRODUCTION

Two methane steam reforming models were implemented in a 1D SOFC stack model in the preceding chapter. Both models were parameterised with the same set of reforming data, derived on Ni-GDC anodes. However, the first model was an empirical power law equation, while a rate determining surface reaction was assumed in the second model. The two models predicted different MSR rates within the stack and, as a result, different species and temperature distributions. This illustrated that accurate methane steam reforming kinetics are required to accurately model the electrochemistry and potentially deteriorating thermal stresses in the stack.

This chapter presents an experimental study of the MSR kinetics on single cells with Ni-GDC anodes. The experimental reforming rates are then used to parameterise and compare four kinetic MSR models. A more comprehensive background of MSR kinetics on SOFC anodes is provided in Section 5.2, after which the experiment and parameter regression are described in Section 5.3 and Section 5.4 respectively. Section 5.5 presents the results of both the experiments and parameter regression. Finally, a kinetic model is selected and compared to previous work in Section 5.6, and conclusions are drawn in Section 5.7.

5.2. REFORMING KINETICS ON SOFC ANODES

The kinetics of the methane reforming reaction have been subject of many studies, both for industrial steam reformers and SOFCs, because:

- Methane is a simple and abundant hydrocarbon molecule;
- Methane is the main constituent of natural gas [129, 289];
- The reformate of other hydrocarbons and alcohols, such as methanol, typically contains methane [290, 291];

The MSR reaction has been studied extensively for commercial steam reformers to produce hydrogen from natural gas. More recently, researchers have investigated the kinetics of the steam reforming reaction on SOFC anode materials as well. Three classes of MSR kinetics may be distinguished in these studies: Multi-step reaction mechanisms, intrinsic surface reaction models assuming a rate determining step a catalyst and empirical global PL kinetics. Comprehensive overviews of methane steam reforming in SOFCs have been presented in dedicated literature reviews [37, 292].

Multi-step mechanisms describe the kinetics with a sequence of intermediate steps, consisting of adsorption, surface reaction and desorption processes. The rate is determined by the slowest intermediate reaction, which may change for different temperature as well as reactant and product partial pressures. A heterogeneous multi-step mechanism consisting of 42 different intermediate reactions was derived by Hecht et al. [258] for a Ni-YSZ cermet anode.

A single rate determining step is assumed to describe the overall reaction kinetics in classical surface chemistry theory [293]. LH, HW and ER kinetics are well-known surface reaction mechanisms which assume a single rate determining reaction on an

active catalyst reaction site. However, the availability of these active reaction sites may be compromised by competitive adsorption of reactants, reaction intermediates and products [294]. LH kinetics have been reported by Nakagawa et al. [295] for a Ni-YSZ-CeO_2 anode, and Dicks et al. [296] derived HW kinetics for a Ni-YSZ anode.

The majority of the internal MSR kinetics reported for SOFCs is of the PL type, especially those derived on functional anodes. These models implicitly assume that the complex surface chemistry involved in the reforming reaction can be disregarded, and the kinetics are described by global reaction orders for the reactants and sometimes products involved in the reaction instead. PL kinetics for SOFC cermet anodes are, among others, derived by Ahmed et al. [262], Timmerman et al. [297] and Fan et al. [263].

Some authors simplify the kinetics even further and assume that the MSR is approximately first order (FO) in methane, and influences of other reactants and products can be neglected. For example, Belyaev et al [298] reported such kinetics for a Ni-ZrO_2-CeO_2 electrode. The FO kinetics reported by Achenbach et al. [299] for a Ni-ZrO_2 substrate are to this day probably the most frequently applied reforming model in reduced order and control-oriented dynamic SOFC stack models [48, 256].

Global reaction mechanisms such as PL or FO may capture the intrinsic kinetics in specific cases, for example if the adsorption of a single reactant is rate limiting and there is no inhibiting effect of other species on the catalyst surface. However, they may not capture the rate limiting step when the operating conditions change. This was demonstrated in previous work, where a PL rate equation was shown to predict the global reforming rates with accuracies comparable with an intrinsic HW model, but the spatial distribution of the reforming reaction predicted by the two models differed substantially [264].

Extensive multi-step reaction mechanisms, as developed by Hecht et al. [258], can fully describe the complex interdependency between surface adsorption, desorption and surface coverage by reaction intermediates. However, their parameterisation requires a substantial amount experimental data, since such models have a many degrees of freedom. Developing multi-step reforming kinetics based on data obtained on functional cell assemblies is, therefore, impractical. Instead, these reforming experiments are usually conducted on substrate materials rather than complete and functional cell assemblies [258, 296, 299].

Although detailed mechanistic studies are indispensable to understand the complex surface chemistry of the reforming reaction, it is difficult to use kinetics derived on varying substrate materials with deviating thicknesses, pore size distribution, particle size distribution and catalyst loading into control-oriented dynamic stack models of SOFC stacks [255]. For example, MSR kinetics have been primarily investigated for porous Ni-YSZ anodes, but many SOFC developers use ceria based cermet anodes, as these are reported to have a higher tolerance to carbon deposition [300]. In addition, the large system of equations obtained is typically very stiff and, therefore, not convenient for application in control-oriented dynamic models [261].

MSR was studied on Ni-GDC anodes of functional SOFC assemblies in previous experimental work in this group, both under open and closed circuit conditions [261, 263]. The methane partial pressure was shown to have a promoting effect on the reaction rate, while steam was shown to affect the reforming rate negatively. Although the hydrogen oxidation reaction increases the steam concentration as well, it consistently increased the

overall reforming rate in the experiments. This may be explained by a non-monotonic dependency on the steam partial pressure, the increased driving force due to the addition of steam, a local increase of the cell temperature or so-called *non-faradaic electrochemical modification of catalytic activity (NEMCA)* [301].

In a follow-up study, kinetic models of the PL and HW type were regressed from the experimental data and implemented in a 3D CFD model of the single cell test station [264]. Both kinetic models showed good agreement with the original data derived on single cells. However, the PL kinetics predicted a relatively flat reaction rate distribution along the flow direction, while the reforming rate decreased sharply from inlet to outlet according to the HW mechanism. As a result, higher temperature gradients were predicted with the HW mechanism than the PL kinetics.

HW kinetics have been proposed for the MSR reaction, and a dependency on the steam-to-hydrogen (SH) ratio is commonly reported [129, 261, 264, 289, 296, 302, 303]. However, the SH ratio varies from inlet to outlet in DIR SOFCs. Steam is usually mixed with the unreformed fuel to suppress the solid carbon formation through the methane dissociation, Boudouard and reverse gas shift reactions, thus leading to a high SH ratio at the inlet [226]. The SH then decreases as steam is consumed and hydrogen is produced by the MSR reaction, after which the SH increases again due to the hydrogen oxidation reaction. Therefore, intrinsic reforming kinetics need to capture the effect of the SH ratio correctly.

The influence of methane and steam is commonly quantified in experimental studies and accounted for in rate equations, but the effect of hydrogen is rarely reported. Therefore, most MSR models may not capture the rate limiting step due to the large SH variations in DIR SOFCs. Dicks et al [296] studied the effect of the hydrogen partial pressure on the reforming rate experimentally, reporting an enhancing effect. However, in other studies the effect of hydrogen is commonly included on the basis of data fitting adequacy only [261, 302]. Therefore, further study of the rate limiting step in the intrinsic MSR kinetics on SOFC anodes is required, taking into account the influence of the SH ratio.

Previous experimental work on DIR in Ni-GDC anodes of functional SOFC assemblies focussed on the influence of the partial pressures of methane and steam and the electrochemical reaction. The results of Fan et al. [263] demonstrated the need to derive detailed surface reaction mechanisms on functional SOFC assemblies, and HW kinetics were subsequently derived by Thattai et al. [261]. These kinetics suggest that the hydrogen partial pressure affects the DIR rate, but this hypothesis could not be confirmed as the effect of hydrogen was not studied in the experiment.

In this study, not only the influence of the partial pressures of methane and steam on the direct internal MSR are investigated, but the hydrogen partial pressure as well. Experimental methane reforming rates are derived on functional single cell SOFCs with Ni-GDC cermet anodes for various fuel gas compositions and temperatures. The conversions are then used to regress kinetic models of the FO, PL, LH and HW type for the internal MSR reaction. These kinetic models are then compared to select the most adequate reaction mechanism.

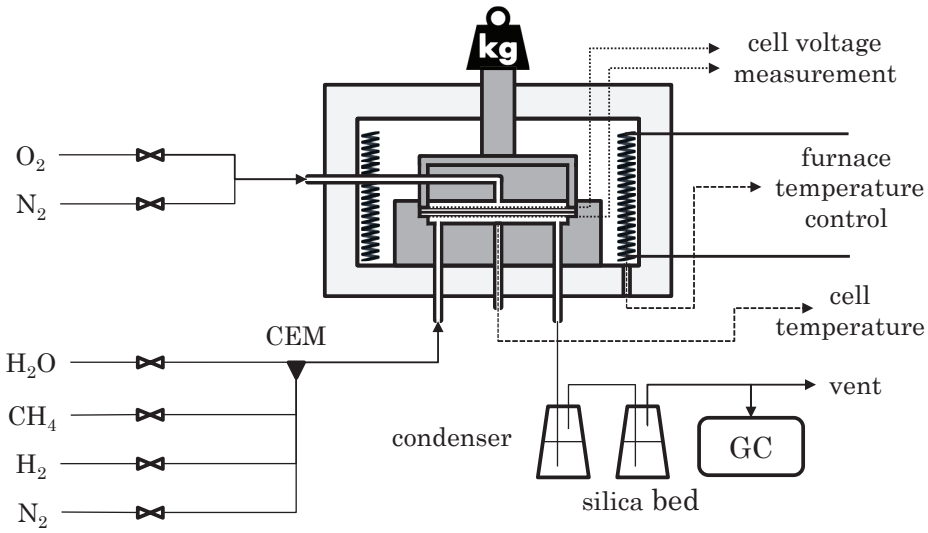

Figure 5.1: Schematic overview of the experimental single cell setup.

5.3. EXPERIMENTAL

5.3.1. EXPERIMENTAL SETUP

The reforming experiments are carried out in a single cell test setup, shown in Figure 5.1, on a 10x10 cm electrolyte supported cell (ECS2, H.C. Starck) with a 100 μm thick YSZ electrolyte, an active area of 81 cm^2 (9x9 cm) and a 35 μm thick Ni-GDC (Ni-$Gd_{0.1}Ce_{0.9}O_{1.95}$) cermet anode consisting of approximately 57 wt% NiO. A 40 μm thick layer of LSM ($La_{1-x}Sr_xMnO_{3-\delta}$) functions as the cathode.

The cells are placed in a ceramic holder with fuel and air manifolding. A 0.5 mm platinum mesh serves as a current collector on both anode and cathode side. A 0.54 mm ceramic seal is placed at the anode side, and a 0.5 mm thermiculite (mica) frame seals the cathode side. Weight is added on top of the ceramic holder to compress the mica seal and ensure gas tightness of the assembly, as well as proper electrode-current collector contact.

Dry gases are supplied from gas bottles and controlled with mass flow controllers (Bronkhorst EL-FLOW). Steam is mixed with the dry gases using a controlled evaporator mixer (Bronkhorst LiQUI-FLOW and CEM). The temperature is controlled with thermocouples located in the furnace heating coils and the ceramic cell holder, close to the centre of the cell. The furnace heating power is controlled through the temperature of the heating coils and adjusted to maintain a constant temperature of the ceramic cell holder for different gas composition, assuming that the cell temperature is approximately the same.

5.3.2. CATALYST REDUCTION, GAS ANALYSIS AND STABILITY

The nickel catalyst is reduced by increasing the hydrogen concentration in the feed gas from 2 to 100 vol% over a period of 4 h at a temperature of 950°C. This procedure was developed and used in previous experiments on the same type of cells [261, 263]. The current-voltage characteristics are then determined to verify that the cell is reduced successfully.

A gas chromatograph (Agilent 490 micro gas chromatograph) is used to analyse the dried anode outlet gas composition. The anode off-gas is passed through a water bubbling condenser to remove steam, and further dried in a silica gel bed to prevent moisture from entering the gas chromatograph. The mole fractions of hydrogen, methane, carbon monoxide and nitrogen are analysed using a Molsieve 5A column, while the concentration of carbon dioxide in the dry gas is determined with the aid of a PoraPLOT U column. An external method, calibrated using gas bottles with known compositions, is used to calculate the gas concentrations in the sampled dry anode gas.

The methane conversion in the experiment is calculated from a carbon balance, assuming that methane is converted to CO and CO_2 only

$$x_{CH_4} = \frac{n^{in}_{CH_4} - n^{out}_{CH_4}}{n^{in}_{CH_4}} = \frac{y_{CO} + y_{CO_2}}{y_{CO} + y_{CO_2} + y_{CH_4}}, \tag{5.1}$$

where y_i is the molar fraction of species i. It was shown in previous work that reforming on the current collector can be neglected for temperatures below 800°C, hence all reforming can be assumed to take place on the SOFC anode [261].

Figure 5.2a shows an example of the dry composition obtained from gas analysis over time, compared to the dry composition calculated from the carbon balance in Equation (6.2), assuming that the WGS reaction is in chemical equilibrium. This result confirms the gas analysis is accurate for the compositions of interest, since the calculated nitrogen and hydrogen mole fractions match well with the values determined with gas chromatography.

Additional tests are carried out to verify the stability and reproducibility of the experimental results. Figure 5.2b shows that the reforming rate stabilises within 24 hours after switching from dry hydrogen to a mixture containing methane and steam. The reforming rate is found to be stable few hours after changing the experimental temperature, and within an hour after the gas composition is changed.

5.3.3. REFORMING EXPERIMENTS

The conditions for the reforming experiments are chosen such that:

- The temperatures and gas compositions are representative for SOFC operating conditions;
- The conditions differ sufficiently from each other to identify significant dependencies from the results;
- The influences of the methane, steam and hydrogen partial pressure and temperature can be determined independent from each other.

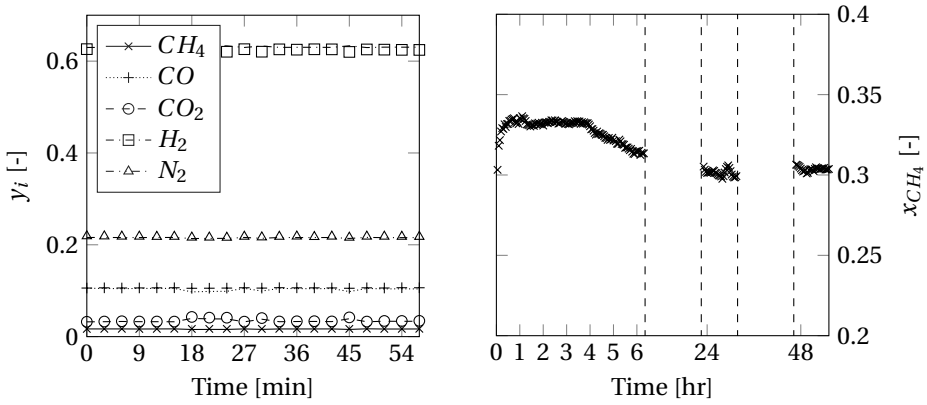

(a) Measured and calculated gas composition. (b) Stabilisation of methane conversion.

Figure 5.2: Measured dry gas composition (symbols) compared to the calculated with Equation (6.2) (lines) (Figure 5.2a) and stabilisation of the methane conversion at 700°C after switching from dry hydrogen to methane (Figure 5.2b).

5

As such, the gas composition and temperature are varied within a relevant range, but do not represent specific SOFC operating points. The methane mole fraction and total flow rates are chosen such that the experimental methane conversions are always well below chemical equilibrium, to ensure that the reforming rate is limited by the kinetics of the reforming reaction. A flow of 2 Nl min^{-1} simulated air with 80 vol% nitrogen and 20 vol% oxygen is supplied at the cathode.

Various fuel compositions with methane, steam and hydrogen are supplied to the anode, and nitrogen is added to maintain a constant total volume flow rate of 2 Nl min^{-1}. The SC ratio is varied from 1.5 to 3, which is a common range used to prevent carbon deposition. The SH ratio is varied from 1 to 18, representing the varying hydrogen and steam concentrations from inlet to outlet. Table 5.1 provides an overview of the experimental gas compositions.

The experiments are carried out at cell temperatures of 700, 725, 750 and 775°C, as these are close to the temperature typically encountered at the entrance region of a SOFC stack. No current was drawn from the cell during the reforming experiments, although current-voltage characteristics were occasionally determined to verify that the cell was still functioning.

The experiments were conducted over a consecutive period of twelve days, or about 280 hours, with the cell continuously operating under internal reforming conditions. The reforming rate was stabilised for at least two hours after changing the gas composition, and over night after changing the temperature. The SOFC performance was stable over this period as well as in the 14 days prior to the experiment, during which initial tests were conducted to determine appropriate gas compositions, flows and stabilisation times.

Table 5.1: Experimental anode inlet gas compositions and the SC and SH ratios.

	y [-]					
Composition	CH_4	H_2O	H_2	N_2	SC	SH
A	0.18	0.36	0.36	0.1	2	1
B	0.18	0.36	0.18	0.28	2	2
C	0.18	0.36	0.12	0.34	2	3
D	0.18	0.36	0.04	0.42	2	9
E	0.2	0.36	0.04	0.4	1.8	9
F	0.22	0.36	0.04	0.38	1.64	9
G	0.24	0.36	0.04	0.36	1.5	9
H	0.24	0.48	0.04	0.24	2	12
I	0.24	0.6	0.04	0.12	2.5	15
J	0.24	0.72	0.04	0	3	18

Total flow = 2 Nl min^{-1}, T = 700, 725, 750 and 775°C

5.3.4. CARBON DEPOSITION

Solid carbon formation can deteriorate the anode by blocking pores and reactions sides. Therefore, carbon deposition should be avoided during normal SOFC operation. Carbon deposition might occur via the methane cracking, Boudouard and reverse gasification reactions:

$$CH_4 \rightleftharpoons C(s) + 2H_2 \tag{5.2}$$

$$2CO \rightleftharpoons C(s) + CO_2 \tag{5.3}$$

$$H_2 + CO \rightleftharpoons C(s) + H_2O \tag{5.4}$$

Cerium oxide possesses improved resistance against carbon depositing due to its oxygen storage capacity. Therefore, solid carbon deposited on the catalyst suface may be removed by a reaction with lattice oxygen:

$$nC(s) + CeO_2 \rightleftharpoons nCO + CeO_{2-n} \tag{5.5}$$

Whether carbon deposition is thermodynamically favourable depends on the gas composition, temperature, pressure and type of carbon formed, and can be determined from equilibrium calculations. Figure 5.3a indicates C-H-O compositions for which carbon formation is thermodynamically expected in a ternary diagram at a temperature of 700°C, assuming that the carbon type formed is graphite. The experimental gas compositions from Table 5.1 are indicated in Figure 5.3a as well, revealing that the formation of this type of carbon is thermodynamically not expected.

Although graphite formation is thermodynamically not expected, it may still occur if the speed of individual carbon deposition reactions is higher than the removal reactions [304]. In addition, other types of carbon with different thermodynamic properties, such carbon nano fibres, may form on the anode. To ensure that the cell is not degraded by carbon deposition, the cell is cooled down after the experiment in inert gases (nitrogen) and analysed with scanning electron microscopy (SEM) and energy dispersive X-ray

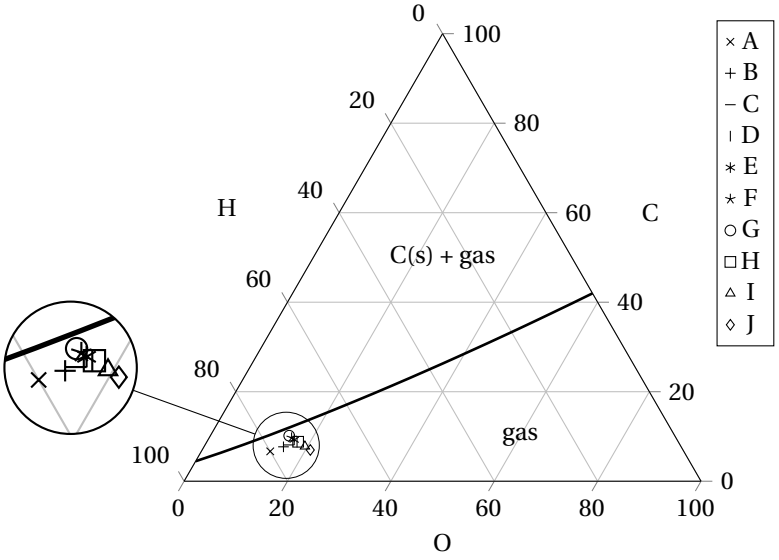

(a) Ternary diagram for a C-H-O mixture.

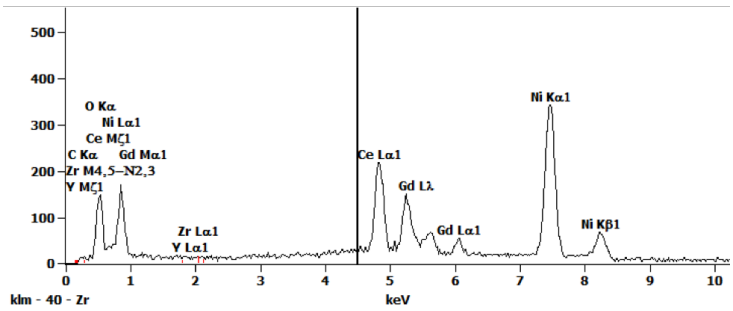

(b) EDX analysis after experiment.

Figure 5.3: Ternary diagram for solid carbon formation (Figure 5.3a) and the result of an EDX analysis showing no carbon peak at 0.277 keV (Figure 5.3b).

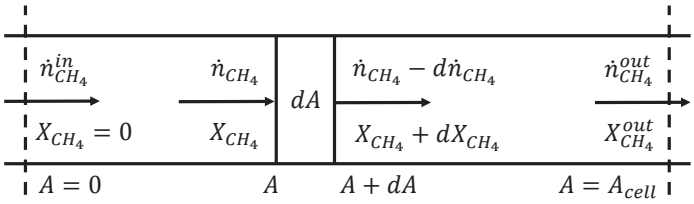

Figure 5.4: Schematic overview of the IPFR reactor model (Figure 5.4).

spectroscopy (EDX). The EDX analysis in Figure 5.3b shows the expected peaks for nickel, cerium, and gadolinium, but not for carbon, which would be expected at 0.227 keV.

5.4. KINETIC MODEL REGRESSION

The experimental methane conversions are used to parameterise different rate equations for the MSR reaction using an ideal plug flow reactor (IPFR) model, developed for this purpose. The following sections provide details on the assumption in the IPFR model, the kinetic models parameterised and the regression method employed.

5.4.1. IDEAL PLUG FLOW REACTOR MODEL

The IPFR model assumes that the reacting flow passes through a catalyst bed while it is ideally mixed in the radial direction, but axial diffusion or mixing does not take place. In that case, the reaction rate for an infinitely small reactor area is given by

$$-r_{MSR} = \frac{d(\dot{n}_{CH_4})}{dA} = \frac{d(\dot{n}^{in}_{CH_4}(1-x_{CH_4}))}{dA} = -\dot{n}^{in}_{CH_4}\frac{d(x_{CH_4})}{dA}, \tag{5.6}$$

where r_{MSR} is the area specific reforming rate, $\dot{n}_{CH_4}$ is the molar flow of methane and A is the active cell area. The total active cell area then follows from:

$$A = \dot{n}^{in}_{CH_4}\int_0^{x^{out}_{CH_4}} \frac{dx_{CH_4}}{r_{MSR}} \tag{5.7}$$

A schematic overview is shown in Figure 5.4. Since the active cell area is known, this equation can be used to regress parameters in an expression for the reaction rate r_{MSR}, provided that it is a function of methane conversion x_{CH_4}. Reaction rates of gasses are generally written as a function of the partial pressures of reactants and products, as these can be assumed to be proportional to the activity for ideal gasses. Therefore, the partial pressures of the gasses are written as function of the methane conversion rate. The partial pressures in the gas mixture follow from:

$$p_{CH_4} = f(1-x_{CH_4}) \tag{5.8}$$

$$p_{H_2O} = f(SC - x_{CH_4} - x_{CO}) \tag{5.9}$$

$$p_{H_2} = f\,(HC + 3x_{CH_4} + x_{CO}) \tag{5.10}$$

$$p_{CO} = f\,(x_{CH_4} - x_{CO}) \tag{5.11}$$

$$p_{CO_2} = f\,x_{CO} \tag{5.12}$$

Here, SC and HC are the steam- and hydrogen-to-carbon ratio respectively and x_{CO} is the fraction of carbon monoxide that is converted to carbon dioxide by the WGS reaction. The factor f corrects for the total experimental pressure and the increase in the total flow as a result of the MSR reaction

$$f = p\left(\frac{\sum_i \dot{n}_i^{in}}{\dot{n}_{CH_4}^{in}} + 2\,x_{CH_4}\right)^{-1}, \tag{5.13}$$

where p is the total pressure in the experiment. The WGS reaction can be assumed to be in chemical equilibrium along the reactor, as it generally proceeds much faster than the MSR reaction [48]. The equilibrium can be calculated using the van 't Hoff relation, Equation (4.7).

Equations (4.3), (4.4) and (5.9) to (5.12) can be subsequently solved to obtain an expression for x_{CO} as a function of SC, HC, K_{WGS} and x_{CH_4}. In this way, expressions are derived for the partial pressures in the reacting gas mix as a function of the experimental conditions and x_{CH_4}. The active cell area can now be calculated as a function of the experimental conditions and rate expression using Equation (5.7). Since the active cell area is known and constant, this is used to regress parameters in kinetic models.

5.4.2. KINETIC MODELS

The objective of this study is to identify the rate determining kinetics of the MSR reaction on Ni-GDC anodes, which may be captured by a classical surface reaction model, such as LH or HW kinetics, or a global model, for example PL or FO kinetics. In addition, global kinetics can be helpful to get estimates of the partial pressure and temperature dependency of more complex kinetics. The PL, FO, LH and HW kinetics are described in this section.

POWER LAW AND FIRST ORDER KINETICS

PL expressions provide a convenient means to describe the dependency of the rate of a chemical reaction without knowledge of the complex surface chemistry involved. Since the partial pressures of methane, steam and hydrogen were varied in the experiment, the PL equation takes the form

$$r_{MSR} = k\,p_{CH_4}^{\alpha}\,p_{H_2O}^{\beta}\,p_{H_2}^{\gamma}\left(1 - \frac{Q_{MSR}}{K_{MSR}}\right), \tag{5.14}$$

where the quotient of the reaction quotient Q_{MSR} and the equilibrium constant for the MSR reaction K_{MSR} determines the deviation from chemical equilibrium and, hence, the driving force of the reaction

$$\text{(driving force)} = \left(1 - \frac{Q_{MSR}}{K_{MSR}}\right) = 1 - \frac{1}{K_{MSR}}\,\frac{\alpha_{CO}\,\alpha_{H_2}^3}{\alpha_{CH_4}\,\alpha_{H_2O}}, \tag{5.15}$$

where the activity α_i of species i is calculated according to Equation (4.5).

The values reported in literature for the reaction orders α, β and γ vary. Although the reaction order for methane is commonly reported to be around unity, reaction orders for steam vary from -2 to 2 in literature. The influence of the hydrogen partial pressure is rarely reported, probably because it is a product and not a reactant of the MSR reaction and, therefore, is assumed to have no influence on the reaction rate. An Arrhenius temperature dependency is usually assumed for the rate constant k:

$$k = k_0\, exp\Big(-\frac{E_a}{\bar{R}T}\Big) \tag{5.16}$$

The FO expression is essentially similar to the PL equation, but assumes that the reaction is first order in methane and independent of the partial pressures of other reactants and products. FO kinetics have, for example, been reported by Achenbach and Riensche [299] for SOFC cermet anodes. Although FO kinetics may appear somewhat crude, the reaction orders reported with regard to methane are indeed often close to unity. In addition, parameterising a FO reaction model is relatively straightforward, as only the temperature dependent reaction constant has to be determined experimentally.

5

LANGMUIR-HINSHELWOOD KINETICS

LH kinetics are commonly used to describe the surface chemistry involved in catalysed reactions. The fractional surface coverage of reactants and products is described by Langmuir isotherms. Generally, surface reaction models take the form

$$r = \frac{\text{(kinetic factor)}}{\text{(adsorption isotherm)}}\,\text{(driving force)}, \tag{5.17}$$

where the kinetic factor describes the dependency of the rate determining step on the gas species involved, the adsorption isotherm accounts for the available active reaction sites and the driving force similar as introduced in the Power-Law rate equation.

LH kinetics assume that a bimolecular reaction between two reactants adsorbed on neighbouring sites is rate determining, and adsorption is described by Langmuir isotherms, leading to:

$$r_{MSR} = \frac{k\,\bar{K}_{CH_4}\,\bar{K}_{H_2O}\,p_{CH_4}^{\alpha}\,p_{H_2O}^{\beta}}{(1+\bar{K}_{CH_4}\,p_{CH_4}^{\alpha}+\bar{K}_{H_2O}\,p_{H_2O}^{\beta})^{\gamma}}\Big(1-\frac{Q_{MSR}}{K_{MSR}}\Big) \tag{5.18}$$

Here, $\bar{K}_i$ is the adsorption constant of species i. The values of α and β depend on the specific adsorption mechanism on the catalyst surface, i.e. the number of unoccupied reaction sites required for adsorption, and γ is the number of active reaction sites involved in the rate determining step. Adsorption groups in Equation (5.18) may be neglected if their adsorption is limited. The adsorption enthalpies and entropies follow from the van 't Hoff relation. Hence, the temperature dependence of the Langmuir adsorption constants follows from:

$$\bar{K}_i = \bar{A}_i\, exp\Big(-\frac{\Delta\bar{H}_i}{\bar{R}T}\Big) \tag{5.19}$$

Thermodynamic consistency requires that $\bar{A} > 0$ and $\Delta\bar{H} < 0$, such that the adsorption constant $\bar{K}$ is positive and decreases with temperature.

HOUGEN-WATSON KINETICS

The classical LH equation was extended by Hougen and Watson for complex surface reactions. The possible rate determining step is not limited to reactions on the catalyst surface, but may originate from adsorption, formation and desorption of reactants, products and reaction intermediates. The adsorption isotherm may contain reaction intermediates and products as well.

HW kinetics have been reported both for MSR on industrial catalysts, for example be Xu et al. [129] and Hou et al. [289], and SOFC anodes by Dicks et al. [296] and Thattai et al. [261]. In these studies rate expressions are reported of the form

$$r_{MSR} = \frac{k\, p_{CH_4}\, p_{H_2O}^{\alpha} / p_{H_2}^{\beta}}{(1 + \cdots + \bar{K}_{H_2O} \frac{p_{H_2O}}{p_{H_2}})^{\gamma}} \left(1 - \frac{Q_{MSR}}{K_{MSR}}\right), \tag{5.20}$$

and, interestingly, the adsorption of oxygen as a surface intermediate, described by the adsorption group $\bar{K}_{H_2O} \frac{p_{H_2O}}{p_{H_2}}$, is reported by all. Values of 0 to 1 are reported for β, while the value of γ may be as high as 2.5. Adsorption effects from carbon monoxide and hydrogen are commonly reported as well.

5

PARAMETER REGRESSION

The kinetic models introduced in Section 5.4.2 are parameterised and evaluated using the IPFR model described in Section 5.4.1. The algorithm uses Equation (5.7), which calculates the known active area A, to parameterise different kinetic models. The regression of PL kinetics does not require such an elaborate approach, as all parameters are functions of different independent variables: the reaction orders are determined by different reactant and product partial pressures, and the activation energy by the temperature dependence. LH and HW kinetics, however, contain several temperature dependent constants. Therefore, all constants are functions of the temperature and regression is aided by a more accurate initial guess. The algorithm comprises three consecutive steps to efficiently regress the non-linear set of equations:

- Minimisation of the coefficient of variation of A for each individual experimental temperature to obtain initial guesses of rate constants, reaction orders and adsorption constants for the next step;
- Minimisation of the coefficient of variation of A including the logarithmic temperature dependence of rate and adsorption constants to obtain an initial guess for the final step;
- Minimisation of $|1 - R^2|$ for the entire data set. Equation (5.7) is solved for $x_{CH_4}^{out}$ with the known active area A for this purpose to predict overall methane reforming rates with the IPFR model for the kinetics of interest.

The Nelder-Mead simplex algorithm is employed in each subsequent minimisation step. A schematic overview of this procedure is shown in Figure 5.5.

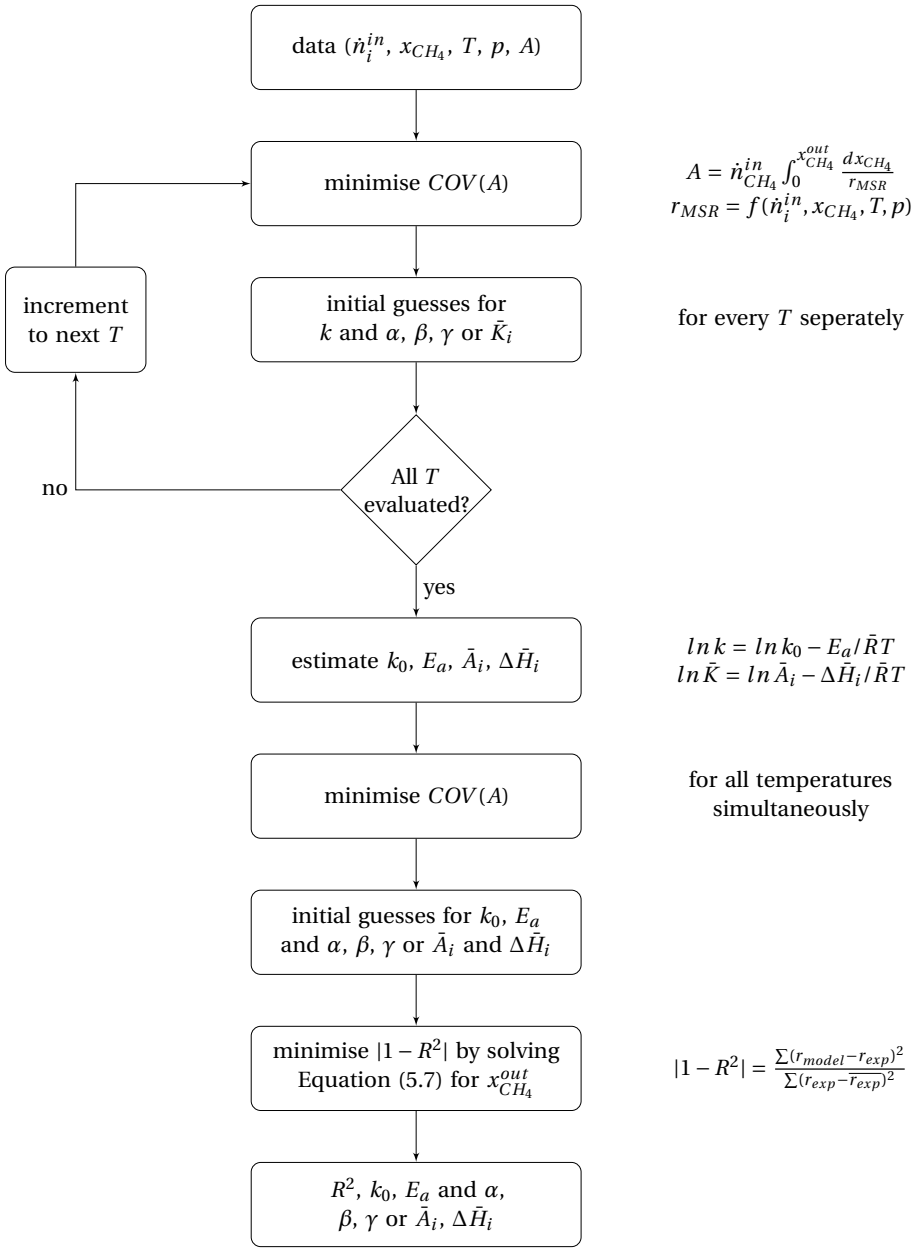

Figure 5.5: A flowchart of the procedure used to regress the kinetic model parameters (Figure 5.5).

5.4.3. THERMODYNAMIC CONSISTENCY

The Langmuir adsorption constant in Langmuir-Hinshelwood and Hougen-Watson models should be thermodynamically consistent and, therefore, meet three thermodynamic rules and two guidelines [293, 294]:

- **Rule 1**: Adsorption is an exothermic process. Therefore, the enthalpy of adsorption should be negative: $\Delta\bar{H}^0 < 0$.
- **Rule 2 & 3**: The entropy should decrease after adsorption, thus $\Delta\bar{S}^0 < 0$ (rule 2). Moreover, a molecule can only lose the entropy it possessed prior to adsorption. Hence, $-\Delta\bar{S}^0 < s_g^0$. Together, these rules lead to $0 < -\Delta\bar{S}^0 < s_g^0$.
- **Guideline 1 & 2**: Two guidelines have been proposed to further assess the plausibility of the adsorption constants. Combined these empirical relations yield $10 \leq -\Delta\bar{S}^0 \leq 12.2 - 0.0014\,\Delta\bar{H}^0$, with the units of energy in cal mol^{-1}. Converted to J mol^{-1} this gives $41.84 \leq -\Delta\bar{S}^0 \leq 51.04 - 0.0014\,\Delta\bar{H}^0$.

These rules and guidelines are evaluated using the van 't Hoff equation

$$ln(\bar{K}) = -\frac{\Delta\bar{G}^0}{\bar{R}T} = -\frac{\Delta\bar{H}^0}{\bar{R}T} + \frac{\Delta\bar{S}^0}{\bar{R}}, \tag{5.21}$$

and the entropy of adsorption is thus calculated from the adsorption constants:

$$\Delta\bar{S}^0 = ln(\bar{A}) \cdot \bar{R} \tag{5.22}$$

It is evident from Equation (5.21) that the value of $\Delta\bar{S}^0$ depends on the units of the pre-exponential factor $\bar{A}$, which is important to obtain meaningful results [293, 294]. The enthalpy and entropy values should be taken at the reference state, which is usually the atmospheric pressure. This is the case for tabulated gas phase entropy values and the constants in the empirical guidelines as well. Therefore, the pressure units in $\bar{A}$, if any, should be either taken in atm, or the gas phase entropies and empirical constants have to be converted to consistent units.

5.5. RESULTS

5.5.1. EXPERIMENTS

The experimental data obtained in the experiment is shown in Table 5.2 and Figure 5.6. Figure 5.6a shows that a higher methane partial pressure results in a higher reforming rate, which is consistent with previous findings. Figure 5.6b reveals a slight decrease in the MSR rate for higher steam partial pressures, which seems to be more pronounced for lower temperatures and reforming rates. Finally, Figure 5.6c shows the influence of the hydrogen partial pressure on the overall reaction rate. Although a slight increment in the reforming rate is apparent for higher hydrogen partial pressures is apparent.

The experimentally observed influences of the methane and steam partial pressures on the reforming rate agree with the trends reported in earlier work on Ni-GDC anodes [261, 263]: A non-proportional but strong influence of the methane partial pressure

Table 5.2: Experimental methane conversion fraction x_{CH_4} for the evaluated gas compositions and temperatures.

	Composition									
T (°C)	A	B	C	D	E	F	G	H	I	J
700	0.304	0.304	0.305	0.296	0.272	0.267	0.260	0.256	0.252	0.248
725	0.443	0.435	0.437	0.432	0.432	0.417	0.409	0.402	0.389	0.373
750	0.627	0.629	0.625	0.623	0.617	0.610	0.602	0.599	0.597	0.591
775	0.794	0.787	0.786	0.784	0.772	0.764	0.755	0.762	0.765	0.752

and a slight but significant effect of higher steam partial pressures. A negative effect of a higher steam partial pressure on the reaction rate may be explained by competitive adsorption of steam or a related reaction intermediate on the catalyst surface, which limits available reaction sites. Such an effect has been reported in many experimental investigations [261–263, 295, 296, 305].

Denominators in HW kinetics often contain an adsorption group consistent with dissociative adsorption of steam into gaseous hydrogen and surface-adsorbed oxygen:

$$\bar{K}_{H_2O}\frac{p_{H_2O}}{p_{H_2}} \tag{5.23}$$

A positive effect of hydrogen is thus expected for conditions where steam is reported to have a negative influence, although this may be counteracted by a negative contribution of the hydrogen partial pressure in the kinetic factor, as proposed by Xu et al. [129]. In that case a strong non-monotonic dependency on the hydrogen partial pressure is expected, but no such effect is observed for the experimental SH ratios ranging from 1 to 18.

5.5.2. PARAMETER REGRESSION

Two global reaction mechanisms have been fitted to the experimental data: The first one first order in methane and, hence referred to as FO, and the second one of the PL type with reaction orders for the experimentally evaluated species, i.e. methane, steam and hydrogen respectively. In addition, various forms of the LH and HW kinetics have been evaluated. Especially the HW model enables many possible rate equations, as the rate determining kinetics may be governed by an adsorption or desorption step, and the adsorption group can include any reactant, product or reaction mechanism. However, any feasible reaction mechanism should:

- Provide a sound qualitative explanation for the experimental observations;
- Give a high quality fit with the experimental data, i.e. R^2 close to 1;
- Be thermodynamically consistent.

The majority of the evaluated possible kinetic expressions could be rejected as they did fail to satisfy at least one of the criteria listed above. Two models were selected as they

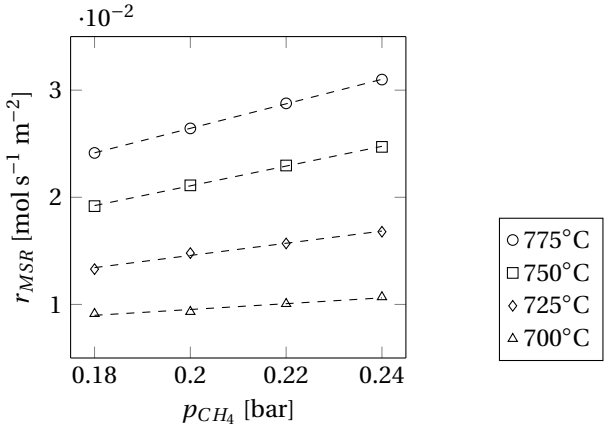

(a) Methane partial pressure
(p_{H_2O} = 0.36 bar, p_{H_2} = 0.04 bar).

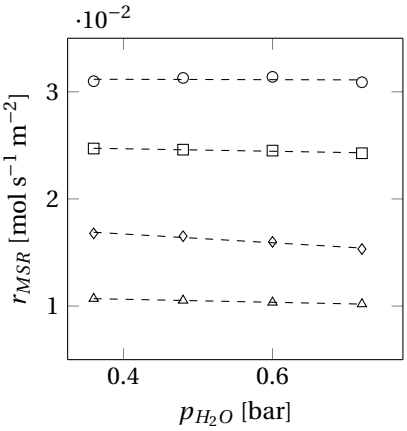

(b) Steam partial pressure
(p_{CH_4} = 0.24 bar, p_{H_2} = 0.04 bar).

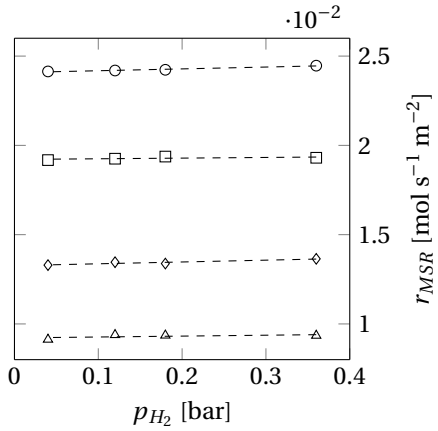

(c) Hydrogen partial pressure
(p_{CH_4} = 0.18 bar, p_{H_2O} = 0.36 bar).

Figure 5.6: Experimentally observed MSR reaction rates for the evaluated temperatures and different partial pressures of methane (Figure 5.6a), steam (Figure 5.6b) and hydrogen (Figure 5.6c).

performed equally well against the listed criteria: One with the classical LH formulation and the other of the HW type. Table 5.3 provides an overview of the equations obtained and the regressed parameters. In addition, Figure 5.7 shows the overall reforming rates predicted by the models in Table 5.3 for different gas compositions and temperatures compared to the experimental values.

FIRST ORDER KINETICS

The FO model is by far the most straightforward of the four models presented and only requires determination of a temperature dependent rate constant. Nonetheless, the

Table 5.3: Overview of the rate equations and parameters obtained through regression of the experimental data.

$$r_{MSR} = k\, p_{CH_4}^{\alpha}\, p_{H_2O}^{\beta}\, p_{H_2}^{\gamma} \left(1 - \frac{Q_{MSR}}{K_{MSR}}\right)$$

Parameter	α [-]	β [-]	γ [-]	k_0 [mol s^{-1} m^{-2} bar$^{-\alpha-\beta-\gamma}$]	E_a [J mol^{-1}]	R^2
FO	1	-	-	9.472e8	190.5e3	0.9930
PL	0.8954	-0.0619	0.0693	9.799e7	173.1e3	0.9965

$$r_{MSR} = \frac{k \tilde{K}_{CH_4} \tilde{K}_{H_2O}\, p_{CH_4} \sqrt{p_{H_2O}}}{(1 + \tilde{K}_{CH_4}\, p_{CH_4} + \tilde{K}_{H_2O} \sqrt{p_{H_2O}})^2} \left(1 - \frac{Q_{MSR}}{K_{MSR}}\right)$$

Parameter	$\bar{A}_{CH_4}$ [bar^{-1}]	$\Delta\bar{H}_{CH_4}$ [J mol^{-1}]	$\bar{A}_{H_2O}$ [bar$^{-0.5}$]	$\Delta\bar{H}_{H_2O}$ [J mol^{-1}]	k_0 [mol s^{-1} m^{-2}]	E_a [J mol^{-1}]	R^2
LH	4.2e-3	-54.76e3	1.9e-3	-62.17e3	1.467e10	207.6e3	0.9980

$$r_{MSR} = \frac{k\, p_{CH_4}}{(1 + \tilde{K}_{CH_4}\, p_{CH_4} + \tilde{K}_{H_2O} \frac{p_{H_2O}}{p_{H_2}})^2} \left(1 - \frac{Q_{MSR}}{K_{MSR}}\right)$$

Parameter	$\bar{A}_{CH_4}$ [bar^{-1}]	$\Delta\bar{H}_{CH_4}$ [J mol^{-1}]	$\bar{A}_{H_2O}$ [-]	$\Delta\bar{H}_{H_2O}$ [J mol^{-1}]	k_0 [mol s^{-1} m^{-2} bar^{-1}]	E_a [J mol^{-1}]	R^2
HW	2.8e-3	-48.33e3	6.78e-5	-45.45e3	2.787e7	158.5e3	0.9981

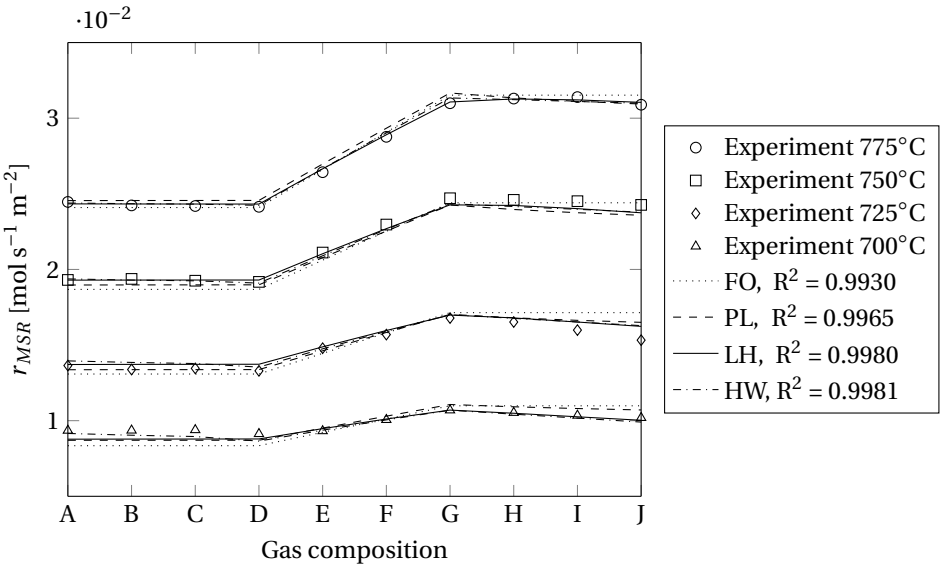

Figure 5.7: Experimentally observed overall MSR rates and rates predicted in the IPFR model with the parameterised rate equations.

FO model describes the experimental results with reasonable accuracy, although the activation energy of 190.5 kJ mol^{-1} is higher than what is commonly reported. With the exception of Belyaev et al. [298], who reported a value of 162 kJ mol^{-1} for a first order in methane reaction model, most authors report values ranging from 80 to 100 kJ mol^{-1}.

It is evident from Figure 5.7 that the FO model predicts the influences of the methane partial pressure with reasonable accuracy, although the effect of methane seems to be overestimated for lower temperatures. As expected, the FO model does not predict a change in the overall reforming rate for higher hydrogen and steam partial pressures. This results in an overestimation of the reforming rate, especially for high steam partial pressures and low temperatures.

POWER LAW KINETICS

The PL model has three degrees of freedom more than the FO model, with reaction orders for methane, steam and hydrogen fitted to the experimental data. Therefore, the PL model describes the rate increasing and decreasing effects of the hydrogen and steam partial pressures respectively and the fit to the experimental data is improved. With 173.1 kJ mol^{-1} the activation energy is lower than for the FO model, but still higher than commonly reported.

The prediction of the reforming rates is particularly improved for higher steam partial pressures, since the decreasing effect of steam is now described correctly. In addition, the influence of the methane partial pressure is captured more accurately. Despite a slightly positive reaction order γ, an increase in the hydrogen partial pressure does not seem to result in a substantial increase in the reforming rate.

Table 5.4: Values of the adsorption enthalpies and entropies at the reference state for methane and steam in the LH and HW kinetics, and evaluation of their thermodynamic consistency.

Model	Species	$\Delta\bar{H}^0$ [J mol^{-1}]	$\Delta\bar{S}^0$ [J mol^{-1} K^{-1}]	$0 < -\Delta\bar{S}^0 < s_g^0$	$41.84 \leq -\Delta\bar{S}^0 \leq 51.04 - 0.0014\,\Delta\bar{H}^0$
LH	CH_4	-62.17e3	-52.09	$0 < 52.09 < 188.8$	$41.84 \leq 52.09 \leq 138.1$
	H_2O	-62.17e3	-45.5	$0 < 45.5 < 186.1$	$41.84 \leq 45.5 \leq 127.7$
HW	CH_4	-48.33e3	-48.87	$0 < 48.33 < 188.8$	$41.84 \leq 48.33 \leq 118.7$
	H_2O	-45.45e3	-79.81	$0 < 79.81 < 186.1$	$41.84 \leq 79.81 \leq 114.7$

LANGMUIR-HINSHELWOOD KINETICS

The LH model assumes a rate determining reaction between associatively adsorbed methane and dissociatively adsorbed steam on a single site. This mechanism is in good agreement with a methane reaction order somewhat below one in the PL model, due to competitive adsorption of methane at lower temperatures. In addition, the dissociative adsorption of steam seems in good agreement with the a decrease in the reaction rate for higher steam partial pressures, which is more pronounced at lower temperatures.

The Langmuir adsorption constants in both the LH and HW kinetics must obey the laws of thermodynamics, as discussed in Section 5.4.3. Table 5.4 shows the enthalpy and entropy of the fitted Langmuir adsorption constants for methane and steam in the LH and HW model. Table 5.4 shows that the enthalpies for both methane and steam are negative for the LH model, and both adsorption entropies satisfy the thermodynamic laws and guidelines as well. Therefore, the proposed LH mechanism is thermodynamically consistent.

Figure 5.7 shows that the effects of the methane and steam partial pressures on the overall reforming rate are correctly captured. The LH kinetics account for the temperature dependency of the reaction site inhibiting associative adsorption of methane and dissociative adsorption of steam. Therefore, the *apparent* reaction orders for methane and steam may change with temperature, which clearly improves the agreement with the experimental data compared to the FO and PL kinetics. However, the LH kinetics do not account for influences of the hydrogen partial pressure.

HOUGEN-WATSON KINETICS

The kinetic factor in the HW model is first order in methane, which indicates that associative methane adsorption on the catalyst could be the rate determining step. Kinetic factors based on surface reaction or desorption controlled rate limiting kinetics did not result in satisfactory fitting. Table 5.4 shows that the adsorption constants in the HW model are thermodynamically consistent. While the adsorption step in the LH model assumes dissociation into hydrogen and hydroxyl atoms

$$\bar{K}_{H_2O}\, p_{H_2O}\, \theta_s^2 = \theta_{OH}\, \theta_H, \tag{5.24}$$

with θ_i the surface coverage of species i and s indicating an unoccupied reaction site, the HW assumes dissociation into gaseous hydrogen and surface-adsorbed oxygen, yielding:

$$\bar{K}_{H_2O}\, p_{H_2O}\, \theta_s = p_{H_2}\, \theta_O \tag{5.25}$$

As a result, the surface coverage of oxygen will decrease for higher hydrogen partial pressures. Therefore, the dissociative adsorption group in the HW model depends on the steam-to-hydrogen ratio and not on the absolute steam partial pressure, and as such predicts an increased reforming rate for higher hydrogen partial pressures. This is in agreement with the reaction orders for steam and hydrogen in the PL model, being of equal magnitude and opposite sign.

Table 5.4 shows that the proposed HW mechanism is thermodynamically consistent, as the enthalpies for both methane and steam are negative and both adsorption entropies satisfy the thermodynamic laws and guidelines. Overall, the predictions of the reforming rate in Figure 5.7 by the HW model are comparable to the LH kinetics. The HW kinetics account for a slight positive effect of the hydrogen partial pressure on the reforming rate, but the deviation from the LH kinetics is only visible for the lowest temperatures. As a result, the R^2 value is only marginally improved.

5.6. DISCUSSION

5.6.1. MODEL COMPARISON

Figure 5.8 shows the spatial distribution of the MSR rate r_{msr} calculated with the plug flow reactor model for the different kinetic models, the four different experimental temperatures and gas composition D, the gas composition with average SC and SH ratios and minimal methane, steam and hydrogen partial pressures. All models resemble first order in methane behaviour for the highest temperatures and only deviate at the entrance region. This suggests that the MSR kinetics may be assumed to be first order in methane at temperatures ≥750°C. However, at lower temperatures the difference between FO and other kinetic models increases as adsorption effects become more important.

Figure 5.9 shows the reforming rates predicted with the different kinetic models at 725°C and four different gas compositions: A, with the lowest SH ratio, D, with average SH and SC ratio, G, with the lowest SC ratio and J with both the highest SC and SH ratio. The kinetic models predict similar spatial distributions for gas composition A, but the predictions start to deviate as either the SH or SC ratio changes. The SH ratio affects the PL and HW kinetics in particular, while the SC ratio is important for the LH model. As a result, the predictions vary substantially for composition J, which has the highest ratios if both SH and SC.

The FO and LH both predict a monotonically decreasing MSR rate along the cell length, but the rate is initially lower according to the LH kinetics and decreases less towards the outlet. FO kinetics seem to over predict MSR at the entrance of the cell and under predict the rate at the outlet of the cell for most conditions. Both the PL and HW kinetics include an effect of the hydrogen partial pressure, which results in non-monotonic behaviour of the reaction rate: The MSR initially increases due to a promoting effect of the hydrogen partial pressure, and eventually decreases again. This is particularly the case for the HW kinetics at low temperatures and high SH ratios.

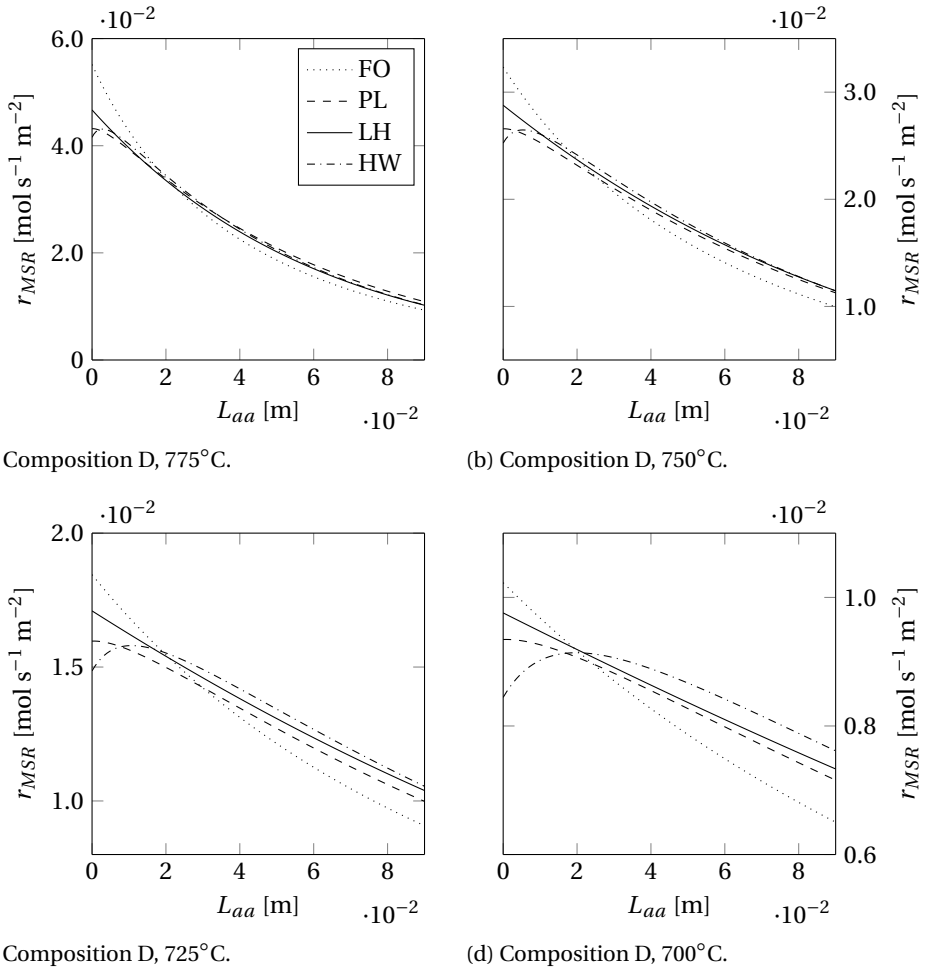

(a) Composition D, 775°C.

(b) Composition D, 750°C.

(c) Composition D, 725°C.

(d) Composition D, 700°C.

Figure 5.8: Local MSR rate from single cell inlet to outlet predicted with the four different kinetic models and the IPFR model for four different temperatures and gas composition D.

5.6.2. MODEL SELECTION

Global reaction kinetics can be derived from MSR data collected on complete cell assemblies with relative ease. However, they can only accurately calculate the local reforming rates and resulting thermal stresses if they capture the intrinsic rate determining step. Both the FO and PL model seem to over predict the MSR reaction rate for low temperatures and high steam partial pressures. Surface reaction mechanisms, such as LH or HW kinetics, yield a single rate equation with a limited number of model parameters, while they are intrinsically valid if the rate determining step is constant for the conditions of interest.

The LH and HW reaction mechanisms both show good agreement with the experimentally observed overall MSR rates, but there are reasons to argue that the LH model is

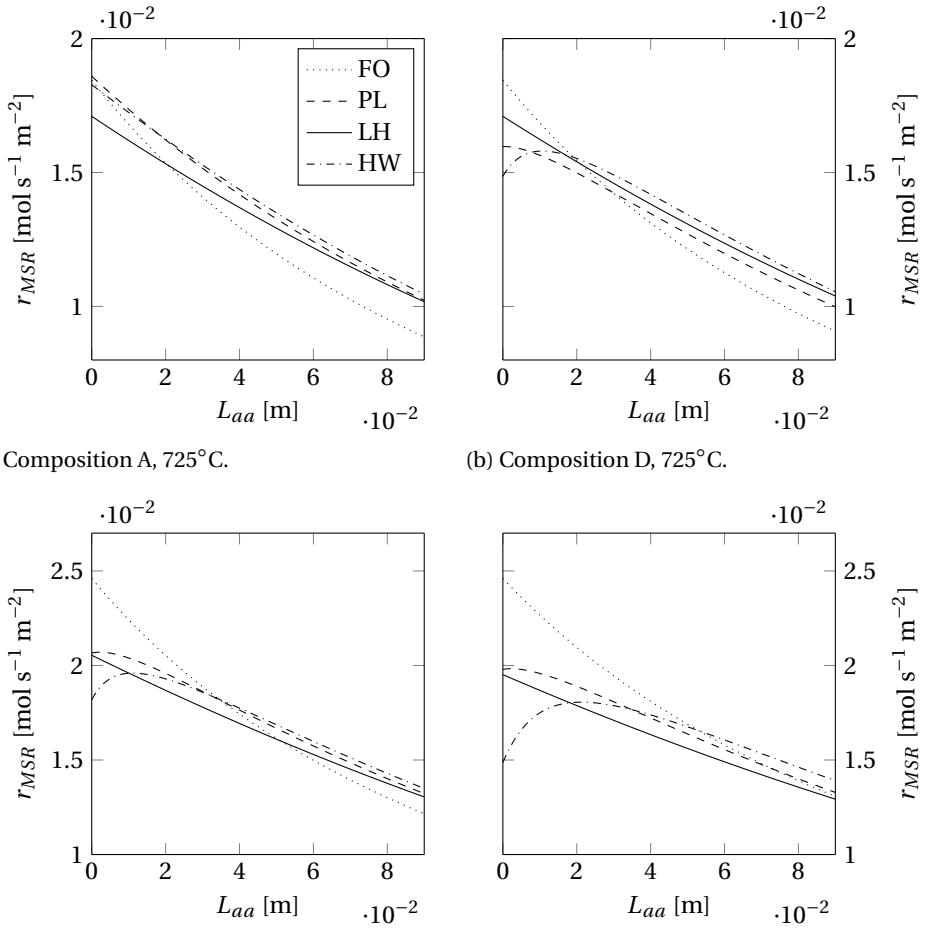

(a) Composition A, 725°C.

(b) Composition D, 725°C.

(c) Composition G, 725°C.

(d) Composition J, 725°C.

Figure 5.9: Local MSR rate from single cell inlet to outlet predicted with the four different kinetic models and the IPFR model for four different gas compositions at 725°C.

more sound than the HW mechanism. First of all, HW models can take many forms while the LH model is much more restricted. As such, there may always be a HW extension of a LH model which yields a better fit to the experimental data. However, the HW fit is not significantly better than the LH model, improving the R^2 value from 0.998 to 0.9981. The simplest model that provides a sound explanation for the experimental data is usually preferred.

Secondly, Figure 5.6c shows that the effect of hydrogen is modest, even though the hydrogen molar fraction was varied from 0.04 to 0.36. It cannot be ruled out that this effect originates from measurement inaccuracies or side effects. Ceria can catalyse the MSR reaction as well, and the hydrogen partial pressure will affect the oxidation state of GDC and may, therefore, enhance the catalytic activity [306]. In addition, the

thermal conductivity of hydrogen is higher than nitrogen. Therefore, replacing nitrogen by hydrogen will improve heat transfer towards the endothermic reaction sites and increase the local cell temperature.

Finally, methane adsorption is assumed to be the rate determining step in the HW model, but is included in the denominator as well. Effectively, this means that the rate limiting methane adsorption is inhibited by methane adsorbed on active sites for methane adsorption, which is physically unlikely. Although HW expressions without the methane adsorption group have been parameterised as well, these either yielded lower R^2 values than the LH model or were found to be thermodynamically inconsistent.

For all reasons listed above, the LH model is selected as the most plausible reaction mechanism on the investigated Ni-GDC anode. Since the model is based on an intrinsic rate determining surface reaction mechanism, it may be applied for conditions close to the experimental range with some confidence. Moreover, it is expected to give an accurate spatial distribution of the internal reforming rate from inlet to outlet to predict temperature gradients in SOFC stacks. Figure 5.10 illustrates the capability of the kinetic model to calculate the spatial distributions of the partial pressures from inlet to outlet for the reforming rates predicted with the LH model for four different temperatures and gas compositions.

5.6.3. FINAL CONSIDERATIONS

Fan et al [263] and Thattai et al. [261] reported MSR kinetics derived from experimental reforming data obtained on the same Ni-GDC anode cells. The strong but non-proportional dependence on the methane partial pressure and slight negative effect of the steam partial pressures were found in those studies as well. Although the activation energies were somewhat lower, the rate constants found for the three different data sets are within the same range, which gives confidence in the repeatability and applicability of the kinetics proposed in this study.

The HW kinetics proposed in previous work suggest that the hydrogen partial pressure may affect the MSR reaction rate [261]. This effect of hydrogen was based on kinetic models reported in literature and fitting adequacy, as it could explain the promoting effect of the electrochemical reaction. The influence of the hydrogen partial pressure on DIR was studied experimentally in this work. However, no evidence of a significant effect was found. Therefore, it is unlikely that the electrochemical reaction promotes the DIR rate by decreasing the hydrogen partial pressure.

Detailed information of temperatures and gas compositions along the cell would allow to discriminate between different kinetic models based on the temperature profile along the cell, since the distribution of the reaction rate predicted with the models is distinctively different (Figures 5.8 and 5.9). However, the current experimental setup does not allow to determine temperatures and gas compositions in situ, e.g. along the cell length. Therefore, work is commencing on a modification that should enable us to determine the temperature profile with non-intrusive techniques.

Although typical electrochemical degradation rates of commercial SOFCs are <1% per 1000 hours [307], the DIR experiments carried out in this work may induce cumulative damage to the cell. The reduction in the catalytic activity towards the DIR reaction is not

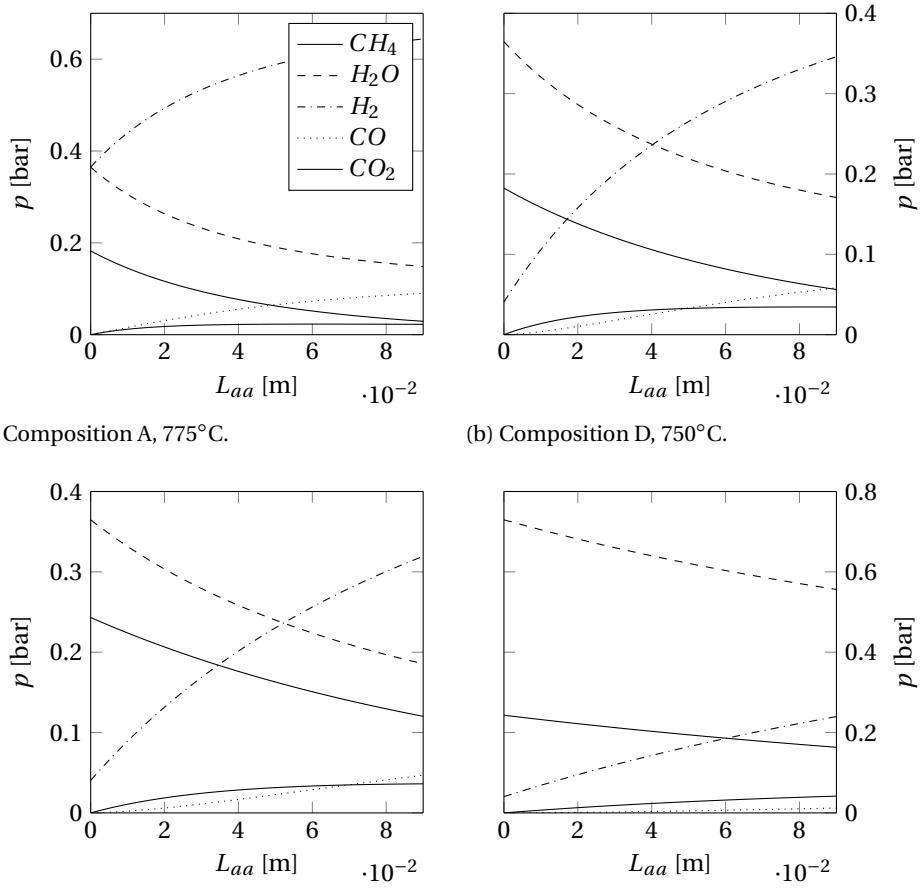

(a) Composition A, 775°C.

(b) Composition D, 750°C.

(c) Composition G, 725°C.

(d) Composition J, 700°C.

Figure 5.10: Predicted gas composition distribution from single cell inlet to outlet by the IPFR model and the LH kinetics for four different temperatures and four different gas compositions.

necessarily proportional to electrochemical degradation, since the degradation mechanism may be different. However, it cannot be ruled out that the reforming measurements are to some extend affected by enhanced cell degradation.

The SOFC performed stable during the experimental campaign, and no evidence for carbon deposition was found in an ex-situ analysis after the experiment. In addition, the open circuit voltage, tracked during the reforming experiments to monitor the stability of the cell, did not reveal enhanced degradation rates. Nonetheless, it is advised to quantify the both electrochemical degradation and the decrease in the MSR rate due to cell degradation in future experiments, both to ascertain that degradation did not affect the kinetic model fits and validate the degradation rates reported in literature.

5.7. CONCLUSIONS

An experimental investigation into the individual influences of the methane, steam and hydrogen partial pressures on the direct internal MSR reaction on a functional Ni-GDC cermet anode of a single electrolyte supported SOFC was presented. A strong but non-proportional dependence of the MSR rate on the methane partial pressure and a slight negative dependence on the steam partial pressure was found. This is in good agreement with previously reported data for similar single cells. Despite the evaluation of a wide range of hydrogen partial pressures no significant effect on the MSR was observed.

An IPFR model was used to regress kinetic parameter for rate equations of the PL, FO, LH and HW type. It was shown that all four kinetic models can predict the experimental overall reforming rates with reasonable accuracies. However, the global PL and FO kinetics were found to over predict the reforming kinetics for lower temperatures and higher steam partial pressures. Intrinsic LH and HW kinetics performed equally well, but a LH mechanism for associative adsorption of methane and dissociative adsorption of steam

$$r_{MSR} = \frac{k\,\bar{K}_{CH_4}\,\bar{K}_{H_2O}\,p_{CH_4}\,\sqrt{p_{H_2O}}}{(1+\bar{K}_{CH_4}\,p_{CH_4}+\bar{K}_{H_2O}\,\sqrt{p_{H_2O}})^2}\left(1-\frac{Q_{MSR}}{K_{MSR}}\right), \tag{5.26}$$

was selected because it showed good statistical agreement with the experimental data, provided a simple and physically sound explanation and was thermodynamically consistent. The kinetic model was shown to be in good agreement with results obtained in previous experiments on similar single cells with Ni-GDC anodes.

The LH kinetics can be implemented in the 1D dynamic model of a DIR SOFC with Ni-GDC anodes, developed in Chapter 4, to calculate the spatial distributions of species and temperature in the stack and predict its electrochemical performance. This will be used in the next chapter to compare different reforming concepts, based on either water or anode off-gas recirculation and either isothermal or adiabatic pre-reforming.

6

REFORMING CONCEPTS IN SOFC SYSTEMS

This chapter has been submitted to Applied Energy.

6.1. INTRODUCTION

It was concluded in Chapter 3 that off-design conditions and internal reforming in SOFCs require detailed modelling of the stack, for which a 1D dynamic model was developed in Chapter 4. Appropriate reforming kinetics are required to simulate DIR in the stack, which were subsequently derived in Chapter 5. In this chapter, these kinetics are implemented in the dynamic stack model to simulate different internal reforming concepts and off-design conditions, and analyse the implications on both stack and system level.

The cell voltages obtained from stack simulations are used in a thermodynamic system analysis, in analogy to Chapter 3, to calculate the efficiency of the investigated system concepts. In addition, the temperature gradients in the stack are reported as an indicator of the thermal stresses. Section 6.2 provides a background on reforming in SOFC systems, from which four concepts are selected and described in Section 6.3. Section 6.4 describes both the stack and system simulations. The results are subsequently presented in Section 6.5, and Section 6.6 presents the concluding findings.

6.2. REFORMING IN SOFC SYSTEMS

Although the fuel can be entirely reformed externally, the reforming reaction may proceed directly on the SOFC anode as well [35]. DIR improves heat integration in the system, since the heat and steam produced in the hydrogen oxidation reaction are directly used to reform the fuel. In addition, the endothermic reforming reaction reduces the cathode air flow required to cool the SOFCs, which limits the parasitic power consumption from the air blower [38].

DIR thus seems beneficial from a system integration perspective, but may compromise the electrochemical reactions and increase thermal stresses in the SOFC stack [250]. The endothermic steam reforming reaction typically occurs primarily at the entrance of the stack, where the methane partial pressure is high, while the exothermic hydrogen oxidation reaction will be most prominent at the hot outlet part of the stack. This reduces the temperature at the inlet of the stack, which in turn increases the temperature gradient and electrochemical losses [255].

The challenges introduced by DIR can be mitigated by partially pre-reforming the fuel. To drive the reforming reaction, heat and steam have to be supplied to an external pre-reformer. Rather than producing them externally, both heat and steam can be obtained from the exhaust gases of the SOFC to enhance the overall system efficiency. Two types of pre-reforming are commonly employed in SOFC systems:

- Adiabatic reforming, for which only the heat available in the reactive flow is used and the temperature reduces due to the endothermic reforming reaction;
- Allothermal reforming, in which a constant reformer temperature is maintained with heat supplied from an external source, for example from hot exhaust gases.

Similarly, steam is often supplied by either of the following two methods:

- Water recirculation (WR), where water is condensed from exhaust gas, evaporated and mixed with the fresh fuel;

Table 6.1: Overview of different reforming strategies, with heat and steam either provided directly by the electrochemical reaction (AOGR and adiabatic pre-reforming) or indirectly from the exhaust gases (WR and allothermal pre-reforming).

		Steam		
		exhaust	electrochemical	notes
Heat	exhaust	WR and allothermal reforming	AOGR and allothermal reforming	low u_{ox} complete combustion
	electrochemical	WR and adiabatic reforming	AOGR and adiabatic reforming	high u_{ox} uncombusted effluents
	notes	$u_{f,sp} = u_{f,gl}$ water trap, pump and evaporator	$u_{f,sp} < u_{f,gl}$ recirculation blower or ejector	

- Anode off-gas recirculation (AOGR), where a part of the anode outlet gas is recirculated and mixed with the fresh fuel.

Combining these options yields four different pre-reforming concepts in SOFC systems, shown in Table 6.1.

The anode and cathode outlet gases of the SOFC are usually mixed and passed through a catalytic burner, which generates steam and increases the temperature of the outlet gases further. The hot flue gas can be used to supply heat to both an allothermal pre-reformer and evaporator. Water can be subsequently condensed from the cooled exhaust gases, evaporated and mixed with the fresh fuel for WR [252, 308].

Although allothermal pre-reforming and WR offer a simple method to use hydrocarbon fuels in SOFC systems, a substantial amount of useful heat may be destroyed in the evaporator, pre-reformer and pre-heaters, which compromises heat available for consumers or thermal bottoming cycles [226]. Alternatively, the heated allothermal pre-reformer may be replaced by an adiabatic reformer, which reduces fuel conversion and heat demand. WR can be avoided by recirculating a part of the steam-containing anode outlet gas [252].

AOGR omits the need for a condenser and evaporator and may result in more homogenous conditions in the stack, but introduces additional challenges [253]. A sufficient amount of anode off-gas has to be recirculated to suppress carbon formation, which depend on the fuel gas composition, operating temperature and fuel utilisation in the

stack [254]. In addition, the recirculation blowers should withstand the high anode off-gas temperatures, and few available products are capable to do so reliably with acceptable lifetime [309].

Ejectors offer an alternative for high temperature AOGR in SOFCs, since they have no moving parts, but are more difficult to control [241]. Another option is low temperature AOGR, in which the hot effluents from the anode exhaust are cooled down, recirculated at low temperature, and heated up again [250, 252, 253]. Net electrical efficiencies of 60% LHV are projected for such a system developed by Powell et al. [250]. Moreover, the authors argue that the combination of adiabatic pre-reforming and low temperature AOGR used in their system reduces thermal quenching in the stack.

Peters et al. [252] evaluated the potential combined heat and power efficiency of several system layouts with AOGR thermodynamically. However, the reforming and electrochemical reactions in the SOFC are not modelled in detail, while different reforming concepts may be expected to affect the stack performance as well. Therefore, the implications of different reforming concepts on the efficiency, power density and thermal stresses of the stack are not considered.

The effect of different reforming concepts in SOFC systems on both stack and the system is analysed in this chapter. Methane is used as a model fuel, but the results are relevant for other organic compounds as well, since methane is a commonly present in reformates of those fuels [290, 291]. Stack operation is simulated with a 1D DIR SOFC model and methane steam reforming (MSR) kinetics, developed in Chapters 4 and 5. System models of the investigated reforming concepts are developed in an in-house developed flow sheet program, in analogy to Chapter 3.

The stack simulations are used to obtain the electrochemical characteristics of the SOFC for different system configurations and operating conditions, such as temperatures, fuel compositions and fuel utilisations. In addition, the temperature gradients are reported as they are an indicator for the thermal stresses in the stack, which affect the lifetime of the SOFC. The current-voltage characteristics are then used in system models to calculate the efficiency of the investigated system concepts for various fuel utilisations, nominal operating conditions and either a constant stack power or maximum stack efficiency.

6.3. REFORMING CONCEPTS

The reforming concepts in Table 6.1 are studied in detail through stack and system simulations. Exemplary system layouts are defined for all four options to analyse and compare the investigated concepts.

6.3.1. ALLOTHERMAL PRE-REFORMING AND WATER RECIRCULATION

The first reforming concept, shown in Figure 6.1a, is a conventional option based on allothermal reforming and WR. The fresh fuel is mixed with steam and partially reformed in an allothermal pre-reformer, heated with hot flue gas from the off-gas burner. In addition, the flue gas is used to pre-heat the cathode air and evaporate water, condensed from the cooled exhaust gases.

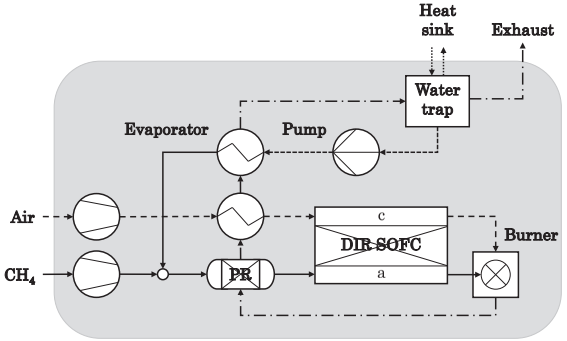

(a) WR, allothermal pre-reforming.

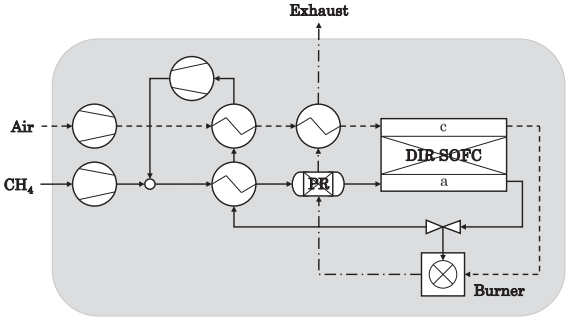

(b) AOGR, allothermal pre-reforming.

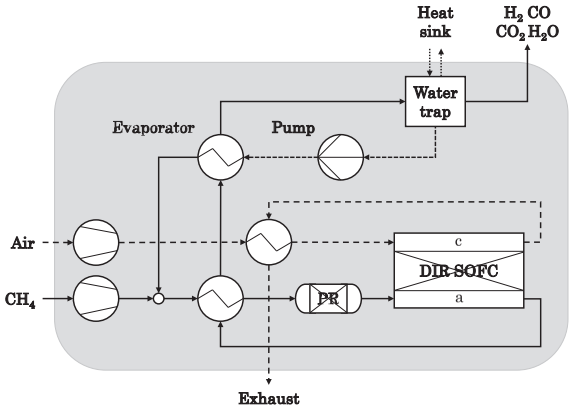

(c) WR, adiabatic pre-reforming.

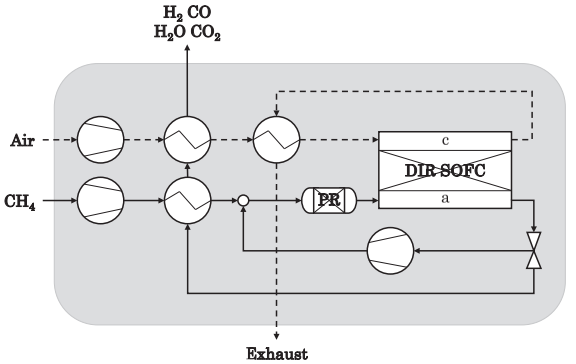

(d) AOGR, adiabatic pre-reforming.

Figure 6.1: Flow sheets of the investigated reforming configurations.

6.3.2. ALLOTHERMAL PRE-REFORMING AND ANODE OFF-GAS RECIRCULATION

The second concept, shown in Figure 6.1b, combines allothermal pre-reforming with AOGR. Similar to the previous configuration, the hot off-gas burner exhaust gas is used to heat the allothermal pre-reformer. However, a part of the anode off-gas is recirculated to provide steam for reforming. In addition, the gases are cooled to a temperature of 120°C to avoid high temperature AOGR. The layout is based on a low temperature AOGR configuration proposed by Engelbracht et al. [253].

6.3.3. ADIABATIC PRE-REFORMING AND WATER RECIRCULATION

The third reforming concept omits the use of an off-gas burner entirely. Instead, the mixture of fuel and steam is only pre-heated and passed through an adiabatic pre-reformer. Similar to the first configuration, steam is condensed from the anode-off gas, evaporated and mixed with the fuel. However, steam can be condensed more easily in this configuration, since the anode off-gas is not mixed with cathode air and has a high steam concentration. Moreover, the un-burned fuel, consisting of hydrogen and carbon monoxide may be further utilised in other utilities, for example in combined heat, hydrogen and power production, low temperature fuel cells or thermal bottoming cycles [226].

6.3.4. ADIABATIC PRE-REFORMING AND ANODE OFF-GAS RECIRCULATION

The last reforming concept uses the heat and steam produced by the electrochemical reaction only, combining high temperature AOGR and adiabatic pre-reforming. A part of the anode off-gas is recycled, while the remaining part is used to pre-heat both fuel and air. Heat from the cathode air is recuperated as well, but the remaining energy in the exhaust gases can be used in other applications. Similar configurations have been proposed in several studies, although some use ejectors instead of high temperature recirculation blowers [241].

6.4. MODELLING AND SIMULATION

Both stack and system models are used to investigate the implications of different reforming concepts on SOFC systems. Section 6.4.1 discusses the calculation of anode inlet compositions and temperatures for different system configurations and operating conditions. The calculated anode inlet conditions are then used to simulate the corresponding current-voltage characteristics of and temperature gradients in the SOFC stack with a dynamic model, described in Section 6.4.2. The cell voltages calculated with the stack model are then implemented in corresponding system models discussed in Section 6.4.3. Section 6.4.4 summarises the overall simulation procedure and simulated conditions.

6.4.1. ANODE INLET COMPOSITION AND TEMPERATURE

The composition and temperature of the fuel flow entering the anode compartment of the SOFC vary for different system configurations and operating conditions. The composition

depends, for example, on the ratio of steam or recirculated anode flow to the fresh fuel flow for the WR and AOGR concepts respectively. Similarly, the anode inlet temperature is equal to the reformer temperature for allothermal pre-reforming, but follows from thermodynamic equilibrium calculation in case of adiabatic pre-reforming.

The anode inlet compositions and temperatures are calculated assuming that the flow is in chemical equilibrium at the anode inlet. The chemical equilibrium composition is calculated through Gibbs free energy minimisation. This is solved iteratively for adiabatic reforming, since the equilibrium composition is a function of the outlet temperature, while the outlet temperature in turn follows from an energy balance resulting from the equilibrium composition.

For the AOGR cases, an appropriate amount of recirculation has to be selected. The reforming ratio is adjusted for different global fuel utilisations ($u_{f,gl}$) in this study, to maintain a constant oxygen-to-carbon (OC) ratio. The amount of recirculation required can be shown to follow from

$$RR = \frac{\dot{n}_{recycle}}{\dot{n}_{an}^{out}} = \frac{\text{OC ratio}}{(2C + H/2 - O)\, u_{f,gl}}, \tag{6.1}$$

where C, H and O are the number of carbon, hydrogen and oxygen atoms in an average fresh fuel molecule respectively. The effective fuel utilisation in the stack decreases for higher recirculation ratios, and the fuel utilisation for a single pass follows from from:

$$u_{f,sp} = \frac{u_{f,gl}\,(1 - RR)}{1 - RR\, u_{f,gl}} \tag{6.2}$$

Whether carbon formation is thermodynamically favourable depends on the temperature, pressure and fractions of carbon, hydrogen and oxygen in the fuel. This can be visualised in a CHO ternary phase diagram, shown in Figure 6.2. The black lines indicate the region where solid carbon formation is thermodynamically expected (C(s)+gas) for 500, 600 and 700°C, while the grey lines represent constant OC ratios in the fuel mixture of 1.5, 2 and 2.5. The dash-dotted lines show how the carbon, hydrogen and oxygen fraction of methane are changing when diluted with either WR or AOGR.

Figure 6.2 shows that carbon formation is thermodynamically not favourable when WR is used and the OC ratio is above 1.5. For AOGR, however, OC ratios in excess of 2.5 are required to ensure that carbon deposition is thermodynamically not expected at a temperature of 500°C. Whether carbon depositing will indeed occur depends on the type of carbon formed and the individual reaction kinetics of carbon depositing and removal reactions [304]. For example, Halinen et al. [254] observed no carbon depositing 600°C for conditions where it was thermodynamically expected.

6.4.2. STACK MODELLING

The stack is simulated with 1D a dynamic model of a Staxera/Sunfire ISM V3.3, developed and validated in Chapter 4. A schematic overview of the ISM is shown in Figure 4.2. Two Mk200 stacks are placed on top of each other, making a total of 60 cells. Fuel and air manifolding are integrated in the stack and ISM respectively. The Mk200 stacks

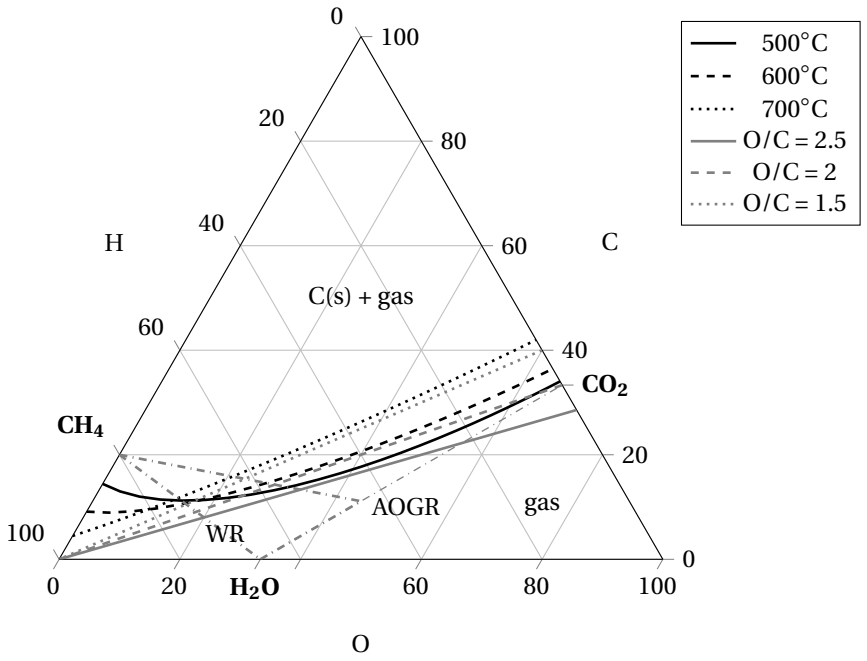

Figure 6.2: Ternary phase diagram for carbon, hydrogen and oxygen.

are assumed to be equipped with ESC2 cells from Kerafol/H.C. Starck with a nickel-gadolinium doped cerium oxide (Ni-GDC) anode, yttrium stabilised zirconia (3YSZ) electrolyte and 8YSZ/lanthanum strontium manganese (LSM)-LSM double layer cathode.

The stack is modelled as a 1D plug flow reactor with individual temperature layers for air, fuel, positive electrode-electrolyte-negative electrode (PEN) assembly and the interconnect, all discretised in the flow direction. Periodic boundary conditions are imposed on the interconnect, effectively assuming an infinitely repeated stack assembly. Heat transfer effects in the inactive in- and outflow regions as well as heat losses to the surroundings are included as well. A schematic overview of the modelling approach is shown in Figure 4.2.

The main dimensions and properties of the ISM have been obtained in Chapter 4, and are summarised in Table 4.1. Table 6.2 summarises the most important operating conditions as well. The manufacturer specifies a maximum PEN temperature of 850°C, which is achieved by adjusting the cathode air inlet temperature and volume flow. However, a minimum air flow of 40 Nl min^{-1} is advised to ensure proper air distribution and prevent local hotspots or air starvation. The model is used to calculate the spatial distributions of the hydrogen oxidation reaction and DIR rate from inlet to outlet with the electrochemical model validated in Chapter 4 and the MSR kinetics derived in Chapter 5

Table 6.2: Advised operating parameters for the ISM V3.3 from Sunfire/Staxera with ESC cells from Kerafol/H.C. Starck.

Operating parameters	Units	Value
Max PEN temperature, T_{PEN}^{max}	[°C]	850
Min air flow, $\dot{V}_{ca}^{min}$	[Nl min^{-1}]	40
Max stack current, I_{stack}^{max}	[A]	30
Min stack voltage, U_{stack}^{min}	[V]	36

6.4.3. SYSTEM MODELLING

The system calculations are performed in the in-house developed thermodynamic flowsheet calculation program Cycle-Tempo, with component models and parameters described in Chapter 3. The Cycle-Tempo package incorporates built-in thermodynamic component models of pumps, blowers, heat exchangers, evaporators, moisture separators, reformers, combustors and fuel cells [246, 247]. The system of equations is subsequently solved to calculate pressures, flows and temperatures in every system node. These are then used to calculated the gross and net system efficiencies.

The SOFC is modelled as an allothermal ideal plug flow reactor in Cycle-Tempo, assuming that the reforming and water gas shift reactor are in equilibrium. However, the user can provide various SOFC parameters for off-design calculations, and this is used to implement the cell voltages calculated with the 1D dynamic stack model in the system models. However, the remaining operating conditions, such as mass flows, temperatures and pressure drop are calculated with the system models. The heat loss from the ISM to the environment, $\dot{Q}_{loss}$, is calculated relative to the electric power produced by the stack, due to limitations in the SOFC model of Cycle-Tempo:

$$\dot{Q}_{loss} = \dot{q}_{loss} P_{SOFC,DC} \tag{6.3}$$

Chemical equilibrium is assumed in the pre-reformer, and complete combustion in the off-gas burner. The losses in rotating equipment are calculated from their isentropic and mechanical efficiencies. The flue gas leaving the moisture separator is assumed to be saturated at 25°C. An overview all parameters used in the system analysis is provided in Table 6.3.

6.4.4. STACK AND SYSTEM SIMULATIONS

Two types of models are used to study the implications of different reforming concepts. Stack simulations provide detailed insight in the effect of different reforming concepts on the SOFC, and the results are used in system models to calculate the overall system efficiencies. The overall simulation procedure is as follows:

1. The anode inlet compositions and temperatures are calculated for different system configurations and operating conditions;

Table 6.3: Overview of the parameters used in the system model, based on manufacturer specifications and Chapter 3.

System parameter	**Units**	**Value**
Stack outlet temperature, T^{out}_{stack}	[°C]	825
Air inlet temperature, T^{in}_{air}	[°C]	725
Allothermal reformer temperature, T_{ref}	[°C]	600
Fuel pre-heating temperature (IR), T^{in}_{fuel}	[°C]	775
Adiabatic reformer inlet temperature, T^{in}_{ref}	[°C]	775
Evaporator outlet temperature, T^{out}_{eva}	[°C]	120
LT-AOGR blower inlet temperature, T^{in}_{AOGR}	[°C]	120
Moisture separator temperature, T^{out}_{ms}	[°C]	25
Anode pressure drop, Δp_{an}	[bar]	0.03
Cathode pressure drop, Δp_{ca}	[bar]	0.05
Heat exchanger pressure drop, Δp_{hex}	[bar]	0.02
Pre-reformer pressure drop, Δp_{ref}	[bar]	0.02
Off-gas burner pressure drop, Δp_{burner}	[bar]	0.02
Relative heat loss, $\dot{q}_{loss}$	[-]	0.2
Isentropic efficiency blower, $\eta_{is,blower}$	[-]	0.7
Mechanical efficiency blower, $\eta_{m,blower}$	[-]	0.8
Isentropic efficiency pump, $\eta_{is,pump}$	[-]	0.85
Mechanical efficiency pump, $\eta_{m,pump}$	[-]	0.9
Inverter efficiency, $\eta_{inverter}$	[-]	0.95

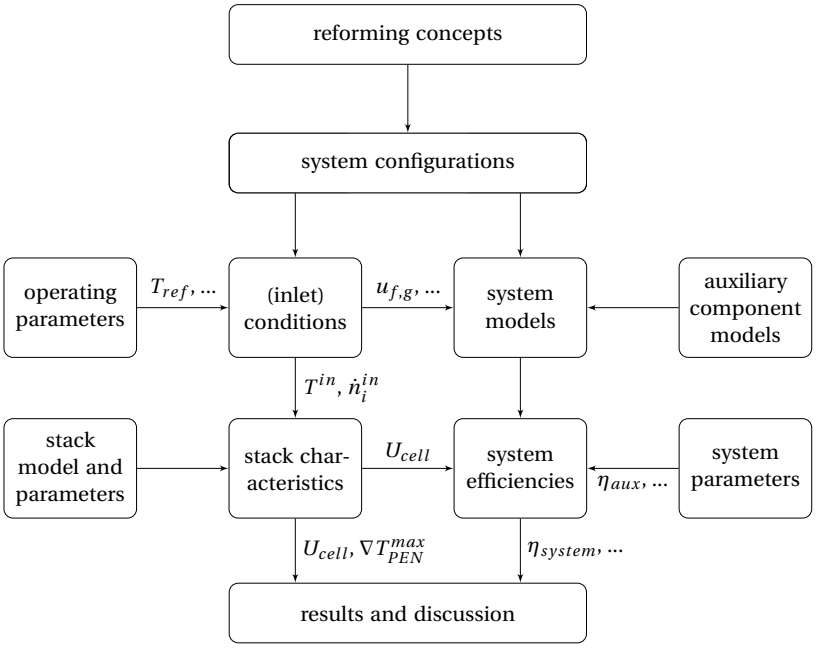

Figure 6.3: Flowchart of the procedure used to simulate the investigated reforming concepts.

2. The anode inlet compositions and temperatures are used to simulate current voltage characteristics of and temperature gradient in the stack for different system configurations and operating conditions;

3. The simulated cell voltages are implemented in the system models to calculate the overall system efficiencies for nominal operating conditions, a range of global fuel utilisations and:

   (a) A constant stack power of 1 kWe, which is achieved at different voltages for the investigated reforming concepts;

   (b) The maximum cell voltage, achieved at the minimum stack current required to sustain the stack temperature for the minimum cathode air flow of 40 Nl min^{-1}.

Figure 6.3 shows a schematic overview of this simulation process.

STACK SIMULATIONS

The current voltage characteristics are determined by simulating stack operation for each of the investigated configuration. The stack performance is mapped by increasing the stack current from 15 to 27 A for various stack currents and global fuel utilisations. Additional off-design operating conditions are simulated by changing the OC ratio, cathode air inlet temperature and pre-reformer (inlet) temperature. An overview of the simulated stack parameters is provided in Table 6.4.

Table 6.4: Overview of the simulated stack and system operating conditions.

Stack simulations	Unit	Nominal	Range	Interval
Stack current, I_{stack}	[A]	24	15-27	0.5
Fuel utilisation, $u_{f,gl}$	[-]	0.8	0.7-0.9	0.025
Air inlet temperature, T_{air}^{in}	[°C]	725	675-775	10
Allothermal pre-reformer, T_{ref}	[°C]	600	550-650	10
Adiabatic pre-reformer, T_{ref}^{in}	[°C]	775	750-800	5
OC ratio	[-]	2	1.5-2.5	0.1

System simulations	
Global fuel utilisation ($u_{f,gl}$)	varied from 0.7 to 0.9
T_{air}^{in}, T_{ref}, T_{ref}^{in}, and OC ratio	nominal conditions
U_{cell} and ∇T_{PEN}^{max}	obtained from stack simulations

Cases
(a): Stack power (P_{stack}) of 1 kWe
(b): Maximum cell voltage (U_{cell})

The manufacturer advices to control the temperature of the stack by adjusting the cathode air flow. The control objective is a maximum PEN temperature of 850°C, with a minimum air flow of 40 Nl min^{-1} to ensure proper gas distribution in the stack and avoid oxygen starvation at the cathode. As described in Chapter 4, a feedback controller with proportional and integral (PI) gain is implemented in the model to adjust the cathode air flow for each operating current, such that the maximum PEN temperature is achieved.

The average stack temperature falls rapidly if the stack current is lower than the minimum required to maintain the maximum PEN temperature for the minimum air flow. As a consequence, the ohmic resistance increases and the electrochemical performance reduces. These conditions are not included in the results, since it is undesirable to operate the stack at these conditions.

SYSTEM SIMULATIONS

The cell voltages obtained from the stack simulations are used to calculate the corresponding system efficiencies, as is visualised in Figure 6.3. The system efficiencies are calculated for various fuel utilisations, nominal operating conditions and two scenarios: A constant stack power of 1 kW and operation at the minimum stack current required to sustain the stack temperature at the minimum cathode air flow. This results in the maximum cell voltage and, therefore, highest stack efficiencies. An overview of the simulated conditions and scenarios is shown in Table 6.4.

6.5. RESULTS AND DISCUSSION

The results of the three simulation steps are divided in three separate sections: The anode inlet compositions calculated for different system configurations and operating conditions are presented in Section 6.5.1. The results of the stack simulations are discussed in Section 6.5.2. First, differences in the stack operating characteristics for the investigated reforming strategies are presented, after which contours plots of the cell voltage and maximum PEN temperature gradients are shown for both nominal and off-design operating conditions. The corresponding system efficiencies at nominal conditions are then presented in Section 6.5.3.

6.5.1. ANODE INLET COMPOSITION AND TEMPERATURE

Figure 6.4 shows the methane concentrations in the fuel gas for various OC ratios and pre-reformer (inlet) temperatures. The maximum allothermal pre-reformer temperature and adiabatic pre-reformer inlet temperatures are based on an SOFC outlet temperature of 825°C, specified by the stack manufacturer [265, 266]. Higher allothermal pre-reformer temperatures may require more heat than available in the exhaust gases, while hardly any methane is reformed at temperatures below 550°C. Similarly, adiabatic pre-reformer temperatures in excess of 800°C lead to a low heat transfer rate in the fuel pre-heater.

The selected reforming conditions result in methane partial pressures ranging from less than 0.04, for high OC ratios and reformer temperatures, to over 0.26 for low OC ratios and adiabatic reforming. The differences between the two allothermal reforming cases, shown in Figures 6.4a and 6.4b respectively, are small. However, AOGR results in slightly lower methane partial pressures compared to WR due to dilution with carbon dioxide. A similar effect can be observed when comparing the two adiabatic pre-reforming cases.

Figure 6.4c shows that adiabatic pre-reforming results in substantially higher methane partial pressures than allothermal pre-reforming when WR is used, especially for low OC ratios. For AOGR, shown in Figure 6.4d, the methane partial pressures are similar for allothermal and adiabatic pre-reforming. A combination of AOGR and adiabatic pre-reforming results in lower methane partial pressures and higher reformer outlet temperatures than WR and adiabatic pre-reforming.

Figure 6.5a shows the RR and $u_{f,sp}$ for various OC ratios and global fuel utilisations. The recirculation ratio increases for higher OC ratios and lower global fuel utilisations. This affects the methane partial pressures for AOGR and adiabatic reforming, as can be seen in Figure 6.5b. The methane partial pressure decreases for higher recirculation ratios, while the outlet temperature seems more related to the fuel utilisation for a single pass. OC ratios above 2 are commonly used in SOFC systems to suppress carbon deposition.

6.5.2. STACK SIMULATIONS

The stack simulations results are presented in three parts: Section 6.5.2 presents the spatial distributions of the reforming rate, current density, temperature and temperature gradient for nominal operating conditions. Contours of the cell voltage and maximum temperature gradients are presented in Section 6.5.2 for various stack currents and fuel

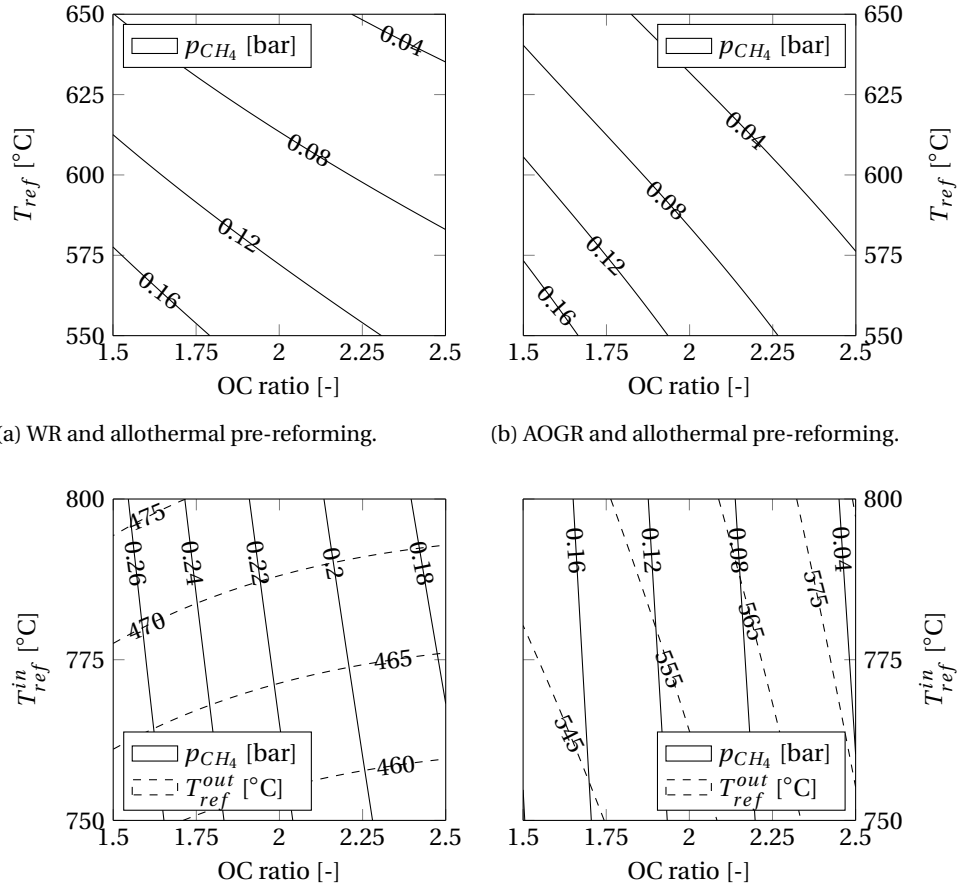

(a) WR and allothermal pre-reforming.

(b) AOGR and allothermal pre-reforming.

(c) WR and adiabatic pre-reforming.

(d) AOGR and adiabatic pre-reforming.

Figure 6.4: Methane partial pressures and outlet temperatures of adiabatic reformers for different reforming configurations, OC ratios and reformer (inlet) temperatures.

utilisations, and Section 6.5.2 presents these contours for various stack currents and other off-design conditions.

SPATIAL DISTRIBUTIONS

Figure 6.6 shows the simulated distributions of the MSR reaction rate, current density, PEN temperature and PEN temperature gradient from inlet to outlet for the nominal operating condition specified in Table 6.4. Figure 6.6a shows that the MSR rate is initially highest for the WR case with allothermal pre-reforming, while it is more equally distributed when anode off-gas is recirculated. Adiabatic pre-reforming result in lower reformer outlet temperatures, and subsequently reduces the entrance temperature of the stack. Therefore, the MSR is initially lower for the two adiabatic cases.

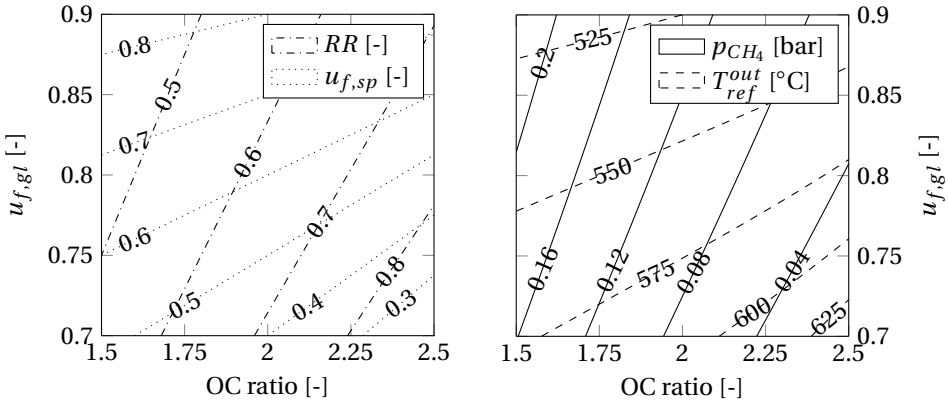

(a) Required RR and resulting $u_{f,sp}$.

(b) AOGR and adiabatic pre-reforming.

Figure 6.5: RR and $u_{f,sp}$ (Figure 6.5a) and methane partial pressures and adiabatic reformer outlet temperatures (Figure 6.5b) for various OC ratios and $u_{f,gl}$ when AOGR is employed, for a reformer inlet temperature of 775°C.

The current density distribution, shown in Figure 6.6b, behaves inversely to the MSR reaction rate: The current density is relatively equally distributed in both the allothermal pre-reforming concepts, but triples from inlet to outlet for the adiabatic pre-reforming. Both the DIR rate and current density distribution have a strong dependency on the local PEN temperature, shown in Figure 6.6c. The temperature difference from inlet to outlet is higher for adiabatic than allothermal reforming conditions. In addition, the temperature increases slower for AOGR than WR, due to lower fuel utilisation for a single pass, which increases the fuel flow and reduces concentration losses near the outlet.

Figure 6.6d shows the local PEN temperature gradients calculated form the simulated PEN temperature gradients. The difference in the maximum temperature gradient between WR and AOGR is negligible for allothermal pre-reforming, although it occurs somewhat later for AOGR. However, the maximum temperature gradient almost doubles for adiabatic pre-reforming, and is higher for WR than AOGR. Overall, the simulations show that allothermal pre-reforming results in higher stack voltages and smaller temperature gradients than adiabatic pre-reforming, even though the adiabatic pre-reformer inlet temperature assumed is 175°C higher than the allothermal pre-reforming temperature.

FUEL UTILISATION

The previous section showed detailed spatial distributions within the stack, but for nominal conditions only. However, fuel utilisations, reformer (inlet) temperature and OC ratios vary in practice. Therefore, a range of off-design conditions is simulated as well. Figure 6.7 shows contours for constant simulated cell voltages and maximum PEN temperature gradients for various global fuel utilisations and stack currents for the investigated reforming concepts. Stack currents which are insufficient to maintain the operating temperature of 850°C at the minimum air flow of 40 Nl min^{-1} are not included.

The cell voltage and maximum PEN temperature gradient are primarily determined

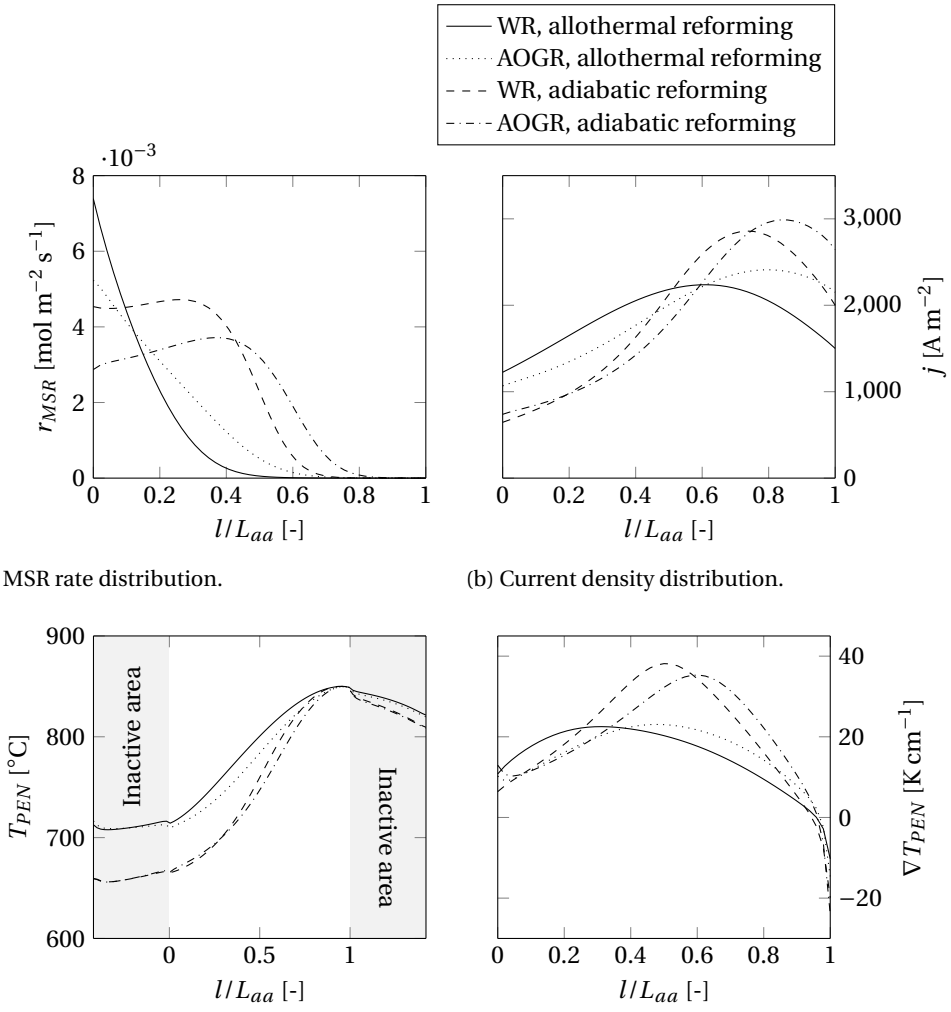

(a) MSR rate distribution.

(b) Current density distribution.

(c) PEN temperature distribution.

(d) PEN temperature gradient.

Figure 6.6: Spatial distribution of the MSR rate, current density, PEN temperature and PEN temperature gradient in the SOFC stack for the investigated reforming configurations and the nominal conditions specified in Table 6.4.

by the stack current for the allothermal pre-reforming configuration with WR, and only a weak function of the global fuel utilisation. The effect of the global fuel utilisation is higher in the case of AOGR, since it changes the recirculation ratio: A high recirculation ratio is required to maintain an OC ratio at low fuel utilisations, which cools down the entrance of the stack and increases the temperature gradient from inlet to outlet.

Adiabatic pre-reforming reduces the fuel inlet temperature and increases the methane partial pressure. As a result, lower cell voltages and, subsequently, higher stack currents

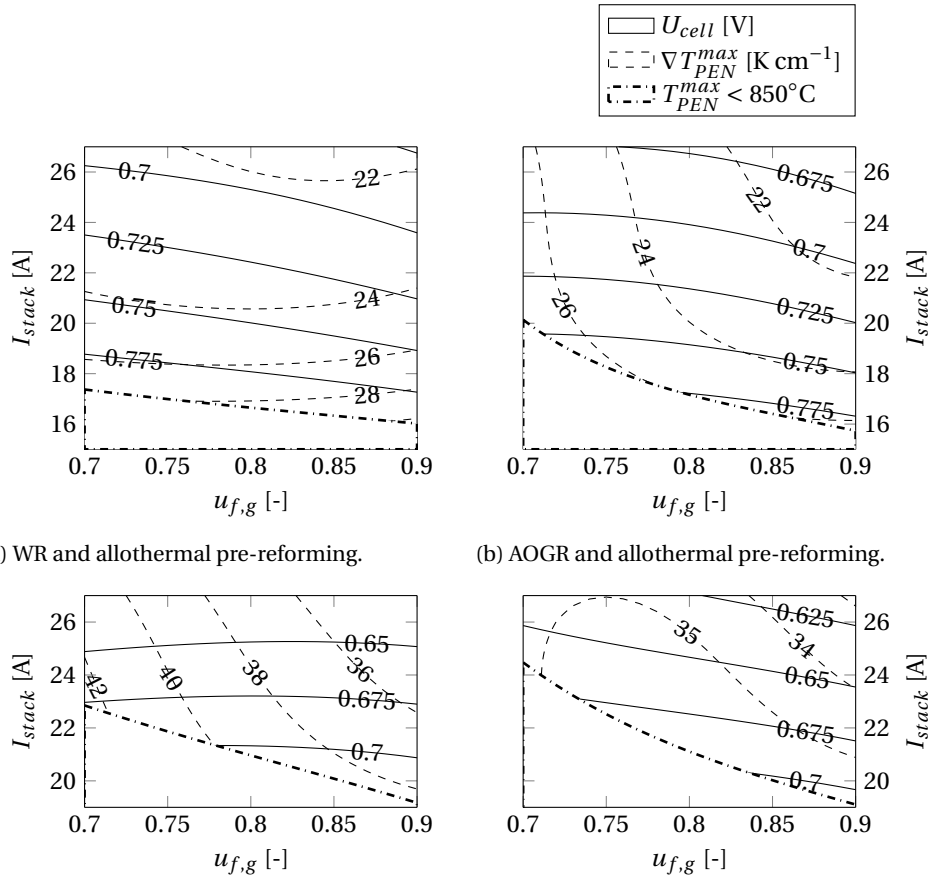

(a) WR and allothermal pre-reforming.

(b) AOGR and allothermal pre-reforming.

(c) WR and adiabatic pre-reforming.

(d) AOGR and adiabatic pre-reforming.

Figure 6.7: Cell voltages and maximum PEN temperature gradients in the stack for different reforming configurations, fuel utilisations and stack currents.

are required to generate sufficient heat for internal reforming, while maintaining the maximum PEN temperature of 850°C. The increased temperature difference from inlet to outlet results in notably higher temperature gradients in the stack compared to the allothermal pre-reforming case. In addition, the maximum PEN temperature gradient is a strong function of the global fuel utilisation when water is recirculated.

AOGR reduces the cell voltages in the stack in all simulated cases, despite the lower fuel utilisation for a single pass. This is a result of the constant OC assumed in this study, which lowers the hydrogen-to-carbon ratios compared to WR. In practice, the lower single pass fuel utilisation may offer advantages in the fuel distribution within the stack, reducing cell-to-cell variations and allowing higher global fuel utilisations. The 1D model used in this study does, however, not account for cell-to-cell variations.

On the other hand, AOGR reduces the temperature gradients in the stack, especially for adiabatic pre-reforming. This is most effective if the recirculation ratio is low and the single pass fuel utilisation is high, since a high single pass fuel utilisation results in a more homogeneous current density distribution in the stack. The high current density at the hot outlet section of the stack is constrained by the increasing concentration losses for high single pass fuel utilisations.

The cell voltages are generally lower for adiabatic pre-reforming and AOGR than allothermal pre-reforming and WR, which is amplified by the lower cell voltages or higher fuel utilisations required to maintain the desired operating temperature. This reveals the trade-off between operating at high current density to increase the power density, lower the specific product costs and reduce thermal stresses, versus operating at low current densities to increase the stack voltage and efficiency.

OTHER OPERATING CONDITIONS

Figure 6.8 shows contours of constant cell voltage and maximum PEN temperature gradient for changes in the pre-reformer (inlet) temperature, air inlet temperature and OC ratio. Figure 6.8a shows contours for allothermal pre-reformer temperatures from 550 to 650°C for the system with WR. This result shows that increasing the reformer temperature may reduce the maximum temperature gradient in the stack as much as 5 K cm^{-1}. However, Figure 6.8c shows that an increase in the adiabatic pre-reformer inlet temperature has little effect on the maximum temperature gradients in the stack.

Figure 6.8b shows that increasing the air temperature increases the cell voltage in the stack and reduces the maximum PEN temperature gradient in a SOFC stack operated with an allothermal pre-reformer and AOGR. Although this may improve SOFC performance, the heat available in the outlet gases should be sufficient to pre-heat the incoming air to the required temperature. In addition, the size and cost of the air pre-heater will increases as a consequence.

The OC ratio affects stack operation particularly for AOGR, since it determines the recirculation ratio and fuel utilisation for a single pass. Figure 6.8d shows that an increase in the OC ratio from 1.5 to 2.5 decreases the cell voltage in the stack, but reduces the temperature gradient in the stack as well, from over 38 to less than 32 K cm^{-1}.

Overall, the results in Figure 6.8 demonstrate the capability of the stack model to simulate the off-design performance of a commercial SOFC stack. The changes in the pre-reformer (inlet) temperature, air inlet temperature and OC ratio were simulated for the other investigated reforming concepts as well. These results are included as supplementary material (Figures A.1 to A.3).

6.5.3. SYSTEM SIMULATIONS

The stack simulations provide detailed insight in the effects of different reforming concepts on the electrochemistry and temperature gradients in the stack. Although the stack efficiency is directly proportional to the cell voltage, the overall system efficiency is affected by the parasitic power consumed by the balance of plant components as well. Therefore, system models are developed to calculate the corresponding system efficiencies.

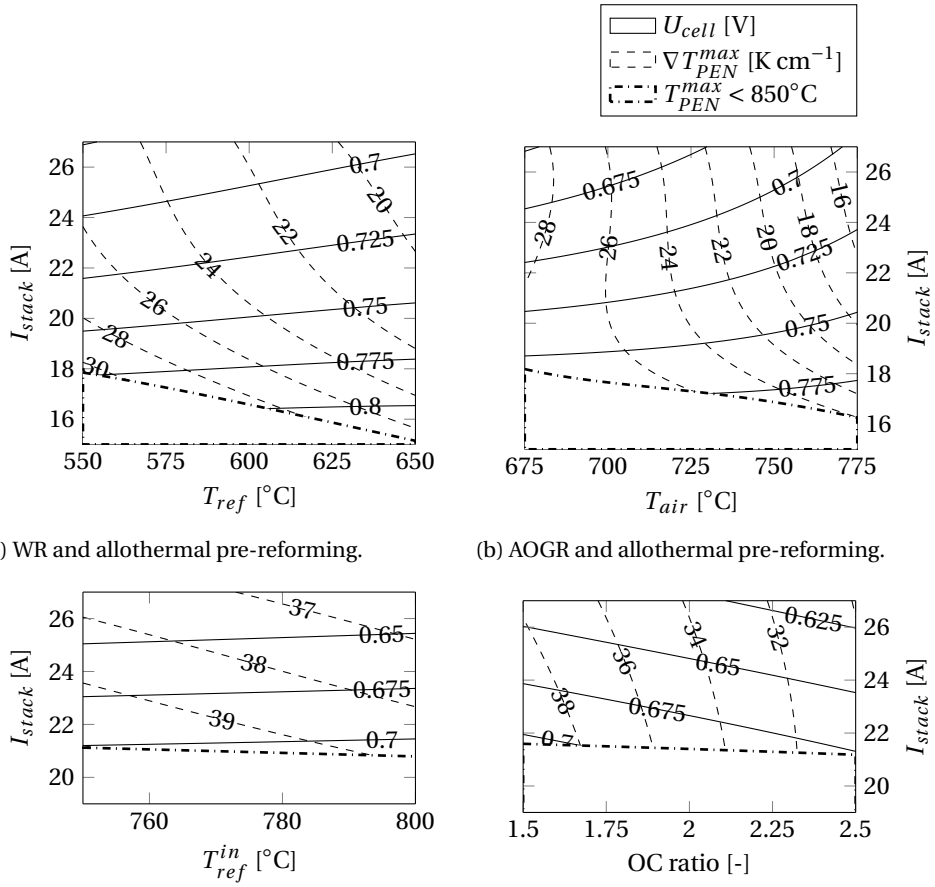

(a) WR and allothermal pre-reforming.

(b) AOGR and allothermal pre-reforming.

(c) WR and adiabatic pre-reforming.

(d) AOGR and adiabatic pre-reforming.

Figure 6.8: Cell voltages and maximum PEN temperature gradients in the stack for different reforming configurations and changes in the allothermal pre-reformer temperature (Figure 6.8a) and adiabatic pre-reformer inlet temperature (Figure 6.8c) for WR and various cathode air inlet temperatures (Figure 6.8b) and OC ratios (Figure 6.8d) for AOGR.

The system efficiencies are calculated for nominal conditions in two scenarios: A constant stack power of 1 kWe is assumed in the first scenario, to allow a comparison for the same stack size and, thus, similar capital expenditure. The second scenario assumes operation at the lowest current required to support a stack temperature of 850°C for the minimum air flow of 40 Nl min^{-1}, which results in the maximum cell voltage and stack efficiency.

CONSTANT STACK POWER

Figure 6.9 shows the results of the system calculations for a constant stack power of 1 kW and global fuel utilisations from 0.7 to 0.9. Figure 6.9a shows that the cell voltages are

clearly higher for the cases with allothermal than adiabatic pre-reforming. WR generally yields higher cell voltages than AOGR, except for adiabatic pre-reforming at low fuel utilisations, where the high degree of DIR cools down the stack substantially. As a result, the cell voltage increases with fuel utilisation for WR and adiabatic pre-reforming, while it decreases in all other cases.

The stack efficiency is proportional to the cell voltage and global fuel utilisation, as can be seen in Figure 6.9c. For adiabatic reforming at low fuel utilisation, the stack efficiency is consequently lower for WR than AOGR, but higher for fuel utilisations in excess of 0.76. The highest stack efficiency is attained with WR and allothermal pre-reforming, but the difference with WR and adiabatic pre-reforming decreases as the fuel utilisation increases.

The oxygen utilisation is inversely correlated with the cathode air flow, thus a decreasing oxygen utilisation indicates an increase in the parasitic power consumption by the cathode air blower. The oxygen utilisation, shown in Figure 6.9b, decreases for lower cell voltages and more pre-reforming, due to the higher air flow required to cool the stack.

Adiabatic pre-reforming reduces the parasitic power consumption by the air blower compared to allothermal reforming. Consequently, the difference between between the net efficiency of systems with adiabatic pre-reforming and allothermal pre-reforming reduces compared to the stack efficiency, as can be seen in Figure 6.9d. The net system efficiency with adiabatic pre-reforming and WR even exceeds that of the allothermal pre-reforming and AOGR, despite the higher cell voltages achieved by the latter.

Higher degrees of internal reforming increase potentially deteriorating temperature gradients in the stack as well. Figure 6.9e shows that the PEN temperature gradients are about 10 K cm^{-1} higher for system configurations with adiabatic pre-reforming compared to concepts with allothermal pre-reforming, which might compromise the stack lifetime.

MAXIMUM CELL VOLTAGE

Figure 6.10 presents the results for stack operation at the maximum cell voltage (i.e. minimum cathode air flow) and nominal conditions. Figure 6.10a shows that the cell voltage is virtually constant around 0.8 V for the system with allothermal pre-reforming and WR. The cell voltage increases with the fuel utilisation for the other system configurations, as more heat is available to reform the fuel and maintain the stack temperature for the same fuel flow. Similar to the case of constant stack power, the highest cell voltage is obtained with allothermal pre-reforming and WR, and the voltage decreases when adiabatic pre-reforming or AOGR is adopted instead.

Figure 6.10c shows that the highest stack efficiency is attained at the maximum fuel utilisation, and decreases proportionally with the cell voltage from 65.6% for allothermal pre-reforming and WR to 58.3% for adiabatic pre-reforming and AOGR, a difference of 7.3% point. The net system efficiency, shown in Figure 6.10d, follows a similar trend. However, the maximum system efficiency decreases from 61.4% for allothermal pre-reforming and water recycling to 56.4% for adiabatic pre-reforming and AOGR, a reduction of 5% point only.

High cell voltages enhance both stack and system efficiency, but the low currents reduce the electric power produced by the stack, as can be seen in Figure 6.10b. The lower stack currents for allothermal pre-reforming result in substantially lower stack powers compared to adiabatic pre-reforming. Interestingly, AOGR results in higher stack powers

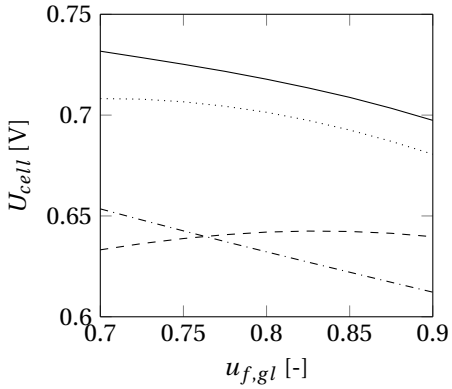

(a) Cell voltage.

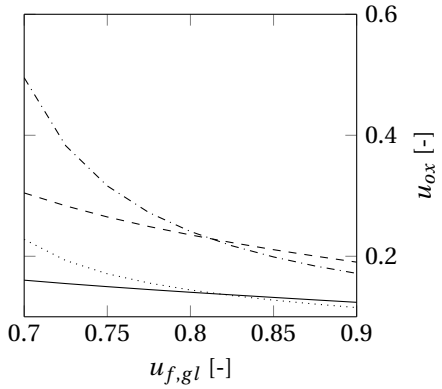

(b) Oxygen utilisation.

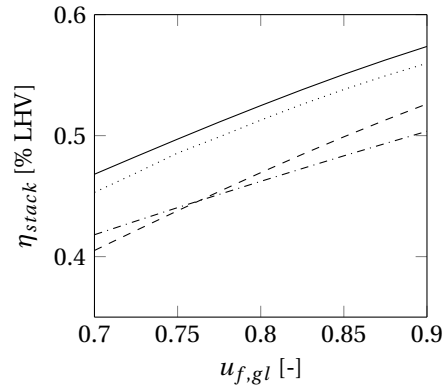

(c) Stack efficiency.

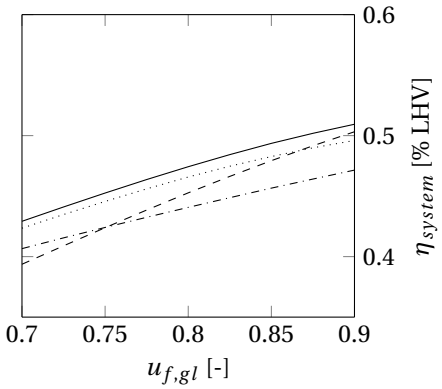

(d) System efficiency.

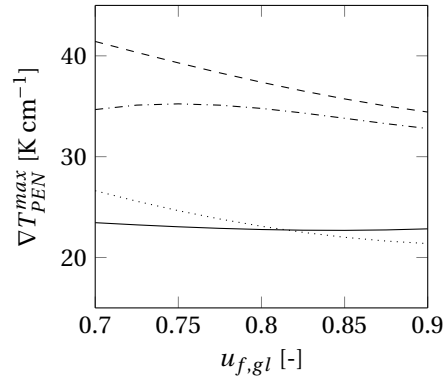

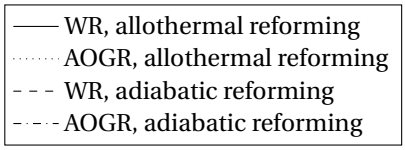

(e) Maximum PEN temperature gradient.

Figure 6.9: Results of the system simulation for different reforming configurations at reference operating conditions and a constant stack power of 1 kWe.

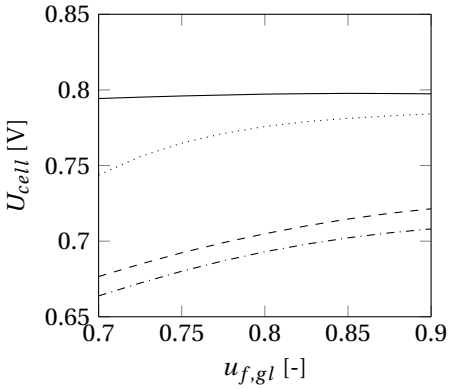

(a) Cell voltage.

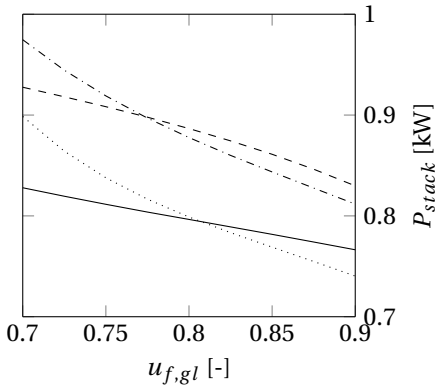

(b) Stack power.

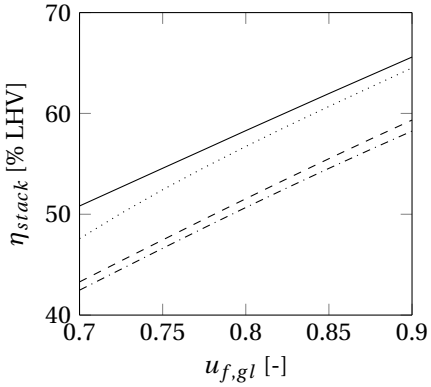

(c) Stack efficiency.

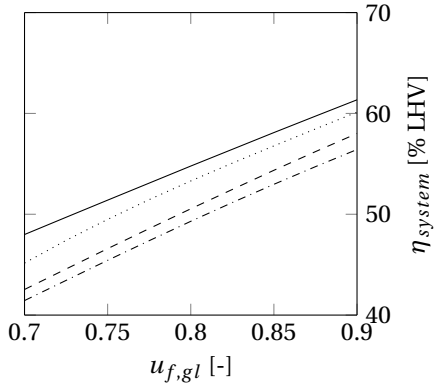

(d) System efficiency.

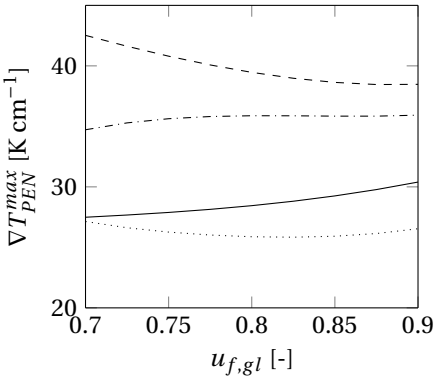

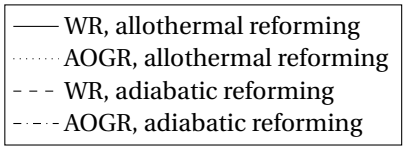

(e) Maximum PEN temperature gradient.

Figure 6.10: Results of the system simulation for different reforming configurations at reference operating conditions and the minimum air flow specified by the manufacturer.

for lower fuel utilisations, but this trend reverses for higher fuel utilisations. Therefore, AOGR seems to be most interesting for lower fuel utilisations, since both the power density and stack efficiency are reduced compared to WR for $u_{f,gl} > 0.8$.

Figure 6.10e shows that there are substantial differences in the maximum temperature gradients in the stack. Since the air flow is the same for all cases (i.e. the minimum), these differences originate from the magnitude, temperature and composition of the fuel flow or stack current. The maximum temperature gradient increases with fuel utilisation in the WR case for allothermal pre-reforming, but decreases for adiabatic pre-reforming. The lowest temperature gradients are observed for a combination of AOGR and allothermal pre-reforming, while WR and adiabatic pre-reforming result in the highest temperature gradients.

Only heat from the electrochemical reaction is used in the adiabatic pre-reforming cases to reform the fuel, omitting the use of heat produced by an off-gas burner. This limits the heat available for pre-reforming and, therefore, the maximum voltage and minimum fuel utilisation. However, adiabatic reforming is interesting if the fuel or heat can be further utilised, for example in combined heat, hydrogen and power production or hybrid operation with internal combustion engines or low temperature fuel cells.

The ISM assumed this study dissipates 200 to 250 W of heat to the surroundings, depending on the operating conditions. If the fuel is pure hydrogen or fully pre-reformed, this helps to remove the heat produced by the exothermic hydrogen oxidation reaction and avoids excessive cathode air flows. However, the results demonstrate that heat insulation becomes more important if the stack is operated with high degrees of internal reforming, since the minimum air flow dictates a minimal operating current to sustain the operating temperature, and limits the maximum achievable cell voltage.

Overall, the results demonstrate that an inclusive analysis at both stack and balance of plant level is indispensable to assess the consequences of different reforming concepts in SOFC systems. Stack simulations are required to accurately predict the electrochemical performance of the stack and identify potentially deteriorating operating conditions, but losses in the balance of plant are just as important.

6.6. CONCLUSIONS

Four SOFC system configurations, representing reforming concepts with either allothermal or adiabatic pre-reforming and either WR or AOGR, were simulated on both and stack level. Stack simulations were used to predict the electrochemical performance of the stack and temperature gradients in the PEN structures for the investigated reforming concepts, and the corresponding system efficiencies were calculated in a thermodynamic analysis.

Adiabatic pre-reforming and AOGR reduce the cell voltage in the stack compared to allothermal pre-reforming and WR for nominal operating conditions. In addition, the temperature gradients increase for adiabatic pre-reforming, due to the lower degree of pre-reforming, and decrease for higher stack currents and global fuel utilisations. Relatively low cell voltages are required to sustain the desired stack operating temperature of the stack for high degrees of internal reforming and low fuel utilisations.

The highest system efficiencies are obtained for allothermal pre-reforming and WR.

However, a high stack efficiency does not necessarily result in a high system efficiency. This is, for example, the case when comparing allothermal pre-reforming and AOGR with adiabatic pre-reforming and WR. As expected, a trade-off exists between high system efficiency and stack power. In addition, AOGR improves the power density compared to WR for low fuel utilisations, but yields lower power densities for higher fuel utilisations. This illustrates the importance to consider both stack and system operation for the design of a robust and efficient SOFC system.

The results suggest that isothermal pre-reforming and WR may be appropriate choices for stand-alone systems, yielding high efficiencies and low thermal stresses. However, adiabatic pre-reforming and AOGR may be interesting for applications where low system cost or high power density are more important. In addition, both may prove advantageous when the SOFC is integrated with thermal cycles, since less heat and/or fuel is required for pre-reforming and/or steam evaporation. This is discussed in the next chapter, together with opportunities and challenges of maritime applications of SOFC systems.

7

MARITIME APPLICATION OF SOFC SYSTEMS

7.1. INTRODUCTION

Chapter 2 discussed the application of fuel cell systems in the maritime field in general, pointing out the potential of applying internal reforming SOFC-combined cycle to reduce the emissions of ships. Therefore, these systems were further studied in Chapters 3 to 6 with a thermodynamic analysis of SOFC-combined cycles, dynamic modelling of DIR stacks, determination of the rate determining step in the MSR reaction on SOFC anodes and an evaluation of different reforming concepts in SOFC systems.

This chapter discusses challenges and opportunities of the application of internal reforming SOFC-combined cycles on-board ships. Integration of SOFC with reforming and thermal cycles is summarised and discussed in Section 7.2, after which Section 7.3 presents maritime power and energy requirements. Application of internal reforming SOFC-combined cycles for maritime power generation is then analysed Section 7.4, from which challenges and opportunities of SOFC application on ships are identified and discussed in Section 7.5. Finally, the status and an outlook of maritime SOFC application are given in Section 7.6.

7.2. SOFC SYSTEMS

Different fuel cell types and their suitability for maritime application were discussed in Chapter 2, showing that SOFC systems fuelled with energy dense hydrocarbon fuels may be an attractive solution for ships with long mission requirements, especially when coupled with thermal cycles and if the fuel is reformed internally. SOFC integration with thermal cycles and reforming was subsequently studied in Chapters 3 to 6, and the results are summarised and discussed in this section.

7.2.1. SUMMARY

Integration with gas turbines, a steam turbine and a reciprocating engine was thermodynamically analysed in Chapter 3 and compared to stand-alone operation. The thermodynamic analysis showed that integration with gas turbines is most beneficial for low fuel utilisations, low cell voltages, high stack temperatures and if the SOFC is pressurised. However, the steam bottoming cycle proved to be more advantageous at high fuel utilisations, high cell voltages, low stack temperatures and if the SOFC is operated at ambient pressures. The reciprocating engine combined cycle, which uses unconverted fuel in the outlet gas instead of heat, behaves similar to the steam turbine combined cycle, but achieves slightly lower efficiencies.

An isothermal IPFR SOFC model was used for the power density calculations in Chapter 3, thus assuming a constant stack temperature. However, the temperature may change substantially from the SOFC inlet to outlet, especially when fuel is reformed internally. Therefore, detailed 1D dynamic models were developed in Chapter 4 of both single cells and stacks. The stack model was used to compare an in crease from zero to the rated current with either a step change or the ramp suggested by the manufacturer. This showed that stepping the stack current results in low voltages and increased temperature gradients, which might damage the stack.

The single cell model was used to validate empirical and intrinsic reforming kinetics, derived from data obtained in single cell experiments. Both kinetic models were used to model internal methane reforming in the stack. The results indicated that the DIR reaction is kinetically limited at the simulated operation conditions. More realistic temperature profiles were calculated with both kinetic reforming models, which is important to accurately estimate thermal stress inducing temperature gradients in the stack. However, the empirical and intrinsic reforming kinetics predicted a different spatial distribution of the DIR reaction within the stack, suggesting that further study on the intrinsic rate determining step in the internal reforming reaction is required.

Reforming experiments on single cells with Ni-GDC anodes were presented in Chapter 5. The experimental reforming rates were used to regress and compare different kinetic models. A classical LH mechanism was selected, consistent with associative adsorption of methane and dissociative adsorption of steam, because it was in good statistical agreement with the experimental data, provided a sound physical explanation and was thermodynamically consistent.

Hydrocarbon fuels are commonly pre-reformed with a combination of either WR or AOGR and either allothermal or adiabatic reforming. AOGR and adiabatic reforming can simplify the system and enhance efficiency, but may result in increased temperature profiles within the SOFC compared to WR and isothermal reforming. Therefore, different reforming concepts were compared in Chapter 6 using the system modelling methods presented in Chapter 3, dynamic DIR SOFC stack model developed in Chapter 4 and internal reforming kinetics derived in Chapter 5.

Both AOGR and adiabatic reforming were found to reduce the cell voltage compared to WR and isothermal reforming for the same stack power. In addition, higher stack currents were required to maintain the desired operating temperature. Although this limited the efficiency at stack level, the system efficiency was shown to increase in some cases due to a reduced parasitic power consumption by the air blower. However, the temperature gradients increased considerably when adiabatic reforming was used.

7.2.2. REFORMING IN SOFC-COMBINED CYCLES

The integration options of SOFCs with thermal cycles investigated in Chapter 3 were based on a single reforming concept to enable a direct comparison of the results. AOGR and adiabatic reforming were selected, since this optimises the use of heat and steam from the electrochemical reaction for reforming and, therefore, maximises the exergy available in the thermal cycle. However, the evaluation of different reforming concepts in Chapter 6 showed that AOGR and adiabatic reforming reduce the power density and increase the thermal stresses in the stack compared to WR and isothermal reforming.

Other combinations of either AOGR or WR and either adiabatic or isothermal reforming may be applied to SOFC-combined cycles as well. However, they may affect various integration options differently. For example, condensing steam from the exhaust gasses is more difficult if the temperature or air overstoichiometry is high, which is typically the case for SOFC-gas turbine combined cycles. In addition, isothermal reforming requires high temperature heat, which compromises the available heat for additional power generation in a thermal cycle.

Figure 7.1a shows the pressurised SOFC-gas turbine cycle as analysed in Chapter 3. WR may be difficult in this integration scheme, since exhaust gases typically have a high temperature and are possibly diluted with air bypassed to the combustor. Moreover, high TITs are required to ensure that the turbine outlet temperature is sufficient to recuperate heat, and the increased pressure drop affects the turbine work negatively. Therefore, adiabatic pre-reforming and AOGR seem most appropriate for this system. The reduction in the cell voltage compared to isothermal pre-reforming and WR may be compensated by the lower fuel utilisation and higher operating pressure. Moreover, the cathode air inlet temperature can be increased with only limited additional exergy losses, due to adiabatic temperature rise in the compressor.

Figure 7.1b shows a modified version of the atmospheric pressure SOFC-gas turbine combined cycle Chapter 3, in which the adiabatic pre-reformer is replaced by a heated isothermal pre-reformer. Although WR is still difficult in this scheme due to the high exhaust temperatures, potentially high air overstoichiometry and increased pressure drop, the high temperature exhaust gases can be used to heat the reformer without decreasing the TIT or mass flow in the gas turbine. It was shown in Chapter 6 that isothermal pre-

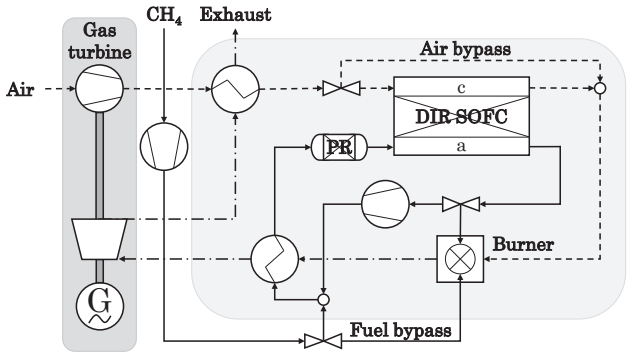

(a) Pressurised SOFC-gas turbine combined cycle with adiabatic pre-reforming and AOGR.

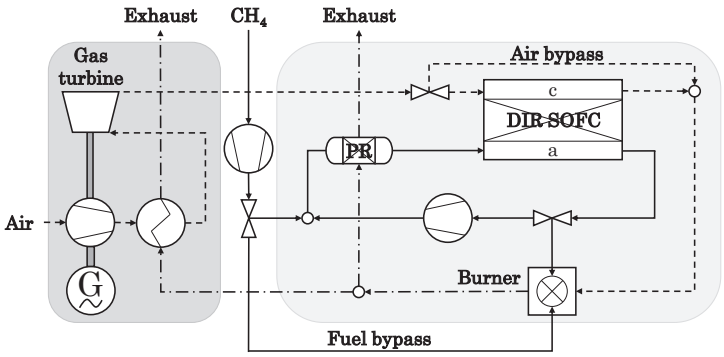

(b) Atmosperic pressure SOFC-gas turbine combined cycle with isothermal pre-reforming and AOGR.

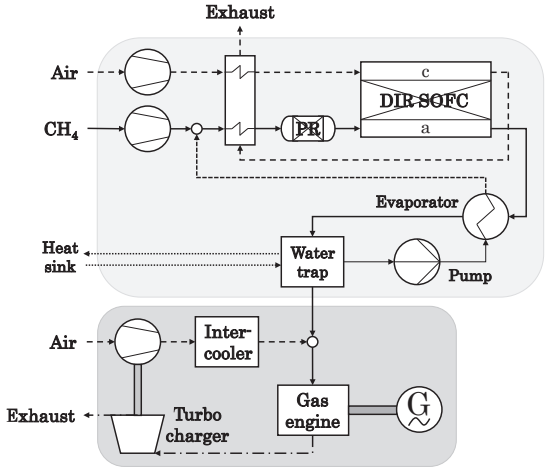

(c) SOFC-reciprocating engine combined cycle with adiabatic pre-reforming and WR.

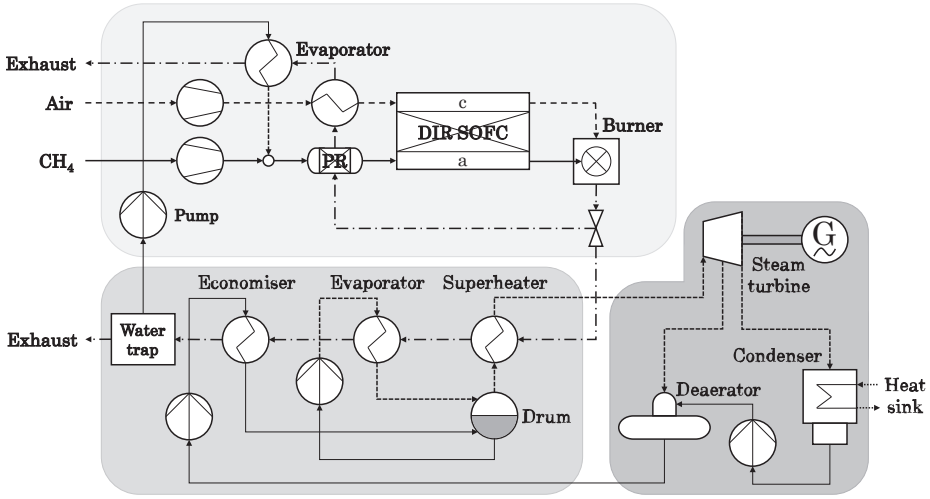

(d) SOFC-steam turbine combined cycle with isothermal pre-reforming and WR.

Figure 7.1: Flow sheets of the investigated stand-alone and combined cycle configurations.

reforming increases the power density in the stack and reduces the thermal stresses compared to adiabatic pre-reforming. Isothermal pre-reforming increases the air flow required to cool down the stack, but the turbine provides the additional power for the compressor.

WR is straightforward in SOFC-reciprocating engine combined cycles: water is already condensed from the anode outlet gases prior to the engine, since it has an adverse effect on the combustion characteristics of the gas mixture. This water may be evaporated with

the hot anode off-gas, which is already cooled to condensate steam out and improve its combustion characteristics, and mixed with fresh fuel. Adiabatic pre-reforming may be the most feasible solution, since no heat is available for pre-reforming from an afterburner. An example of such a layout is shown in Figure 7.1c.

The exhaust gas temperatures from the SOFC-steam turbine combined cycle are typically low, due to the relatively low temperature driving force in the evaporator and economiser. The additional back pressure affects the power consumption by the air and fuel blowers, but not the power generated in the steam turbine. Therefore, Figure 7.1d shows a layout of a SOFC-steam turbine combined cycle with WR from the HRSG exhaust. In addition, a part of the high temperature burner exhaust gases is used to isothermally pre-reform the fuel. This enables high operating voltages in the SOFC and, therefore, high combined cycle efficiencies. However, it should be noted that high air overstoichiometries may still limit water recovery from the exhaust gases in this system.

7.2.3. SOFC DEVELOPMENT STATUS

SOFC systems have been under development for several decades. The majority of these systems is configured to use natural gas or biogas, as both are widely available. Thousands of micro-CHP systems with a capacity of about 1 kW electric have been deployed in Japan and Europe [310]. Some of these systems have demonstrated electrical efficiencies in excess of 60% based on the LHV [41]. However, the capital cost is typically still too high to have a decent return on investment without governmental support programs [213].

Nowadays, SOFC are applied on considerable scale as grid-independent power for critical loads, for example in data centres, delivering up to 250 kWe for a single unit with LHV efficiencies in excess of 50% [311]. SOFCs are selected for these applications because of their high reliability and availability and low operating costs compared to the local electricity grid, but government funding schemes are usually still required to cover the relatively high capital costs [59, 312].

SOFC-based APUs have been developed for a variety of applications, for example as an alternative for idling truck engines [313]. Similar systems have been developed for unmanned aerial vehicles, range extenders in electric cars, portable power generators, vessels, airplanes and military applications [175, 290, 314–317]. These systems typically use a diesel or other conventional transport fuels, and the electrical efficiency is typically sacrificed for power density and rapid cold-start capability [318].

Demonstrators of SOFCs combined with gas turbines have been developed by the Siemens Westinghouse Power Corporation and Rolls-Royce Fuel Cell Systems, later acquired by LG Corp, with power ratings of 220 and 250 kW electric respectively [311, 319]. More recently, Mitsubishi Hitachi Power Systems developed a SOFC-gas turbine combined system for electric powers up to 1 MW, named MEGAMIE [320]. A 250 kW system demonstrator of the system was successfully operated for 10,000 hours and achieved an electrical efficiency of 55% based on the LHV.

7.3. MARITIME POWER AND ENERGY REQUIREMENTS

7.3.1. TOWARDS EMISSION-FREE SHIPPING

The shipping sector plays an important role in global trade, food supply, harvesting of offshore energy, whether from fossil or in the future renewable sources. Today, the sector relies primarily on fuels from fossil feedstock and diesel engines for propulsion and electricity generation [5]. Although this is cost effective and reliable, the use of fossil diesel fuel results in GHG, PM and SO_X emissions [10]. In addition, diesel engines emit VOCs due to incomplete combustion, and NO_X due to the high combustion temperatures and pressures [6].

The IMO targets a reduction in the GHG emission of 50% relative to 2008 to make shipping more sustainable [9]. In addition, stringent limits have been announced on NO_X and SO_X emissions, most notably in ECAs [10]. Therefore, it is expected that fossil fuels will eventually be replaced by renewables. Moreover, clean technologies for on-board power generation are highly desired. The shipping industry will have to start adopting alternative fuels and drives systems already in the years to come to meet these targets, since vessels are typically in service for several decades.

The use of so-called *drop-in fuels*, such as biofuels or synthetic fuels, may enable the elimination of GHG emissions from the maritime industry [11]. However, it is unclear if these can be produced at the scale and price level required for shipping. Several alternative fuels were discussed in Chapter 2, such as hydrogen, synthetic fuels, alcohols, ethers or ammonia. However, the most suitable fuel choice depends on the entire chain including production, transport, storage, bunkering and use on-board [18]. For example, while hydrogen production from renewable electricity is expected to be cheap compared synthetic diesel, it is more difficult to transport and store. It was shown in Chapter 2 that energy dense fuels may be preferred for ships with longer mission requirements.

Even if fuels from fossil feedstock are eventually replaced by renewable alternatives, the emissions related to the combustion process in diesel engines will pertain, most notably VOCs and NO_X. These may be reduced by improvements to the combustion process or exhaust gas after-treatment, such as selective catalytic reduction [19, 20]. Fuel cells, on the other hand, enable the conversion of fuel into electricity for auxiliaries or all-electric propulsion with high efficiencies and virtually no pollutant emissions [50].

The systems proposed in Chapter 3 can reduce both GHG and pollutant emissions, even if fossil fuels like LNG are used in a transition phase. The fuel consumption is reduced due to the high fuel efficiency, while electricity generation with the SOFC reduces the specific NO_X emissions. The emissions of SO_X are inevitably reduced as a fortunate side effect, since SOFCs tolerate only a very small amount of sulfur and it has to be removed from the fuel stream in the system.

7.3.2. MARITIME ENERGY DEMAND

The shipping sector includes a wide variety of ships, with various dimensions and mission requirements. Examples are:

- Passenger: cruise ships, super yachts and ferries;

- Fishing: trawlers, seiners, drifters, long liners and crabbers;
- Near coastal: barges and tugs;
- Ocean-going: container ships, tankers, bulkers;
- Offshore: exploration, support, production and construction;
- Specialities: dredgers, heavy lift and Roll-on/Roll-off;
- Other: research vessels, non-profit, military and fireboats.

The amount of installed power and energy carried varies from vessel to vessel and depends, among others, on the size of the ship, mission, operational profile and auxiliary systems. The total installed power may vary from hundreds of kWs for smaller inland vessels up to as much as 70 MW for the largest container ship and even over 100 MW for aircraft carriers. Energy is used in multiple forms and for multiple purposes, including:

- Mechanical: propulsion, pumps, compressors, fans, winches, tools etc.;
- Electrical: electrical drives, thrusters, lighting, appliances, sensors, navigation, safety systems etc.;
- Heat/steam: space, fuel, water and cargo heating, cleaning/laundry, evaporators etc.;
- Cooling: intercooler, air conditioning, storage, machinery, sensors etc.

The division between the power consumed for propulsion and auxiliary systems depends largely on the type of vessel and its mission. For example, container ships require primarily mechanical power for propulsion, while dredgers need a substantial amount of mechanical power for their dredge pumps as well [321]. Some vessels, such as super yachts and cruise ships, have a substantial demand for heating, ventilation and air conditioning. Ocean-going fish trawlers have facilities to process and freeze caught fish [322, 323]. Military vessels typically need large amounts of both electric power and cooling for weapon and sensor systems [324].

7.3.3. MARITIME POWER GENERATION

Although the specific power requirements differs between vessels, the vast majority uses diesel engines to generate mechanical power from fuel oils, and sometimes auxiliary boilers for heat. The mechanical power may be used directly for propulsion and other rotary equipment, or is used to produce electricity with a generator. The generated electric power may then be used for propulsion or auxiliaries, such as thrusters, hotel load, ventilation, air conditioning and cooling. Heat is typically distributed in the form of thermal oil, steam or hot water, and cooling in the form of chilled water.

Propulsion and power generation architectures are reviewed by Geertsma et al. [325], including diesel-direct, hybrid and full electric propulsion, electric power generation with diesel generator sets, batteries, fuel cells and hybrids, and electric power distribution

through AC and DC networks. Hybrid and full-electric propulsion can offer advantages if the hotel load is substantial or the operating profile varies, and can reduce maintenance and noise emissions and increase the availability.

Baldi et al. [322] analyses the energy and exergy losses of a cruise ship based on measurements from one year of operation in the Baltic Sea. The ship uses diesel-direct propulsion, diesel generator sets to generate electric power and heat recovery steam generator (HRSG) to recover waste heat from the engines. The results show that 46% of the energy is used for propulsion, while heat and electricity each account for 27% of the energy use on board. This illustrates that less than halve of the energy may be used for propulsion on cruise ships. The authors study the use of SOFCs to generate electricity and heat for the same cruise ship in later work [326].

Figure 7.2 shows an example of a conventional on-board power system. Propulsion power is either produced by the main engines or the electric machines. Electric power is generated by two diesel generator sets and distributed via an AC network to the main consumers, including electric drives, auxiliaries, hotel load and the chilled water plant. In this case, the heating demand of the vessel is covered with heat recovery steam generators installed on the engines and two auxiliary boilers.

An example of an on-board power system with high temperature fuel cells is shown in Figure 7.2. The fuel cells supply electric power via a DC-DC converter to a DC network. DC networks are expected to improve the efficiency and reduce the size and weight of the electric components, but require coordinated control to prevent stability issues and an alternative to the AC circuit breakers [327]. A battery bank is included to provide power during system start-up, transients and peak-shaving. The electric machines are fed through variable frequency drives, and a HRSG is used to recover waste heat from the fuel cell cooling circuit or hot exhaust gases for heat utilities.

7.4. MARITIME APPLICATION OF SOFC SYSTEMS

7.4.1. SYSTEM POWER AND DENSITY

Ships typically have MWs of installed power on board, divided in power required for propulsion and auxiliary electricity generators for hotel requirements. Small inland ships typically already have hundreds of kWs of power installed and larger vessels even over 100 MWs, which is high compared to land-based transportation [328]. Although the division between propulsion and hotel load varies, the latter can be substantial, for example in cruise ships, military vessels and dredgers [321, 322, 324].

Today, the high power ratings of ships are a challenge for most fuel cell suppliers, which typically have a limited production volume. Many PEMFC systems are targeted for automotive application, with stack sizes in the range of 100 kW [16]. SOFC systems modules have been developed for powers up to 300 kW for a single unit, but these units contain a large number of stacks [311, 329]. Although manufacturers have developed SOFC stacks up to 16 kW electric, they are more commonly sized in the range of 0.5 to 5 kW [330].

The space on-board ships for power systems is limited, since it compromises the room available for the mission relevant equipment, such as freight, machinery or passengers.

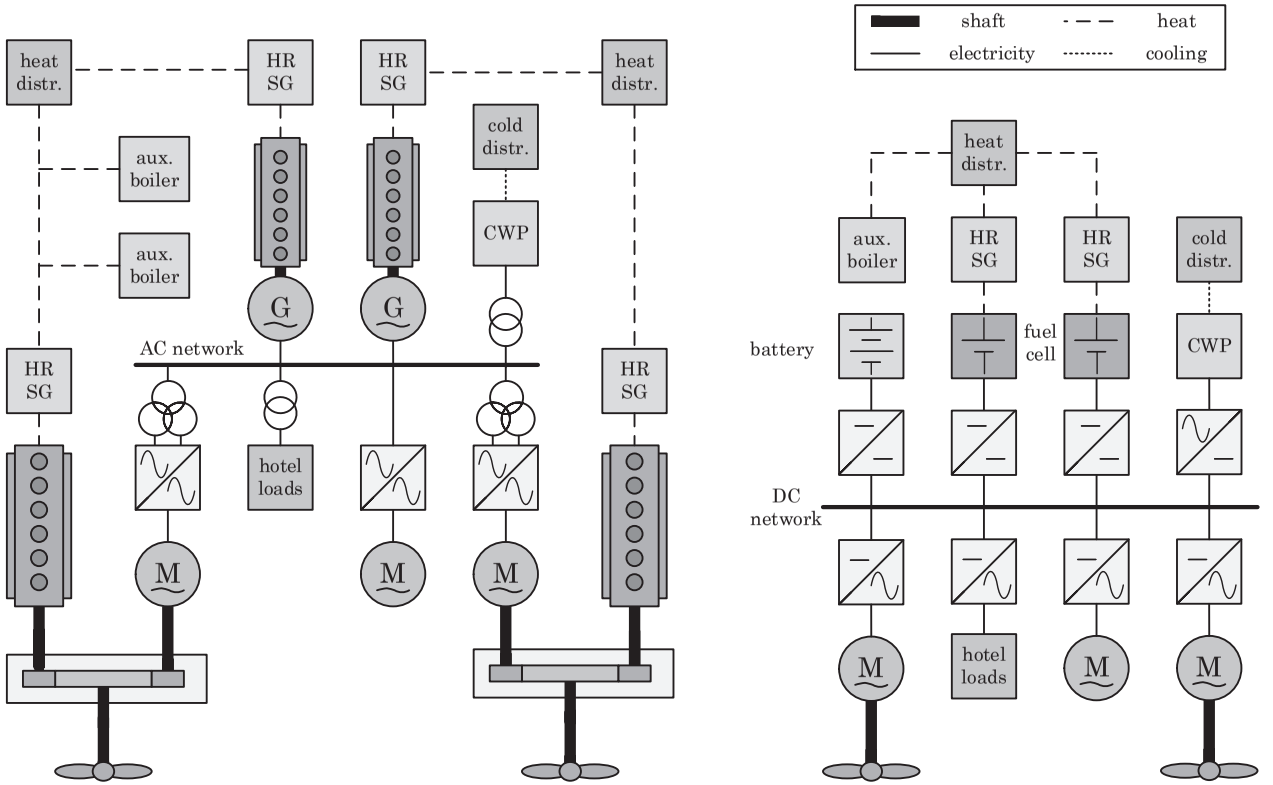

Figure 7.2: Examples of on-board power distribution systems based on hybrid mechanical propulsion, diesel generators and an AC distribution network (left) and based on high temperature fuel cell systems, a battery pack, full electric propulsion and a DC distribution network (right). In both cases heat recovery steam generator (HRSGs) a chilled water plant (CWP) are used to supply heat or steam and cold respectively.

Weight is important as it affects buoyancy and stability of the vessel [331]. Therefore, the power density of the generator and energy density of the logistic fuel have strong implications on the ability of the ship to fulfil its mission.

SOFC systems typically have a limited power density compared to conventional electricity generators and PEMFC systems. This is mostly due to the size of the BoP, which includes heat exchangers, (pre-)reformers, burners, blowers, pumps, filters and power electronics [27]. In addition, high temperature components need appropriate thermal isolation. However, larger systems with proper integration of high temperature components in the so-called *hot box* may achieve higher specific powers than the small-scale systems deployed today.

Although fully optimised SOFC systems may still have lower power densities than diesel-generator sets, their modularity enables to distribute them over the ship. This allows flexibility in the design of the vessel, which is more difficult with conventional diesel engines [332]. Direct mechanical propulsion dictates the location of main diesel engines, while diesel-generator sets cannot be placed close to passenger spaces due to the noise and vibrations they produce. Moreover, small diesel-generator sets have low electrical efficiencies compared to larger ones, while the efficiency of small SOFCs is usually similar to larger systems.

PEMFCs have a high power density if no fuel processing equipment is required [16]. However, the energy density of hydrogen storage systems is limited compared to diesel fuel. As a result, the total system hydrogen fuel cell system may become up to five times larger than a diesel-based solution. Since this compromises the space available for cargo, passengers or equipment, ships with a relatively large bunker space compared to the machinery space may prefer to use more energy dense logistic fuels, such as alkanes, alcohols or ethers, at the cost of a somewhat larger electricity generator. Therefore, SOFCs may offer an interesting solution for vessels with long mission requirements [49].

7.4.2. EFFICIENCY AND LIFE-CYCLE COSTS

The fuel efficiency of power generation largely determines the operating costs of a vessel, the specific emissions and the operating range for a given fuel bunker volume. The efficiency of maritime diesel and gas generator sets is usually in the range of 35-45% [166, 167]. SOFCs have proven their capability to produce electricity from natural gas with efficiencies up to 65% LHV in stand-alone operation, and electrical efficiencies in excess of 70% are projected for combined cycles [42, 44]. In addition, efficiencies of 55% may be achieved by SOFC systems with integrated diesel reformers, and efficiencies in excess of 60% have been achieved with hydrogen fuelling [290, 333].

SOFC systems not only achieve higher electrical efficiencies than reciprocating engine generator sets, they do so at relatively small power scale. For example, electrical efficiencies in excess of 60% LHV have been demonstrated with a 1.5 kWe CHP generator [41]. Moreover, fuel cell systems attain peak efficiencies in part-load, while conventional engine generator sets are most efficient at rated power [334, 335]. Most ships almost never operate at rated power. In addition, small SOFC electricity generators may be placed close to relevant consumers, reducing distribution losses [332].

The fuel costs may be reduced with SOFC-based electricity generation, but as of today

these savings are not sufficient to justify the high capital cost. The cost of SOFC systems is currently in the range of 5,000 to 25,000 \$ kW^{-1} depending on the system size, without installation and mark-up [336]. Although this is at least one order of magnitude higher than heavy duty diesel generator sets, the cost may be substantially reduced by advanced manufacturing and scale-up. Figure 7.3 reproduces results from a bottom-up study by Scataglini et al. [337], expecting that the stack and system cost of SOFC CHP products may be reduced from 5,387 and 14,682 \$ kW^{-1} respectively for an annual production volume of 100 units of 1 kWe, to 166 and 531 \$ kW^{-1} for 50,000 units of 250 kWe. The question is how to get to those production volumes.

Next to the fuel and capital cost, the total cost of ownership of power systems is affected by the system lifetime and maintenance costs. The yearly operating hours of ships vary from 4,000 hours for passenger vessels up to over 6,500 hours for international cargo ships [4]. Engines can achieve total life times of 25 years, but require regular maintenance varying from daily checks and weekly filter cleaning to yearly decarbonisation and, eventually, a complete overhaul once in about five years [338, 339].

The capital cost of automotive PEMFCs is decreasing lately, but these are typically designed to operate for only 5,000 hours. Fuel cell systems have few rotating parts, but the lifespan of the system is limited by degradation of the stack and can thus be extended by regular stack replacement. PEMFC systems for heavy duty applications are typically designed to operate for 80,000 hours, with stack replacement every 20,000 to 30,000 hours [340]. This would result in a system lifetime of 12 to 20 years, with stack replacement required every 3 to 7 years. Stack replacement is expected to be the most substantial maintenance requirement, but inspection, filter cleaning and sensor calibration may be necessary as well [341].

SOFC manufacturers target stack lifetimes of 40,000 to 80,000 hours and even longer system lifetimes, since they typically target stationary applications with an uninterrupted power demand [342]. Early SOFC systems have been reported to require stack replacement after 1.5 to 3 years of continuous operation. More recently, stack lifetimes over 5 years are reported by SOFC manufacturers [343]. A laboratory stack recently reached 100,000 hours of continuous operation, but with a total degradation that is too high for practical applications [344]. Improved stack designs demonstrate substantially lower degradation rates, but time will tell how long they can be operated before stack replacement is economically more attractive.

The degradation and resulting lifetime of fuel cell systems is determined by the materials used and manufacturing quality, but by the operating conditions and operational profile as well. The degradation of SOFC stacks is affected by the number of thermal cycles, due to heating and cooling of the stack, and redox cycles, which occur if the anode is re-oxidised and reduced due to exposure to air [343]. In addition, high temperature gradients, low cell voltages and high cell voltages are reported to increase degradation rates. Therefore, integration with thermal cycles may improve the system lifetime, since fast load transients may be covered by the thermal cycle, and it enables operation at lower fuel utilisation and higher cell voltages [345, 346].

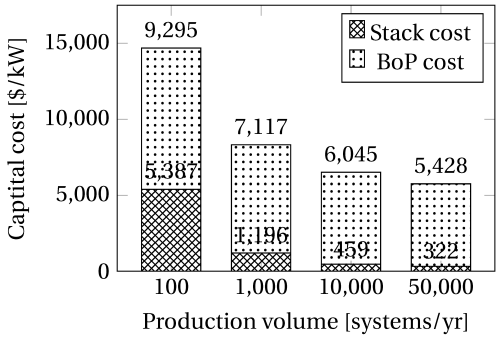

(a) 1 kWe SOFC CHP system.

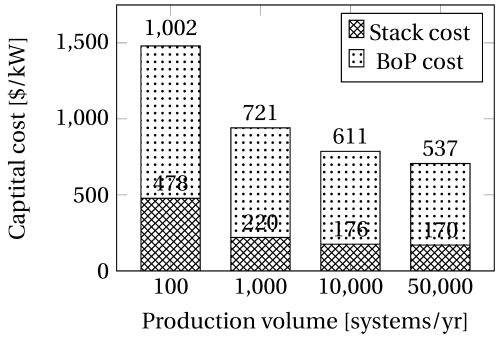

(b) 50 kWe SOFC CHP system.

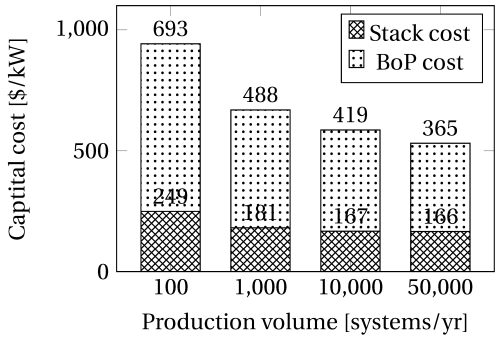

(c) 250 kWe SOFC CHP system.

Figure 7.3: Direct capital stack and BoP cost for 1, 50 and 250 kWe SOFC CHP systems, i.e. without mark-up and installation, from a bottom-up cost estimation by researchers from the University of California [337].

7.4.3. SYSTEM DYNAMICS

Transient capabilities of marine engines and generators are described by two characteristics: the load step acceptance, which is the allowable instantaneous power increment

by adding more fuel before the running into the smoke limit or thermal overloading of the engine, and the time required to speed up the turbocharger and reach a new stable operating point [347]. Diesel engines can typically step about 30% of their power rating instantly, while gas (Otto) engines may be restricted to load steps as small as 10%, depending on the operating point, since fuel injection is restricted by the small margin between engine knock and misfiring [348]. The time required to reach a new stable operating point varies from a few seconds, for high-speed four-stroke engines, up to several minutes for heavy duty two-stroke engines [347].

Automotive PEMFC systems typically have excellent transient capabilities. A cold start takes seconds, while load transients typically take less than a second [349, 350]. The electrochemical reactions respond to load changes in milliseconds, but the BoP needs time to adjust fuel, air and coolant flow to a new operating point. Therefore, a limit on load transients is typically used to avoid increased stack degradation and prolong the lifetime of the system [351]. This is particularly important in heavy duty applications with many operating hours, such as ships.

SOFC system dynamics are usually slow compared to reciprocating engines and low temperature fuel cells. Although the electrochemical reactions are fast, the relatively large thermal mass and BoP dominate the time required to reach a new stable operating point [352]. Rate limiters are usually advised by stack manufacturers, since rapid changes to the operating point may induce potentially deteriorating conditions in the stack, such as high temperature gradients, which induce thermal stresses, or fuel starvation, which may re-oxidise the anode [353].

The cold start-up of SOFCs may take particularly long, and ranges from 30 minutes for low temperature stacks with metal supported cells, targeted for transport applications, to several hours for high temperature systems with electrolyte supported cells, developed for stationary power plants [318, 354]. This is mostly due to the large thermal mass, which has be heated slowly to prevent damage to the stack, typically using the off-gas burner. Once a minimum temperature is reached, electric current can be drawn and support further heating [355].

Load transients are less restricted in SOFCs, since the desired operating temperature is already achieved. The flows provided by the balance of plants components still have to be adjusted, but these have typically much lower time constants than the thermal inertia [356]. A combination of model predictive control and feedback control is typically used to maintain a constant temperature and fuel utilisation in the stack [357]. Nonetheless, the load ramp is typically limited to prevent overshooting and undershooting of critical operating parameters, since the SOFC may need minutes to reach a new stable operating point after the load is changed [353].

7.4.4. RELIABILITY, AVAILABILITY, MAINTAINABILITY AND SAFETY

Power systems are commonly assessed on the basis of the so-called *RAMS parameters*: reliability, availability, maintainability and safety. These qualify the ability of the system to perform its function, remain functional, be repaired if required and not harm its environment. All are crucial for mission critical on-board power systems, as ships are typically operated for many hours on a yearly basis, often in demanding and remote locations

at sea, where loss of power can be catastrophic. Therefore, classification societies have established a framework to certify that vessels comply with relevant rules and technical standards.

Fuel cell systems may offer a number of advantages over conventional systems on RAMS parameters. Fuel cell systems tend to degrade rather than fail due to the limited number of moving parts and limited operating temperatures and pressures [358]. In addition, fuel cell systems are highly modular, which reduces the risk of single-point failures. Efficiency differences between small and large fuel cell systems are typically due to the BoP only, while installing several smaller diesel engines may increase the fuel consumption considerably [332].

SOFC systems usually consist of several 5 to 50 kWe modules, which in turn contain a number of stacks, typically ranging from 1 to 5 kWe, assembled of 30 to 100 cells in series [329]. Although fuel cells degrade over time, a failure in a single cell or stack will not result in significant loss of power in properly designed SOFC systems, since a number of submodules will be installed on most ships [290]. SOFC manufacturers target stack lifetimes in excess of 40,000 hours, since their systems are applied for continuous, uninterrupted power supply in stationary applications [342]. Therefore, SOFC are expected to offer a high reliability and availability [359].

Maintenance in fuel cell systems involves regular inspection and calibration of gas detection systems, occasional replacement of filters and sorbents as well as maintenance to the rotating parts of the BoP, and occasionally stack replacement [360]. The majority of these tasks may be carried out by properly educated crew on-board without compromising the functionality of the ship, due to the modularity of fuel cell systems. More invasive maintenance, such as stack replacement, is a specialist task comparable to an overhaul procedure of a reciprocating engine [361].

The most important safety hazard introduced by fuel cell systems is the use of low flashpoint fuels and presence of flammable gases. However, SOFCs do enable the use of non-hydrogen fuels, such as renewable LNG, alcohols, ethers and ammonia. Although most of these are low flash point fuels as well and may introduce additional safety hazards, such as toxicity, avoiding the storage of large quantities of an extremely volatile flammable gas may significantly reduce safety hazards and related regulatory pressure.

Hydrogen is extremely flammable, can form explosive mixtures, is easily ignited, and is present at some point in any fuel cell system, even if hydrocarbon fuels are used [362]. In addition, toxic carbon monoxide is produced during on-board reforming of hydrocarbon fuels. However, the associated risks can be mitigated by installing forced ventilation, double walled pilings, safety valves and gas detection systems [204]. In addition, the fuel storage and fuel cell installation should be separated from each other as well as safe areas and engine rooms. These and other regulatory aspects are discussed in detail by Vogler et al. [339].

7.4.5. EMISSIONS AND COMFORT

The emissions of GHGs, most notably carbon dioxide, and HAPs, such as NO_X, SO_X, VOCs and PM are an increasing concern for the maritime sector. Therefore, emission regulations are becoming increasingly stringent. Examples are the energy efficiency

design index (EEDI) for vessels, global sulfur limits and the designation of ECA's with stringent limits on SO_X and NO_X emissions. More recently, the IMO agreed to reduce the emissions of GHGs from the maritime sector with 50% by 2050. In addition, the harmful effects on marine life due to underwater noise radiated by ships is becoming increasingly important, especially in port areas.

SOFC systems enable the reduction of all of these emissions. The emissions of CO_2 are reduced even if fuels from fossil feedstock are used, due to the high electrical efficiency, while the absence of a high temperature combustion process results in virtually no NO_X emissions [363]. In addition, SOFCs tolerate a limited amount of sulfur in the fuel, while soot formation is to be avoided to prevent damage to the anode [364]. Therefore, the emissions of SO_X and PM are of no concern. Neither are the emissions of VOCs, since a catalytic after burner is used to oxidise combustible elements in the exhaust gases [365]. As a result, SOFC fuelled with LNG have practically no methane slip, which is a common issue with reciprocating gas engines [5].

Even if fuels from fossil feedstocks are used in the transition towards a fully renewable energy infrastructure, the high electrical efficiency of SOFC systems enables the reduction of GHG emissions compared to the conventional systems. The LHV efficiencies up to 65% for stand-alone systems and in excess of 70% for combined cycle systems are substantially higher than the efficiencies up to 45% of conventional diesel engine generators [166, 167]. However, it should be noted that additional conversion losses are introduced if SOFCs are used for propulsion or hybridised with auxiliary electricity storage components, such as batteries, flywheels and supercapacitors [366].

The GasDrive concept, to which this dissertation contributes, proposes to reduce emissions with LNG, an SOFC-reciprocating engine combined cycle and air lubrication with exhaust gases and drag reducing nano-hull coatings. The adoption of LNG may reduce CH_2 emissions with 25%, compared to diesel, the combined cycle with 30-50% compared to a gas engine, and the combination of air lubrication and drag might reduce fuel consumption by 10-20%. Together, the reduction potential may be as high as 50-70%, which might be sufficient to reach the GHG reduction objective of IMO, depending on the fleet size development.

Fuel cells produce little noise and vibrations, due to the limited number of moving parts in the system. This enables a reduction in the noise radiated by vessels, which is important in several applications, such as marine research vessels, dredgers, super yachts, inland ships and naval vessels, and sensitive areas, for example ports [54]. Moreover, radiated noise is expected to be subjected to future regulations, especially in vulnerable ecosystems [367]. The low noise and vibration profile of fuel cell systems enables improving of comfort for passengers and personnel on-board, as well as power generation close to large consumers without isolation. Rivarolo et al. [332] point out that this offers valuable opportunities for cruise ships.

7.5. CHALLENGES AND OPPORTUNITIES

This section highlights the most important challenges and opportunities of SOFC application on ships, based on the analysis presented in the previous section.

7.5.1. CHALLENGES

Cost and production volume Although the number of applications and total size of the fuel cell market is continuously increasing, the production volume of most fuel cell systems is still limited compared to conventional systems. Today, the supply chains and technical support is typically insufficient for large scale application. SOFC systems are particularly expensive these days, and it is anticipated that the capital cost should be reduced by at least one order of magnitude, which requires a combination of technology development and increased production volume [337].

Power density The limited power density of currently available SOFC systems is a concern for naval architects and marine engineers, since it affects the size allocated for power generation and, potentially, the buoyancy and stability of vessels. However, the modularity of fuel cells relax restrictions to the distribution of power generation systems on the vessel. In addition, it should be noted that the majority of SOFC systems is developed for stationary power generation, for which power density is less critical, and the density of SOFC is usually dominated by the size of the BoP. It should be noted that the relative size of the BoP can be probably decreased for larger power modules.

Load transients The limited load following capabilities of SOFCs pose another important challenge for maritime applications. The transient requirements vary from vessel to vessel, and are, for example, less of critical for a container vessel sailing at constant speed than for a tug boat. Still, hybridisation with auxiliary electricity storage or thermal cycles will be necessary to cope with load steps. Although this increases complexity and introduces additional conversion losses in the drive train, it adds redundancy and enables the power plant to operate in the most efficient point.

Start-up times SOFCs systems are preferably operated continuously to limit the number of start/stop cycles. Although most vessels have a continuous power requirement, even in port, the majority of on-board power systems will be occasionally shut-down. A complete system shut-down may require a long and slow system start-up procedure, during which the system is available for power generation. Moreover, thermal cycling of the stack causes accelerated stack degradation due to mismatches in the thermal expansion coefficients of different layers in the SOFC, limiting its lifetime.

Lifetime Reaching the lifetimes required for stationary applications is typically still a challenge for SOFC systems. Challenges include redox cycling of the fuel electrode, for example at high fuel utilisations, sealing problems or interruption of the fuel supply, as well as thermal stresses induced by internal reforming and load transients, carbon depositing and sulfur poisoning when fuels from fossil origin are used.

7.5.2. OPPORTUNITIES

Fuel efficiency SOFC systems can be configured to produce electricity from a variety of fuels, ranging from hydrogen to low-sulfur diesel, with high efficiencies, especially

when combined with thermal cycles. Therefore, they may reduce the fuel consumption of ships and enable to reduce the fuel cost and storage space. Moreover, high efficiencies reduce the fuel specific emissions as long as fuels from fossil feedstocks are used in the transition towards an energy infrastructure based on renewables. Energy dense fuels can be reformed internally, improving heat integration, enhancing system efficiency and reducing the size and cost of the system.

Reduced emissions SOFC systems emit virtually no NO_X, SO_X, PM and VOCs and are, therefore, expected to comply with future emission regulations without the need for exhaust gas after-treatment systems, such as SCRs and scrubbers. This partially justifies a higher investment cost compared to conventional reciprocating engines, which have to adopt expensive counter measures as they face a fundamental trade-off between high efficiencies and low NO_X formation, both favoured by high combustion temperatures.

Improved comfort and safety The low HAP emissions of SOFC systems improves the air quality on deck, enhancing comfort and safety for passengers and working crews. The low noise levels and vibrations produced by fuel cell systems improve comfort on-board as well. SOFC power generators may be distributed over the vessel without an increase in fuel consumption or the need for noise and vibration isolation. Therefore, they may be located close to large consumers, which reduced transmission losses and improves redundancy.

Combined heat, cooling and power The high operating temperature of SOFCs enables further use of the heat produced by the electrochemical reaction, which may be used for space and water heating, thermal bottoming cycles, absorption refrigeration systems or combinations of these. For example, Ozcan et al. [368] proposed a system based on an internal reforming SOFC, organic Rankine cycle and adsorption chiller producing electric power, hot water and space cooling. Such systems are especially interesting for application with a substantial heating or cooling requirement, such as cruise ships, super yachts and fishing vessels. Figure 7.4 shows an example of a trigeneration system producing electricity, heat and cooling with a SOFC system combined with a reciprocating engine and adsorption refrigeration cycle.

Combined cycles Integration with thermal cycles enables high electrical efficiencies. The specific investment cost may be reduced as well, since conventional power systems are typically more affordable. In addition, gas turbines and reciprocating engines have good transient capabilities and can quickly adjust to changing loads, giving the SOFC system time to adjust to the new operating point. Moreover, the SOFC can be operated at a relatively low fuel utilisation, and the stack current may not have to be increased to compensate for power losses due to degradation. Both may reduce degradation and increase the lifetime of SOFC stacks.

Hybrid systems Even if SOFCs are not physically integrated with thermal cycles, hybridisation may provides additional advantages for ships. For example, SOFCs may be used to provide continuous base load electricity with high efficiencies, while reciprocating

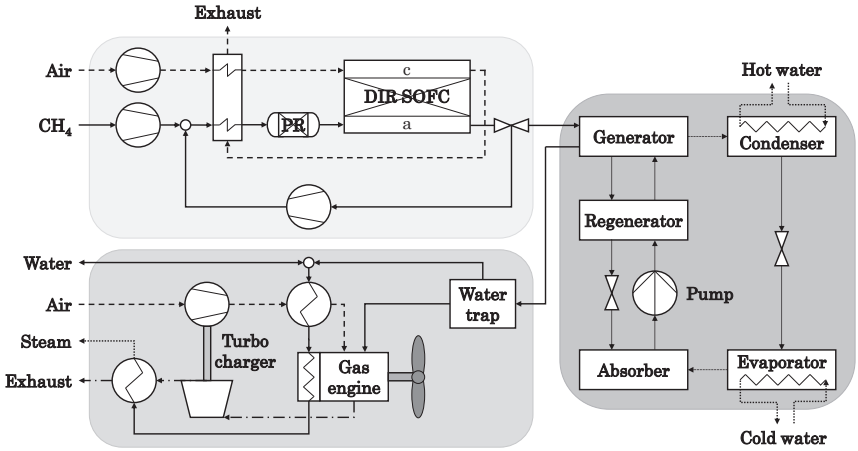

(a) Flowsheet of a SOFC-reciprocating engine-absorption refrigeration trigeneration system.

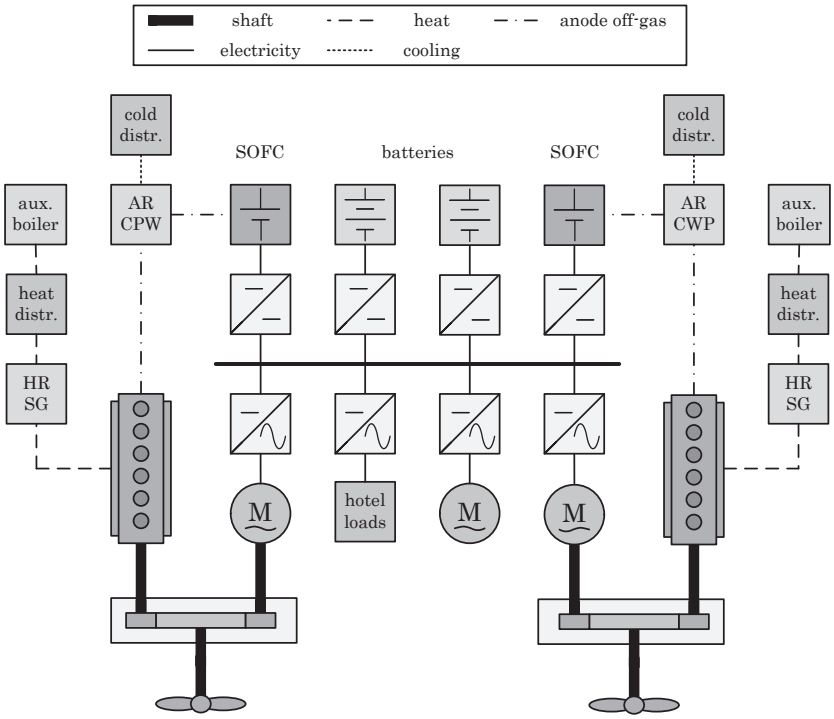

(b) On-board configuration based on two SOFC-reciprocating engine-absorption refridgeration trigeneration systems.

Figure 7.4: Flow sheet of a trigeneration system based on a SOFC-reciprocating engine combined cycle (Figure 7.4a) and possible on-board system layout (Figure 7.4b) The absorption refrigeration cycle uses heat from the anode off-gas, and a HRSG is installed on the gas engine. Moreover, the gas engine can be used for direct mechanical propulsion.

engines or gas turbines deal with interrupted and transient loads. In addition, auxiliary energy storage systems, such as batteries, super capacitors or flywheels may be used to cover for the limited transient capabilities and enable operating the SOFC at its most efficient load.

Lifetime Although system lifetimes are still a challenge to most SOFC developers, stack lifetimes in excess of 40,000 hours can be achieved, which is long compared to other fuel cell technologies. Stack lifetimes of PEMFCs are, for example, usually limited to 20,000-30,000 hours. A stack lifetime of 40,000 hours implies that the stack has to be replaced every 6 to 10 years in most commercial vessels, which is comparable to current engine overhaul intervals. Moreover, the reduced number of rotating parts may reduce maintenance requirements compared to conventional engines.

Reliability and availability Today, SOFCs are commonly used in stationary mission critical applications, such as datacentres. Their modularity, limited number of moving parts and tendency to degrade rather than fail make SOFC systems a reliable power source with a high availability, which is important for on-board power generation systems as well. Therefore, application of SOFC systems on ships may improve redundancy and availability of on-board power systems and potentially allow the removal of superfluous back-up power systems.

7.6. STATUS AND OUTLOOK

7.6.1. STATUS

Attractive prospects, such as high efficiencies and low emissions, have motivated a number of studies and demonstrators of SOFC systems for ships. Already back in 2001 Rolls-Royce Strategic Systems Engineering released a report on the application on various fuel cell types in surface ships, including SOFCs. Despite almost twenty years of further development, the conclusions back then regarding the efficiency, emissions, power density and transient response still hold.

A few years later, two major research and demonstration projects on maritime SOFC application commenced. The FELICITAS project investigated SOFC application in heavy-duty transport applications, including ships [369]. However, marinisation and demonstration of a SOFC system was impeded by the low power density and restricted maturity of core components. Trigeneration system concepts based on SOFC integration with gas turbines and absorption refrigeration cycles for combined power, heating and cooling were studied as well [179].

A 20 kWe SOFC APU fuelled with methanol was developed in the METHAPU project and demonstrated in 2010 on the car-carrier 'Undine'. A comparative LCA of methanol fuelled SOFC APUs was carried out during the project [118]. The results from the METHAPU project motivated the development of a conceptual design of an offshore supply vessel with two 250 kWe SOFC APUs fuelled with methanol [187].

The SchIBZ project started in 2009 with the objective to develop a 500 kWe fuel cell APU with an integrated reformer for low-sulfur diesel. Initial system studies showed that

electrical efficiencies up to 55% can be achieved by a SOFC based system [53]. This was later confirmed in a detailed exergetic analysis, trough optimisation of the oxygen-to-carbon ratio and RR in the system [370, 371]. A 50 kWe demonstrator was developed, achieving a gross electrical efficiency of 50% with potential for further improvement [290].

The interest in maritime application of SOFCs is increasing lately, due to the urgency of the energy transition in the maritime industry, adoption of alternative ship fuels, such as LNG, and rapid development of fuel cell technology in other sectors. For example, the application of SOFC was considered for an arctic patrol vessel, a naval vessel collecting, processing and transmitting acoustic data and a naval surface vessel [73, 80, 372].

The work in this dissertation is carried out in the Dutch national GasDrive project, which commenced in 2016 and aims to *minimise emissions and energy losses at sea with LNG combined prime movers, underwater exhausts and nano hull materials.* This includes the application of internal reforming SOFCs combined with thermal cycles, most notably reciprocating engines, the conventional solution for maritime power generation. Such a hybrid system is expected to achieve high efficiencies at reduced capital cost, increased power density and improved transient capabilities. The development of a technology demonstrator is foreseen in future follow-up research projects.

The application of SOFCs in shipping was the subject of at least nine scientific publications in the last year alone, which clearly demonstrates the incremental interest on the subject [226, 326, 332, 359, 370, 371, 373–375]. This includes publications related to the SchIBZ and GasDrive projects, two studies on the application of SOFCs in cruise ships, an analysis for a water taxi, and an investigation of a SOFC-gas turbine combined system for an ethane carrier.

7.6.2. OUTLOOK

The interest in SOFC application on ships is increasing in recent years, mostly driven by the need to reduce emissions of GHGs and HAPs, the increasing availability of LNG as a bunker fuel for ships and the maturing SOFC systems fuelled with natural gas for land-based stationary applications. SOFC based power systems have the potential to generate electricity, heat and cooling on-board with high efficiencies, practically no hazardous emissions and producing little noise and vibrations with high reliability and availability.

SOFC systems may become a serious alternative for the conventional electricity generators based on reciprocating engines only once the remaining challenges, such as the low power density, limited transient capabilities and safety hazards, have been appropriately addressed. However, scaling and cost reduction remain the most important challenge for all fuel cell suppliers. These challenges can only be appropriately addressed by coordinated action of multiple stakeholders involved.

The increasing uptake of LNG as a ship fuel facilitates the demonstration of existing SOFC products onboard. These projects allow to solve integration issues on vessels, investigate the impact of the marine environment on the system operation and lifetime, and develop safety standards and class rules. The demonstration phase may be followed by the introduction of small SOFC APUs for mission critical systems.

Results of several on-going projects are expected in the near future, for example of the 50 kWe SOFC system with an integrated low-sulfur diesel reformer developed in

Table 7.1: An overview of research projects and publications on the maritime application of SOFCs.

Projects

Period	Acronym	Topic	Projcect lead
2005-2008	FELICITAS	Development of a SOFC-GT system for heavy duty transport	Fraunhofer Institute
2006-2009	METHAPU	Demonstration of a 20 kW methanol-fuelled SOFC APU on-board	Wärtsilä Corporation
2009-2016	SchIBZ	Development of a 50 kW SOFC APU with integrated diesel reformer	ThyssenKrupp MS
2016-2020	GasDrive	Maritime application of LNG-fuelled SOFC-combined cycles	TU Delft
2017-2022	SchIBZ 2	On-board demonstration the SOFC with integrated diesel reformer	ThyssenKrupp MS

Publications

Year	Topic	Authors
2001	An analysis of the application of fuel cells, including SOFCs, in surface ships	Bourne et al. [173]
2010	Comparative LCA of methanol-fuelled SOFCs as APU on-board ships (METHAPU)	Strazza et al. [118]
2011	SOFC-GT trigeneration system for marine applications (FELICITAS)	Tse et al. [179]
2012	Design of different diesel based fuel cell systems for seagoing vessels (SchIBZ)	Leites et al. [53]
2012	Design of a green arctic patrol vessel with hybrid SOFC electricity generation	Weidle et al. [372]
2012	Investigation into the shipboard integration of SOFCs a military patrol vessel	Cohen et al. [73]
2013	Design and thermodynamic analysis of an SOFC system for naval surface ships	Ezgi et al. [80]
2013	Thermodynamic analysis of an SOFC-GT power plant for marine applications	Welaya et al. [376]
2014	Conceptual design of an offshore platform supply vessel, methanol-fuelled SOFC APU	Díaz-de-Baldasano et al. [187]
2016	General review of maritime fuel cell application, including SOFCs	van Biert et al. [49]
2017	Development of a maritime 50 kW SOFC demonstrator with integrated diesel reformer	Nehter et al. [290]
2018	Exergy analysis of the diesel pre-reforming SOFC system with AOGR (SchIBZ)	Huerta et al. [370, 371]
2018	Energy management of a cruise ship with different distributed generation technologies	Rivarolo et al. [332]
2018	Integration of solid oxide fuel cells in cruise ship energy systems	Baldi et al. [326]
2018	Performance and availability of a marine SOFC-GT system in an ethane carrier	Ahn et al. [359]
2018	Thermodynamic comparison of different SOFC-combined cycles	van Biert et al. [226]

the SchIBZ project. This system is to be demonstrated on board the MS Forester in the recently commenced follow-up of the program. New demonstration projects may be expected in the near future, for example on cruise ships, which are increasingly adopting LNG as a low-emission alternative to diesel and combine a high demand for electric power, heating and cooling with a requirement for passenger comfort.

The deployment of SOFCs as main auxiliary power system will require the development of dedicated maritime products with improved power generation capacity, power density, transient capability and lifetime, at a lower capital cost. Waste heat recovery systems may be employed as well. Next to LNG, SOFC systems should be configured to run on renewable alternatives introduced in the maritime industry, for example methanol or ammonia.

Integration with thermal cycles is a long term endeavour, due to the added complexity of these systems. However, integration with reciprocating engines seems interesting for ships, as they are expected to offer more flexibility, a higher power density and a lower cost compared to more sophisticated alternatives. In addition, such systems may facilitate the use of SOFC systems for propulsive power by improving transient capabilities.

8

CONCLUSIONS AND RECOMMENDATIONS

8.1. CONCLUSIONS

Global agreements force the shipping sector to reduce the emissions of GHGs, HAPs and radiated noise of their operations. Therefore, ship owners are actively exploring the adoption of alternative fuels, for example LNG, hydrogen and other synthetic fuels, and clean energy conversion technologies, such as fuel cells. SOFC can generate electricity from energy dense hydrocarbon fuels with high efficiencies while producing few hazardous compounds and radiating little noise. Even higher efficiencies may be attained if the fuel is internally reformed and thermal cycles are used to generate additional electricity from heat or unburned fuel in the exhaust gases. Therefore, this dissertation aimed to *determine how SOFCs can be integrated with reforming and thermal cycles to reduce the emissions of ships.* More specifically, the following contributions were made:

- Maritime fuel cell application was reviewed;
- SOFC integration concepts with thermal cycles were thermodynamically analysed and compared;
- Dynamic models of a DIR SOFC stack and single cell setup were developed and validated;
- MSR was studied experimentally on single SOFCs with Ni-GDC anodes to determine intrinsic DIR kinetics;
- Reforming concepts in SOFC systems were analysed and compared with stack and system simulations;
- Maritime application of SOFC systems was analysed and discussed.

The following conclusions are drawn regarding these contributions:

Maritime fuel cell application Maritime application was reviewed in general with regard to fuel efficiency, gravimetric and volumetric density, dynamic behaviour, environmental impact, safety, regulations and economics. This showed that liquefied hydrogen-fuelled LT-PEMFC systems may be suitable for ships with refuelling options after several hours, but high temperature fuel cells and more energy dense fuels, such as alkanes, alcohols, ethers or ammonia, may be preferred for vessels with longer mission requirements. However, hybridisation with thermal power plants or auxiliary electricity storage may be required to make up for the limited transient capabilities. In addition, the power density of fuel cell systems has to be increased, the capital cost substantially reduced and classification standard for maritime fuel cell systems need to be further developed.

SOFC integration with thermal cycles The integration of SOFCs with steam turbines, reciprocating engines and gas turbines was thermodynamically analysed and compared for a range of fuel utilisations, cell voltages, stack temperatures and gas turbine compression ratios. In addition, an exergy analysis was used to assess the thermodynamic losses in individual components and identify potential improvements for the investigated SOFC-combined cycles.

The thermodynamic analysis shows that the electrical efficiency of SOFCs combined with steam cycles or reciprocating engines increases for higher fuel utilisations, while an optimum exists for integration concepts with gas turbines. This optimum depends on the SOFC operating parameters, since it occurs when the SOFC afterburner outlet temperature matches the desired TIT. Matching of the HRSG and SOFC afterburner temperature enhances the efficiency of the steam turbine combined cycle, while the efficiency of SOFC-gas turbine combined cycles may be further improved by adjustment of the gas turbine pressure ratio. A substantial amount of exergy is destroyed in the moisture separator of the reciprocating engine combined cycle.

The comparison of different SOFC-combined cycles shows that electrical efficiencies in excess of 70% can be achieved by integration with steam turbines at high cell voltages, high fuel utilisations and low stack temperatures. The reciprocating engine combined cycle has similar characteristics, but achieves slightly lower electrical efficiencies. Integration with gas turbines is more efficient at low fuel utilisations, moderate cell voltages and high stack temperatures. This may yield smaller systems and reduced capital costs, since higher power densities can be achieved at these conditions.

Dynamic modelling of DIR SOFC stacks 1D dynamic models of a SOFC stack and single cell test station were developed to analyse the effects of DIR, off-design conditions and load transients on the temperature distribution and power density. The stack model was validated with load curves reported by the stack manufacturer for three different fuel compositions, while the single cell model was used to validate two kinetic MSR models fitted to date derived on single cells in earlier work. Both kinetic models were implemented in the stack model to simulate temperature profiles with DIR. In addition, a load transient from zero to rated power was simulated.

Validation of the stack model for three different fuel compositions suggests that the hydrogen pressure affects the anode activation overpotentials significantly. A global square root dependency on the hydrogen partial pressure shows good agreement with the power curves reported by the manufacturer. The two MSR models predict different temperature profiles for DIR, indicating that further study on the intrinsic rate limiting kinetics is required. The transient simulations show that a step change in the stack current results in severe undershooting of the cell voltages and a peak in the local temperature gradients. This can be avoided by limiting the current ramp rate, but in that case it takes more time to reach the requested stack power.

Experimental study on DIR kinetics The influences of the methane, steam and hydrogen partial pressures and temperature on the MSR reaction were experimentally studied on a single cell with Ni-GDC anodes. Experimental methane conversions were measured and used to regress parameters for different kinetic DIR models with an isothermal IPFR model. The models were then subsequently discriminated and compared to identify a plausible rate determining mechanism.

A LH mechanism consistent with associative adsorption of methane and dissociative adsorption of steam shows good statistical agreement with the experimental data, provides a simple and physically sound explanation and is thermodynamically consistent. The kinetic model is in good agreement with results obtained in previous experiments on

similar single cells with Ni-GDC anodes as well.

Reforming concepts in SOFC systems The LH kinetics obtained from the experimental study were implemented in the dynamic stack model to simulate temperature profiles and cell voltages for various reforming concepts in SOFC systems, based on either allothermal or adiabatic pre-reforming and either WR or AOGR. The cell voltages from the stack simulations were then implemented in thermodynamic system models for an overall comparison of the electrical efficiencies, power densities and temperature gradients in the stack.

Both adiabatic reforming and AOGR reduce the cell voltage compared to allothermal reforming and WR. In addition, adiabatic reforming induces high temperature gradients in the stack. AOGR increases the stack power density compared to WR for low global fuel utilisations, but this trend reverses for fuel utilisations over ~ 0.76. Allothermal pre-reforming and water recirculation result in the highest stack and system efficiencies, but high stack efficiencies do not necessarily result in high system efficiencies. For example, high degrees of DIR lower the stack temperature, cell voltage and stack efficiency, but reduce the parasitic power consumption by the cathode air blower as well.

Maritime application of SOFC systems Maritime application of SOFC systems was analysed, discussing power density, efficiency, life-cycle costs, dynamics, reliability, availability, maintainability, safety, emissions and comfort. It is concluded that capital cost and start-up times need to be reduced, and load following capabilities and power density require improvement. However, SOFC systems can provide electricity, heating and cooling from a variety of fuels with high efficiency, reliability and availability, while they produce virtually no HAPs, noise and vibrations. Therefore, SOFC system integration with reforming and thermal cycles may provide the enabling technology for the transition of the maritime sector towards emission-free shipping.

8.2. RECOMMENDATIONS

Several integration concepts of SOFCs with thermal cycles were shown to achieve high electric efficiencies. However, variations in the SOFC operating conditions were affected the investigated combined cycles systems differently. These operating parameters determine the power density in the stack and load sharing between the SOFC and thermal cycles as well, and consequently affect the capital cost of these systems. Therefore, a trade-off may exist between high efficiencies, yielding low operating costs, and high power densities, reducing the capital costs. This trade-off may be explored, for example, by analysing the levelised cost of electricity. In addition, part-load and transient operation need further study to determine the total fuel saving potential for ships.

Integration of SOFCs with reciprocating engines is still a relatively new and unstudied concept, and the design investigated in this work is only one of many possible system layouts. For example, heat recovery from the engine exhaust gases for pre-heating or pre-reforming, as well as shared use of the turbocharger can enhance the combined cycle efficiency. However, both options compromise the ability to operate the SOFC and engine independently and complicate the system. Alternatively, the gas engine may be operated

only partially on anode off-gas. Although this would reduce the combined cycle efficiency, it may enhance the operational flexibility, increase the specific power of the engine and reduce the capital cost.

Validation of the stack model for three different fuel compositions suggested that the partial pressure of hydrogen, and possibly steam, affect the anode activation overpotential significantly. This may be partly due to the equipotential effect described by Bessler et al. [274], and partly due to the rate determining step in the electrochemical reaction, which may vary for different anode materials and operating conditions. Since the hydrogen and steam partial pressure vary substantially from inlet to outlet in SOFCs, the rate determining mechanism of the electrochemical hydrogen oxidation reaction should be determined for relevant anode materials and operating conditions.

The one-dimensional DIR SOFC models developed in this dissertation are formulated dynamically and can, therefore, be used to model transient operation. However, the transient simulations could not be validated due to a lack of data, which should be taken up in future work. In addition, the stack model can be integrated with BoP component models, such as reformers, heat exchangers, blowers and afterburners, or with thermal cycles, to study part-load and transient operation of integrated systems and develop adequate control strategies.

Rate determining MSR kinetics were derived in this dissertation for ESCs with Ni-GDC cermet anodes at temperatures of 700-775°C. However, the rate determining mechanism may change for other cell designs, for example anode supported, and anode materials, such as Ni-YSZ. In addition, other cells may be operated at different temperatures and pressures. The methodology presented in this dissertation may be used to obtain DIR kinetics for those cell and stack types as well.

Methane was used in this dissertation as a model fuel, because it is a simple, stable and abundant hydrocarbon molecule and the main constituent of LNG. However, other fuels, such as hydrogen, ammonia, methanol or other synthetic fuels may become relevant in the future. Therefore, the systems analysed in this dissertation may be adjusted for other fuels to calculate the electrical efficiency and study integration with fuel processing or thermal cycles. The dynamic stack model and MSR kinetics may be used without notable adjustments, provided that an ammonia cracker or pre-reformer converts the fuel of choice into a mixture of hydrogen and/or nitrogen, steam, carbon monoxide, carbon dioxide and methane. However, the kinetics of the ammonia cracking reaction may have to be determined if ammonia is to be used without external conversion.

SOFC application on ships is primarily impeded by the high capital cost, limited transient capabilities and absence of classification rules and standards. However, it is expected that the capital cost will decrease in the coming years as the technology matures and production volumes for stationary application increase. In the meantime, improvement of the transient capabilities or integration with auxiliary electricity storage components should be further studied. In addition, experience is preferably gained with on-board demonstration systems, to identify and address issues related to on-board application and develop classification standards.

A

APPENDIX

A.1. DATA FOR RAGONE CHARTS

Table A.1: Gravimetric and volumetric power density and efficiency ranges for heat engine generators, fuel cells and fuel processing equipment, based on literature and commercially available systems. For fuel cell systems, a 50% upper margin is added to account for their limited development state, their modularity, the possible removal of exhaust stacks and sound isolation bedplates, and a smaller cooling system.

Heat engines	**Gravimetric density [W/kg]**	**Volumetric density [W/l]**	**LHV efficiency [%]**
Diesel genset	45-71.5	32.5-55	30-45
Gas genset	45-65	30-45	35-47
Gas turbine genset	100-1200	45-450	25-40
Fuel cell systems			
PEMFC (H_2)	250-1000	300-1550	40-60
MCFC (NG/syngas)	7.75-25	1.75-20	40-55
SOFC (NG/syngas)	8-80	4-32	45-60
Fuel processing			
Ammonia cracker	50-250	50-115	80-90
MeOH SR	25-120	22-45	70-90
DME SR	30-150	40-75	85-95
Diesel SR	20-40	20-50	75-90

A.2. STACK SIMULATION RESULTS

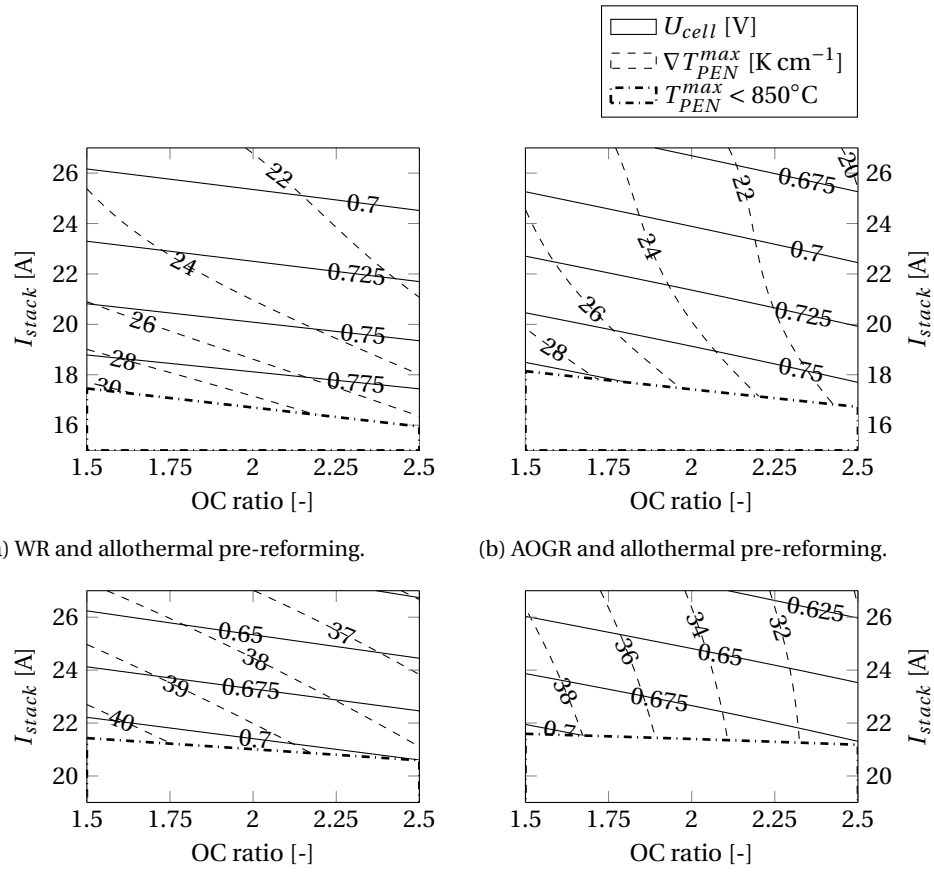

(a) WR and allothermal pre-reforming.

(b) AOGR and allothermal pre-reforming.

(c) WR and adiabatic pre-reforming.

(d) AOGR and adiabatic pre-reforming.

Figure A.1: Cell voltages and maximum PEN temperature gradients in the stack for different reforming configurations, oxygen-to-carbon ratios and stack currents.

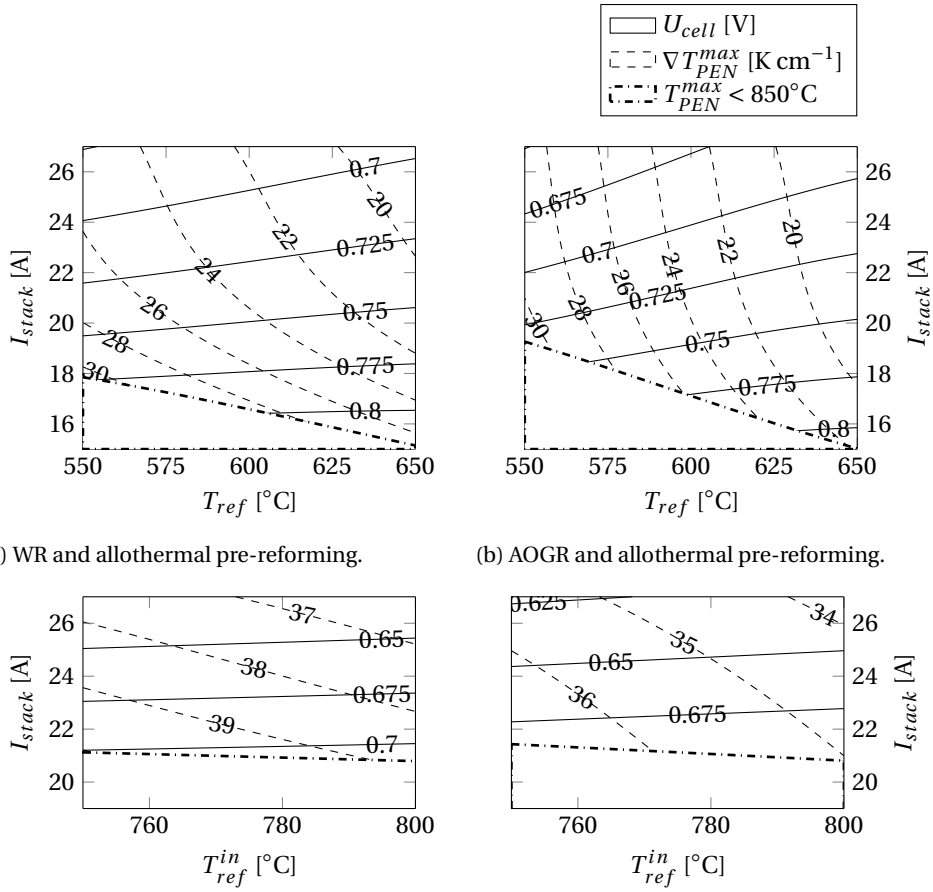

(a) WR and allothermal pre-reforming.

(b) AOGR and allothermal pre-reforming.

(c) WR and adiabatic pre-reforming.

(d) AOGR and adiabatic pre-reforming.

Figure A.2: Cell voltages and maximum PEN temperature gradients in the stack for different reforming configurations, reformer temperatures and stack currents.

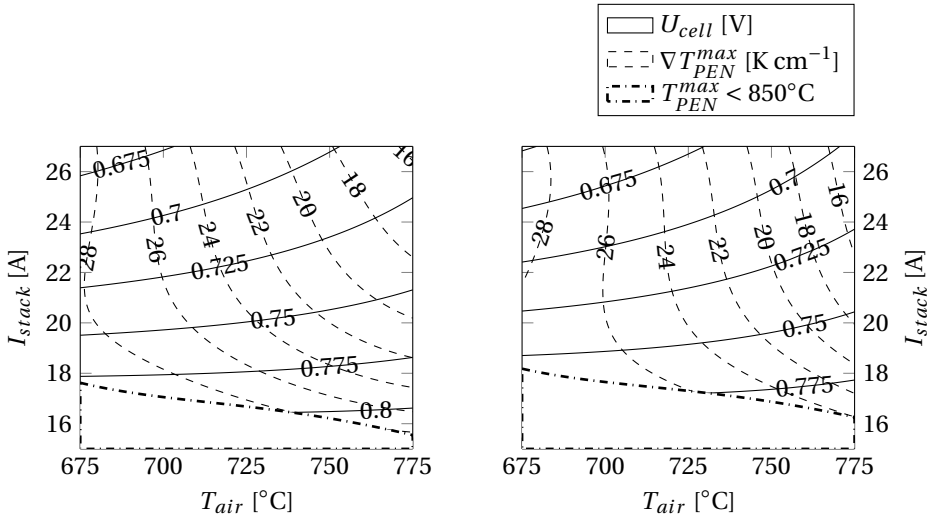

(a) WR and allothermal pre-reforming.

(b) AOGR and allothermal pre-reforming.

(c) WR and adiabatic pre-reforming.

(d) AOGR and adiabatic pre-reforming.

Figure A.3: Cell voltages and maximum PEN temperature gradients in the stack for different reforming configurations, cathode air inlet temperatures and stack currents.

REFERENCES

[1] Z. Kosowska-Stamirowska, C. Ducruet, and N. Rai, *Evolving structure of the maritime trade network: evidence from the Lloyd's Shipping Index (1890–2000),* Journal of Shipping and Trade **1**, 10 (2016).

[2] Ø. Endresen, M. S. Eide, and T. Longva, *Maritime forecast to 2050 - Energy Transition Outlook 2018 - DNV GL*, Tech. Rep. (DNV-GL, 2018).

[3] A. Miola, B. Ciuffo, E. Giovine, and M. Marra, *Regulating air emissions from ships,* The State of the Art on Methodologies, Technologies and Policy Options. Joint Research Centre Reference Report, Luxembourg , 978 (2010).

[4] V. Eyring, H. Köhler, A. Lauer, and B. Lemper, *Emissions from international shipping: 2. Impact of future technologies on scenarios until 2050,* Journal of Geophysical Research: Atmospheres (1984–2012) **110** (2005).

[5] S. Bengtsson, K. Andersson, and E. Fridell, *A comparative life cycle assessment of marine fuels liquefied natural gas and three other fossil fuels,* Proceedings of the Institution of Mechanical Engineers, Part M: Journal of Engineering for the Maritime Environment **225**, 97 (2011).

[6] R. Kurtenbach, K. Vaupel, J. Kleffmann, U. Klenk, E. Schmidt, and P. Wiesen, *Emissions of NO, NO_2 and PM from inland shipping,* Atmospheric Chemistry and Physics **16**, 14285 (2016).

[7] D. Gerard and L. B. Lave, *Implementing technology-forcing policies: The 1970 Clean Air Act Amendments and the introduction of advanced automotive emissions controls in the United States,* Technological Forecasting and Social Change **72**, 761 (2005).

[8] H. J. Schellnhuber, S. Rahmstorf, and R. Winkelmann, *Why the right climate target was agreed in Paris,* Nature Climate Change **6**, 649 (2016).

[9] A. Halff, L. Younes, and T. Boersma, *The likely implications of the new IMO standards on the shipping industry,* Energy Policy **126**, 277 (2019).

[10] S. Brynolf, M. Magnusson, E. Fridell, and K. Andersson, *Compliance possibilities for the future ECA regulations through the use of abatement technologies or change of fuels,* Transportation Research Part D: Transport and Environment **28**, 6 (2014).

[11] L. Zhang and G. Hu, *Supply chain design and operational planning models for biomass to drop-in fuel production,* Biomass and Bioenergy **58**, 238 (2013).

[12] F. Burel, R. Taccani, and N. Zuliani, *Improving sustainability of maritime transport through utilization of Liquefied Natural Gas (LNG) for propulsion,* Energy **57**, 412 (2013).

[13] C. Deniz and B. Zincir, *Environmental and economical assessment of alternative marine fuels,* Journal of Cleaner Production **113**, 438 (2016).

[14] S. de Breucker, E. Peeters, and J. Driesen, *Possible applications of plug-in hybrid electric ships,* in *Electric Ship Technologies Symposium* (IEEE, 2009) pp. 310–317.

[15] J. Kast, R. Vijayagopal, J. J. Gangloff, and J. Marcinkoski, *Clean commercial transportation: Medium and heavy duty fuel cell electric trucks,* International Journal of Hydrogen Energy **42**, 4508 (2017).

[16] T. Yoshida and K. Kojima, *Toyota MIRAI fuel cell Vehicle and progress toward a future hydrogen society,* The Electrochemical Society Interface **24**, 45 (2015).

[17] Y. Ligen, H. Vrubel, and H. H. Girault, *Mobility from renewable electricity: infrastructure comparison for battery and hydrogen fuel cell vehicles,* World Electric Vehicle Journal **9**, 3 (2018).

[18] P. Gilbert, C. Walsh, M. Traut, U. Kesieme, K. Pazouki, and A. Murphy, *Assessment of full life-cycle air emissions of alternative shipping fuels,* Journal of Cleaner Production **172**, 855 (2018).

[19] F. Millo, M. G. Bernardi, and D. Delneri, *Computational analysis of internal and external EGR strategies combined with Miller cycle concept for a two stage turbocharged medium speed marine diesel engine*, Tech. Rep. (SAE Technical Paper, 2011).

[20] T. C. Tow, D. A. Pierpont, and R. D. Reitz, *Reducing particulate and NOx emissions by using multiple injections in a heavy duty DI diesel engine*, Tech. Rep. (SAE Technical Paper, 1994).

[21] A. Azzara, D. Rutherford, and H. Wang, *Feasibility of IMO Annex VI Tier III implementation using Selective Catalytic Reduction,* Tech. Rep. (International Council on Clean Transportation (ICCT) Washington, DC, 2014).

[22] S. M. Correa, *A review of NO_X formation under gas-turbine combustion conditions,* Combustion science and technology **87**, 329 (1993).

[23] Q. Yan, H. Toghiani, and H. Causey, *Steady state and dynamic performance of proton exchange membrane fuel cells (PEMFCs) under various operating conditions and load changes,* Journal of Power Sources **161**, 492 (2006).

[24] F. de Bruijn, *The current status of fuel cell technology for mobile and stationary applications,* Green Chemistry **7**, 132 (2005).

[25] T. Wilberforce, A. Alaswad, A. Palumbo, M. Dassisti, and A. G. Olabi, *Advances in stationary and portable fuel cell applications,* International Journal of Hydrogen Energy **41**, 16509 (2016).

[26] C. Christen and D. Brand, *IMO Tier 3: Gas and Dual Fuel Engines as a Clean and Efficient Solution,* CIMAC **187** (2013).

[27] A. Dicks and D. A. J. Rand, *Fuel cell systems explained* (Wiley Online Library, 2018).

[28] S. C. Singhal, *Solid oxide fuel cells,* The Electrochemical Society Interface **16**, 41 (2007).

[29] N. Minh, J. Mizusaki, and S. C. Singhal, *Advances in Solid Oxide Fuel Cells: Review of Progress through Three Decades of the International Symposia on Solid Oxide Fuel Cells,* ECS Transactions **78**, 63 (2017).

[30] M. C. Tucker, *Progress in metal-supported solid oxide fuel cells: A review,* Journal of Power Sources **195**, 4570 (2010).

[31] Y. B. Matus, L. C. de Jonghe, C. P. Jacobson, and S. J. Visco, *Metal-supported solid oxide fuel cell membranes for rapid thermal cycling,* Solid State Ionics **176**, 443 (2005).

[32] A. B. Stambouli and E. Traversa, *Solid oxide fuel cells (SOFCs): a review of an environmentally clean and efficient source of energy,* Renewable and sustainable energy reviews **6**, 433 (2002).

[33] M. Homel, T. M. Gür, J. H. Koh, and A. V. Virkar, *Carbon monoxide-fueled solid oxide fuel cell,* Journal of Power Sources **195**, 6367 (2010).

[34] P. V. Aravind, J. P. Ouweltjes, N. Woudstra, and G. Rietveld, *Impact of biomass-derived contaminants on SOFCs with Ni/Gadolinia-doped ceria anodes,* Electrochemical and Solid-State Letters **11**, B24 (2008).

[35] N. Laosiripojana and S. Assabumrungrat, *Catalytic steam reforming of methane, methanol, and ethanol over Ni/YSZ: the possible use of these fuels in internal reforming SOFC,* Journal of Power Sources **163**, 943 (2007).

[36] V. Liso, A. C. Olesen, M. P. Nielsen, and S. K. Kær, *Performance comparison between partial oxidation and methane steam reforming processes for solid oxide fuel cell (SOFC) micro combined heat and power (CHP) system,* Energy **36**, 4216 (2011).

[37] D. Mogensen, J.-D. Grunwaldt, P. V. Hendriksen, K. Dam-Johansen, and J. U. Nielsen, *Internal steam reforming in solid oxide fuel cells: Status and opportunities of kinetic studies and their impact on modelling,* Journal of Power Sources **196**, 25 (2011).

[38] V. M. Janardhanan, V. Heuveline, and O. Deutschmann, *Performance analysis of a SOFC under direct internal reforming conditions,* Journal of Power Sources **172**, 296 (2007).

[39] J.-M. Klein, Y. Bultel, S. Georges, and M. Pons, *Modeling of a SOFC fuelled by methane: From direct internal reforming to gradual internal reforming,* Chemical Engineering Science **62**, 1636 (2007).

[40] C. K. Lin, T. T. Chen, Y. P. Chyou, and L. K. Chiang, *Thermal stress analysis of a planar SOFC stack,* Journal of Power Sources **164**, 238 (2007).

[41] R. Payne, J. Love, and M. Kah, *Generating electricity at 60% electrical efficiency from 1-2 kWe SOFC products,* ECS Transactions **25**, 231 (2009).

[42] L. Mastropasqua, S. Campanari, P. Iora, and M. C. Romano, *Simulation of Intermediate-Temperature SOFC for 60%+ Efficiency Distributed Generation,* in *13*.

[43] A. Ploner, A. Hagen, and A. Hauch, *Classical statistical methodology for accelerated testing of solid oxide fuel cells,* Journal of Power Sources **395**, 379 (2018).

[44] S. Campanari, L. Mastropasqua, M. Gazzani, P. Chiesa, and M. C. Romano, *Predicting the ultimate potential of natural gas SOFC power cycles with CO_2 capture–Part A: Methodology and reference cases,* Journal of Power Sources **324**, 598 (2016).

[45] A. Massardo and F. Lubelli, *Internal reforming solid oxide fuel cell-gas turbine combined cycles (IRSOFC-GT): Part A - Cell model and cycle thermodynamic analysis,* in *ASME 1998 International Gas Turbine and Aeroengine Congress and Exhibition*.

[46] M. Rokni, *Thermodynamic analysis of an integrated solid oxide fuel cell cycle with a rankine cycle,* Energy Conversion and Management **51**, 2724 (2010).

[47] S. H. Park, Y. D. Lee, and K. Y. Ahn, *Performance analysis of an SOFC/HCCI engine hybrid system: System simulation and thermo-economic comparison,* International Journal of Hydrogen Energy **39**, 1799 (2014).

[48] P. Aguiar, C. Adjiman, and N. P. Brandon, *Anode-supported intermediate temperature direct internal reforming solid oxide fuel cell. I: model-based steady-state performance,* Journal of Power Sources **138**, 120 (2004).

[49] L. van Biert, M. Godjevac, K. Visser, and P. V. Aravind, *A review of fuel cell systems for maritime applications,* Journal of Power Sources **327**, 345 (2016).

[50] A. B. Stambouli and E. Traversa, *Fuel cells, an alternative to standard sources of energy,* Renewable and Sustainable Energy Reviews **6**, 295 (2002).

[51] H. C. Patel, T. Woudstra, and P. V. Aravind, *Thermodynamic analysis of solid oxide fuel cell gas turbine systems operating with various biofuels,* Fuel cells **12**, 1115 (2012).

[52] *GE developing hybrid SOFC-gas engine for distributed generation,* Fuel Cells Bulletin **2013**, 5 (2013).

[53] K. Leites, A. Bauschulte, M. Dragon, S. Krummrich, and P. Nehter, *SchIBZ-design of different diesel based fuel cell systems for seagoing vessels and their evaluation,* ECS Transactions **42**, 49 (2012).

[54] G. Sattler, *Fuel cells going on-board,* Journal of Power Sources **86**, 61 (2000).

[55] T. J. McCoy, *Trends in ship electric propulsion,* in *Power Engineering Society Summer Meeting*, Vol. 1 (IEEE, 2002) pp. 343–346.

[56] J. Langston, S. Suryanarayanan, M. Steurer, M. Andrus, S. Woodruff, and P. Ribeiro, *Experiences with the simulation of a notional all-electric ship integrated power system on a large-scale high-speed electromagnetic transient simulator,* in *Power Engineering Society General Meeting* (IEEE, 2006) p. 5.

[57] S. C. Singhal, *Advances in solid oxide fuel cell technology,* Solid State Ionics **135**, 305 (2000).

[58] E. D. Wachsman and K. T. Lee, *Lowering the temperature of solid oxide fuel cells,* Science **334**, 935 (2011).

[59] A. C. Riekstin, S. James, A. Kansal, J. Liu, and E. Peterson, *No more electrical infrastructure: Towards fuel cell powered data centers,* in *Proceedings of the Workshop on Power-Aware Computing and Systems* (ACM, 2013) p. 5.

[60] B. Thorstensen, *A parametric study of fuel cell system efficiency under full and part load operation,* Journal of Power Sources **92**, 9 (2001).

[61] Y. Wang, K. S. Chen, J. Mishler, S. C. Cho, and X. C. Adroher, *A review of polymer electrolyte membrane fuel cells: technology, applications, and needs on fundamental research,* Applied Energy **88**, 981 (2011).

[62] W. Dai, H. Wang, X.-Z. Yuan, J. J. Martin, D. Yang, J. Qiao, and J. Ma, *A review on water balance in the membrane electrode assembly of proton exchange membrane fuel cells,* International Journal of Hydrogen Energy **34**, 9461 (2009).

[63] M. S. Çögenli, S. Mukerjee, and A. B. Yurtcan, *Membrane electrode assembly with ultra low platinum loading for cathode electrode of PEM fuel cell by using sputter deposition,* Fuel Cells **15**, 288 (2015).

[64] J. J. Baschuk and X. Li, *Carbon monoxide poisoning of proton exchange membrane fuel cells,* International Journal of Energy Research **25**, 695 (2001).

[65] X. Cheng, Z. Shi, N. Glass, L. Zhang, J. Zhang, D. Song, Z.-S. Liu, H. Wang, and J. Shen, *A review of PEM hydrogen fuel cell contamination: Impacts, mechanisms, and mitigation,* Journal of Power Sources **165**, 739 (2007).

[66] J. O. Jensen, Q. Li, C. Pan, N. J. Bjerrum, H. C. Rudbeck, T. Steenberg, D. Stolten, and T. Grube, *Ongoing efforts addressing degradation of high temperature PEMFC,* Report Nr.: Schriften des Forschungszentrums Jülich/Energy & Environment (2010).

[67] J. Zhang, Z. Xie, J. Zhang, Y. Tang, C. Song, T. Navessin, Z. Shi, D. Song, H. Wang, D. P. Wilkinson, *et al.*, *High temperature PEM fuel cells,* Journal of power Sources **160**, 872 (2006).

[68] J. P. P. Huijsmans, G. J. Kraaij, R. C. Makkus, G. Rietveld, E. F. Sitters, and H. T. J. Reijers, *An analysis of endurance issues for MCFC,* .

[69] A. Kulkarni and S. Giddey, *Materials issues and recent developments in molten carbonate fuel cells,* Journal of Solid State Electrochemistry **16**, 3123 (2012).

[70] R. T. Leah, A. Bone, A. Selcuk, D. Corcoran, M. Lankin, Z. Dehaney-Steven, M. Selby, and P. Whalen, *Development of highly robust, volume-manufacturable metal-supported SOFCs for operation below 600°C,* ECS Transactions **35**, 351 (2011).

[71] S. Pellegrino, A. Lanzini, and P. Leone, *Techno-economic and policy requirements for the market-entry of the fuel cell micro-CHP system in the residential sector,* Applied Energy **143**, 370 (2015).

[72] R. J. Kee, H. Zhu, and D. G. Goodwin, *Solid-oxide fuel cells with hydrocarbon fuels,* Proceedings of the Combustion Institute **30**, 2379 (2005).

[73] L. Cohen, A. Tate, and N. Weinhold, *Investigation into the implications of fuel cell shipboard integration into the T-AGOS 19 class*, Tech. Rep. (DTIC Document, 2012).

[74] M. Kickulies, *Fuel cell power for maritime applications,* Fuel Cells Bulletin **2005**, 12 (2005).

[75] S. Krummrich, B. Tuinstra, G. Kraaij, J. Roes, and H. Olgun, *Diesel fuel processing for fuel cells—DESIRE,* Journal of Power Sources **160**, 500 (2006).

[76] S. Allen, E. Ashey, D. Gore, J. Woerner, and M. Cervi, *Marine applications of fuel cells: A multi-agency research program,* Naval Engineers Journal **110**, 93 (1998).

[77] R. M. Privette, T. A. Flynn, M. A. Perna, R. Holland, S. Rahmani, C. Wood-burn, S. W. Scoles, and R. C. Watson, *2.5 MW PEM fuel cell system for navy ship service power,* (2002).

[78] S. Specchia, G. Saracco, and V. Specchia, *Modeling of an APU system based on MCFC,* International Journal of Hydrogen Energy **33**, 3393 (2008).

[79] S. Bensaid, S. Specchia, F. Federici, G. Saracco, and V. Specchia, *MCFC-based marine APU: Comparison between conventional ATR and cracking coupled with SR integrated inside the stack pressurized vessel,* International Journal of Hydrogen Energy **34**, 2026 (2009).

[80] C. Ezgi, M. T. Çoban, and Ö. Selvi, *Design and thermodynamic analysis of an SOFC system for naval surface ship application,* Journal of Fuel Cell Science and Technology **10**, 031006 (2013).

[81] S. Alkaner and P. Zhou, *A comparative study on life cycle analysis of molten carbon fuel cells and diesel engines for marine application,* Journal of Power Sources **158**, 188 (2006).

[82] S. Lee, J. G. Speight, and S. K. Loyalka, *Handbook of alternative fuel technologies* (CRC Press, 2014).

[83] H. B. Gray, *Powering the planet with solar fuel,* Nature Chemistry **1**, 7 (2009).

[84] S. Dahl and I. Chorkendorff, *Solar-fuel generation: towards practical implementation,* Nature Materials **11**, 100 (2012).

[85] H. B. Goyal, D. Seal, and R. C. Saxena, *Bio-fuels from thermochemical conversion of renewable resources: a review,* Renewable and Sustainable Energy Reviews **12**, 504 (2008).

[86] S. C. Roy, O. K. Varghese, M. Paulose, and C. A. Grimes, *Toward solar fuels: photocatalytic conversion of carbon dioxide to hydrocarbons,* ACS Nano **4**, 1259 (2010).

[87] J. Newman, P. G. Hoertz, C. A. Bonino, and J. A. Trainham, *Review: an economic perspective on liquid solar fuels,* Journal of The Electrochemical Society **159**, A1722 (2012).

[88] R. Metkemeijer and P. Achard, *Comparison of ammonia and methanol applied indirectly in a hydrogen fuel cell,* International Journal of Hydrogen Energy **19**, 535 (1994).

[89] M. Klell, *Storage of hydrogen in the pure form,* in *Handbook of hydrogen storage: new materials for future energy storage*, edited by M. Hirscher and K. Hirose (John Wiley & Sons, 2010) Chap. 1, pp. 1–37.

[90] H. K. Woud and D. Stapersma, *Design of propulsion and electric power generation systems*, Vol. 1902536479 (IMarEST, 2002).

[91] T. A. Semelsberger, R. L. Borup, and H. L. Greene, *Dimethyl ether (DME) as an alternative fuel,* Journal of Power Sources **156**, 497 (2006).

[92] R. K. Ahluwalia, T. Q. Hua, J.-K. Peng, S. Lasher, K. McKenney, J. Sinha, and M. Gardiner, *Technical assessment of cryo-compressed hydrogen storage tank systems for automotive applications,* International Journal of Hydrogen Energy **35**, 4171 (2010).

[93] S. M. Aceves, F. Espinosa-Loza, E. Ledesma-Orozco, T. O. Ross, A. H. Weisberg, T. C. Brunner, and O. Kircher, *High-density automotive hydrogen storage with cryogenic capable pressure vessels,* International Journal of Hydrogen Energy **35**, 1219 (2010).

[94] D. J. Durbin and C. Malardier-Jugroot, *Review of hydrogen storage techniques for on board vehicle applications,* International Journal of Hydrogen Energy **38**, 14595 (2013).

[95] L. Schlapbach and A. Züttel, *Hydrogen-storage materials for mobile applications,* Nature **414**, 353 (2001).

[96] J. A. Turner, *Sustainable hydrogen production,* Science **305**, 972 (2004).

[97] T. Taner, *Alternative Energy of the Future: A Technical Note of PEM Fuel Cell Water Management,* J Fundam Renewable Energy Appl **5**, 2 (2015).

[98] P. P. Edwards, V. L. Kuznetsov, W. I. F. David, and N. P. Brandon, *Hydrogen and fuel cells: towards a sustainable energy future,* Energy Policy **36**, 4356 (2008).

[99] C. M. White, R. R. Steeper, and A. E. Lutz, *The hydrogen-fueled internal combustion engine: a technical review,* International Journal of Hydrogen Energy **31**, 1292 (2006).

[100] K. Hirose and M. Hirscher, *Handbook of hydrogen storage: new materials for future energy storage* (John Wiley & Sons, 2010).

[101] Y. H. Kim, K.-W. Jun, H. Joo, C. Han, and I. K. Song, *A simulation study on gas-to-liquid (natural gas to Fischer–Tropsch synthetic fuel) process optimization,* Chemical Engineering Journal **155**, 427 (2009).

[102] G. Cinti, A. Baldinelli, A. Di Michele, and U. Desideri, *Integration of solid oxide electrolyzer and Fischer-Tropsch: A sustainable pathway for synthetic fuel,* Applied Energy **162**, 308 (2016).

[103] Y. Xiang, J. Zhou, B. Lin, X. Xue, X. Tian, and Z. Luo, *Exergetic evaluation of renewable light olefins production from biomass via synthetic methanol,* Applied Energy **157**, 499 (2015).

[104] B. Guo and A. Ghalambor, *Natural gas engineering handbook* (Elsevier, 2014).

[105] Y. M. Kurle, S. Wang, and Q. Xu, *Simulation study on boil-off gas minimization and recovery strategies at LNG exporting terminals,* Applied Energy **156**, 628 (2015).

[106] É. S. Van-Dal and C. Bouallou, *Design and simulation of a methanol production plant from CO_2 hydrogenation,* Journal of Cleaner Production **57**, 38 (2013).

[107] S. K. Das and K. K. Gadde, *Computational fluid dynamics modeling of a catalytic flat plate fuel reformer for on-board hydrogen generation,* Journal of Fuel Cell Science and Technology **10**, 061005 (2013).

[108] Y. Bang, S. J. Han, J. Yoo, J. H. Choi, K. H. Kang, J. H. Song, J. G. Seo, J. C. Jung, and I. K. Song, *Hydrogen production by steam reforming of liquefied natural gas (LNG) over trimethylbenzene-assisted ordered mesoporous nickel–alumina catalyst,* International Journal of Hydrogen Energy **38**, 8751 (2013).

[109] S. Brynolf, E. Fridell, and K. Andersson, *Environmental assessment of marine fuels: liquefied natural gas, liquefied biogas, methanol and bio-methanol,* Journal of Cleaner Production **74**, 86 (2014).

[110] X. Peng and D. Cao, *Computational screening of porous carbons, zeolites, and metal organic frameworks for desulfurization and decarburization of biogas, natural gas, and flue gas,* AIChE Journal **59**, 2928 (2013).

[111] A. Buonomano, F. Calise, M. D. d'Accadia, A. Palombo, and M. Vicidomini, *Hybrid solid oxide fuel cells–gas turbine systems for combined heat and power: A review,* Applied Energy **156**, 32 (2015).

[112] I. Ridjan, *Integrated electrofuels and renewable energy systems,* Ph.D. thesis (2015).

[113] E. Alberico and M. Nielsen, *Towards a methanol economy based on homogeneous catalysis: methanol to H_2 and CO_2 to methanol,* Chemical Communications **51**, 6714 (2015).

[114] C. Pan, R. He, Q. Li, J. O. Jensen, N. J. Bjerrum, H. A. Hjulmand, and A. B. Jensen, *Integration of high temperature PEM fuel cells with a methanol reformer,* Journal of Power Sources **145**, 392 (2005).

[115] S. J. Andreasen, S. K. Kær, and S. Sahlin, *Control and experimental characterization of a methanol reformer for a 350 W high temperature polymer electrolyte membrane fuel cell system,* International Journal of Hydrogen Energy **38**, 1676 (2013).

[116] G. C. Bandlamudi, M. Steffen, T. Meijer, and A. Heinzel, *Internal reforming methanol fuel cell development,* in *Meeting Abstracts*, 3 (The Electrochemical Society, 2015) pp. 644–644.

[117] B. Hu, M. Keane, K. Patil, M. K. Mahapatra, U. Pasaogullari, and P. Singh, *Direct methanol utilization in intermediate temperature liquid-tin anode solid oxide fuel cells,* Applied Energy **134**, 342 (2014).

[118] C. Strazza, A. Del Borghi, P. Costamagna, A. Traverso, and M. Santin, *Comparative LCA of methanol-fuelled SOFCs as auxiliary power systems on-board ships,* Applied Energy **87**, 1670 (2010).

[119] M. Xu, J. H. Lunsford, D. W. Goodman, and A. Bhattacharyya, *Synthesis of dimethyl ether (DME) from methanol over solid-acid catalysts,* Applied Catalysis A: General **149**, 289 (1997).

[120] R. Vakili, E. Pourazadi, P. Setoodeh, R. Eslamloueyan, and M. R. Rahimpour, *Direct dimethyl ether (DME) synthesis through a thermally coupled heat exchanger reactor,* Applied Energy **88**, 1211 (2011).

[121] H. Chen, C. W. Fan, and C. Yu, *Analysis, synthesis, and design of a one-step dimethyl ether production via a thermodynamic approach,* Applied Energy **101**, 449 (2013).

[122] E. P. Murray, S. J. Harris, and H. Jen, *Solid oxide fuel cells utilizing dimethyl ether fuel,* Journal of the Electrochemical Society **149**, A1127 (2002).

[123] S. Freni, N. Mondello, S. Cavallaro, G. Cacciola, V. N. Parmon, and V. A. Sobyanin, *Hydrogen production by steam reforming of ethanol: a two step process,* Reaction Kinetics and Catalysis Letters **71**, 143 (2000).

[124] C. Zamfirescu and I. Dincer, *Using ammonia as a sustainable fuel,* Journal of Power Sources **185**, 459 (2008).

[125] T. Hejze, J. O. Besenhard, K. Kordesch, M. Cifrain, and R. R. Aronsson, *Current status of combined systems using alkaline fuel cells and ammonia as a hydrogen carrier,* Journal of Power Sources **176**, 490 (2008).

[126] A. Klerke, C. H. Christensen, J. K. Nørskov, and T. Vegge, *Ammonia for hydrogen storage: challenges and opportunities,* Journal of Materials Chemistry **18**, 2304 (2008).

[127] R. Lan, J. T. S. Irvine, and S. Tao, *Ammonia and related chemicals as potential indirect hydrogen storage materials,* International Journal of Hydrogen Energy **37**, 1482 (2012).

[128] K. Ahmed and K. Föger, *Approach to equilibrium of the water-gas shift reaction on a Ni/zirconia anode under solid oxide fuel-cell conditions,* Journal of Power Sources **103**, 150 (2001).

[129] J. Xu and G. F. Froment, *Methane steam reforming, methanation and water-gas shift: I. Intrinsic kinetics,* AIChE Journal **35**, 88 (1989).

[130] M. Mitchell, P. J. A. Kenis, *et al.*, *Ceramic microreactors for on-site hydrogen production from high temperature steam reforming of propane,* Lab on a Chip **6**, 1328 (2006).

[131] I. K. Sung, I. K. Christian, M. Mitchell, D. P. Kim, and P. J. A. Kenis, *Tailored macroporous SiCN and SiC structures for high-temperature fuel reforming,* Advanced Functional Materials **15**, 1336 (2005).

[132] C. O. Colpan, I. Dincer, and F. Hamdullahpur, *Thermodynamic modeling of direct internal reforming solid oxide fuel cells operating with syngas,* International Journal of Hydrogen Energy **32**, 787 (2007).

[133] Y. Yi, A. D. Rao, J. Brouwer, and G. S. Samuelsen, *Fuel flexibility study of an integrated 25kW SOFC reformer system,* Journal of Power Sources **144**, 67 (2005).

[134] R. Peters, E. Riensche, and P. Cremer, *Pre-reforming of natural gas in solid oxide fuel-cell systems,* Journal of Power Sources **86**, 432 (2000).

[135] R. Peters, R. Dahl, U. Klüttgen, C. Palm, and D. Stolten, *Internal reforming of methane in solid oxide fuel cell systems,* Journal of Power Sources **106**, 238 (2002).

[136] J. Meusinger, E. Riensche, and U. Stimming, *Reforming of natural gas in solid oxide fuel cell systems,* Journal of Power Sources **71**, 315 (1998).

[137] D. Dissanayake, M. P. Rosynek, K. C. Kharas, and J. H. Lunsford, *Partial oxidation of methane to carbon monoxide and hydrogen over a Ni/Al_2O_3 catalyst,* Journal of Catalysis **132**, 117 (1991).

[138] A. Lindermeir, S. Kah, S. Kavurucu, and M. Mühlner, *On-board diesel fuel processing for an SOFC–APU—Technical challenges for catalysis and reactor design,* Applied Catalysis B: Environmental **70**, 488 (2007).

[139] F. Yagi, A. Nagumo, Y. Wada, M. Shimura, S. Asaoka, and S. Wakamatsu, *Process for preparing synthesis gas by autothermal reforming,* (2002), US Patent 6,340,437.

[140] A. Ersoz, H. Olgun, S. Ozdogan, C. Gungor, F. Akgun, and M. Tırıs, *Autothermal reforming as a hydrocarbon fuel processing option for PEM fuel cell,* Journal of Power Sources **118**, 384 (2003).

[141] B. Lindström, J. A. J. Karlsson, P. Ekdunge, L. de Verdier, B. Häggendal, J. Dawody, M. Nilsson, and L. J. Pettersson, *Diesel fuel reformer for automotive fuel cell applications,* International Journal of Hydrogen Energy **34**, 3367 (2009).

[142] D. S. Newsome, *The water-gas shift reaction,* Catalysis Reviews Science and Engineering **21**, 275 (1980).

[143] R. Suwanwarangkul, E. Croiset, E. Entchev, S. Charojrochkul, M. D. Pritzker, M. W. Fowler, P. L. Douglas, S. Chewathanakup, and H. Mahaudom, *Experimental and modeling study of solid oxide fuel cell operating with syngas fuel,* Journal of Power Sources **161**, 308 (2006).

[144] O. Costa-Nunes, R. J. Gorte, and J. M. Vohs, *Comparison of the performance of Cu–CeO_2–YSZ and Ni–YSZ composite SOFC anodes with H_2, CO, and syngas,* Journal of Power Sources **141**, 241 (2005).

[145] C. Wheeler, A. Jhalani, E. J. Klein, S. Tummala, and L. D. Schmidt, *The water–gas-shift reaction at short contact times,* Journal of Catalysis **223**, 191 (2004).

[146] A. F. Ghenciu, *Review of fuel processing catalysts for hydrogen production in PEM fuel cell systems,* Current opinion in solid state and materials science **6**, 389 (2002).

[147] D. J. Moon, K. Sreekumar, S. D. Lee, B. G. Lee, and H. S. Kim, *Studies on gasoline fuel processor system for fuel-cell powered vehicles application,* Applied Catalysis A: General **215**, 1 (2001).

[148] M. Echigo and T. Tabata, *Development of novel Ru catalyst of preferential CO oxidation for residential polymer electrolyte fuel cell systems,* Catalysis today **90**, 269 (2004).

[149] A. Manasilp and E. Gulari, *Selective CO oxidation over Pt/alumina catalysts for fuel cell applications,* Applied Catalysis B: Environmental **37**, 17 (2002).

[150] I. H. Son, M. Shamsuzzoha, and A. M. Lane, *Promotion of Pt/γ-Al_2O_3 by new pretreatment for low-temperature preferential oxidation of CO in H_2 for PEM fuel cells,* Journal of catalysis **210**, 460 (2002).

[151] R. A. Dagle, Y. Wang, G. Xia, J. J. Strohm, J. Holladay, and D. R. Palo, *Selective CO methanation catalysts for fuel processing applications,* Applied Catalysis A: General **326**, 213 (2007).

[152] C. Galletti, S. Specchia, G. Saracco, and V. Specchia, *CO-selective methanation over Ru–γAl_2O_3 catalysts in H_2-rich gas for PEM FC applications,* Chemical Engineering Science **65**, 590 (2010).

[153] C. Galletti, S. Specchia, and V. Specchia, *CO selective methanation in H_2-rich gas for fuel cell application: microchannel reactor performance with Ru-based catalysts,* Chemical Engineering Journal **167**, 616 (2011).

[154] G. Ercolino, M. A. Ashraf, V. Specchia, and S. Specchia, *Performance evaluation and comparison of fuel processors integrated with PEM fuel cell based on steam or autothermal reforming and on CO preferential oxidation or selective methanation,* Applied Energy **143**, 138 (2015).

[155] P. Djinović, C. Galletti, S. Specchia, and V. Specchia, *Ru-based catalysts for CO selective methanation reaction in H_2-rich gases,* Catalysis Today **164**, 282 (2011).

[156] N. W. Ockwig and T. M. Nenoff, *Membranes for hydrogen separation,* Chemical Reviews **107**, 4078 (2007).

[157] Y. Lin and M.-H. Rei, *Study on the hydrogen production from methanol steam reforming in supported palladium membrane reactor,* Catalysis Today **67**, 77 (2001).

[158] G. Q. Lu, J. C. D. da Costa, M. Duke, S. Giessler, R. Socolow, R. H. Williams, and T. Kreutz, *Inorganic membranes for hydrogen production and purification: a critical review and perspective,* Journal of Colloid and Interface Science **314**, 589 (2007).

[159] S. Uemiya, N. Sato, H. Ando, T. Matsuda, and E. Kikuchi, *Steam reforming of methane in a hydrogen-permeable membrane reactor,* Applied catalysis **67**, 223 (1990).

[160] J. Yang, C.-H. Lee, and J.-W. Chang, *Separation of hydrogen mixtures by a two-bed pressure swing adsorption process using zeolite 5A,* Industrial & engineering chemistry research **36**, 2789 (1997).

[161] S.-I. Yang, D.-Y. Choi, S.-C. Jang, S.-H. Kim, and D.-K. Choi, *Hydrogen separation by multi-bed pressure swing adsorption of synthesis gas,* Adsorption **14**, 583 (2008).

[162] S. Sircar and T. C. Golden, *Purification of hydrogen by pressure swing adsorption,* Separation Science and Technology **35**, 667 (2000).

[163] P. R. Westmoreland and D. P. Harrison, *Evaluation of candidate solids for high-temperature desulfurization of low-Btu gases,* Environmental Science & Technology **10**, 659 (1976).

[164] O. van Rheinberg, K. Lucka, H. Köhne, T. Schade, and J. T. Andersson, *Selective removal of sulphur in liquid fuels for fuel cell applications,* Fuel **87**, 2988 (2008).

[165] I. I. Novochinskii, C. Song, X. Ma, X. Liu, L. Shore, J. Lampert, and R. J. Farrauto, *Low-temperature H_2S removal from steam-containing gas mixtures with ZnO for fuel cell application. 1. ZnO particles and extrudates,* Energy & Fuels **18**, 576 (2004).

[166] *Diesel and gas engines generator sets and propulsion systems,* Brochure (2016).

[167] *Wärtsilä – Engines & Generating sets,* Brochure (2016).

[168] A. K. Ådnanes, *Maritime electrical installations and diesel electric propulsion* (ABB, 2003).

[169] P. Yadav, R. Kumar, S. K. Panda, and C. S. Chang, *An improved harmony search algorithm for optimal scheduling of the diesel generators in oil rig platforms,* Energy Conversion and Management **52**, 893 (2011).

[170] P. P. Walsh and P. Fletcher, *Gas turbine performance* (John Wiley & Sons, 2004).

[171] D. Woodyard, *Pounder's marine diesel engines and gas turbines* (Butterworth-Heinemann, 2009).

[172] V. Adams, *Possible fuel cell applications for ships and submarines,* Journal of Power Sources **29**, 181 (1990).

[173] C. Bourne, T. Nietsch, D. Griffiths, and J. Morley, *Application of fuel cells in surface ships* (Harwell Laboratory, 2001).

[174] K. B. Ludvigsen and E. Ovrum, *Fuel Cells for Ships,* DNV Research and Innovation, Position Paper (2012).

[175] H. Sumi, T. Yamaguchi, H. Shimada, Y. Fujishiro, and M. Awano, *Development of a portable SOFC system with internal partial oxidation reforming of butane and steam reforming of ethanol,* ECS Transactions **80**, 71 (2017).

[176] R. Kehlhofer, B. Rukes, F. Hannemann, and F. Stirnimann, *Combined-cycle gas & steam turbine power plants* (Pennwell Books, 2009).

[177] C. Sprouse and C. Depcik, *Review of organic Rankine cycles for internal combustion engine exhaust waste heat recovery,* Applied thermal engineering **51**, 711 (2013).

[178] G. Shu, Y. Liang, H. Wei, H. Tian, J. Zhao, and L. Liu, *A review of waste heat recovery on two-stroke IC engine aboard ships,* Renewable and Sustainable Energy Reviews **19**, 385 (2013).

[179] L. K. C. Tse, S. Wilkins, N. McGlashan, B. Urban, and R. Martinez-Botas, *Solid oxide fuel cell/gas turbine trigeneration system for marine applications,* Journal of Power Sources **196**, 3149 (2011).

[180] M. Rokni, *Thermodynamic analysis of SOFC (solid oxide fuel cell)–Stirling hybrid plants using alternative fuels,* Energy **61**, 87 (2013).

[181] A. Chaudhari and R. Stobart, *Investigation of optimum operating range for a solid oxide fuel cell-IC engine hybrid system,* in *IEEE Conference on Electric and Hybrid Vehicles* (IEEE, 2006) pp. 1–6.

[182] A. Fernandes, T. Woudstra, A. van Wijk, L. Verhoef, and P. V. Aravind, *Fuel cell electric vehicle as a power plant and SOFC as a natural gas reformer: An exergy analysis of different system designs,* Applied Energy **173**, 13 (2016).

[183] H. Chen, T. N. Cong, W. Yang, C. Tan, Y. Li, and Y. Ding, *Progress in electrical energy storage system: A critical review,* Progress in Natural Science **19**, 291 (2009).

[184] P. J. Hall and E. J. Bain, *Energy-storage technologies and electricity generation,* Energy policy **36**, 4352 (2008).

[185] B. C. C. Chan, *The state of the art of electric, hybrid, and fuel cell vehicles,* Proceedings of the IEEE **95**, 704 (2007).

[186] S. Krummrich and J. Llabrés, *Methanol reformer–The next milestone for fuel cell powered submarines,* International Journal of Hydrogen Energy **40**, 5482 (2015).

[187] M. C. Díaz-de Baldasano, F. J. Mateos, L. R. Núñez-Rivas, and T. J. Leo, *Conceptual design of offshore platform supply vessel based on hybrid diesel generator-fuel cell power plant,* Applied Energy **116**, 91 (2014).

[188] Y. Gogotsi and P. Simon, *True performance metrics in electrochemical energy storage,* Science Magazine **334**, 917 (2011).

[189] R. S. Gemmen, *Analysis for the effect of inverter ripple current on fuel cell operating condition,* Journal of Fluids Engineering **125**, 576 (2003).

[190] P. Thounthong, V. Chunkag, P. Sethakul, B. Davat, and M. Hinaje, *Comparative study of fuel-cell vehicle hybridization with battery or supercapacitor storage device,* IEEE Transactions on Vehicular Technology **58**, 3892 (2009).

[191] D. McLarty, Y. Kuniba, J. Brouwer, and S. Samuelsen, *Experimental and theoretical evidence for control requirements in solid oxide fuel cell gas turbine hybrid systems,* Journal of Power Sources **209**, 195 (2012).

[192] P. Thounthong, S. Rael, and B. Davat, *Energy management of fuel cell/battery/supercapacitor hybrid power source for vehicle applications,* Journal of Power Sources **193**, 376 (2009).

[193] K. Rajashekara, J. MacBain, M. J. Grieve, *et al.*, *Evaluation of SOFC hybrid systems for automotive propulsion applications,* in *Industry Applications Conference*, Vol. 3 (IEEE, 2006) pp. 1593–1597.

[194] A. F. Burke, *Batteries and ultracapacitors for electric, hybrid, and fuel cell vehicles,* Proceedings of the IEEE **95**, 806 (2007).

[195] R. T. Doucette and M. D. McCulloch, *A comparison of high-speed flywheels, batteries, and ultracapacitors on the bases of cost and fuel economy as the energy storage system in a fuel cell based hybrid electric vehicle,* Journal of Power Sources **196**, 1163 (2011).

[196] M. Altmann, W. Weindorf, and M. Weinberger, *Life Cycle Analysis results of fuel cell ships,* EU Project Contract (2004).

[197] A. Simons and C. Bauer, *A life-cycle perspective on automotive fuel cells,* Applied Energy **157**, 884 (2015).

[198] R. W. Howarth, *A bridge to nowhere: methane emissions and the greenhouse gas footprint of natural gas,* Energy Science & Engineering **2**, 47 (2014).

[199] E. Stephenson, A. Doukas, and K. Shaw, *Greenwashing gas: Might a 'transition fuel' label legitimize carbon-intensive natural gas development?* Energy Policy **46**, 452 (2012).

[200] M. Pehnt, *Life-cycle analysis of fuel cell system components,* Handbook of Fuel Cells (2003).

[201] S. Basu, *Future directions of fuel cell science and technology,* in *Recent trends in fuel cell science and technology* (Springer, 2007) pp. 356–365.

[202] F. Baratto and U. M. Diwekar, *Life cycle assessment of fuel cell-based APUs,* Journal of Power Sources **139**, 188 (2005).

[203] J. W. Pratt and A. P. Harris, *Vessel cold-ironing using a barge mounted PEM fuel cell: project scoping and feasibility,* Tech. Rep. (Sandia National Laboratories, 2013).

[204] F. Vogler and G. Würsig, *Fuel cells in maritime applications challenges, chances and experiences,* in *The 4th International Conference on Hydrogen Safety (ICHS)* (2011).

[205] Y. Zhan, Y. Guo, J. Zhu, and H. Wang, *Intelligent uninterruptible power supply system with back-up fuel cell/battery hybrid power source,* Journal of Power Sources **179**, 745 (2008).

[206] J. M. Neff, S. Ostazeski, W. Gardiner, and I. Stejskal, *Effects of weathering on the toxicity of three offshore Australian crude oils and a diesel fuel to marine animals,* Environmental Toxicology and Chemistry **19**, 1809 (2000).

[207] T. Krilić, *News from IMO,* Transactions on Maritime Science **4**, 54 (2015).

[208] J. Garche and L. Jürissen, *Applications of fuel cell technology: status and perspectives,* The Electrochemical Society Interface **24**, 39 (2015).

[209] L. Chick, M. Weimar, G. Whyatt, and M. Powell, *The Case for Natural Gas Fueled Solid Oxide Fuel Cell Power Systems for Distributed Generation,* Fuel Cells **15**, 49 (2015).

[210] Y. Oono, A. Sounai, and M. Hori, *Influence of the phosphoric acid-doping level in a polybenzimidazole membrane on the cell performance of high-temperature proton exchange membrane fuel cells,* Journal of Power Sources **189**, 943 (2009).

[211] H. Chen, P. Pei, and M. Song, *Lifetime prediction and the economic lifetime of Proton Exchange Membrane fuel cells,* Applied Energy **142**, 154 (2015).

[212] D. L. Greene and G. Duleep, *Status and prospects of the global automotive fuel cell industry and plans for deployment of fuel cell vehicles and hydrogen refueling infrastructure,* Tech. Rep. (Oak Ridge National Laboratory, 2013).

[213] I. Staffell and R. Green, *The cost of domestic fuel cell micro-CHP systems,* International Journal of Hydrogen Energy **38**, 1088 (2013).

[214] N. Brandon, A. Blake, D. Corcoran, D. Cumming, A. Duckett, K. El-Koury, D. Haigh, C. Kidd, R. Leah, G. Lewis, *et al.*, *Development of metal supported solid oxide fuel cells for operation at 500–600°C,* Journal of Fuel Cell Science and Technology **1**, 61 (2004).

[215] J. Otomo, J. Oishi, T. Mitsumori, H. Iwasaki, and K. Yamada, *Evaluation of cost reduction potential for 1 kW class SOFC stack production: Implications for SOFC technology scenario,* International Journal of Hydrogen Energy **38**, 14337 (2013).

[216] Y. D. Lee, K. Y. Ahn, T. Morosuk, and G. Tsatsaronis, *Exergetic and exergoeconomic evaluation of a solid-oxide fuel-cell-based combined heat and power generation system,* Energy Conversion and Management **85**, 154 (2014).

[217] J. Thijssen, *Solid oxide fuel cells and critical materials: A review of implications*, Tech. Rep. (US Department of Energy, National Energy Technology Laboratory, 2011).

[218] H. R. Ellamla, I. Staffell, P. Bujlo, B. G. Pollet, and S. Pasupathi, *Current status of fuel cell based combined heat and power systems for residential sector,* Journal of Power Sources **293**, 312 (2015).

[219] J. Thijssen, *The impact of scale-up and production volume on SOFC manufacturing cost,* US Department of Energy, National Energy Technology Laboratory, Morgantown, WV (2007).

[220] V. P. McConnell, *Now, voyager? The increasing marine use of fuel cells,* Fuel cells bulletin **2010**, 12 (2010).

[221] *Fuel cell system on FellowSHIP supply vessel is hybridised,* Fuel Cells Bulletin **2012**, 3 (2012).

[222] J. Schneider, S. Dirk, D. Stolten, and T. Grube, *ZEMShip,* in *18th World Hydrogen Energy Conference* (2010) pp. 16–21.

[223] *METHAPU prototypes methanol SOFC for ships,* Fuel Cells Bulletin **2008**, 4 (2008).

[224] *Sunfire 50 kW SOFC for ship-integrated fuel cell project in Germany,* Fuel Cells Bulletin **2015**, 3 (2015).

[225] *e4ships – brennstoffzellen im maritimen einsatz,* http://http://www.e4ships.de, accessed: 2015-05-29.

[226] L. van Biert, T. Woudstra, M. Godjevac, K. Visser, and P. V. Aravind, *A thermodynamic comparison of solid oxide fuel cell-combined cycles,* Journal of Power Sources **397**, 382 (2018).

[227] S. Harvey and H. Richter, *Gas turbine cycles with solid oxide fuel cells—Part I: Improved gas turbine power plant efficiency by use of recycled exhaust gases and fuel cell technology,* Journal of energy resources technology **116**, 305 (1994).

[228] Y. Haseli, I. Dincer, and G. F. Naterer, *Thermodynamic modeling of a gas turbine cycle combined with a solid oxide fuel cell,* International Journal of Hydrogen Energy **33**, 5811 (2008).

[229] L. Tan, C. Yang, and N. Zhou, *Synthesis/design optimization of SOFC–PEM hybrid system under uncertainty,* Chinese Journal of Chemical Engineering **23**, 128 (2015).

[230] S. Campanari, *Full load and part-load performance prediction for integrated SOFC and microturbine systems,* in *ASME 1999 International Gas Turbine and Aeroengine Congress and Exhibition* (American Society of Mechanical Engineers, 1999) pp. V002T04A003–V002T04A003.

[231] S. Campanari, *Full load and part-load performance prediction for integrated SOFC and microturbine systems,* Journal of Engineering for Gas Turbines and Power **122**, 239 (2000).

[232] P. Costamagna, L. Magistri, and A. Massardo, *Design and part-load performance of a hybrid system based on a solid oxide fuel cell reactor and a micro gas turbine,* Journal of Power Sources **96**, 352 (2001).

[233] S. H. Chan, H. K. Ho, and Y. Tian, *Multi-level modeling of SOFC–gas turbine hybrid system,* International Journal of Hydrogen Energy **28**, 889 (2003).

[234] S. K. Park and T. S. Kim, *Comparison between pressurized design and ambient pressure design of hybrid solid oxide fuel cell–gas turbine systems,* Journal of Power Sources **163**, 490 (2006).

[235] F. Calise, M. D. d'Accadia, A. Palombo, and L. Vanoli, *Simulation and exergy analysis of a hybrid solid oxide fuel cell (SOFC)–gas turbine system,* Energy **31**, 3278 (2006).

[236] R. Roberts, J. Brouwer, F. Jabbari, T. Junker, and H. Ghezel-Ayagh, *Control design of an atmospheric solid oxide fuel cell/gas turbine hybrid system: Variable versus fixed speed gas turbine operation,* Journal of Power sources **161**, 484 (2006).

[237] M. Gandiglio, A. Lanzini, P. Leone, M. Santarelli, and R. Borchiellini, *Thermoeconomic analysis of large solid oxide fuel cell plants: Atmospheric vs. pressurized performance,* Energy **55**, 142 (2013).

[238] M. M. Whiston, W. O. Collinge, M. M. Bilec, and L. A. Schaefer, *Exergy and economic comparison between kW-scale hybrid and stand-alone solid oxide fuel cell systems,* Journal of Power Sources **353**, 152 (2017).

[239] M. A. Azizi and J. Brouwer, *Transient analysis of 220 kW solid oxide fuel cell-gas turbine hybrid system using computational fluid dynamics results,* ECS Transactions **71**, 289 (2016).

[240] K. Sasaki, S. Taniguchi, Y. Shiratori, A. Hayashi, T. Oshima, M. Nishihara, Y. Tachikawa, T. Daio, T. Kawabata, M. Fujita, *et al.*, *Smart fuel cell demonstration project: A challenge to realize SOFC-powered campus,* ECS Transactions **68**, 171 (2015).

[241] E. Riensche, J. Meusinger, U. Stimming, and G. Unverzagt, *Optimization of a 200 kW SOFC cogeneration power plant. Part II: variation of the flowsheet,* Journal of Power Sources **71**, 306 (1998).

[242] D. Aquaro and M. Pieve, *High temperature heat exchangers for power plants: Performance of advanced metallic recuperators,* Applied Thermal Engineering **27**, 389 (2007).

[243] E. Hu, Z. Huang, B. Liu, J. Zheng, and X. Gu, *Experimental study on combustion characteristics of a spark-ignition engine fueled with natural gas–hydrogen blends combining with EGR,* International Journal of Hydrogen Energy **34**, 1035 (2009).

[244] M. Altosole, G. Benvenuto, U. Campora, M. Laviola, and R. Zaccone, *Simulation and performance comparison between diesel and natural gas engines for marine applications,* Proceedings of the Institution of Mechanical Engineers, Part M: Journal of Engineering for the Maritime Environment **231**, 690 (2017).

[245] M. Henke, J. Kallo, K. A. Friedrich, and W. G. Bessler, *Influence of pressurisation on SOFC performance and durability: a theoretical study,* Fuel Cells **11**, 581 (2011).

[246] N. Woudstra, T. P. van der Stelt, and K. Hemmes, *The thermodynamic evaluation and optimization of fuel cell systems,* Journal of Fuel Cell Science and Technology **3**, 155 (2006).

[247] A. de Groot, *Advanced exergy analysis of high temperature fuel cell systems*, Ph.D. thesis, Delft University of Technology (2004).

[248] P. Costamagna, A. Selimovic, M. Del Borghi, and G. Agnew, *Electrochemical model of the integrated planar solid oxide fuel cell (IP-SOFC),* Chemical Engineering Journal **102**, 61 (2004).

[249] I. Pilatowsky, R. J. Romero, C. A. Isaza, S. A. Gamboa, P. J. Sebastian, and W. Rivera, *Thermodynamics of fuel cells,* in *Cogeneration Fuel Cell-Sorption Air Conditioning Systems* (Springer, 2011) pp. 25–36.

[250] M. Powell, K. Meinhardt, V. Sprenkle, L. Chick, and G. McVay, *Demonstration of a highly efficient solid oxide fuel cell power system using adiabatic steam reforming and anode gas recirculation,* Journal of Power Sources **205**, 377 (2012).

[251] J. Li, G. Cao, X. Zhu, and H. Tu, *Two-dimensional dynamic simulation of a direct internal reforming solid oxide fuel cell,* Journal of Power Sources **171**, 585 (2007).

[252] R. Peters, R. Deja, L. Blum, J. Pennanen, J. Kiviaho, and T. Hakala, *Analysis of solid oxide fuel cell system concepts with anode recycling,* International Journal of Hydrogen Energy **38**, 6809 (2013).

[253] M. Engelbracht, R. Peters, L. Blum, and D. Stolten, *Analysis of a solid oxide fuel cell system with low temperature anode off-gas recirculation,* Journal of The Electrochemical Society **162**, F982 (2015).

[254] M. Halinen, *Improving the performance of solid oxide fuel cell systems,* Ph.D. thesis, VTT Technical Research Centre of Finland (2015).

[255] L. van Biert, M. Godjevac, K. Visser, and P. V. Aravind, *Dynamic modelling of a direct internal reforming solid oxide fuel cell stack based on single cell experiments,* Applied Energy **250**, 976 (2019).

[256] H. Xi and J. Sun, *A low-order dynamic model for planar solid oxide fuel cells using online iterative computation,* Journal of Fuel Cell Science and Technology **5**, 041015 (2008).

[257] A. Sorce, A. Greco, L. Magistri, and P. Costamagna, *FDI oriented modeling of an experimental SOFC system, model validation and simulation of faulty states,* Applied Energy **136**, 894 (2014).

[258] E. S. Hecht, G. K. Gupta, H. Zhu, A. M. Dean, R. J. Kee, L. Maier, and O. Deutschmann, *Methane reforming kinetics within a Ni–YSZ SOFC anode support,* Applied Catalysis A: General **295**, 40 (2005).

[259] V. M. Janardhanan and O. Deutschmann, *CFD analysis of a solid oxide fuel cell with internal reforming: Coupled interactions of transport, heterogeneous catalysis and electrochemical processes,* Journal of Power Sources **162**, 1192 (2006).

[260] P. Hofmann, K. D. Panopoulos, L. E. Fryda, and E. Kakaras, *Comparison between two methane reforming models applied to a quasi-two-dimensional planar solid oxide fuel cell model,* Energy **34**, 2151 (2009).

[261] A. Thallam Thattai, L. van Biert, and P. V. Aravind, *On direct internal methane steam reforming kinetics in operating solid oxide fuel cells with nickel-ceria anodes,* Journal of Power Sources **370**, 71 (2017).

[262] K. Ahmed and K. Foger, *Kinetics of internal steam reforming of methane on Ni/YSZ-based anodes for solid oxide fuel cells,* Catalysis Today **63**, 479 (2000).

[263] L. Fan, L. van Biert, A. Thallam Thattai, A. H. M. Verkooijen, and P. V. Aravind, *Study of methane steam reforming kinetics in operating solid oxide fuel cells: influence of current density,* International Journal of Hydrogen Energy **40**, 5150 (2015).

[264] L. van Biert, A. Thallam Thattai, and P. V. Aravind, *Predicting MSR rates in SOFCs using experimental data and CFD methods,* ECS Transactions **78**, 2823 (2017).

[265] *Staxera GmbH (D). SOFC stack modules for decentralized power generation,* Presentation available at the web site https://www.h2fc-fair.com/hm10/images/pdf/staxera01.pdf (2010), accessed: 2018-10-09.

[266] *Staxera GmbH (D). Technical Documentation Integrated Stack Module (ISM),* Technical report available at the web site http://www.fuelcellmarkets.com/content/images/articles/00864_AS_Dokumentation_ISM.pdf (2010), accessed: 2018-10-09.

[267] M. Gallo, D. Marra, M. Sorrentino, C. Pianese, and S. F. Au, *A versatile computational tool for model-based design, control and diagnosis of a generic solid oxide fuel cell integrated stack module,* Energy conversion and management **171**, 1514 (2018).

[268] K. J. Kattke, R. J. Braun, A. M. Colclasure, and G. Goldin, *High-fidelity stack and system modeling for tubular solid oxide fuel cell system design and thermal management,* Journal of Power Sources **196**, 3790 (2011).

[269] S. Hosseini, V. A. Danilov, P. Vijay, and M. O. Tadé, *Improved tank in series model for the planar solid oxide fuel cell,* Industrial & Engineering Chemistry Research **50**, 1056 (2010).

[270] C. H. Shomate, *A method for evaluating and correlating thermodynamic data,* The Journal of Physical Chemistry **58**, 368 (1954).

[271] W. G. Mallard, *National Institute of Standards and Technology Chemistry Web Book,* (2003).

[272] S. Liu, C. Song, and Z. Lin, *The effects of the interconnect rib contact resistance on the performance of planar solid oxide fuel cell stack and the rib design optimization,* Journal of Power Sources **183**, 214 (2008).

[273] D. A. Noren and M. A. Hoffman, *Clarifying the Butler–Volmer equation and related approximations for calculating activation losses in solid oxide fuel cell models,* Journal of Power Sources **152**, 175 (2005).

[274] W. G. Bessler, J. Warnatz, and D. G. Goodwin, *The influence of equilibrium potential on the hydrogen oxidation kinetics of SOFC anodes,* Solid State Ionics **177**, 3371 (2007).

[275] P. Costamagna and K. Honegger, *Modeling of solid oxide heat exchanger integrated stacks and simulation at high fuel utilization,* Journal of the Electrochemical Society **145**, 3995 (1998).

[276] S. H. Chan, K. A. Khor, and Z. T. Xia, *A complete polarization model of a solid oxide fuel cell and its sensitivity to the change of cell component thickness,* Journal of Power Sources **93**, 130 (2001).

[277] H. Yakabe, M. Hishinuma, M. Uratani, Y. Matsuzaki, and I. Yasuda, *Evaluation and modeling of performance of anode-supported solid oxide fuel cell,* Journal of Power Sources **86**, 423 (2000).

[278] B. E. Poling, J. M. Prausnitz, O. John Paul, and R. C. Reid, *The properties of gases and liquids*, Vol. 5 (Mcgraw-hill New York, 2001).

[279] B. Todd and J. B. Young, *Thermodynamic and transport properties of gases for use in solid oxide fuel cell modelling,* Journal of Power Sources **110**, 186 (2002).

[280] K. J. Daun, S. B. Beale, F. Liu, and G. J. Smallwood, *Radiation heat transfer in planar SOFC electrolytes,* Journal of Power Sources **157**, 302 (2006).

[281] A. Wassiljewa, *Warmeleitung in gasgemischen,* Phys. Z **5**, 737 (1904).

[282] E. A. Mason and S. C. Saxena, *Approximate formula for the thermal conductivity of gas mixtures,* The Physics of Fluids **1**, 361 (1958).

[283] J. Brabandt, Q. Fang, D. Schimanke, M. Heinrich, B. E. Mai, and C. Wunderlich, *System relevant redox cycling in SOFC stacks,* ECS Transactions **35**, 243 (2011).

[284] S. Kluge, O. Posdziech, B. E. Mai, and J. Lawrence, *Performance Map of the Staxera Integrated Stack Module with Partly Internal Reforming,* ECS Transactions **25**, 247 (2009).

[285] J. Kupecki, J. Milewski, A. Szczesniak, R. Bernat, and K. Motylinski, *Dynamic numerical analysis of cross-, co-, and counter-current flow configuration of a 1 kw-class solid oxide fuel cell stack,* International Journal of Hydrogen Energy **40**, 15834 (2015).

[286] J. Kupecki, K. Motylinski, and J. Milewski, *Dynamic analysis of direct internal reforming in a SOFC stack with electrolyte-supported cells using a quasi-1D model,* Applied Energy (2017).

[287] A. Greco, A. Sorce, R. Littwin, P. Costamagna, and L. Magistri, *Reformer faults in SOFC systems: Experimental and modeling analysis, and simulated fault maps,* International Journal of Hydrogen Energy **39**, 21700 (2014).

[288] L. van Biert, K. Visser, and P. V. Aravind, *Intrinsic methane steam reforming kinetics on nickel-ceria solid oxide fuel cell anodes,* Journal of Power Sources **443**, 227261 (2019).

[289] K. Hou and R. Hughes, *The kinetics of methane steam reforming over a Ni/α -Al_2O catalyst,* Chemical Engineering Journal **82**, 311 (2001).

[290] P. Nehter, B. Wildrath, A. Bauschulte, and K. Leites, *Diesel based SOFC demonstrator for maritime applications,* ECS Transactions **78**, 171 (2017).

[291] J. Rechberger, R. Schauperl, J. B. Hansen, and P. K. Larsen, *Development of a methanol SOFC APU demonstration system,* ECS Transactions **25**, 1085 (2009).

[292] M. Andersson, J. Yuan, and B. Sundén, *SOFC modeling considering electrochemical reactions at the active three phase boundaries,* International Journal of Heat and Mass Transfer **55**, 773 (2012).

[293] G. F. Froment, K. B. Bischoff, and J. de Wilde, *Chemical reactor analysis and design,* Vol. 2 (Wiley New York, 1990).

[294] M. A. Vannice and W. H. Joyce, *Kinetics of catalytic reactions*, Vol. 134 (Springer, 2005).

[295] N. Nakagawa, H. Sagara, and K. Kato, *Catalytic activity of Ni–YSZ–CeO_2 anode for the steam reforming of methane in a direct internal-reforming solid oxide fuel cell,* Journal of Power Sources **92**, 88 (2001).

[296] A. L. Dicks, K. D. Pointon, and A. Siddle, *Intrinsic reaction kinetics of methane steam reforming on a nickel/zirconia anode,* Journal of Power Sources **86**, 523 (2000).

[297] H. Timmermann, D. Fouquet, A. Weber, E. Ivers-Tiffée, U. Hennings, and R. Reimert, *Internal reforming of methane at Ni/YSZ and Ni/CGO SOFC cermet anodes,* Fuel Cells **6**, 307 (2006).

[298] V. D. Belyaev, T. I. Politova, O. A. Mar'ina, and V. A. Sobyanin, *Internal steam reforming of methane over Ni-based electrode in solid oxide fuel cells,* Applied Catalysis A: General **133**, 47 (1995).

[299] E. Achenbach and E. Riensche, *Methane/steam reforming kinetics for solid oxide fuel cells,* Journal of Power Sources **52**, 283 (1994).

[300] W. Wang, S. P. Jiang, A. I. Y. Tok, and L. Luo, *GDC-impregnated Ni anodes for direct utilization of methane in solid oxide fuel cells,* Journal of Power Sources **159**, 68 (2006).

[301] V. D. Belyaev, T. I. Politova, and V. A. Sobyanin, *Effect of non-faradaic electrochemical modification of catalytic activity,* Solid State Ionics **136**, 721 (2000).

[302] S. Bebelis, A. Zeritis, C. Tiropani, and S. G. Neophytides, *Intrinsic kinetics of the internal steam reforming of CH_4 over a Ni- YSZ- cermet catalyst- electrode,* Industrial & Engineering Chemistry Research **39**, 4920 (2000).

[303] N. M. Bodrov, L. O. Apel'baum, and M. I. Temkin, *Kinetics of the reaction of methane with water vapor on a nickel surface,* Kinetics and Catalysis **5**, 614 (1964).

[304] G. J. Offer, J. Mermelstein, E. Brightman, and N. P. Brandon, *Thermodynamics and kinetics of the interaction of carbon and sulfur with solid oxide fuel cell anodes,* Journal of the American Ceramic Society **92**, 763 (2009).

[305] A. L. Lee, R. F. Zabransky, and W. J. Huber, *Internal reforming development for solid oxide fuel cells,* Industrial & Engineering Chemistry Research **29**, 766 (1990).

[306] E. Ramırez-Cabrera, A. Atkinson, and D. Chadwick, *Catalytic steam reforming of methane over $Ce_{0.9}Gd_{0.1}O_{2-x}$,* Applied Catalysis B: Environmental **47**, 127 (2004).

[307] L. Blum, U. Packbier, I. C. Vinke, and L. G. J. de Haart, *Long-term testing of SOFC stacks at Forschungszentrum Jülich,* Fuel Cells **13**, 646 (2013).

[308] K. Ahmed and K. Föger, *Perspectives in solid oxide fuel cell-based microcombined heat and power systems,* Journal of Electrochemical Energy Conversion and Storage **14**, 031005 (2017).

[309] M. Engelbracht, R. Peters, L. Blum, and D. Stolten, *Comparison of a fuel-driven and steam-driven ejector in solid oxide fuel cell systems with anode off-gas recirculation: Part-load behavior,* Journal of Power Sources **277**, 251 (2015).

[310] M. Yoda, S. Inoue, Y. Takuwa, K. Yasuhara, and M. Suzuki, *Development and commercialization of new residential SOFC CHP system,* ECS Transactions **78**, 125 (2017).

[311] M. Gandiglio, A. Lanzini, and M. Santarelli, *Large stationary solid oxide fuel cell (SOFC) power plants,* in *Modeling, design, construction, and operation of power generators with solid oxide fuel cells* (Springer, 2018) pp. 233–261.

[312] A. J. Ritchie and J. Brouwer, *Design of fuel cell powered data centers for sufficient reliability and availability,* Journal of Power Sources **384**, 196 (2018).

[313] J. Rechberger, A. Kaupert, J. Hagerskans, and L. Blum, *Demonstration of the first European SOFC APU on a heavy duty truck,* Transportation Research Procedia **14**, 3676 (2016).

[314] P. Lindahl, E. Moog, and S. R. Shaw, *Simulation, design, and validation of an UAV SOFC propulsion system,* IEEE Transactions on Aerospace and Electronic Systems **48**, 2582 (2012).

[315] Z. Dimitrova and F. Maréchal, *Environomic design for electric vehicles with an integrated solid oxide fuel cell (SOFC) unit as a range extender,* Renewable Energy **112**, 124 (2017).

[316] M. D. Fernandes, S. T. d. P. Andrade, V. N. Bistritzki, R. M. Fonseca, L. G. Zacarias, H. N. C. Gonçalves, A. F. de Castro, R. Z. Domingues, and T. Matencio, *SOFC-APU systems for aircraft: A review,* International Journal of Hydrogen Energy **43**, 16311 (2018).

[317] J. L. Martin and P. Osenar, *Portable military fuel cell power systems,* ECS Transactions **25**, 249 (2009).

[318] R. C. Samsun, M. Prawitz, A. Tschauder, J. Pasel, P. Pfeifer, R. Peters, and D. Stolten, *An integrated diesel fuel processing system with thermal start-up for fuel cells,* Applied Energy **226**, 145 (2018).

[319] S. E. Veyo, S. D. Vora, K. P. Litzinger, and W. L. Lundberg, *Status of pressurized SOFC/GAS turbine power system development at Siemens Westinghouse,* in *ASME Turbo Expo 2002: Power for Land, Sea, and Air* (American Society of Mechanical Engineers, 2002) pp. 823–829.

[320] H. Irie, K. Miyamoto, Y. Teramoto, T. Nagai, R. Endo, and Y. Urashita, *Efforts toward introduction of SOFC-MGT hybrid system to the market,* Mitsubishi Heavy Ind Tech Rev **54** (2017).

[321] B. T. W. Mestemaker, M. B. Goncalves Castro, H. N. van den Heuvel, and K. Visser, *Dynamic simulation of a vessel drive system with dual fuel engines and energy storage,* Energy , 116792 (2019).

[322] F. Baldi, F. Ahlgren, T.-V. Nguyen, M. Thern, and K. Andersson, *Energy and exergy analysis of a cruise ship,* Energies **11**, 2508 (2018).

[323] S. G. Wang and R. Z. Wang, *Recent developments of refrigeration technology in fishing vessels,* Renewable Energy **30**, 589 (2005).

[324] N. H. Doerry, *Sizing power generation and fuel capacity of the all-electric warship,* in *Electric Ship Technologies Symposium. ESTS'07.* (IEEE, 2007) pp. 1–6.

[325] R. D. Geertsma, R. R. Negenborn, K. Visser, and J. J. Hopman, *Design and control of hybrid power and propulsion systems for smart ships: A review of developments,* Applied Energy **194**, 30 (2017).

[326] F. Baldi, L. Wang, and F. Maréchal, *Integration of solid oxide fuel cells in cruise ship energy systems,* in *Proceedings of the 31st International Conference on Efficiency, Cost, Optimization, Simulation and Environmental Impact of Energy Systems*, CONF (2018).

[327] M. Butcher, R. Maltby, and P. S. Parvin, *Compact DC power and propulsion systems-the definitive solution?* in *Electric Ship Technologies Symposium. ESTS 2009.* (IEEE, 2009) pp. 521–528.

[328] X. Sun, X. Yan, B. Wu, and X. Song, *Analysis of the operational energy efficiency for inland river ships,* Transportation Research Part D: Transport and Environment **22**, 34 (2013).

[329] S. J. McPhail, J. Kiviaho, and B. Conti, *The yellow pages of SOFC technology. International Status of SOFC deployment 2017,* (2017).

[330] A. Torabi, J. Barton, C. Willman, H. Ghezel-Ayagh, E. Tang, and M. Pastula, *Development of solid oxide fuel cells at versa power systems & fuelcell energy,* ECS Transactions **72**, 3 (2016).

[331] A. F. Molland, *The maritime engineering reference book: a guide to ship design, construction and operation* (Elsevier, 2011).

[332] M. Rivarolo, D. Rattazzi, and L. Magistri, *Best operative strategy for energy management of a cruise ship employing different distributed generation technologies,* International Journal of Hydrogen Energy **43**, 23500 (2018).

[333] R. Peters, R. Deja, M. Engelbracht, M. Frank, V. N. Nguyen, L. Blum, and D. Stolten, *Efficiency analysis of a hydrogen-fueled solid oxide fuel cell system with anode off-gas recirculation,* Journal of Power Sources **328**, 105 (2016).

[334] R. Napoli, M. Gandiglio, A. Lanzini, and M. Santarelli, *Techno-economic analysis of PEMFC and SOFC micro-CHP fuel cell systems for the residential sector,* Energy and Buildings **103**, 131 (2015).

[335] A. L. Facci, V. Cigolotti, E. Jannelli, and S. Ubertini, *Technical and economic assessment of a SOFC-based energy system for combined cooling, heating and power,* Applied Energy **192**, 563 (2017).

[336] H. Ammermann, P. Hoff, M. Atanasiu, J. Aylor, M. Kaufmann, and O. Tisler, *Advancing Europe's energy system: stationary fuel cells in distributed generation*, Tech. Rep. (Roland Berger, 2015).

[337] R. Scataglini, A. Mayyas, M. Wei, S. H. Chan, T. Lipman, D. Gosselin, A. D'Alessio, H. Breunig, W. G. Colella, and B. D. James, *A total cost of ownership model for solid oxide fuel cells in combined heat and power and power-only applications*, Tech. Rep. (Lawrence Berkeley National Laboratory, Environmental Energy Technologies Division, 2015).

[338] C. M. Milkie and A. N. Perakis, *Statistical methods for planning diesel engine overhauls in the US coast guard,* Naval Engineers Journal **116**, 31 (2004).

[339] F. Vogler and G. Sattler, *Hydrogen-fueled marine transportation,* in *Compendium of Hydrogen Energy* (Elsevier, 2016) pp. 35–65.

[340] P. Pei, Q. Chang, and T. Tang, *A quick evaluating method for automotive fuel cell lifetime,* International Journal of Hydrogen Energy **33**, 3829 (2008).

[341] M. Knowles, D. Baglee, A. Morris, and Q. Ren, *The state of the art in fuel cell condition monitoring and maintenance,* World Electric Vehicle Journal **4**, 487 (2010).

[342] H. Tu and U. Stimming, *Advances, aging mechanisms and lifetime in solid-oxide fuel cells,* Journal of Power Sources **127**, 284 (2004).

[343] N. Brandon, *Solid oxide fuel cell lifetime and reliability: critical challenges in fuel cells* (Academic Press, 2017).

[344] N. H. Menzler, D. Sebold, and O. Guillon, *Post-test characterization of a solid oxide fuel cell stack operated for more than 30,000 hours: The cell,* Journal of Power Sources **374**, 69 (2018).

[345] V. Zaccaria, D. Tucker, and A. Traverso, *Operating strategies to minimize degradation in fuel cell gas turbine hybrids,* Applied Energy **192**, 437 (2017).

[346] A. Cuneo, V. Zaccaria, D. Tucker, and A. Sorce, *Gas turbine size optimization in a hybrid system considering SOFC degradation,* Applied Energy **230**, 855 (2018).

[347] C. D. Rakopoulos and E. G. Giakoumis, *Diesel engine transient operation: principles of operation and simulation analysis* (Springer Science & Business Media, 2009).

[348] C. W. G. Engines, *Transient response behaviour of gas engines,* CIMAC (2011).

[349] A. A. Amamou, S. Kelouwani, L. Boulon, and K. Agbossou, *A comprehensive review of solutions and strategies for cold start of automotive proton exchange membrane fuel cells,* IEEE Access **4**, 4989 (2016).

[350] K. Nikiforow, J. Pennanen, J. Ihonen, S. Uski, and P. Koski, *Power ramp rate capabilities of a 5 kW proton exchange membrane fuel cell system with discrete ejector control,* Journal of Power Sources **381**, 30 (2018).

[351] Z. Liu, L. Li, Y. Ding, H. Deng, and W. Chen, *Modeling and control of an air supply system for a heavy duty PEMFC engine,* International Journal of Hydrogen Energy **41**, 16230 (2016).

[352] P. Sarkar, L. Yamarte, H. Rho, and L. Johanson, *Anode-supported tubular micro-solid oxide fuel cell,* International Journal of Applied Ceramic Technology **4**, 103 (2007).

[353] G. D'Andrea, M. Gandiglio, A. Lanzini, and M. Santarelli, *Dynamic model with experimental validation of a biogas-fed SOFC plant,* Energy Conversion and Management **135**, 21 (2017).

[354] M. Peksen, *Safe heating-up of a full scale SOFC system using 3D multiphysics modelling optimisation,* International Journal of Hydrogen Energy **43**, 354 (2018).

[355] J. Ki and D. Kim, *Computational model to predict thermal dynamics of planar solid oxide fuel cell stack during start-up process,* Journal of Power Sources **195**, 3186 (2010).

[356] M. Sorrentino, C. Pianese, and Y. G. Guezennec, *A hierarchical modeling approach to the simulation and control of planar solid oxide fuel cells,* Journal of Power Sources **180**, 380 (2008).

[357] D. Vrecko, G. Dolanc, B. Dolenc, D. Vrancic, B. Pregelj, D. Marra, M. Sorrentino, C. Pianese, A. Pohjoranta, and D. Juricic, *Feedforward-feedback control of a SOFC power system: a simulation study,* ECS Transactions **68**, 3151 (2015).

[358] K. Åström, E. Fontell, and S. Virtanen, *Reliability analysis and initial requirements for FC systems and stacks,* Journal of Power Sources **171**, 46 (2007).

[359] J. Ahn, S. H. Park, Y. Noh, B. I. Choi, J. Ryu, D. Chang, and K. L. M. Brendstrup, *Performance and availability of a marine generator-solid oxide fuel cell-gas turbine hybrid system in a very large ethane carrier,* Journal of Power Sources **399**, 199 (2018).

[360] E. Rillo, M. Gandiglio, A. Lanzini, S. Bobba, M. Santarelli, and G. Blengini, *Life cycle assessment (LCA) of biogas-fed solid oxide fuel cell (SOFC) plant,* Energy **126**, 585 (2017).

[361] R. Islam, H. Yu, R. Abbassi, V. Garaniya, and F. Khan, *Development of a monograph for human error likelihood assessment in marine operations,* Safety Science **91**, 33 (2017).

[362] F. Vogler, G. Würsig, D. Stolten, and T. Grube, *New developments for maritime fuel cell systems,* Schriften des Forschungszentrums Jülich/Energy & Environment (2010).

[363] T. Lingstädt, F. Grimm, T. Krummrein, P. Kutne, and M. Aigner, *Atmospheric experimental investigations of a jet-stabilized SOFC Off-gas combustor for a hybrid power plant operated with biogas,* in *AIAA Scitech 2019 Forum* (2019) p. 1677.

[364] D. Papurello, A. Lanzini, S. Fiorilli, F. Smeacetto, R. Singh, and M. Santarelli, *Sulfur poisoning in Ni-anode solid oxide fuel cells (SOFCs): deactivation in single cells and a stack,* Chemical Engineering Journal **283**, 1224 (2016).

[365] T. Lingstädt, F. Grimm, T. Krummrein, S. Bücheler, and M. Aigner, *Experimental investigation of a SOFC off-gas combustor for hybrid power plant usage with low heating values realised by natural gas addition,* in *Proceedings of the GPPS Forum 2018, Global Power and Propulsion Society* (2018).

[366] M. Kalikatzarakis, R. D. Geertsma, E. J. Boonen, K. Visser, and R. R. Negenborn, *Ship energy management for hybrid propulsion and power supply with shore charging,* Control Engineering Practice **76**, 133 (2018).

[367] T. Markus and P. P. S. Sánchez, *Managing and Regulating Underwater Noise Pollution,* in *Handbook on Marine Environment Protection* (Springer, 2018) pp. 971–995.

[368] H. Ozcan and I. Dincer, *Performance evaluation of an SOFC based trigeneration system using various gaseous fuels from biomass gasification,* International Journal of Hydrogen Energy **40**, 7798 (2015).

[369] L. K. C. Tse, S. Wilkins, and R. F. Martinez-Botas, *Dynamic modelling of a SOFC-GT hybrid system for transport applications,* in *European Ele-Drive Conference Brussels, Belgium* (2007).

[370] G. V. Huerta, J. Á. Jordán, M. Dragon, K. Leites, and S. Kabelac, *Exergy analysis of the diesel pre-reforming solid oxide fuel cell system with anode off-gas recycling in the schibz project. part i: Modeling and validation,* International Journal of Hydrogen Energy **43**, 16684 (2018).

[371] G. V. Huerta, J. Á. Jordán, T. Marquardt, M. Dragon, K. Leites, and S. Kabelac, *Exergy analysis of the diesel pre-reforming SOFC-system with anode off-gas recycling in the SchIBZ project. Part II: System exergetic evaluation,* International Journal of Hydrogen Energy **44**, 10916 (2019).

[372] W. S. Weidle, P. Field, and N. Buckley, *Arctic Ship Design Impacts: Green Arctic Patrol Vessel (GAPV) Project*, Tech. Rep. (2012).

[373] H. D. Sapra, Y. Linden, W. van Sluijs, M. Godjevac, and K. Visser, *Experimental investigations of hydrogen-natural gas engines for maritime applications,* in *ASME 2018 Internal Combustion Engine Division Fall Technical Conference*.

[374] H. Nakajima and T. Kitahara, *Real-time electrochemical impedance spectroscopy diagnosis of the solid oxide fuel cell for marine power applications,* Heat and Mass Transfer **54**, 2551 (2018).

[375] D. Song, X. Zhang, R. Neagu, and W. Qu, *Techno-economic analysis and feasibility study of a solid oxide fuel cell-battery hybrid system for water taxi application,* Journal of Electrochemical Energy Conversion and Storage **16**, 021010 (2019).

[376] Y. Welaya, M. Mosleh, and N. R. Ammar, *Thermodynamic analysis of a combined gas turbine power plant with a solid oxide fuel cell for marine applications,* International Journal of Naval Architecture and Ocean Engineering **5**, 529 (2013).

NOMENCLATURE

Acronyms

AC	alternating current
AIP	air-independent propulsion
AOGR	anode off-gas recirculation
APU	auxiliary power unit
ATR	autothermal reforming
BoP	balance of plant
CEM	controlled evaporator mixer
CFD	computational fluid dynamics
CHP	combined heat and power
CNG	compressed natural gas
CPOX	catalytic partial oxidation
DC	direct current
DeS	desulphurisation
DIR	direct internal reforming
DME	dimethyl ether
EEDI	energy efficiency design index
ER	Eley-Rideal
ESC	electrolyte supported cell
FO	first order
GC	gas composition
GDC	gadolinium doped cerium oxide
GHG	greenhouse gas
GT	gas turbine

HAP	hazardous air pollutants
HC	hydrogen-to-carbon
HRSG	heat recovery steam generator
HT	high temperature
HW	Hougen-Watson
IC	interconnect
IIR	indirect internal reforming
IMO	International Maritime Organization
IPFR	ideal plug flow reactor
ISM	integrated stack module
LH	Langmuir-Hinshelwood
LH_2	liquefied hydrogen
LHV	lower heating value
LNG	liquefied natural gas
LPG	liquefied petroleum gas
LSM	lanthanum strontium manganite
LT	low temperature
MCFC	molten carbonate fuel cell
MeOH	methanol
MGO	marine gas oil
MSR	methane steam reforming
NG	natural gas
NO_X	nitrous oxides
OC	oxygen-to-carbon
PAFC	phosphoric acid fuel cell
PEMFC	polymer electrolyte membrane fuel cell
PEN	positive electrode-electrolyte-negative electrode assembly
PL	power law

PM	particulate matter
PrOX	preferential oxidation
PSA	pressure swing adsorption
RAMS	reliability, availability, maintainability, safety
RE	reciprocating engine
SC	steam-to-carbon
SH	steam-to-hydrogen
SMET	selective methanation
SO_X	sulphurous oxides
SOFC	solid oxide fuel cell
SR	steam reforming
ST	steam turbine
TIT	turbine inlet temperature
VOC	volatile organic compound
WGS	water gas shift
WR	water recirculation
YSZ	yttrium stabilised zirconium oxide

Greek Symbols

α	global reaction order CH_4 [-]
β	global reaction order H_2O [-]
δ	relative exergy loss [-]
η	efficiency [-] or [%]
γ	global reaction order H_2 [-]
$\hat{\beta}$	global electrochemical reaction order H_2O [-]
$\hat{\epsilon}$	global electrochemical reaction order O_2 [-]
$\hat{\eta}$	electrochemical overpotential [V]
$\hat{\gamma}$	global electrochemical reaction order H_2 [-]

ι	tortuosity factor [-]
κ	ratio of specific heats [-]
λ	thermal conductivity [W m^{-1} K^{-1}]
ν	stoichiometric reaction coefficient [-]
ω	symmetry factor [-]
Φ	Mason function [-]
ϕ	fugacity constant [-]
Π	pressure ratio [-]
ρ	density [kg m^{-3}]
σ	electrical conductivity [S m^{-1}]
τ	thickness [m]
θ	surface coverage [-]
ε	porosity [m^3 m^{-3}]
ϑ	reaction coordinate [-]

Roman Symbols

$\bar{A}$	pre-exponential adsorption factor [bar^{-x}]
A	area [m^2]
a	activity [-]
C	thermal conductivity coefficient [W m^{-1} K^{-2}]
c_p	heat capacity [J mol^{-1} K^{-1}]
D	diffusion coefficient [m^2 s^{-1}]
d	diameter [m]
$\dot{Ex}$	exergy flow [W]
E_a	activation energy [J mol^{-1}]
ex	specific exergy [J mol^{-1}]
F	Faraday constant [s A mol^{-1}]
f	fraction [-]

$\Delta\bar{G}$	Gibbs free energy change of adsorption [J mol^{-1}]
ΔG	Gibbs free energy change of reaction [J mol^{-1}]
$\bar{h}$	heat transfer coefficient [W m^{-2}]
$\Delta\bar{H}$	enthalpy change of adsorption [J mol^{-1}]
ΔH	enthalpy change of reaction [J mol^{-1}]
h	specific enthalpy [J mol^{-1}]
I	current [A]
j	current density [A m^{-2}]
$\bar{K}$	adsorption constant [bar^{-x}]
$\hat{k}_0$	pre-exponential factor exchange current density [A m^{-2}]
K	chemical equilibrium constant [-]
k	reaction rate constant [mol Pa^x s^{-1} m^{-2}]
k_0	pre-exponential factor reaction constant [mol Pa^x s^{-1} m^{-2}]
L	total length [m]
l	longitudinal coordinate [m]
M	molecular mass [g mol^{-1}]
$\dot{n}$	molar flow [mol s^{-1}]
N	number [-]
Nu	Nusselt number [-]
$\bar{P}$	power density [W$_e$ kg^{-1}], [W$_e$ l^{-1}] or [W m^{-2}]
P	power [W]
p	pressure [Pa] or [bar]
$\dot{Q}$	heat flux [W]
$\dot{q}$	relative heat loss [-]
Q	reaction quotient [-]
$\bar{R}$	universal gas constant [J mol^{-1} K^{-1}]
$\bar{r}$	mean pore radius [m]
R	area specific resistance [Ω m^2]

r	reaction rate [mol s^{-1}]
RR	recirculation ratio [-]
$\Delta\bar{S}$	entropy change of adsorption [J mol^{-1} K^{-1}]
∇T	temperature gradient [K cm^{-1}]
s	specific entropy [J mol^{-1} K^{-1}]
T	temperature [°C]
t	time [s]
U	voltage [V]
u	utilisation factor [-]
$\dot{V}$	volumetric flow [Nl min^{-1}]
V	volume [m^3]
$\bar{W}$	energy density [Wh_e kg^{-1}] or [Wh_e l^{-1}]
w	width [m]
x	conversion [-]
y	mole fraction [mol mol^{-1}]
z	number of electrons exchanged [-]

Superscripts

0	standard conditions
in	inlet
out	outlet

Subscripts

0	reference
aa	active area
act	activation
ad	adsorption
an	anode

aux	auxiliary
ca	cathode
ch	channel
$chem$	chemical
$comp$	compressor
$conc$	concentration
cv	control volume
eff	effective
el	electrolyte
env	environment
eva	evaporator
f	fuel
g	gas
gen	generator
gl	global
h	hydraulic
hex	heat exchanger
i	species i
ins	insulation
is	isentropic
j	species j
k	Knudsen
m	reaction m
$mech$	mechanical
ms	moisture separator
n	constant number
ohm	ohmic
ox	oxygen

ref	reformer
s	solid
sp	single pass
th	theoretical
tm	thermo-mechanical
tpb	triple phase boundary
$turb$	turbine

ACKNOWLEDGEMENTS

The past couple of years has been an incredible journey. I've considered it a privilege to work on cutting edge technology which might contribute to the reduction of the environmental impact of shipping. Of course, a lot of people have contributed to the completion of that journey in many different ways. Although I realise that it is impossible to give proper credit to all of them here, I would like to take this opportunity to express my gratitude to some of them.

First and foremost I want to thank my promotors, prof. dr. Aravind and Rear-Admiral (ME, ret) ir. Klaas Visser, without whom I would not have been able to complete this dissertation. Thank you Aravind, I truly enjoyed the numerous interesting discussions we had, from the very fundamentals of fuel cell technology and its application in ships to the wider societal implications. You always motivated me to strive for high academic standards and present my work on renown international conferences.

Klaas, thank you for arranging a position for me in the team and introducing me to the world of Marine Engineering. Your trust in my abilities has been essential for my personal development. Thank you for giving me the opportunity to involve with others working in the field, such as in the Maritime Hydrogen expert working group of the International Energy Agency. Your enthusiasm and optimism on technology development and ability to change the tables is inspiring.

Thank you dr. Milinko Godjevac for all the interesting discussions and support. Your comments definitely helped to see my work from a different perspective. The thermodynamic analysis would not have been possible without the assistance of ir. Theo Woudstra, who introduced Cycle-Tempo to me. Thank you dr. ir. Aditya Thallam Thattai and dr. Liyuan Fan, I may not have pursued a PhD on this topic without our cooperation on methane steam reforming kinetics during my graduation project. I am proud on what we have learned and happy to see that all three of us authored a publication on this interesting topic.

I was fortunate to work closely together with my paranymphs, Harsh Sapra and Jelle Stam, in the GasDrive project. Thank you both for the excellent cooperation in the past few years, many interesting discussions, a healthy dose of sarcasm, but most of all for being an excellent and joyful company. I would also like to thank the other researchers active in the GasDrive project. Celia Wei and Pim Bullee, we had fun times during our PhD team meetings and your work is an enrichment for the project. Our discussions on society, culture and politics were always very interesting dr. Ali Haseltalab, I am happy to see that you will bring your knowledge on electrical system integration and control to the GasDrive project. A big thanks to prof. dr. Rudy Negenborn: GasDrive would not have run half as smooth without your efforts.

The GasDrive project could not commence without the financial support of Boskalis, Damen, Defence Material Organisation, Feadship, Pon Power, Oceanco, Royal IHC and Wärtsilä. I want thank the industrial members, Isaac Barendregt, Teus van Beek, Michel

Janssen, Pieter van Loon, Evy de Maeyer, Gert-Jan Meijn, Joost Schapendonk, Wim van Sluijs, Fabien Vispoel and Joost Wijnands, and the academic staff of Wageningen University & Research and University of Twente, prof. dr. Tinka Murk and dr. Edwin Foekema, prof. dr. ir. Rob Lammertink, for their valuable contributions during the user committee meetings.

'In learning you will teach, and in teaching you will learn' (Phil Collins): I had the pleasure of working with excellent MSc students during their graduation project. Thank you Floris van Nievelt and Pietro Uva for your efforts, I hope you learned as much from me as I learned from you. A special word of thanks to you, Mark Azzopardi, for laying the foundations for the dynamic SOFC model in your thesis.

This work would not have been possible without all the support from and discussions with other colleges the M&TT and P&E departments. First of all Marc and Rinze, for many interesting and entertaining coffee breaks. Thanks Jie, Johan and Wenbin for creating a nice office environment, and Bas, Menno, Thijs and Xiao for the nice cooperation organising the M&TT PhD lunch events. A very big thanks to Anouk, Dineke, Monique, Patty and Pauline, the department cannot function without your support. I would also like to express my gratitude to the workshop of P&E for the assistance during the experiments.

I want to thank the M&TT staff, Austin, Arthur, Chris, Douwe, Erik, Henk, Hans, Harleigh, Jenny, Jeroen, Koos, Peter, Robert, Roelf and Udai, for creating a warm, collegial and hospital environment, and of course my fellow PhDs, Agnieta, Alina, Carmen, Christopher, Etienne, Erik, Faisal, Ioana, Jun, Jurrit, Kanu, Koen, Lode, Nikos, Pranav, Quingsong, Sui and Tom for the support and discussions in these fun and interesting years. A very big cheers to the fuel cell team, Alessandro, Ali, Alvaro, Ana, Giulia, Hrishikesh, Mayra, Pradeep, Tabish, Vikrant, Vincent and Yashar for the good times we shared. You really made me feel like one of the team!

I am grateful that Royal IHC provided the opportunity to continue my research on this very interesting topic in industry. I want to thank all my colleges at MTI for welcoming me and introducing me to the company, and of course for their patience and understanding in the final phase of my PhD. A special thank you goes to the New Fuels and Drives team: Benny, Bernardete and Henrik, it is a pleasure to work with you.

Where would I be without friends and family? Thanks Jörn and Martin for all the hours we spend together on the racing bike discussing any aspect of life: Mens sana in corpore sana. I want to thank my parents, Kees and Marianne for their unconditional support. A big thanks to loving and supportive siblings, Mendel, Sterre, Briënne, Daam, Reimer and Aidan, what a family we are! Thanks Meike, Mark, Floris and Elies, it makes me happy to see the family extended with such nice people. Thank you Tom, Anja, Joren, Elja en Ruben, the family van der Horst really feels like a second familie to me.

That brings me to the most important person: Dear Sanne, you are the love of my life, what more can I say? Home is where the heart is, and you have been that solid, loving home base for over eight years already. Thank you for all your patience, understanding and support, but most importantly for always being there for me. Nothing can make me more happy and proud than being able to write here that you are my fiancee. I'm looking forward to our future together, curious to see what it will bring us.

Lindert van Biert, Rotterdam, January 2020

CURRICULUM VITÆ

Lindert VAN BIERT

23-04-1990 Born in Rotterdam, the Netherlands

EDUCATION

2002–2009 Secondary School
Stichtse Vrije School, Zeist, the Netherlands

2009–2012 Bachelor of Science in Mechanical Engineering
Delft University of Technology, the Netherlands

2012–2014 Master of Science in Mechanical Engineering
Delft University of Technology, the Netherlands
Track: Process & Energy Technology
Thesis: Direct internal methane steam reforming in operating solid oxide fuel cells: a kinetic modelling approach

2015–2020 Doctor of Philosophy
Delft University of Technology, the Netherlands
Thesis: Solid oxide fuel cells for ships: system integration concepts with reforming and thermal cycles
Promotor: prof. dr. P. V. Aravind
Copromotor: ir. K. Visser

EXPERIENCE

2019–present Research & Developer, *New Fuels and Drives*
MTI part of Royal IHC, Delft, the Netherlands

2013–2014 Research intern
University of Cambridge, United Kingdom

LIST OF PUBLICATIONS

JOURNAL PUBLICATIONS

7. **L. van Biert**, K. Visser, P. V. Aravind, *A comparison of steam reforming concepts in solid oxide fuel cell systems*, Submitted to Applied Energy.

6. **L. van Biert**, K. Visser, P. V. Aravind, *Intrinsic methane steam reforming kinetics on nickel-ceria solid oxide fuel cell anodes*, Journal of Power Sources **443**, 227261 (2019).

5. **L. van Biert**, M. Godjevac, K. Visser, P. V. Aravind, *Dynamic modelling of a direct internal reforming solid oxide fuel cell stack based on single cell experiments*, Applied Energy **250**, 976 (2019).

4. **L. van Biert**, T. Woudstra, M. Godjevac, K. Visser, P. V. Aravind, *A thermodynamic comparison of solid oxide fuel cell-combined cycles*, Journal of Power Sources **397**, 382 (2018).

3. A. Thallam Thattai, **L. van Biert**, P. V. Aravind, *On direct internal methane steam reforming kinetics in operating solid oxide fuel cells with nickel-ceria anodes*, Journal of Power Sources **370**, 71 (2017).

2. **L. van Biert**, M. Godjevac, K. Visser, P. V. Aravind, *A review of fuel cell systems for maritime applications*, Journal of Power Sources **327**, 345 (2016).

1. L. Fan, **L. van Biert**, A. Thallam Thattai, A. H. M. Verkooijen, P. V. Aravind, *Study of Methane Steam Reforming kinetics in operating Solid Oxide Fuel Cells: Influence of current density*, International Journal of Hydrogen Energy **40**, 5150 (2015).

CONFERENCE PROCEEDINGS

4. S. Jafarzadeh, I. Schjølberg, K. Visser, **L. van Biert**, R. d'Amore-Domenech, A. Villalba-Herreros, T. J. Leo, *Fuel cell solutions for maritime applications: possibilities and challenges*, 22nd World Hydrogen Energy Conference (WHEC). Rio de Janeiro, Brazil. (2018).

3. **L. van Biert**, A. Thallam Thattai, P. V. Aravind, *Predicting MSR rates in SOFCs using experimental data and CFD methods*, ECS Transactions **78**, 2823 (2017).

2. **L. van Biert**, K. Visser, P. V. Aravind, *Fuel cell systems for ships and pleasure boats*, International Conference on Battery and Fuel Cell Technology. Dubai, UAE. (2016).

1. **L. van Biert**, K. Visser, P. V. Aravind, *A thermodynamic analysis of integrated SOFC cycles for ships*, Proceedings of the 12th European SOFC & SOE Forum 2016. Luzern, Switzerland. (2016).

SOLID OXIDE FUEL CELLS AND SHIPS: A HAPPY MARRIAGE?

For decades, ships have been propelled by diesel engines. However, there are increasing concerns about their environmental impact. Fuel cells can provide an alternative to convert fuels directly into electricity, with high efficiencies and without hazardous emissions.

Solid oxide fuel cells have a ceramic membrane, which functions at high temperatures. This makes them less prone to contamination, allows internal conversion of various fuels and enables integration with thermal cycles to achieve high combined efficiencies.

So are ships and solid oxide fuel cells a match made in heaven? This dissertation breaks ground on the challenges and opportunities regarding the application of solid oxide fuel cells in ships, internal fuel reforming and integration with thermal cycles.

How do solid oxide fuel cells compare to other power plants? How can we compare different system integration options? Does internal fuel reforming affect the efficiency and lifetime? Can cell experiments provide useful information on overall system performance? These are among the questions addressed in this dissertation.

The reader will learn how solid oxide fuel cell integration with reforming and thermal cycles can provide power on ships with high efficiency and reliability, no pollutant emissions and low noise, but also about the challenges and opportunities of this potentially budding love.

ISBN 987-94-6366-248-2